EXECUTIVE SUMMARY

The aim of the thesis is the identification and modelling of the dominant failure mode in hot forging tooling, used in the production of nickel based superalloy compressor blades.

A preliminary study identified the most frequently occurring part defects that cause tool failure. The forming process was characterised, relevant tooling failure modes were identified and the mechanical properties and microstructure of the tooling was reviewed.

Case studies have been performed identifying the observable damage in worn tooling and investigating the conditions that result in tool failure. The investigation made use of finite element analysis, metrology, metallurgical analysis and thermal measurement. The dominant failure mode was associated with the plastic deformation of the tooling.

Testing was performed to gather sufficient data to allow for the development of a lifing model. Isothermal tensile and fatigue tests were performed under temperatures and strain rates representative of hot forging tooling conditions. The microstructural instability during these conditions was investigated.

A literature review explored state of the art approaches to modelling the plastic flow behaviour of tempered martensitic tool steels for the purpose of tool life prediction.

A lifing model was developed to describe the plastic flow behaviour of tempered martensitic steel. A physical based model developed to describe the creep behaviour of 9-12%Cr tempered martensitic steel has been applied to describe the thermo-mechanical fatigue behaviour of 5%Cr tempered martensitic hot work tool steel.

The model was verified by comparing model predictions to experimental data not used in the development of the model. The model was then applied to predict the life of tooling examined in the case studies. The life predictions were within a factor of 10 from measured die lives measured from the forge.

CONTENTS

Figure list

Table List

1 THE RESEARCH AREA AND MOTIVATION

In hot forging, the workpiece is forced into impressions cut into blocks of material. The blocks with the impressions are called dies or tooling. In the hot forming of nickel based superalloy, the dies suffer high cyclical thermal and mechanical loads. These conditions result in the degradation of the impression, resulting in defects imprinted upon the workpieces. When the part defects develop to a critical amount, the dies have failed, and acceptable workpieces can no longer be formed. The part defect may be a feature affecting the surface finish and\ or the dimensions of the parts formed.

The life of a die not only limits production capacity, but also incurs a significant cost for forging companies. The costs associated with replacing a die include: reduced productivity due to press down time, the cost of manufacturing the new die, and the time taken to set up the press with the new tooling (Cser et al. 1993). The performance measures of hot forming tooling include the total number of parts produced by a die and the quality of the parts produced. The quality of the parts produced affects the extent of rectification operations required.

Multiple operations may be required to change the form of the workpiece into the desired geometry. The intermediate shapes of the workpiece are described as preforms.

The research is interested in identifying and modelling the dominant cause of failure for dies used in the preforming operations in the production of single ended aerofoil blades made out of nickel based superalloy, IN718. The dies are made out of tempered martensitic hot work tool, AISI H13.

The motivation for the development of die life prediction capability includes the ability to improve die life through preform design optimisation, to improve production planning, and to improve die life through optimisation of process parameters.

1.1 RESEARCH AIMS AND OBJECTIVES

Many failure modes contribute to die failure in the tooling used to hot forge nickel alloy components. The failure modes interact to result in the degradation of the die, which results in part defects that cause die failure. The manner in

which the failure modes interact may be defined as the failure mechanism. This is illustrated in Figure 1-1.
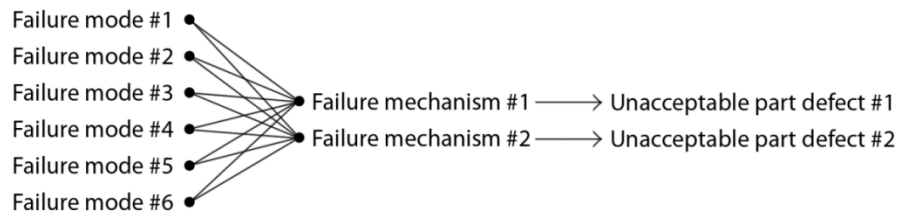
FIGURE 1-1: FAILURE MODES, MECHANISMS AND PART DEFECTS

Examples of failure modes include plastic deformation, abrasive wear, thermal softening and so on. In the context of this thesis, the failure mechanism describes how the failure modes interact to result in the part defect that fails the dies. To determine the dominant failure mode, the failure mechanism must be understood.

The failure mechanism differs depending upon factors such as the workpiece material, the workpiece temperature, the type of press, the press settings, the use of lubrication, die material, the die temperature and the extent of deformation. Process variation may contribute to die failure.

The purpose of this research is to identify the dominant failure mode that dictates life and model the failure to allow life prediction. These aims are summarised below:

a) To identify the dominant failure mode that results in die failure in the hot forming operations of Nickel based superalloy aerofoil blades.

b) To model the dominant damage mode and predict die life.

To satisfy these aims the following objectives are necessary.

1. Characterise the forming process, identify relevant failure modes and evaluate the die material.

2. Perform a failure analysis investigation to identify the dominant failure mode in the forging operations.

3. Perform a literature review into lifing models describing the dominant failure mode.

4. Characterise the die material with respect to the dominant failure mode.

5. Develop the lifing model.

6. Verify the lifing model.

7. Apply the lifing model.

1.2 RESEARCH METHODOLOGY

The research methodology may be split into two stages; a failure analysis methodology applied to investigating the dominant failure mode of the hot forging tooling, and a lifing methodology applied to life prediction of hot forging tooling.

1.2.1 FAILURE ANALYSIS

The failure analysis methodology followed the Six Sigma DMAIC process. This approach was adopted as it was the preferred choice of the manufacturer. The phases of this method are outlined below (Antony et al. 2006; John et al. 2009):

Define: Describe the problem, identify the stakeholders in the project, identify the project goals and create the project charter.

Measure: Determine the variables that need measured, implement measurement techniques of suitable accuracy and collect data. Use statistical tools to examine the data.

Analyse: Identify and verify potential causes of the problem. Determine relationships between the output, process and input. Determine the root cause(s) of the problem.

Improve: Generate and evaluate potential solutions to the problems. Develop and plan the implementation of the improvements. Implement the solutions and measure the response.

Control: Ensure the sustainable and long term success of the project.

The DMAIC project was performed by a multidisciplinary team consisting of the author, Kenny McGuire (Manufacturing Engineer), Ravi Kapur (Metallurgist) and led by Russell Teeling (Forge Manager).

As part of the measure phase, a preliminary study identified the part defects produced as a result of the forging process. A die life measurement system was implemented to gather statistical data to determine the most frequently occurring causes of die failure. Statistical analysis was performed to examine relationships between measured variables.

The work documented in this thesis refers to the "analyse" phase of the DMAIC process. An Ishikawa graph was constructed to assist in identifying the potential root causes of die failure. A failure analysis was performed upon worn tooling obtained from controlled conditions. The investigation was performed following the guidelines given by Aliya (2002). Care was taken to preserve evidence that relates to tool failure and tests were performed in order of least destructive to most destructive.

Sampled forged components were inspected and the worn tooling was obtained under known conditions. The forging process was maintained within the conditions specified by the forge.

The workpiece temperature and die temperature was kept within the process specifications of the component. A complimentary investigation analysed process variation within the forge (Jadhav 2011).

The examination of the worn tooling allowed for the identification of the failure modes that contribute to failure. The progression of the part defects that led to die failure was assessed qualitatively through examining sampled forged components.

The tooling was measured using a 3D scanner before and after the forging trial. The difference in geometry measured was used to assess the location and magnitude of damage to the tooling.

Metallurgical samples were taken at critical locations on the tool. The specimens allowed the examination of the damages surface layers using light microscopy.

Hardness measurements were taken to examine changes in material condition as a result of forging.

Finite element analysis (FEA) was used to simulate the forging process. The finite element models were used to approximate the magnitude of die stress and temperature during a forging operation.

The temperature of the tooling during a production run was measured using a thermal camera. The tool temperature was of interest to understand the role of thermal softening. Non-contact thermal measurement was chosen over the use of thermocouples to mitigate disruption to production. Contact measurement of the die surface at the location of interest is difficult due to the stresses exerted upon the dies.

From these observations and measurements, the failure mechanism was evaluated and the dominant failure mode was identified.

1.2.2   LIFING

The approach taken to die life prediction consists of determining the thermo-mechanical loading responsible for die failure, the material response to the thermo-mechanical loading with respect to failure, and the failure criteria. This is illustrated in Figure 1-2.
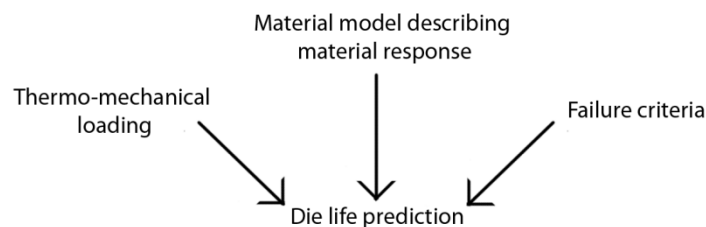
FIGURE 1-2: DIE LIFE PREDICTION REQUIREMENTS

The thermo-mechanical loading describes the loading of the die during a forging cycle. The press exerts a force on to the workpiece. The plastically deforming workpiece exerts a force on to the tooling. The die increases in temperature due to heat transferred from the workpiece and heat generated by friction.

The material response of the tooling is temperature dependent. The material response is strain rate sensitive at high temperature, above the tempering

temperature of the tool steel. Hot work tool steel is known to over-temper during use as hot forging tooling and soften under fatigue loading.

The lifing model describes the degradation of the tooling, resulting in the development of a part defect that fails the tooling. The failure criterion describes the limit to the degradation in the die material.

Finite element analysis has been used to approximate the thermo-mechanical loading of the tool at the location of failure. A failure criterion was developed considering the manner in which the tool failed. The material model describes the relevant material behaviour under the conditions of interest.

1.3   RESEARCH CONTRIBUTIONS

1.3.1   FAILURE ANALYSIS

The plastic deformation of the substrate has been found to be the cause of die failure in nitrided tooling used in the hot forging of nickel based superalloy using a crank press, glassed workpieces and water based graphite lubrication.

The implication of this finding is significant in that the surface degradation of the die may be addressed through improving the resistance to plastic deformation of the substrate opposed to improving the wear resistance of tool surface.

The finding is relevant to similar case hardened hot forging dies that experience high thermo-mechanical loads but have sufficient toughness to avoid failure through catastrophic failure.

1.3.2   MODEL DEVELOPMENT

The physical based models developed to describe the creep behaviour of 9-12% Cr tempered martensitic steel have been examined with respect to the thermo-mechanical fatigue behaviour of 5%Cr-Mo-V tempered martensitic hot work tool steels. The Dyson-Semba model has been adapted to describe the plastic flow behaviour of tool steel. The Basoalto model has been applied to describe athermal behaviour. Athermal behaviour has been identified by regimes where the material does not display significant strain rate sensitivity.

1.3.3   LIFE PREDICTION

A life prediction model has been developed for tooling that fails through plastic deformation. The approach taken describes the thermo-mechanical loading at a representative location of the tool. The failure criterion is based upon the critical amount of strain approximated from failed tooling.

The impact of process variation has been included by varying the die stress and temperature between cycles. The softening resulting from repeated nitriding of the tooling has been taken into account. The impact of variation between batches of die material may be included through variation in the mean values used to describe microstructural features. The lifing model is capable of predicting scatter similar to that observed within the forge with die life predictions an order of magnitude in difference from measured life.

1.4   THESIS STRUCTURE

The thesis has been structured to reflect the objectives outlined in section 1.1. The structure and content of the thesis is shown in Figure 1-3.
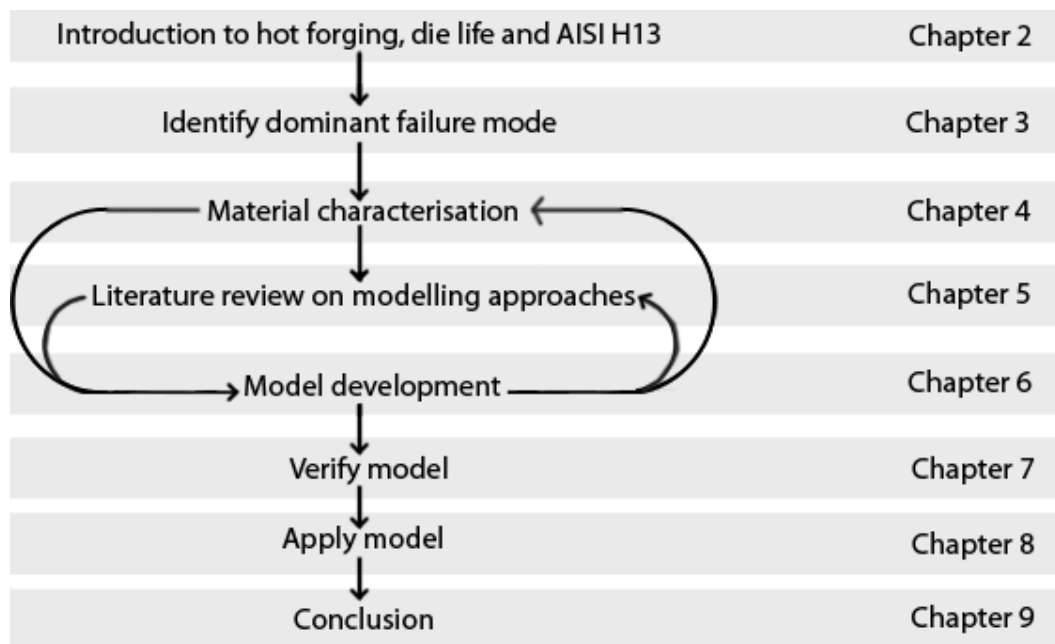
FIGURE 1-3: RESEARCH METHODOLOGY AND THESIS STRUCTURE

Chapter 2 consists of a literature review describing the forging process, relevant failure modes, and the die material.

Chapter 3 presents the findings of the failure analysis performed upon the forging operations of interest. The analysis consists of metrology, metallurgy and finite element analysis. The outcome of chapter 3 is the dominant failure mode that dictates die life.

Chapter 4 describes the material characterisation performed to measure the mechanical properties relevant to the dominant failure mode. Microstructural instability is examined with respect to the observed behaviour and behaviour reported from the literature.

Chapter 5 contains a literature review describing approaches to modelling the dominant failure mode identified in chapter 3. The merits of the different approaches are discussed.

Chapter 6 outlines the development of the lifing model. The model describes the change in material behaviour relevant to the dominant failure mode and the thermo-mechanical loading of hot forging tooling. The developed model builds upon existing models reported in chapter 4.

Chapter 7 tests the developed model. Verification tests determine the ability of the model to predict measured material behaviour relevant to life prediction and to evaluate the conditions where the model may be accurately applied.

Chapter 8 applies the model to predict die life. The model has been applied to determine whether similar die lives may be predicted to those observed in the forge.

Chapter 9 summarises the research contribution. Future work and areas of concern have been highlighted.

2 BLADE FORMING, DIE LIFE AND HOT WORK TOOL STEEL

This chapter describes the forming process of interest, the relevant ways in which hot forging dies fail and the microstructure of the die material. This information is required to investigate the failure of hot forging tooling.

The forming process of interest is the hot extrusion and upsetting of nickel based superalloy, using a mechanical crank press. Key process parameters include the workpiece temperature, the die temperature, the geometry of the workpiece, the geometry of the tooling, the press kinetics, and lubrication.

The failure modes and material behaviour relevant to extrusion and upsetting tooling include wear, corrosion, plastic deformation, thermal softening/ over-tempering, thermal fatigue and mechanical fatigue.

The die material of interest is AISI H13, a high chromium hot work tool steel. The performance of the tooling may be linked to material properties. The material properties are a result of the microstructure. Important microstructural features include the particle phases, martensitic laths and dislocation structure.

2.1 THE HOT FORMING OF IN 718 COMPRESSOR BLADES

The manufacturing processes of interest within this work focus on the pre-forming operations in the production of single ended aerofoil blades. The preform geometries in the hot forming of single ended aerofoil blades are illustrated in Figure 2-1.
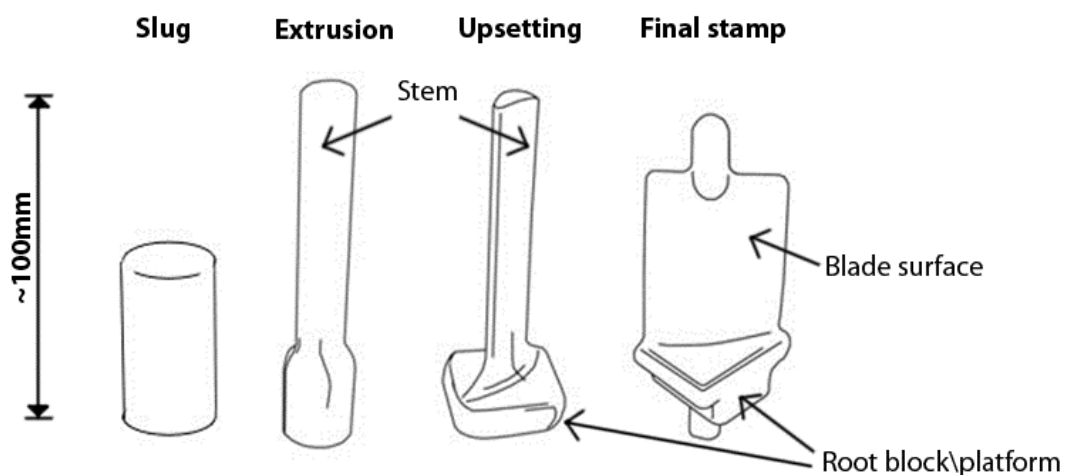
FIGURE 2-1: THE WORKPIECE GEOMETRIES IN THE FORMING OF SINGLE ENDED COMPRESSOR BLADES

The initial workpiece geometry is cylindrical with filleted edges. The first operation is an extrusion operation, to start forming the stem. The second operation is an upsetting operation which forms the root block of the aerofoil blade. The final operation forms the aerofoil blade geometry and completes the root block. The trimming of the flash produced in the final operation is not shown.

The purpose of the research is to identify and model the dominant failure mechanism of the dies used in the extrusion and upsetting operations.

2.1.1   THE WORKPIECE MATERIAL PROPERTIES

The workpiece material of interest is Inconel 718. The workpiece material properties of interest include the flow stress and thermal properties of the alloy. The flow stress impacts the required forging load. The thermal properties impact how the workpiece retains and diffuses heat during the forging operation.

The flow stress of Inconel 718 is highly temperature and strain rate sensitive, making it a difficult alloy to forge. The flow stress is shown in Figure 2-3 (Prasad 1997). The forging operation of interest is performed on a mechanical crank press to reduce the contact time between the workpiece and the die, reducing the heat lost from the workpiece. The trade-off is that the fast ram speed results in high workpiece strain rates, and thus high workpiece flow stresses.

The temperature of the workpiece is important as it impacts the flow stress, and thus the stress imparted onto the tooling. The workpiece loses heat upon removal of the furnace. Heat is lost to the environment through convection, radiation and conduction with the tongs used to transfer the workpiece. When the workpiece is positioned upon the tooling, heat is lost with the environment through convection and radiation and conduction with the tooling. The reduced temperature of the workpiece incurs higher flow stress. The increased flow stress caused by the heat lost through conduction between the workpiece and the tooling is known as the die chilling effect. The thermal properties of the workpiece are shown in Figure 2-2.
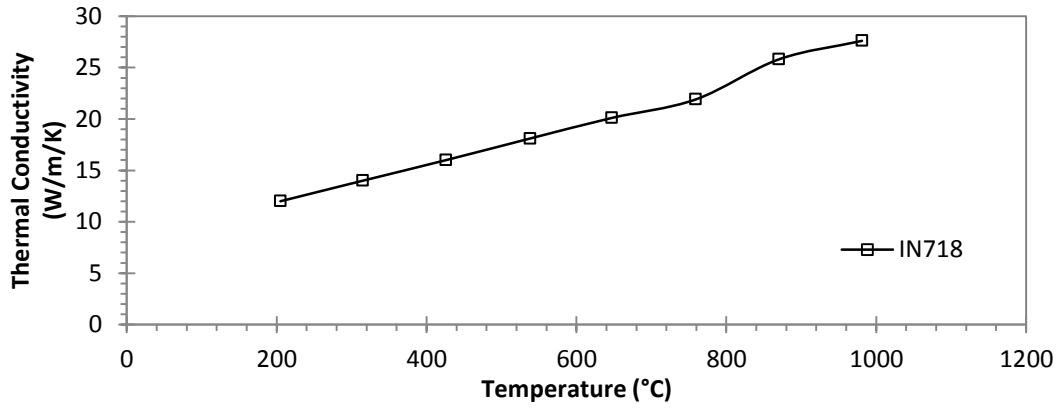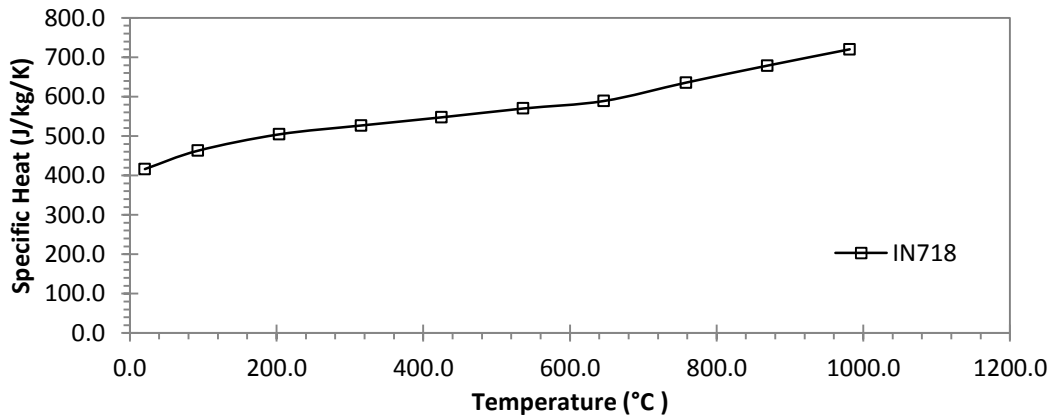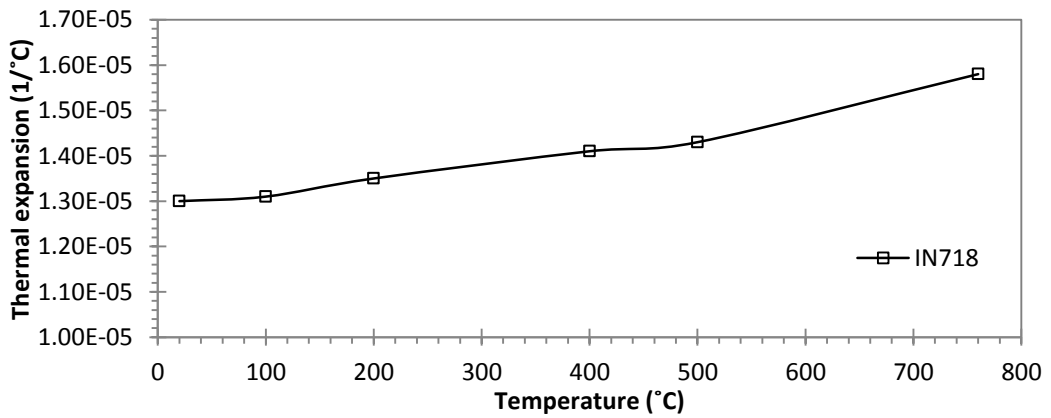
FIGURE 2-2: WORKPIECE MATERIAL PROPERTIES (AFRC, 2010)
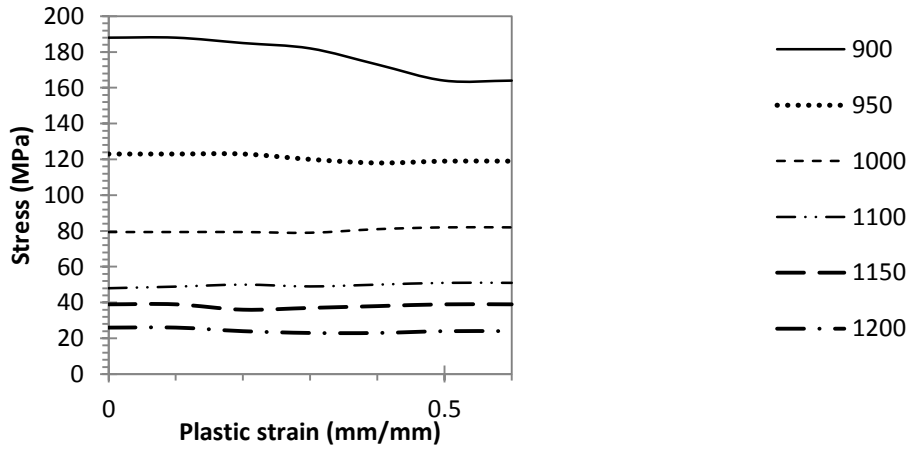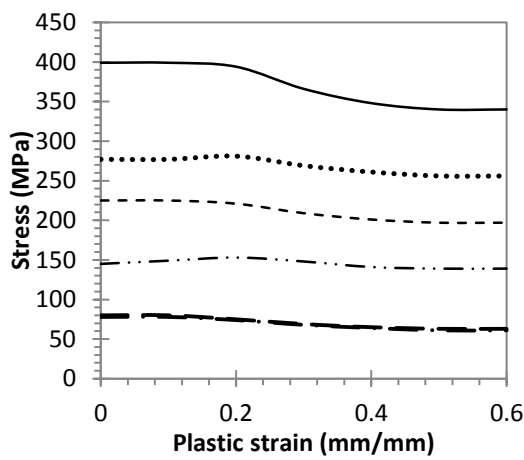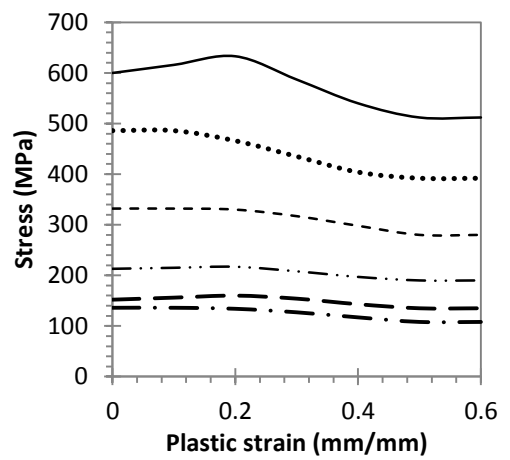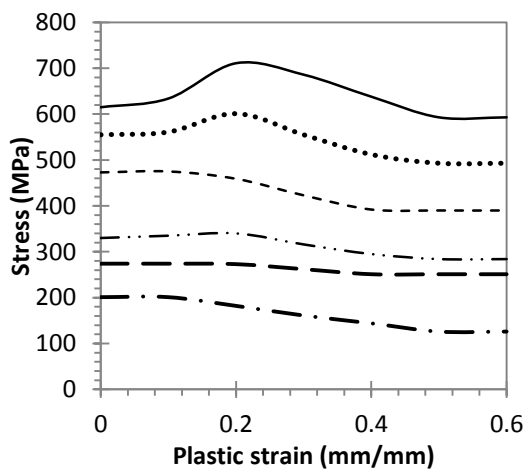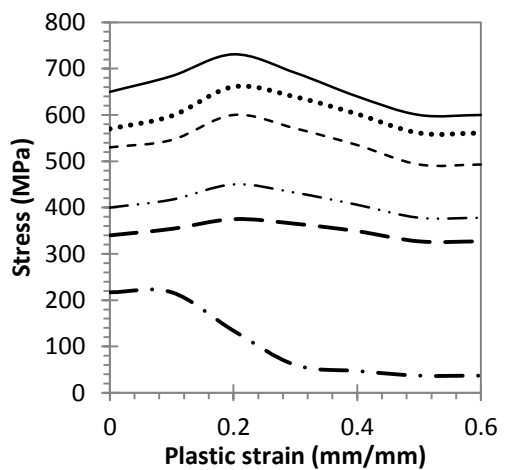
FIGURE 2-3: FLOW STRESS BEHAVIOUR OF IN 718 (PRASAD 1997)

2.1.2 THE DIE MATERIAL PROPERTIES

The die material of interest is AISI H13 hot work tool steel. The properties of interest include the yield strength, the fracture toughness, and thermal properties of the alloy. The manufacturer has chosen this material for the combination of strength and toughness and better hot strength in comparison to alternatives such as AISI H11. The chemical composition of the H13 hot work tool steel is given in Table 2-1.

TABLE 2-1: CHEMICAL COMPOSITION OF H13 HOT WORK TOOL STEEL (WT. %)

Cr	Mo	V	C	Mn	P	S	Ni	Fe	Si
5.139	1.231	0.847	0.361	0.393	0.019	0.006	0.411	bal	1.023

The carbon content dictates strength and hardness however coarse carbides are detrimental to toughness. Chromium, tungsten, titanium, molybdenum and manganese are carbide forming elements (Bazazi 2009). Chromium and Molybdenum act as solid solution strengtheners and Molybdenum also acts to suppress temper embrittlement (Smoljan 2009).

The die material of interest is heat treated to tempered martensite of hardness ranging between 52 to 54HRC. The tool steel is heat treated with a fluidised bed furnace under a nitrogen atmosphere. The heat treatment process is shown in Figure 2-4.
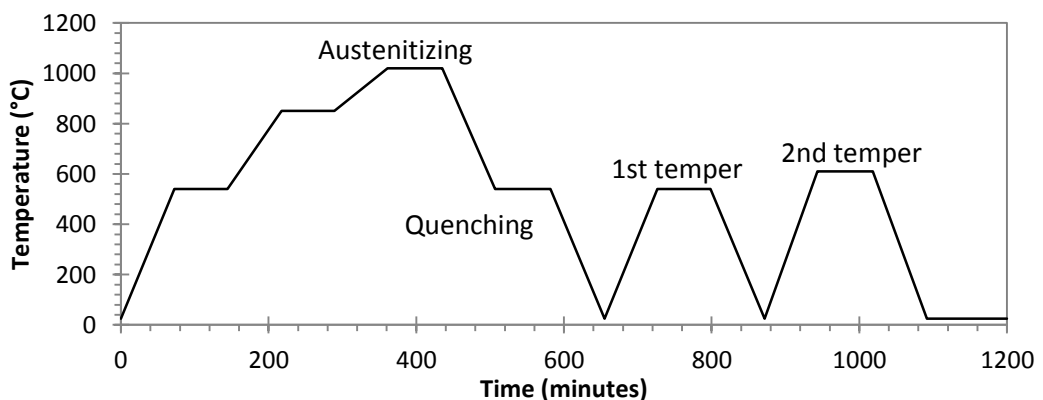
FIGURE 2-4: HEAT TREATMENT OF AISI H13

The initial microstructure prior to heat treatment is ferritic. The ferrite transforms into Austenite during the Austenitization process. The Austenite transforms into martensite during the quenching process. Particles precipitate during the quenching operation. During the tempering operation, the martensite relaxes into tempered martensite and particles continue to precipitate, grow and coarsen. The particle phases may be categorised as either primary particles or secondary particles. Secondary particles precipitate during tempering whilst primary particles are present in the as-quenched condition.

The temperature sensitivity of yield strength and toughness of AISI H13 is shown in Figure 2-5. In figure a), it can be seen that the strength of the material declines at high temperature, making the material more susceptible to wear and plastic deformation. In figure b), it can be seen that H13 displays good hot toughness.

A polynomial equation has been used to fit the temperature sensitivity of the 0.2% proof stress of AISI H13 shown in Figure 2-5b). This is shown in equation 2-1 (Bohler 2010).

$$\sigma_{0.2} = -5.94 \times 10^{-6}T^3 + 0.00344T^2 - 1.30T + 1420 \qquad \textbf{2-1}$$

Where;

$\sigma_{0.2}$ The 0.2% proof stress (MPa)

T Temperature (°C)

Equation 2-1 may be used to approximate the yield strength of AISI H13 considering the temperature of the die during a forging operation. Ou (2008) offers equation 2-2 to describe the temperature dependence of the elastic modulus of AISI H13.

$$E = (-0.11T + 216) * 1000 \qquad \textbf{2-2}$$

Where;

E Young's modulus of H13 (MPa)

The thermal properties of hot work tool steels are important. Heat is transferred from the workpiece and heat is generated through friction during the forging operation. High thermal diffusivity is desirable to reduce the magnitude of

thermal gradients and mitigate thermal fatigue. The thermal properties of AISI H13 are given in Figure 2-6.

$$y = -5.94E{-}06x^3 + 3.44E{-}03x^2 - 1.30E{+}00x + 1.42E{+}03$$
$$R^2 = 1.00E{+}00$$
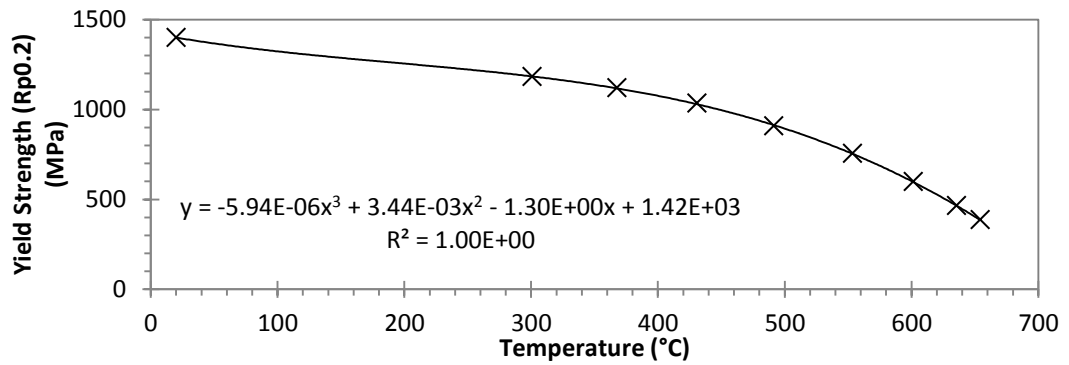
B) TOUGHNESS WITH TEMPERATURE
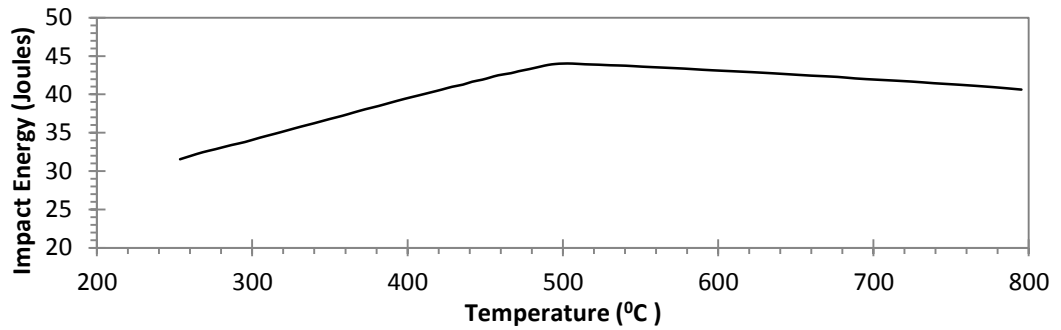
FIGURE 2-5:A) HOT YIELD STRENGTH OF BOHLER 302DE TOOL STEEL HEAT TREATED TO 1600N/MM^2 (BOHLER 2010) AND B) CHARPY V NOTCH TEST RESULTS WITH TEMPERATURE OF H13 (56HRC) (HODOWANY ET AL. 2000)
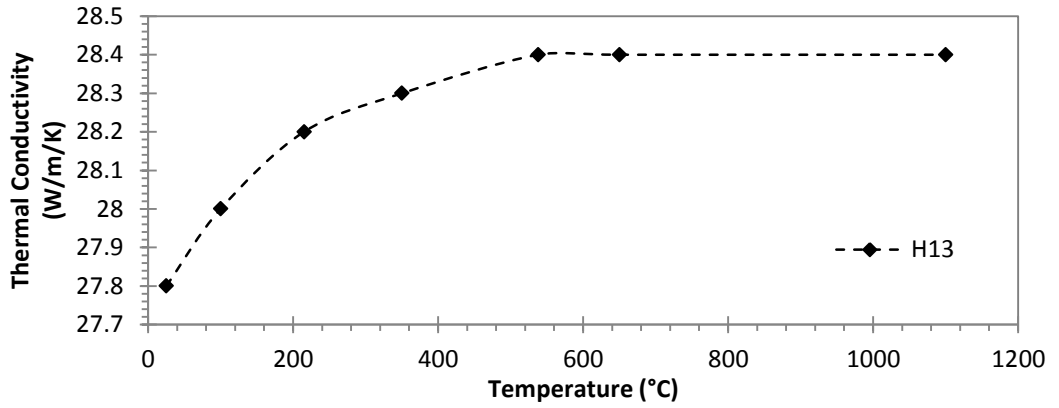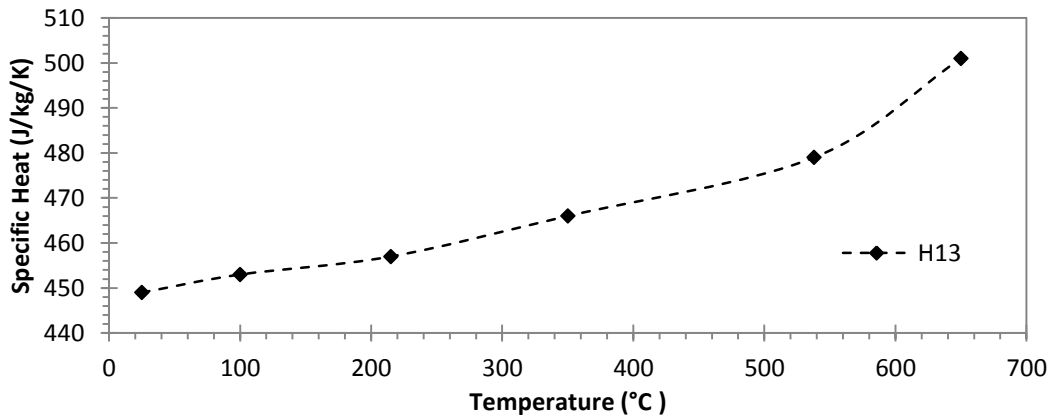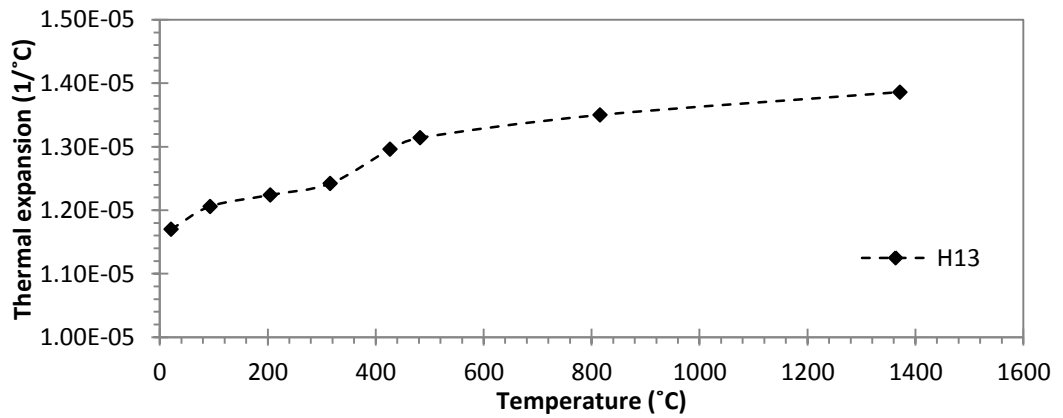
FIGURE 2-6: DIE MATERIAL PROPERTIES (AFRC, 2010)

2.1.3 DIE MATERIAL SURFACE TREATMENT

The tooling of interest is nitrided for improved resistance to abrasive wear and plastic deformation. The nitriding operation forms a diffusion layer and a white layer at the tool surface.

The die material is gas nitrided at a temperature of 525˚C in a mixed atmosphere of carbon and nitrogen using a fluidised bed gas furnace for 48 hours. This results in a nitride depth of 314μm with an 11μm deep white layer, as shown in Figure 2-7a). Figure b) shows hardness measures taken from different depths from the surface. The surface hardness varies between 1000-1200Hv.

A) MICROGRAPH
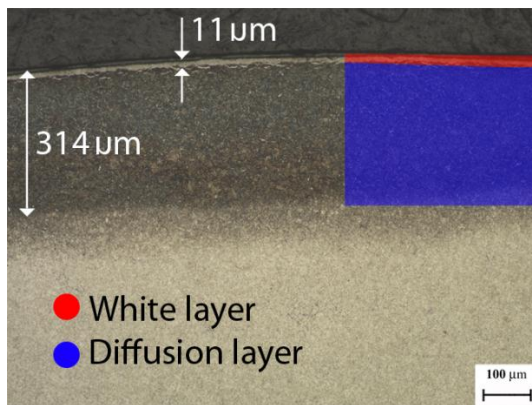
B) HARDNESS MEASURES
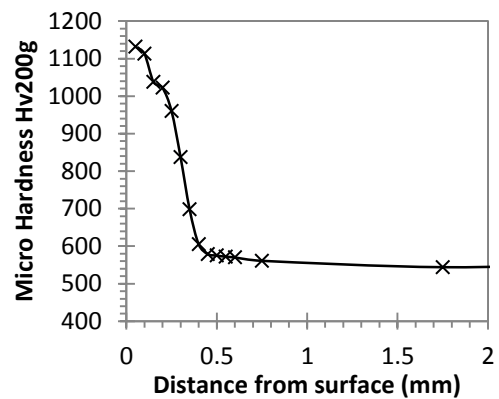
FIGURE 2-7: MICROGRAPH OF NITRIDED AISI H13

The white layer may be made out of two phases; the epsilon phase ($Fe_{2-3}N$) and gamma phase(Fe_4N) (Pessin et al. 2000). A monophase compound layer is reported to have better mechanical properties as the two phases weakly bond together (Strafford et al. 1995). The white layer present in the microstructure is monophase however it is not known whether it is epsilon or gamma phase.

The diffusion layer is formed when elements such as Cr, Al, V and Ti form sub-microscopic precipitates of nitrides which fit interstitially within the martensitic lattice and impede dislocation movement, resulting in higher yield strength (Strafford, Smart et al. 1995).

The performance benefit achieved through nitriding can be attributed to the presence of the white layer, the diffusion zone and compressive stresses (Li et al. 2000).

2.1.4 PRESS KINETICS

The extrusion and upsetting operations are performed using the same dual action mechanical crank press. One operation is performed at a time. The time taken to deform the workpiece is approximately a quarter of a second with a cycle time of half a second. The punch has a total stroke length of 228mm.

The movement of the press may be split into two stages. In the first stage, the top and bottom dies close. In the second stage the punch enters the closed dies and deforms the part. This is illustrated in Figure 2-8.

Figure 2-8a), b) and c) show the different stages of movement of the fly wheel which define the two stages of press kinetics. Figure a) describes the press at rest. Figure b) shows the flywheel in a position that allows for the clamping of the top and bottom dies. Figure c) shows the position where the punch is fully extended.

Figure 2-8 d), e) and f) shows a 2D cross section of the extrusion tooling at the different stages in the movement of the press. Figure d) shows the extrusion tooling when the press is at rest with the workpiece positioned in the tooling. Figure e) shows the top and bottom dies closed. Figure f) shows the punch fully extended and the shape of the extruded workpiece.

Figure 2-8 g), h) and i) shows a 2D cross section of the upsetting tooling for different stages in the movement of the press. The figures illustrate similar conditions of the upsetting tooling as shown for the extrusion tooling.
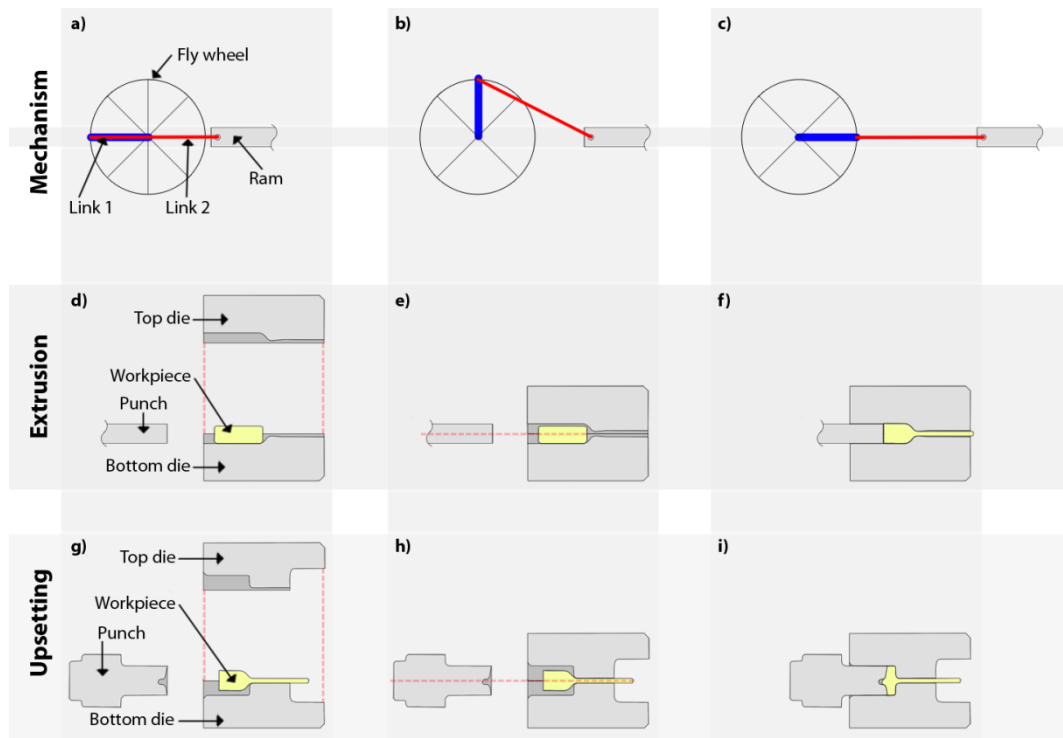
FIGURE 2-8: DUAL-ACTION CRANK PRESS KINETICS

For mechanical crank presses, the velocity of the punch reduces to a halt at the end of the punch stroke, as shown in in Figure 2-9.
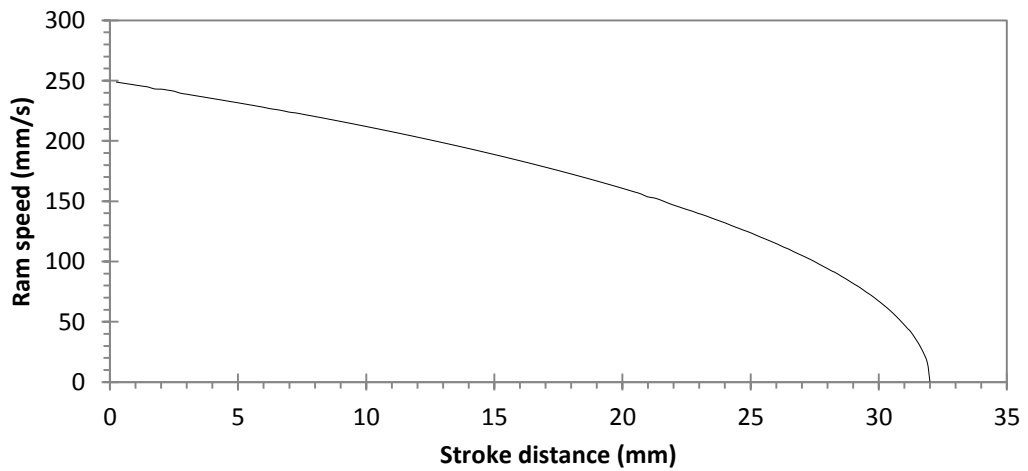
FIGURE 2-9: RAM SPEED WITH RAM STROKE FOR CRANK PRESSES

The slowing of the ram speed impacts the strain rate of the workpiece. The workpiece strain rate is important when forming strain rate sensitive materials such as IN718.

2.1.5 LUBRICATION, HEAT TRANSFER AND FRICTION

Lubrication plays a vital role in improving the surface quality of the formed parts and improving die life. The purposes of lubricants in hot forging include reducing friction, reducing the heat transferred from the billet to the die and to protect the workpiece and die from corrosion.

Water based graphite is applied to the tooling to reduce friction, reduce heat transfer and to protect the tooling. The workpieces are glassed to provide insulation to reduce heat loss upon removal of the workpiece from the furnace.

Lin (2009) performed Cockroft ring tests and measured the friction and heat transfer coefficient descriptive of forging Inconel 718 using a mechanical press with glassed workpiece and graphite lubricant applied to the tooling. A friction value of 0.2 was found to be representative of the upper limit for friction for this forming operation. The heat transfer coefficient was found to be pressure sensitive up to 263MPa. The pressure sensitivity occurs through the increase in directly contacting surface area and reaches a maximum where the entire surface is in contact.

2.1.6 SUMMARY OF THE FORGING CONDITIONS OF INTEREST

The process consists of extruding and upsetting of Inconel 718 at a temperature of 1080°C in dies made out of AISI H13, which are preheated to 240°C. The tooling has been heat treated to a tempered martensitic structure of hardness between 52 and 54HRC. The tooling is nitrided to form a 310μm thick nitride layer with an 11μm thick compound layer. The workpiece has a 30-50μm thick glass coating and water based graphite is sprayed upon the dies before each stroke. The peak forging load for the extrusion and upsetting operations is 30tonnes and 70tonnes for extrusion and upsetting respectively. The upsetting operation occurs immediately after the extrusion operation. The deformation time for each operation is approximately a quarter of a second.

2.2 DIE FAILURE

Die failure occurs when the degradation of the tool results in defects imparted upon the workpiece that cannot be accepted. The reason for failure may be caused by the geometric deviation of the workpiece or the degradation in surface roughness. The extent of acceptable geometric deviation or surface deterioration in the workpiece is location specific and relates to the product's function.

The relevant failure modes include wear, corrosion, plastic deformation, thermal softening\ overaging, creep, thermal fatigue and mechanical fatigue (Summerville et al. 1995; Subramanian et al. 1996). Often failure in hot work dies is attributed to either abrasive wear or plastic deformation (Cser, Geiger et al. 1993; Kim et al. 2005) however the damage evolution is complex and interactions between these mechanisms occur (Kchaou et al. 2009).

The dominant failure mode depends upon factors such as the workpiece material, the temperature it is forged, the velocity that is forged, the amount of workpiece deformation, lubrication, and the die material, die heat treatment and surface treatments (Semiatin 2005). It is possible for the dominant failure mode to change over the life of the die.

2.2.1 WEAR

The interaction between the contacting asperities of the workpiece and tool may result in abrasive or adhesive wear. Abrasive wear describes the cutting of one surface by a harder surface. Adhesive wear describes the welding of the mating asperities and the removal of a combination of both of the mating bodies.

Archard (1956) developed an equation for modelling material removal through wear. Both adhesive and abrasive wear have been modelled using Archard's wear equation shown in equation 2-3 (Painter et al. 1996).

$$wear\ depth = k \int \frac{P.V}{H} dt$$

2-3

Where;

P Normal pressure (MPa)

V Sliding velocity (m/ s)

H   Hardness (Hv)

k   Material constant

Equation 2-3 expresses the empirical relationship relating the wear depth to the applied pressure, sliding velocity and hardness of the die material. Lin (2010) made the hardness of the tool temperature dependent to account for the impact of greater material removal when the tool as at higher temperature. Other authors have included the impact of over-tempering on the tool hardness (Lee et al. 2003; Kim, Lee et al. 2005; Tan 2007; Biglari and Zamani 2008).

Such wear models have been used to determine a wear index for comparing different preform designs (Lee, Kim et al. 2003; Kim, Lee et al. 2005; Tan 2007; Biglari and Zamani 2008).

2.2.2 CORROSIVE WEAR

Corrosive wear occurs when the two rubbing materials are in a corrosive environment. The corrosive reaction forms a tribological film on the surface which would normally retard corrosion from further penetrating into the material. In hot forming, the impact of the workpiece on the die surface can remove such a protective layer and allow further corrosion to occur. The rate of delamination of the corroded layer determines the rate of corrosion (Wang et al. 2008).

2.2.3 PLASTIC DEFORMATION AND CREEP

Plastic deformation is a common cause of failure in hot work tooling, where the tool deforms to such an extent that parts formed are no longer within dimensional tolerance. Some researchers have proposed that creep is also relevant in hot forging tooling (Fang et al. 2002; Berti and Monti 2009).

Martensitic hot work tool steel exhibits complex flow behaviour. Under uniaxial flow the material work hardens, whilst under cyclical loading the material softens over repeated cycles. The flow stress behaviour during uniaxial flow of H11 heat treated to 47HRC is shown in Figure 2-10.
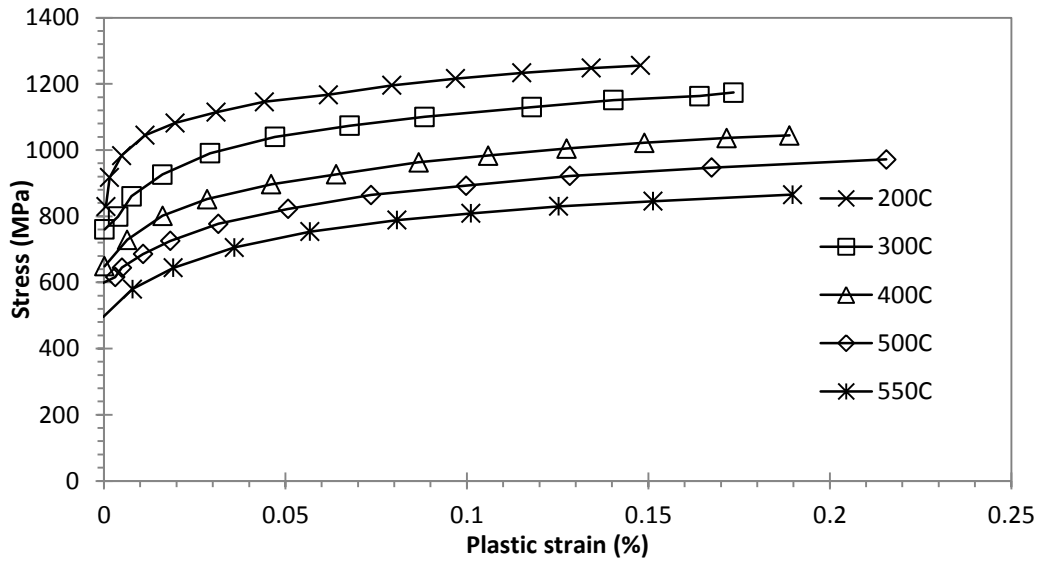
FIGURE 2-10: COMPRESSIVE FLOW STRESS BEHAVIOUR OF H11 TOOL STEEL (BERNHART ET AL. 1999)

Under cyclical loading conditions, martensitic tool steel softens without reaching stabilisation. The isotropic behaviour may be observed in Figure 2-11 which shows the hysteresis loops measured during uniaxial fatigue of AISI H11 tool steel.
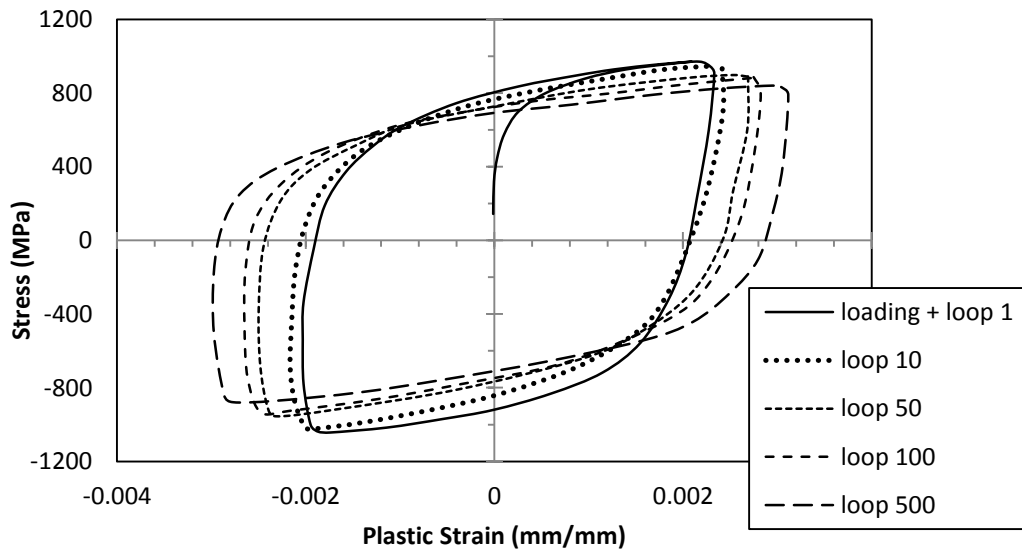
FIGURE 2-11: ISOTHERMAL STRAIN CONTROLLED FATIGUE AT 500°C WITH A SYMMETRICAL STRAIN AMPLITUDE OF ±0.8 (ZHANG ET AL. 2008)

The peak plastic strain measured within the hysteresis loops increase during cyclical loading. The softening behaviour is more easily observed when examining the halved peak stress measured in each cycle. The halved peak stress refers to the sum of the absolute minimum stress and maximum stress within a cycle divided by two. This is shown in Figure 2-12. Zhang et al (2002) performed isothermal fatigue tests with a tensile-compression strain ratio of 1%, at temperature intervals between 200°C and 550°C, with a strain rate of 1.6×10^{-4}/ s.
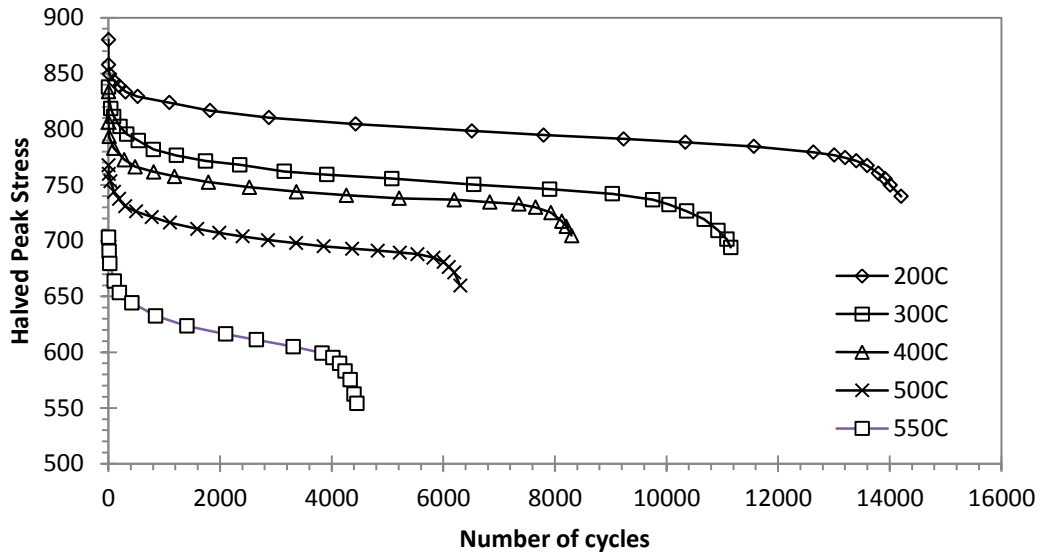
FIGURE 2-12: HALVED PEAK STRESS AMPLITUDES FROM ISOTHERMAL FATIGUE TESTS OF H11 TOOL STEEL (ZHANG ET AL. 2002)

AISI H11 cyclical softens at all temperatures examined. Zhang et al (2002) observed a relationship between the cyclical softening and the strain amplitude under strain controlled fatigue. This suggested that the softening was caused by a strain-induced mechanism. The increase in softening at temperatures above the tempering temperature of the alloy (~500°C) was attributed to the additional contribution of thermally induced mechanism(s). An initial transient drop in halved peak stress results in a drop of ~50MPa in halved peak stress.

Zhang et al (2008) have developed a phenomenological model based upon the approach outlined by Lemaitre and Chaboche (1990). Krumphals et al (2012) is in the process of applying the physical based model developed by Ghoniem et al (1990) describing the creep behaviour of 9-12%Cr tempered martensitic steel to

the plastic deformation behaviour of AISI H11 under hot forging tooling conditions.

2.2.4 THERMAL SOFTENING\ OVERAGING\ OVER-TEMPERING

Hot work tooling reach high temperatures during service. The prolonged exposure to such high temperature results in over-tempering of the tool material. The reduced strength of the die material results in increases susceptibility to plastic deformation and abrasive wear.

Different terminology may be used to describe this behaviour. Thermal softening is used to describe the impact of this behaviour during production. Overaging is applicable to describing the coarsening of strengthening precipitates. Over-tempering includes precipitation kinetics in addition to the changes that occur during the transformation from a tempered martensitic microstructure to a fully annealed ferritic microstructure.

Die failure has been modelled by determining the time taken for thermal softening to reduce the hardness of the die material to a level where plastic deformation is initiated (Kim, Lee et al. 2005). Alternatively, thermal softening has also been included when modelling abrasive wear through a reduction in die hardness (Lee, Kim et al. 2003; Kim, Lee et al. 2005; Tan 2007; Biglari and Zamani 2008). The interaction between the development of a thermally softened substrate and the size of the case hardened layer was explored by Saiki et al (2001). Zhang et al (2008) include the impact of thermal softening when modelling the plastic deformation behaviour of hot work tool steel.

2.2.5 THERMAL FATIGUE

The heat transferred to the die surface and the heat generated through friction result in a thermal gradient at the tool surface. The different rates of thermal expansion within a constrained geometry result in tensile stresses that result in thermal fatigue.

The measures used to quantify thermal fatigue include the time taken for initiation of thermal fatigue cracking, the crack density and the crack length (Babu et al. 1999; Persson et al. 2005).

The surface cracks caused by thermal fatigue are important in regards to causing delamination wear and spallation. Such damage may cause the workpiece surface finish to degrade to an extent deemed unacceptable and fail the tooling. Thermal fatigue is common in hot forging tooling.

2.2.6 MECHANICAL FATIGUE

Mechanical fatigue may lead to delamination of the fractured surface layer or may result in catastrophic failure. Fracture may initiate at stress raisers such as sharp corners, machining marks or from defects within the microstructure close to the tool surface and tensile stress (Chattopadhyay 2001).

The complex interaction between mechanical fatigue and thermal fatigue is described by thermo-mechanical fatigue. The internal stress from the surface pressure applied from the deforming workpiece and the thermal stress combine to determine the stress state of the tooling.

The lifetime of tooling that fail through fatigue may be predicted through modelling the number of cycles until crack initiation or alternatively the number of cycles required for the crack to propogate to catastrophic failure. The appropriate approach depends upon the ductility of the material and whether the die fails upon crack iniation or whether the crack propagates significantly during the lifetime of the tool.

Low cycle fatigue life may be predicted using strain formulated, energy formulated or stress formulated models (Velay et al. 2005). The thermo-mechanical fatigue models found within the literature follow Lematire and Chaboche's (1990) stress formulated approach for life predicion using empirical damage mechanics (Fang, Jiang et al. 2002; Velay, Bernhart et al. 2005; Berti and Monti 2009).

2.2.7 SUMMARY OF THE RELEVANT FAILURE MODES

This section has examined the failure modes that are applicable to hot forging tooling. The tool is failed when the parts produced no longer meet the required surface roughness or dimensional tolerance of the component.

Many failure modes may contribute to die failure. Potential failure modes include abrasive wear, adhesive wear, plastic deformation, corrosion, mechanical

fatigue and thermal fatigue. The cause of failure in hot work tooling has been investigated by Summerville et al (1995), Barrau et al (2003), Bergeron et al (2003), Behrens et al (2007) and Kchaou et al (2009). Complex interactions between failure modes may occur. The dominant failure mode is dependent upon the workpiece, the tool material, the amount of deformation, the type of press, the workpiece temperature, the die temperature, and lubrication. For given conditions, it is necessary to identify the dominant failure mode to allow life prediction.

When die life is limited by wear, Archard's wear equation may be used to predict die life. This approach has been adopted by Painter et al (1996), Bariani et al (1996), Kim et al (2005) and Lin (2009).

Kim et al (2005), Zhang et al (2008) and Krumphals et al (2012) have developed die life prediction models describing life limited by plastic deformation. Kim et al (2005) modelled the number of cycles taken for the initiation of plastic deformation caused by the reduction in tool strength from over-tempering during service. Zhang et al (2008) developed a phenomenological model that captures the flow behaviour and change in material condition of hot work tool steels. Krumphals et al (2012) adapted a physical based model developed to describe the creep behaviour of tempered martensitic steel and have applied it to the thermo-mechanical fatigue loading of hot work tool steels.

Fang et al (2002), Berti and Monti (2009) and Velay et al (2005) have developed continuum damage mechanics models to predict the life of hot work tooling limited by thermo-mechanical fatigue.

The approaches taken to model die life vary in detail in which the material behaviour, boundary conditions or failure criterion are described. To successfully predict die life, it is important to model the correct failure mode. The accuracy of the prediction is dependent upon the accuracy of the description of the loading conditions, the failure criteria and the description of the mechanical response of the die material.

2.3 THE TEMPERED MARTENSITIC MICROSTRUCTURE OF AISI H13

This section reviews the key microstructural features of hot work tool steel that relate to die performance. The change in mechanical properties of tool steel during use as hot forming tooling is a result of microstructural instability.

The microstructure of AISI H13 has been assessed by reviewing published literature describing similar tempered martensitic hot work tool steels and also 9-12% tempered martensitic steels.

The microstructural features present within tempered martensite include prior Austenite grain boundaries, primary particles, martensitic lath boundaries, lath boundary particles, subgrains, and subgrain interior particles. This is illustrated in Figure 2-13.
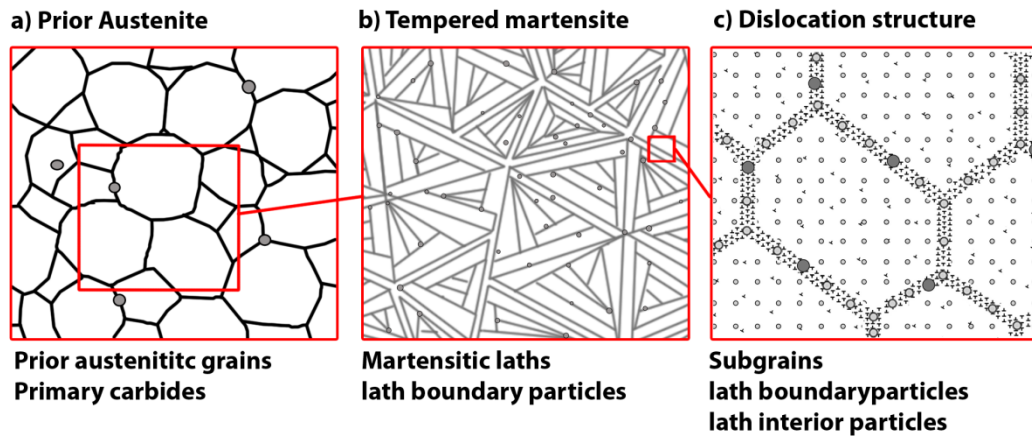
FIGURE 2-13: ILLUSTRATION OF TEMPERED MARTENSITE

The microstructural features associated with the mechanical properties of tempered martensite include the solutes strengthening, precipitate strengthening, dislocation strenghtening and subgrain strengthening (Abe 2008). The relationship between these microstructural features and mechanical strength and the magnitudes of these microstructural features are reviewed in the following sections.

2.3.1 STRENGTHENING FEATURES OF TEMPERED MARTENSITE

2.3.1.1 SOLUTE STRENGTHENING

Solute strengthening may be attributed to the presence of large solute atoms such as Molybdenum or Tungsten, which create lattice distortions that impede dislocation motion (Abe 2008). Solute strengthening has been assumed to be a function of the shear misfit and size misfit caused by the solute atoms (Zander 2009), as shown in equation 2-4.

$$\sigma_s\{\varepsilon_b, \varepsilon_G, c\} \qquad \textbf{2-4}$$

Where;

σ_s Strength provided by solutes (Pa)

ε_b Elastic misfit caused by variation in the Burgers vector (m/ m)

c The fraction of solute strengthening element (%)

ε_G The elastic misfit caused by variation in shear modulus (m/ m)

The resistance to slip provided by solutes may be taken into consideration through a frictional stress similar to the Peierls Nabarro stress (Ghoniem, Matthews et al. 1990).

2.3.1.2 PRECIPITATE STRENGTHENING

The Orowan stress of obstacle bypass may be used to describe the resistance provided by particles within AISI H13 (Engberg and Larrson 1988). The Orowan stress is shown in equation 2-5.

$$\sigma_p = \frac{\alpha_2 M G b}{\lambda_p} \qquad \textbf{2-5}$$

Where;

σ_p Orowan stress of particle bypass (Pa)

α_2 A bounded coefficient

M The Taylor factor

b The Burgers vector (m)

G The shear modulus (Pa)

λ_p The particle spacing (m)

The types of particles reported in as-heat treated tempered martensitic steel are shown in Table 2-2, considering the particle location. Table 2-2 also shows the range in particle radii from published literature regarding tempered martensite (Kadoya et al. 2002; Mebarki et al. 2004; Zhang et al. 2004; Agamennone et al. 2006; Abe 2008; Bischof et al. 2008; Bazazi 2009; Medvedeva et al. 2009). M_7C_3 and M_3C have also been reported to be present in as-heat treated tempered martensitic tool steels (Medvedeva, Bergström et al. 2009). The particle shape, size and volume fraction are related to the particle spacing, and thus the Orowan stress.

TABLE 2-2: TYPICAL PARTICLE SIZES BASED UPON PARTICLE LOCATION

Particle location	Mean radius, r (nm)	Typical particle type
Prior austenite grain boundaries	$300 < r > 100$	$M_{23}C_6$, MX, M_6C
Lath\ subgrain boundary	$70 < r > 5$	$M_{23}C_6$, MX
Lath\ subgrain interior	$40 < r > 1$	MX, M_2X

The particle measurements describing as-heat treated tempered martensitic hot work tool steels have been summarised in Table 2-3. The term ϕ_p refers to the volume fraction of particles. The term r_p refers to the mean particle radius.

TABLE 2-3: PARTICLE MEASUREMENTS OF HOT WORK TOOL STEELS

Particle	Source	ϕ_p	r_p
$M_{23}C_6$	Mebarki et al (2004)	-	100-300nm
Intra-lath particles	Zhang et al (2004)	8.2	30-70nm
MC	Mebarki et al (2004)	-	<40nm
	Medvedeva et al (2009)	-	2-7nm
M_2C	Medvedeva et al (2009)	-	1-3nm
MC and M_6C	Bischof et al (2008)	0.3%	245nm
$M_{23}C_6$	Bischof et al (2008)	2.3%	7nm
MX and M_2C	Bischof et al (2008)	1.9%	1.2nm
MX	Bischof et al (2008)	0.5%	1.2nm

There is a large difference between the mean particle radii and volume fraction of particles measured by Zhang et al (2004) and those measured by Bischof et al (2008). The volume fraction of subgrain interior MX particles measured by Bischof et al (2008) is similar measurements taken by Kadoya et al (2002) and Semba (2003) when characterising 9-12%Cr tempered martensitic steels.

The spacing between intra-lath particles may be approximated by assuming lattice square spacing using equation 2-6. This assumes that the particles are spherical, are of similar size, and are evenly distributed throughout the matrix.

$$\lambda_p = 2\sqrt{{}^2\!/_3}\, r_p \left(\sqrt{\frac{\pi}{4\phi_p}} - 1 \right) \qquad \textbf{2-6}$$

Equation 2-6 may be applied to the intra-lath particles from the measurements shown in Table 2-3 for measurements that include the volume fraction of particles. The estimated particle spacing is shown in Table 2-4.

TABLE 2-4: PARTICLE SPACING OF AS-HEAT TREATED MARTENSITIC HOT WORK TOOL STEEL

Source	Carbide	ϕ_p	r_p	λ_p
Bischof et al (2008)	MX and M_2C	1.9%	1.2nm	11nm
Zhang et al (2004)	Intra-lath	8.2%	36.4nm	125nm

From Table 2-4 it can be seen that there is a large difference in approximated particle spacing from values obtained from the literature. This impacts the Orowan stress and thus the contribution to strength arising from the intra-lath particles.

2.3.1.3 DISLOCATION STRENGTHENING

A Taylor stress may be used to describe the back stress arising from dislocation interaction, as shown in equation 2-7.

$$\sigma_T = \alpha_t G b M \sqrt{\rho_m} \qquad\qquad \textbf{2-7}$$

Where;

α_t A bounded constant

ρ_m The mobile dislocation density (m^{-2})

The dislocation densities reported to describe tempered martensite vary substantially when reviewing published literature describing 5% Cr tempered martensitic hot work tool steels and 9-12% Cr tempered martensitic steels.

The values describing the dislocation density within tempered martensitic hot work tool steels vary by several orders of magnitude. Mebarki et al (2004) measured an initial dislocation density of approximately $2.3 \times 10^{16} m^{-2}$. Krumphals et al (2009) assume a smaller initial total dislocation density of $\sim 1 \times 10^{12} m^{-2}$ with a mobile dislocation density $8 \times 10^{11} m^{-2}$.

Mobile dislocation densities reported in 9-12%Cr tempered martensitic steel vary between $2.9 \times 10^{13} m^{-2}$ to $2 \times 10^{14} m^{-2}$ (Semba 2003; Sauzay et al. 2008; Bazazi 2009). Abe (2008) and Bazazi (2009) report mobile dislocation densities of approximately $1 \times 10^{14} m^{-2}$ in as-heat treated 9-12% Cr tempered martensitic steels. Semba (2003) used a higher value of $2 \times 10^{14} m^{-2}$ when modelling the creep behaviour of 9-12% tempered martensitic steel.

The upper and lower bounds of mobile dislocation density of AISI H13 may be approximated from the range in values reported describing as-heat treated tempered martensite. The upper limit for the mobile dislocation density is given by $2 \times 10^{14} m^{-2}$ and the lower limit given by $1 \times 10^{12} m^{-2}$ (Semba 2003; Krumphals et al. 2009).

2.3.1.4 Subgrain strengthening

A Hall-Petch relationship may be used to describe the strengthening arising from the subgrains within tempered martensite, as shown in equation 2-8 (Abe 2008; Bazazi 2009).

$$\sigma_{sg} = \frac{10Gb}{\lambda_{sg}} \qquad\qquad \textbf{2-8}$$

Where;

σ_{sg} Subgrain strengthening (Pa)

λ_{sg} Subgrain spacing (m)

Martensitic laths form as a result of the quenching operation. Subgrains are described in context of specimens that have experienced creep or fatigue (Kadoya, Dyson et al. 2002; Mebarki, Delagnes et al. 2004). Sawada et al (1999) use the terms subgrain and martensitic lath interchangeably when measuring the change in lath structure during creep of 9-12% Cr tempered martensitic steels. Assuming that subgrains are formed in the rolling operation during the processing of the steel, it is acceptable to refer to lath width and subgrain diameters interchangeably.

Zhang et al (2004) measured a mean lath length and mean lath width of 3.49μm and 1.64μm respectively in as-heat treated AISI H11 hot work tool steel using quantitative image analysis of SEM (scanning electron microscopy) images. The lath width is significantly larger than those measured with regard to 9-12% tempered martensitic steels which have been obtained from quantitative image analysis of TEM (transition electron microscopy) images. It is unknown to what extent the difference is caused by the difference in alloy composition and in measurement method.

The mean lath widths\ subgrain diameters reported from the literature with regard to 9-12% tempered vary between 0.36 μm and 0.7 μm (Sawada, Takeda et al. 1999; Agamennone, Blum et al. 2006; Abe 2008; Sauzay, Fournier et al. 2008; Bazazi 2009). The lath width of AISI H13 may vary between 0.36μm to 1.64μm considering the range in reported values describing tempered martensitic steel.

2.3.2 THERMALLY INDUCED SOFTENING BEHAVIOUR

The thermally induced microstructural instabilities relevant to hot forging tooling include particle coarsening, dislocation annihilation and subgrain/lath coarsening. Extensive research has examined the microstructural instability in the creep of 9-12% Cr tempered martensitic steels. The behaviours relevant to hot forging tooling may be examined from these studies.

2.3.2.1 PARTICLE COARSENING

Particles come out of solution during the quenching stage of the heat treatment of martensitic hot work steels where the single phase system changes into a multiple-phase metastable system (Ratke and Voorhees 2002). The carbide particles nucleate, grow and coarsen during heat treatment and exposure to elevated temperatures. The majority of particles nucleate during the heat treatment process however particles may continue to nucleate during service depending upon the temper.

Bischof et al (2008) measured the coarsening kinetics of particles within tempered martensitic hot work tool steel. Figure 2-14 describes the coarsening of $M_{23}C_6$ lath boundary particles and MX\ M_2X intra-lath particles during overaging at a temperature of 650°C. Hardness measurements are also shown on a separate axis on the graph. A small increase in particle radius is measured alongside a large reduction in hardness. The hardness measurements show that after 24hours at 650°C the hardness is close to the annealed condition. The intra-lath and lath boundary particles have significantly coarsened after this extent of overaging.

Figure 2-15 shows the coarsening kinetics measured by Zhang et al (2004) when overaging AISI H11 at temperatures of either 560°C or 600°C. It can be seen that the increase in temperature from 560°C to 600°C has a large impact upon the coarsening rate of the particles and the softening behaviour resulting from the overaging process. At 560°C there is only a small reduction in micro-hardness after exposure to this temperature for 18 hours.

The sizes of the intra-lath particles measured by Zhang et al (2004) are much larger than the intra-lath particles measured by Bischof et al (2008). The Orowan stress for particle bypass is significantly smaller for the larger particles. Both

studies show significant particle coarsening within temperatures applicable to hot forging tooling.
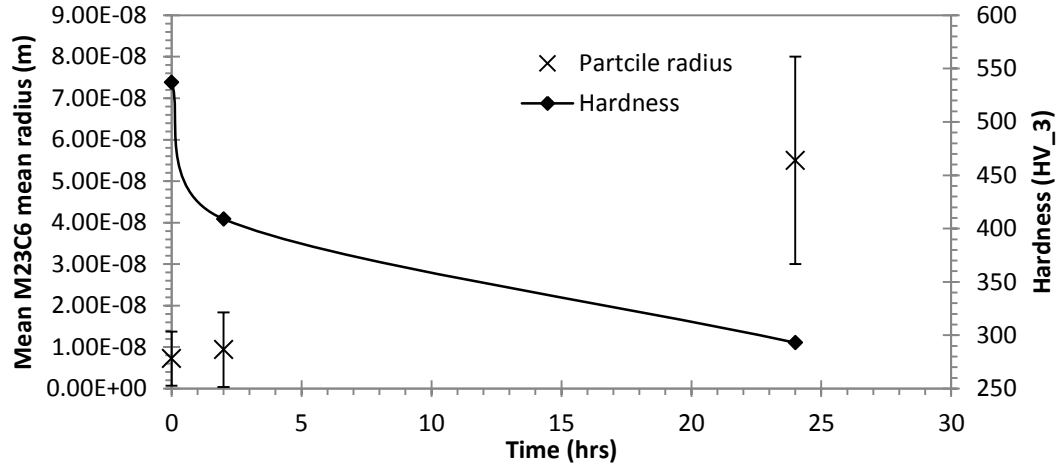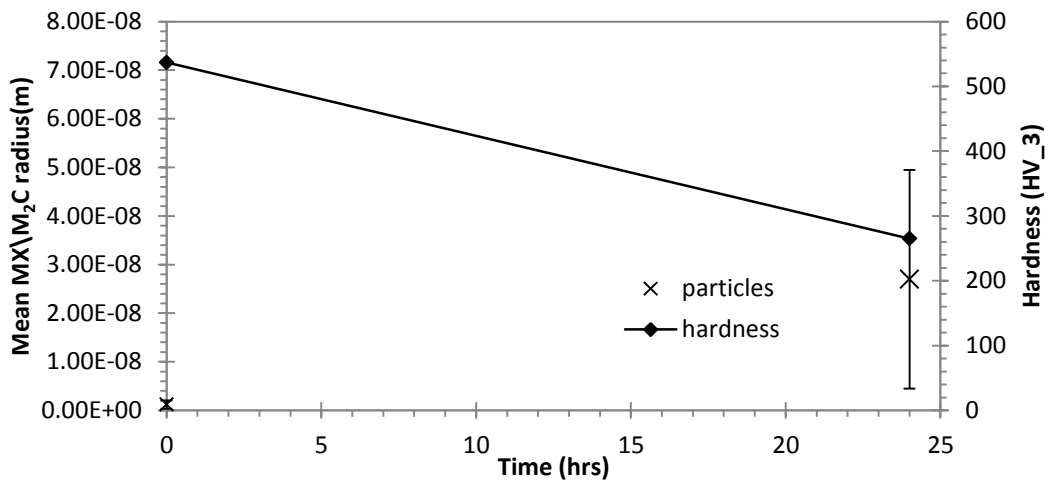
FIGURE 2-14: PARTICLE COARSENING KINETICS MEASURED BY BISCHOF ET AL (2008)

Zhang et al (2004) measured a similar volume fraction of particles in all over-aged specimen however did not distinguish between the type of intra-lath particle. Bischof et al (2008) measured an initial volume fraction of 1.9% of small MX and M_2X particles within the subgrain interior. After 2 hours of overaging at 650°C, Bischof et al (2008) observed that the subgrain boundary $M_{23}C_6$ particles had coarsened at the expense of all the M_2X particles. It can be seen that a

complex interaction occurs between the different types of particles during overaging.
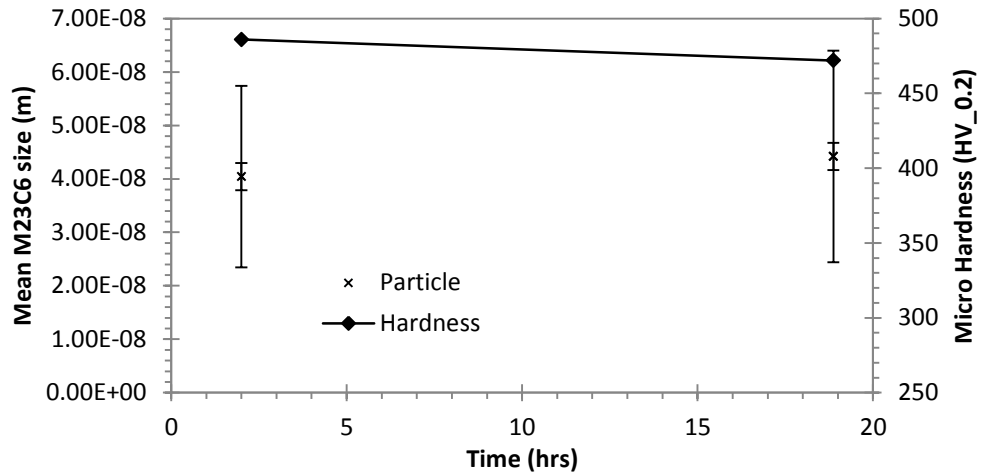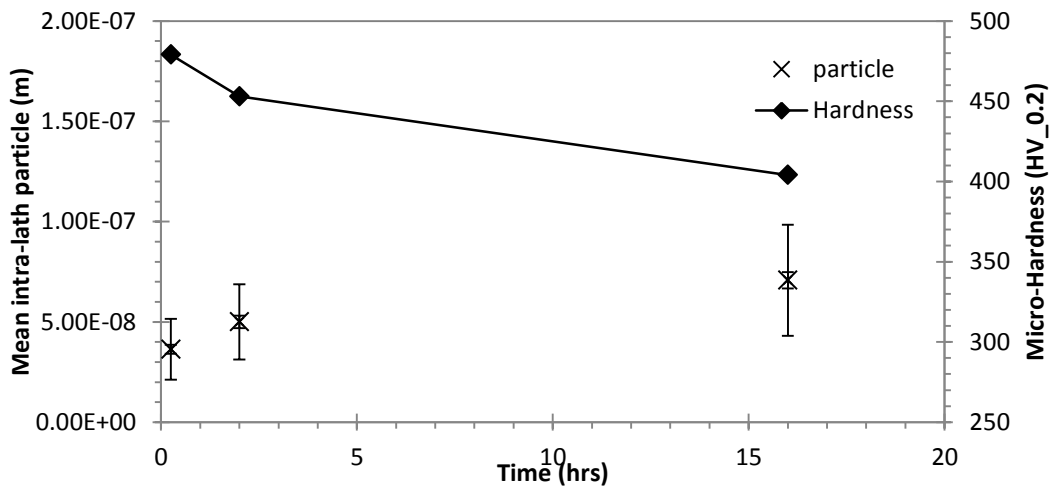
FIGURE 2-15: PARTICLE COARSENING KINETICS MEASURED BY ZHANG ET AL (2004)

2.3.2.2 DISLOCATION ANNIHILATION

Another relevant microstructural instability is thermally induced dislocation annihilation. Mebarki et al (2004) measured dislocation densities in hot work tool steel as a result of over-tempering at different temperatures for 2 hours. The dislocation density measurements from the over-tempered specimen are shown in Figure 2-16.
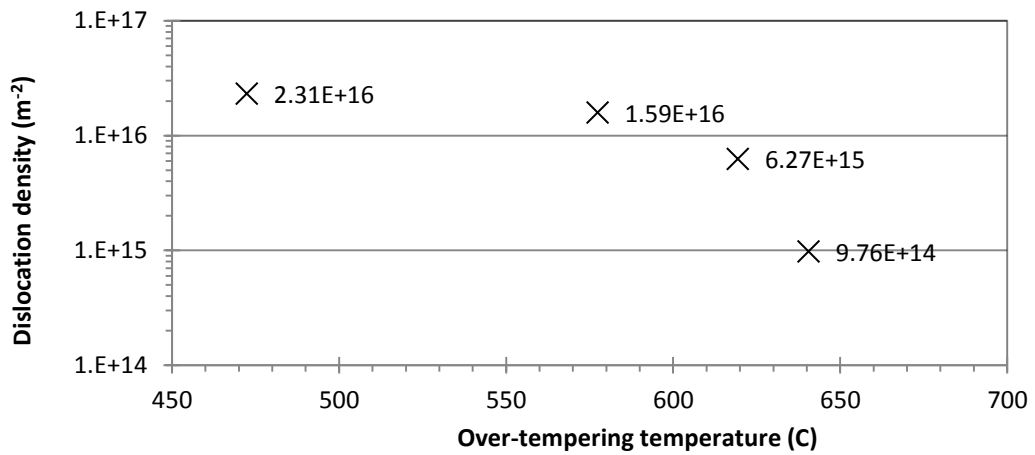
FIGURE 2-16: DISLOCATION DENSITY AS A RESULT OF 2 HOURS OF EXPOSURE TO DIFFERENT OVER-TEMPERING TEMPERATURES (MEBARKI, DELAGNES ET AL. 2004)

A reduction from approximately $2 \times 10^{16} \text{m}^{-2}$ to $1 \times 10^{15} \text{m}^{-2}$ has been measured as a result of over-tempering for 2 hours at 640°C. Such a reduction in dislocation density incurs a significant reduction in Taylor stress arising from dislocation interaction, contributing to the softening observed behaviour observed in the over-tempering of steels.

Bazazi (2009) measured a similar reduction in mobile dislocation density during over-tempering 9-12% Cr tempered martensitic steel at 550°C, as shown in Figure 2-17.
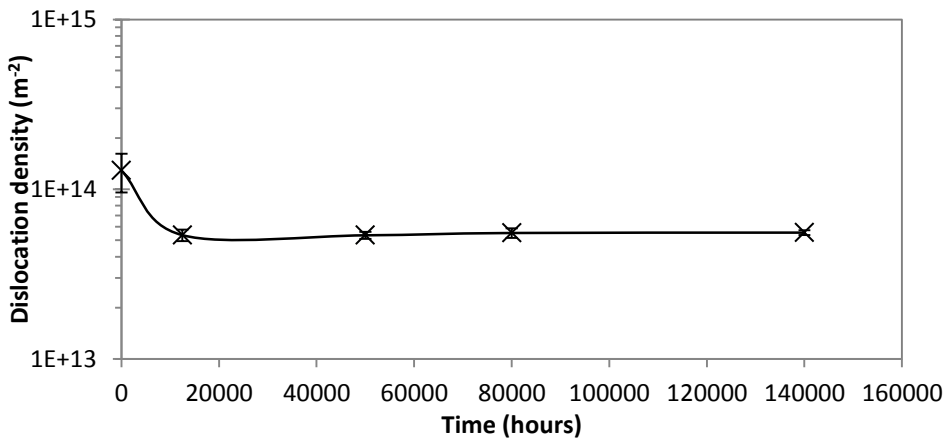
FIGURE 2-17: MOBILE DISLOCATION DENSITY DURING OVER-TEMPERING AT 550°C

The dislocation density reduces from $1.2 \times 10^{14} \text{m}^{-2}$ to a steady state of $5 \times 10^{13} \text{m}^{-2}$. The timescales shown in Figure 2-17 are much greater than those of interest regarding

hot work tool steel. It can be argued that during the conditions of interest, this steady state is not reached.

2.3.2.3 SUBGRAIN\ LATH COARSENING

During over-tempering, the tempered martensite transforms into ferrite, as observed in the annealed condition. A coarsening in the lath width has not been measured during the over-tempering timescales and temperatures relevant to the service conditions of hot work tool steel (Zhang, Delagnes et al. 2004). Bazazi (2009) measured similar behaviour when measuring subgrains or "micro-grains" during over-tempering at 550°C in 9-12% Cr tempered martensitic steel. The measurements were taken from TEM micrographs and the results are shown in Figure 2-18.
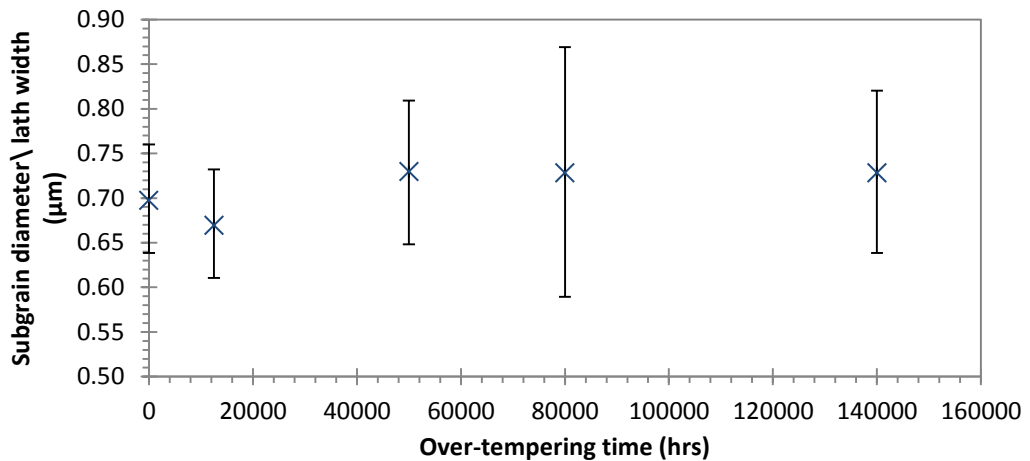
FIGURE 2-18: IMPACT OF OVER-TEMPERING AT 550°C UPON 9-12% CR TEMPERED MARTENSITIC STEEL (BAZAZI 2009)

It can be concluded that within the over-tempering conditions of interest, the thermally induced coarsening of the lath\ subgrain structure is not a significant microstructural instability.

2.3.3 STRAIN-INDUCED SOFTENING BEHAVIOUR

The softening behaviour observed in the creep loading and fatigue loading of tempered martensitic steels has been partially attributed to the formation and coarsening of subgrains (Kadoya, Dyson et al. 2002; Mebarki, Delagnes et al. 2004). The same softening behaviour observed in the fatigue loading of hot work

tool steel is observed in the fatigue loading of 9-12% Cr tempered martensitic steel (Bernhart, Moulinier et al. 1999; Sauzay, Fournier et al. 2008).

The formation of subgrains is associated with the change in dislocations structure from a relatively homogeneous structure of high dislocation density to a heterogeneous dislocation structure of equiaxed subgrains (Sedlacek et al. 2002). The subgrain formation and coarsening described by Kadoya et al (2002) is illustrated in Figure 2-19.
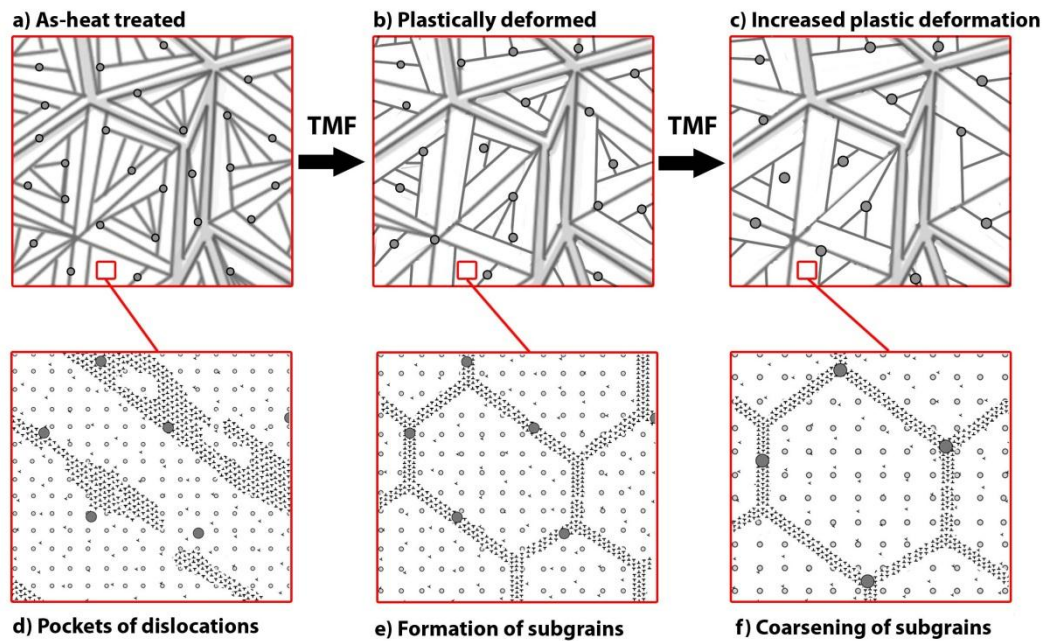
FIGURE 2-19: SUBGRAIN FORMATION AND COARSENING

The following sections describe the reported change in dislocation density and subgrain structure associated with the creep and fatigue of tempered martensite.

2.3.3.1   DISLOCATION KINETICS

The initial dislocation structure consists of pockets of high dislocation density as shown in Figure 2-19d). A heterogeneous dislocation density is formed with the creation of the dislocation structure shown in Figure 2-19e). This is associated with the reduction in mobile dislocation density and the formation of boundary dislocations.

Krumphals et al (2009) modelled the change in mobile, immobile and subgrain boundary dislocations in the cyclical loading of tempered martensitic hot work

tool steel. The immobile dislocations refer to the dislocations that have become pinned by subgrain boundaries. The predicted dislocation kinetics is shown in Figure 2-20.
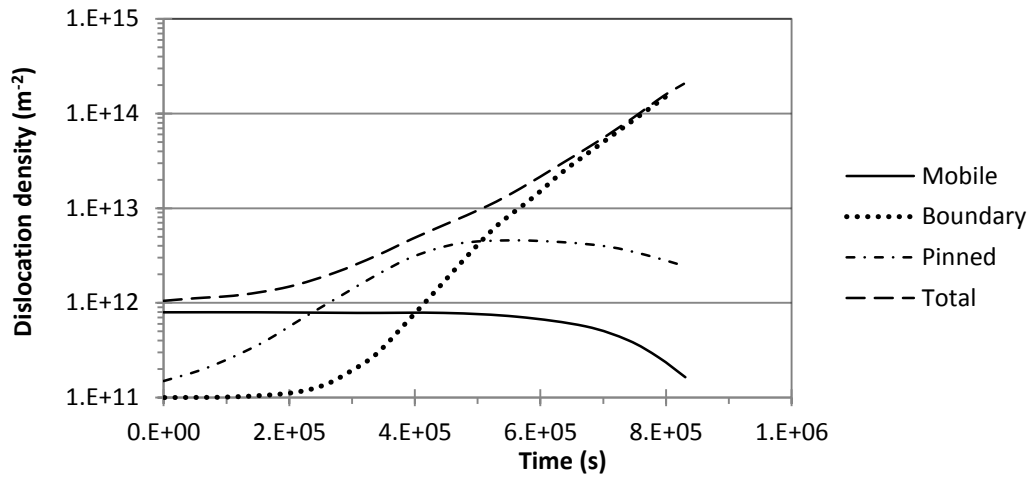
FIGURE 2-20: DISLOCATION KINETICS PREDICTED BY KRUMPHALS ET AL (2009)

Figure 2-20 shows a reduction in mobile dislocation density and an increase in total dislocation density as a response to fatigue loading. A reduction of approximately 80% of mobile dislocations is predicted.

The reduction in mobile dislocation density is in agreement with the measurements taken by Sawada et al (1999) however the increase in total dislocation density conflicts with measurements taken by Sauzay et al (2008) and Mebarki et al (2004). A reduction in total dislocation density was measured as a response to fatigue loading in hot work tool steel and 9% Cr tempered martensitic steels respectively.

Sauzay et al (2008) measured the mobile dislocation density before and after isothermal strain controlled fatigue loading with symmetrical strain amplitude of ±1% and a temperature of 550°C for 1800 cycles. An initial total dislocation density of $1.6 \times 10^{14} m^{-2}$ was measured to reduce to $3.4 \times 10^{13} m^{-2}$ as a response from the cyclical loading. This is a reduction of approximately 80% in total dislocation density.

Bazazi (2009) measured the mobile dislocation density during the creep of 12%Cr tempered martensitic steel at a temperature of 550°C and with a constant stress of 120MPa. The measurements are shown in Figure 2-21.
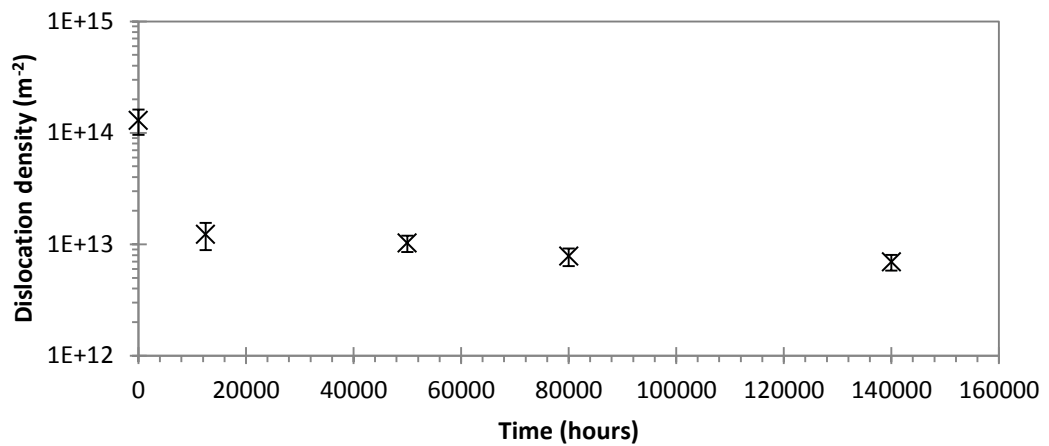
FIGURE 2-21: MOBILE DISLOCATION DENSITY DURING CREEP (550°C @120MPA) (BAZAZI 2009)

The measurements in Figure 2-21 show a sharp reduction of approximately 90% in mobile dislocation density after 12500 hours of creep loading. The measured change in mobile dislocation density during creep are similar to the reductions in total dislocation density measured by Sauzay et al (2008) in the fatigue loading of tempered martensitic steel.

Sawada et al (1999) measured a reduction in mobile dislocation density of 80% as a result of 0.14mm/mm plastic strain during creep at a temperature of 650°C and a load of 98.1MPa.

The measurements taken by Sauzay et al (1999), Sawada et al (1999) and Bazazi (2009) suggest that the mobile dislocation density reduces by approximately 80-90% as a response to fatigue loading.

2.3.3.2 SUBGRAIN COARSENING

From reviewing the literature, no measurements have been found describing the change in subgrain diameter as a response to the fatigue loading of hot work tool steel. Sauzay et al (2008) measured the subgrain coarsening in as-heat treated and fatigued specimen of 9% tempered martensitic steel. A specimen has undergone 1800 cycles of strain controlled fatigue with strain amplitude of ±1% and a

temperature of 550°C. The initial subgrain diameter was approximated at 0.7μm which more than doubled to 1.5μm as a response from the fatigue loading.

Bazazi (2009) measured subgrain, or "micro-grain" coarsening, during the creep of 12%Cr tempered martensitic steel at a temperature of 550°C with a constant stress of 120MPa. The measurements are shown in Figure 2-22.
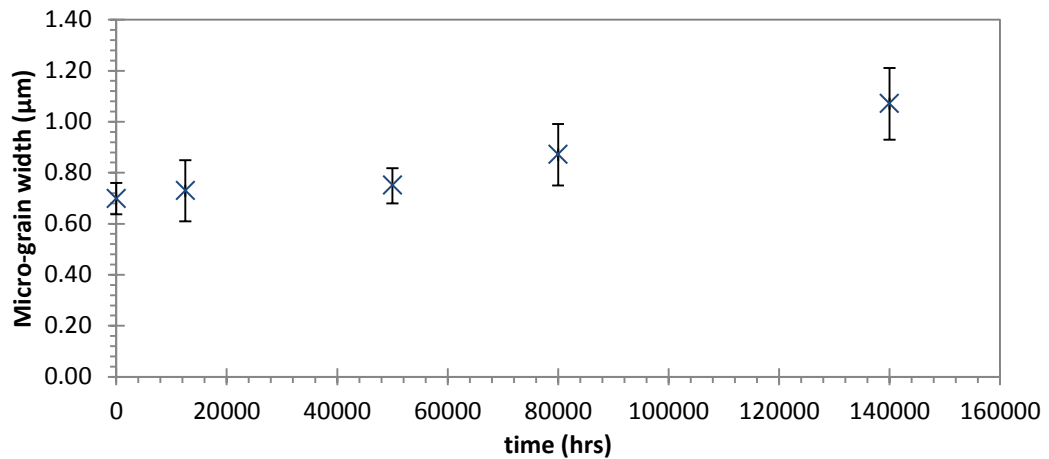
FIGURE 2-22: MICRO-GRAIN COARSENING DURING CREEP LOADING OF 120MPA AT 550°C (BAZAZI 2009)

An increase of 46% in micro-grain width was measured, lower than the coarsening measured in fatigue loading by Sauzay et al (1999). The mean subgrain size measurements taken from Kadoya et al (2002) vary between 0.8μm and 1.6μm.

The subgrain coarsening kinetics of AISI H13 may vary between an increase in subgrain diameter by anywhere between 46-114% when considering the increases reported from fatigue and creep of 9-12% tempered martensitic steels.

2.3.4   DIE MATERIAL SUMMARY

AISI H13 is a chromium hot work tool steel which provides high strength and ductility under the conditions experienced by hot forging tooling. The microstructural features of AISI H13 have been assessed through examining similar tool steels and 9-12% Cr tempered martensitic steels.

Tempered martensite is unstable during use as hot forging tooling. Within the temperatures and time scales of interest, the relevant thermally induced behaviour of interest includes particle coarsening and dislocation annihilation.

Thermally induced subgrain coarsening is not significant under conditions representative of hot forging dies.

The strain induced microstructural instabilities include the formation and coarsening of subgrains. This is associated with the reduction in mobile dislocation density.

The subgrain interior particle size, subgrain diameter and dislocation density of AISI H13 have been evaluated through reviewing published literature describing similar tempered martensitic hot work tool steels and 9-12%Cr tempered martensitic steel. This information is important, as the mechanical response of the tool material during hot forging relate to such microstructural features.

3 THE IDENTIFICATION OF THE DOMINANT FAILURE MODE

The dominant failure mode in the preform tooling used to forge single ended compressor blades has been investigated. The dominant failure mode must be known to guide improvement initiatives and allow for die life prediction. A failure analysis approach has been taken, examining worn tooling and analysing the conditions of the tooling.

This section describes the experimental methods used in the study, the results of the investigation, a discussion of the root cause of die failure and a conclusion.

3.1 EXPERIMENTAL METHODS

3.1.1 METALLURGICAL METHODS

The metallurgical preparation procedure outlined by Vander Voort (2004) was followed. The samples were etched with 1% Nital solution for 3 seconds to reveal the nitride layer. An Olympus GX51 microscope was used for the light microscopy analysis.

The hardness of the surface layers was measured at regular intervals along the damaged surfaces. The measurements were compared to datum specimens of H13 tool steel which had undergone similar heat treatment as the tooling of interest. A Mitutoyo MVK-G1 micro Vickers hardness measurement machine was used with a 200g load.

3.1.2 METROLOGY

The difference in geometry between the initial, as-machined geometry and the worn geometry after forging was assessed using a GOM ATOS ISO 3D camera.

3.1.3 FEA ASSUMPTIONS

Finite element analysis has been used to simulate the extrusion and upsetting preforming operations involved in manufacturing single ended compressor blades. The purpose of the process simulation is to evaluate the thermo-mechanical loading of the tooling. The mechanical loading of the tooling has been assessed through the von Mises stress. The von Mises stress is calculated

from equation 3-1, which is compared to the 0.2% proof stress. The temperature dependence of the 0.2% proof stress is shown in equation 2-1.

$$\bar{\sigma}_v = \frac{1}{\sqrt{2}}\sqrt{(\sigma_1 - \sigma_2)^2 + (\sigma_1 - \sigma_3)^2 + (\sigma_2 - \sigma_3)^2 + 6(\tau_{12}{}^2 + \tau_{23}{}^2 + \tau_{31}{}^2)} \qquad \textbf{3-1}$$

The commercial FEA software DEFORM™ was used to simulate the operation using elastic bodies to represent the extrusion tooling. DEFORM™ has been developed to model the large strains required for forging simulation and includes adaptive re-meshing. The workpiece flow behaviour was obtained from the DEFORM™ material library. The flow stress is shown in Figure 2-3.

The extrusion operation simulation was halved along the line of symmetry. The upsetting operation was modelled in full.

The deformation of the workpiece was modelled as a plastic body with no elastic deformation. The implication of this simplification is that the elastic spring-back of the workpiece is not included in the simulation. At high temperature the elastic modulus of the workpiece is low, resulting in small elastic deflections. For example, at 1050°C and a strain rate of 10/s, the elastic deflection is approximately 1.1%. This is compared to the plastic strain of 230% locked into the workpiece during the extrusion operation.

Die stress was approximated by assuming elastic body tooling. This assumption allows for greater stresses to be predicted than reality. To identify locations prone to plastic deformation, the approximated von Mises stress was compared to the temperature dependent 0.2% proof strength of AISI H13 shown in Figure 2-5 b).

Sensitivity studies were performed to determine acceptable mesh designs for the workpiece and the die. Simulations were performed first with rigid body tooling and plastic workpieces to evaluate different workpiece meshes. Simulations were repeated using elastic dies to determine appropriate mesh designs for the dies.

The sensitivity study showed than a workpiece of minimum and maximum of 0.4mm and 0.88mm element size was acceptable. The workpiece during upsetting had a minimum and maximum element size of 0.8mm and 1.6mm respectively. The upsetting and extrusion die meshes had a minimum element size of 0.5mm.

The heat lost from the workpiece during travel and during waiting times when resting upon the die prior and proceeding forming operations was included in the simulation.

The simulations included the heat lost from the workpiece to the environment through convection and radiation. It was assumed that the effective heat transfer coefficient descriptive of heat loss through convection was approximated by 20 W/ m^2/ K (Groseclose et al. 2008).

Table 3-1 summarises the simulation steps and convection, conduction and friction values. The material properties of the workpiece and die are shown in section 2.1.1.

TABLE 3-1: BOUNDARY CONDITIONS

Stage	Time (s)	Convection (W/ m^2/ K)	Conduction (W/ m^2)/ K	Friction shear factor
1) Workpiece moved on to the extrusion die	2	20	-	-
2) Workpiece makes contact with extrusion die	2	-	1000	-
3) Extrusion of the workpiece	0.25	-	24000	0.2
4) Workpiece remains upon extrusion die	1	-	1000	-
5) Workpiece moved to upsetting die	2	20	-	-
6) Workpiece makes contact with the upsetting die	2	-	1000	-
7) Upsetting of the workpiece	0.25	-	24000	0.2
8) Workpiece remains upon the upsetting die	1	-	1000	-

The same heat transfer and friction conditions are assumed to describe the upsetting operation as the extrusion operation. As the upsetting operation occurs immediately after the extrusion operation, the workpiece is not re-glassed. The heat transfer and friction would differ due to the difference in properties of the deformed glass in the upsetting operation, however, investigating this difference was not feasible within the scope of this research.

3.1.4 THERMAL MEASUREMENT

The temperature of the tooling is of interest to determine whether the tool temperature increases during a production run. The tool temperature impacts the mechanical response.

The tool temperature has been measured using a thermal camera. The camera was a DIAS Pyroview 380L, with a spectral range between 8 to 14μm. The camera was calibrated to measure temperature between 0 and 500°C. The data was recorded at 12.5Hz. The software Pyrosoft professional was used for recording and evaluating thermal imaging data.

To measure temperature using a thermal camera, the emissivity of the surface of interest must be known. The emissivity of the surface describes the ratio of energy that is absorbed by the object of interest compared to a perfect black body. Black bodies absorb almost 100% of the radiated energy.

The emissivity of the tool surface with and without a graphite coating has been considered to allow the temperature measurement using a thermal camera. An experiment was performed to determine the variation of the surface emissivity with changing temperature for a coated and uncoated surface.

Each surface condition was heated to 400°C and then allowed to cool to room temperature whilst the thermal radiation and tool surface temperature was measured with the thermal camera and a thermocouple. The temperature measured from the thermocouple was used to determine the emissivity of the tool surface.

The surface of interest was grinded with 180 grit paper to form a uniform surface finish. The surface roughness achieved is similar to an as-machined die surface. The specimen material was obtained from off-cuts from the metallurgical analysis performed during the case studies.

A calibrated K type thermocouple probe was attached to the sample and the readings were recorded using a NI DAQmx data logger connected to a laptop. The software NI signal express was used to record the data. The experimental setup is shown in Figure 3-1.
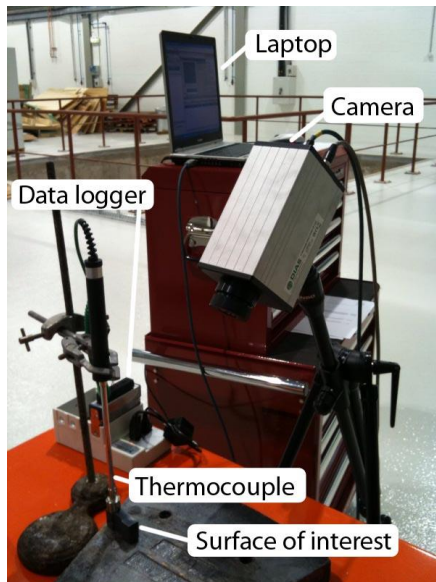
FIGURE 3-1: EMISSIVITY MEASUREMENT

Each experiment was repeated by reheating the sample in the furnace. Thermal images of the lubricated and un-lubricated samples are shown in Figure 3-2.

A) AS POLISHED   **B) LUBRICATED**
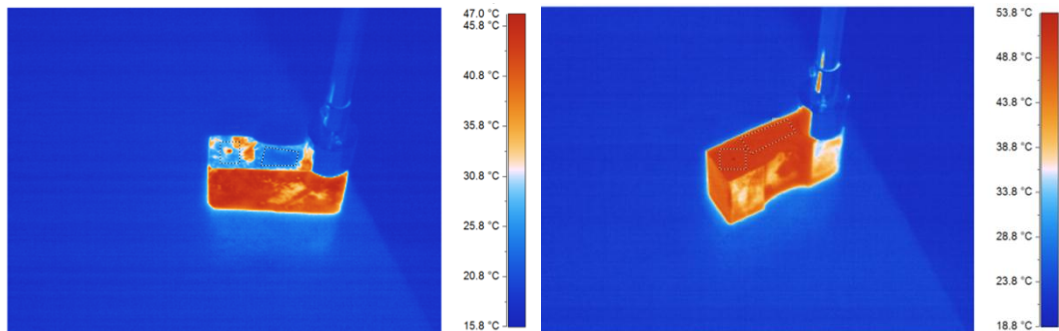
FIGURE 3-2: THERMAL IMAGE OF SAMPLE DURING COOLING

The emissivity was measured by calibrating the thermal camera reading to align with the temperature measured from the thermocouple. The emissivity of the polished surface was measured at 0.32±0.07 whilst the lubricated surface had an emissivity of 0.82±0.06.

The method outlined by Taylor (2010) has been followed to determine the measurement error from temperature measurement using a thermal camera. The error of the reading from the thermal camera is calculated by determining the

percentage change in output from a 1°C rise in object temperature. The equation is shown below (Taylor 2010):

$$\%/°C = 100 \times \frac{C_2}{\lambda T^2}$$

<div align="right">3-2</div>

Where;

$\%/°C$ Percentage change per degree

c_2 Planck's second constant

λ Wavelength (m)

T Temperature (K)

The measurement error in Kelvin is given below:

$$measurement\ error = \frac{\%\ error\ in\ emissivity}{\%/C}$$

<div align="right">3-3</div>

The percentage error in emissivity is 7% for the as-machined surface condition and 6% for the graphite coated condition. Equation 3-3 is used to determine the error in all temperature measurements. The measurement error is temperature sensitive and is shown in Figure 3-3. The measurement error increases with wavelength, temperature and the error in emissivity. The error involved when analysing the temperature using a wavelength of 14µm is to be used in the calculations as this is the worst case scenario.
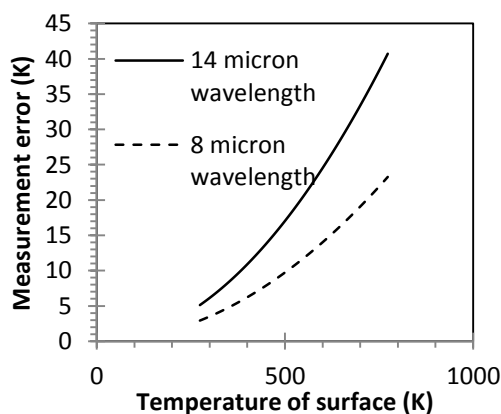
A) POLISHED SURFACE   B) LUBRICATED SURFACE
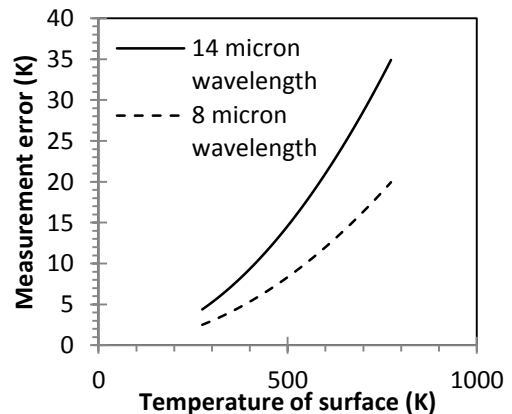
FIGURE 3-3: MEASUREMENT ERROR CONSIDERING THE WAVELENGTH OF THE THERMAL CAMERA AND ERROR IN EMISSIVITY

3.2 RESULTS

The results from the investigation has been categorised into three sections; the examination of the extrusion tooling, the examination of the upsetting tooling and the examination of the thermal cycle.

The examination of the extrusion and upsetting operations include 3D scan measurements, metallurgical observations and FEA approximations of die stress and temperature. The findings have been separated into different locations that relate to the part defects that fail the tooling.

The third section outlines the findings from the investigation into the thermal cycle of the preform tooling. The over-tempering behaviour of the die material has been measured to evaluate the role of thermal softening during production.

3.2.1 THE EXTRUSION TOOLING

The extrusion tooling open vertically to allow for the removal of the workpiece as illustrated in Figure 2-8. A cross section through the line of vertical line of symmetry of the tool set up is shown in Figure 3-4.
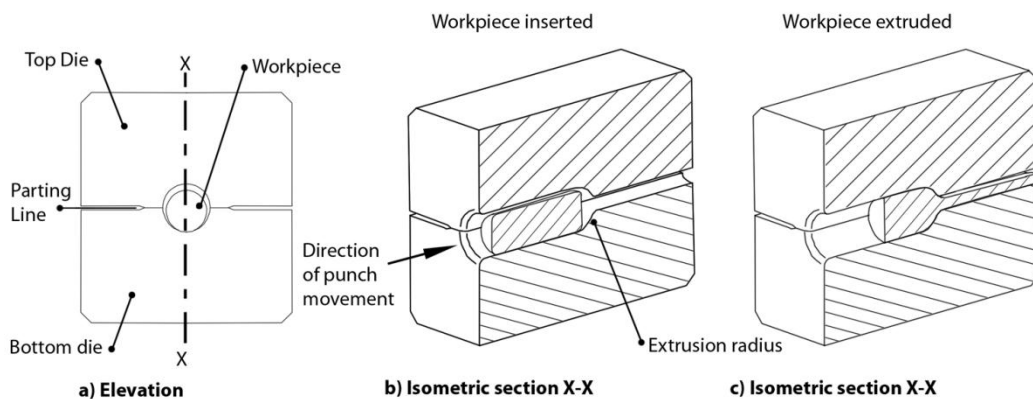
FIGURE 3-4: CROSS SECTION OF TOOL SET UP.

The terminology used to describe the part damage consists of "scoring" and "flashing". Scoring describes the grooves formed on the extruded surface which extend along the aerofoil blade. The acceptable depth and density of scoring marks varies depending upon the product.

"Flashing" describes the damage where the workpiece flows between the parting-line. A maximum tolerance exists for the "flashing" defect which varies from part to part. The rate of part defect formation from one trial is shown in Figure 3-5.

The scoring and flashing damage is observed upon the majority of parts produced. Similar damage is observed upon the tool surface, relating the part defect to the worn die surface.
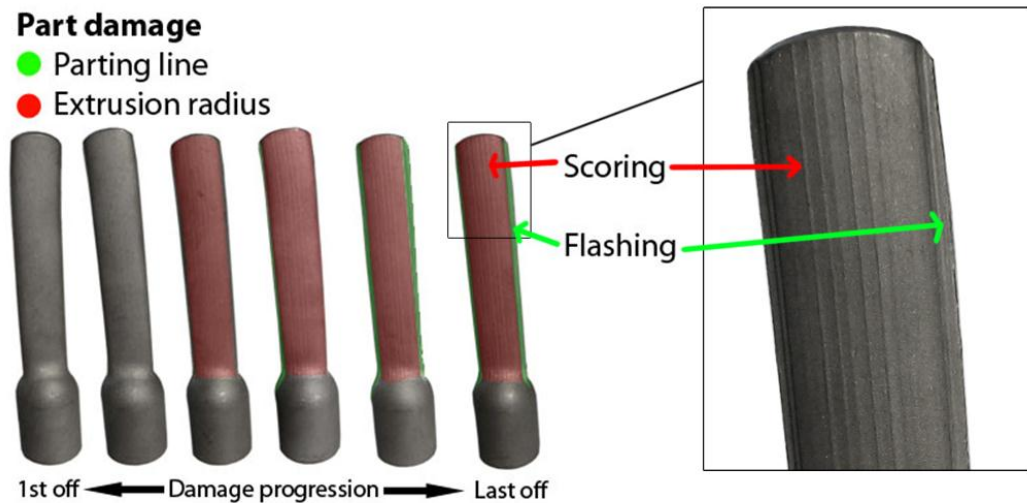
FIGURE 3-5: PART DAMAGE LOCATION AND TERMINOLOGY

3.2.1.1 EXAMINATION OF THE FAILED TOOLING

Figure 3-6 reports the geometrical difference between the initial and worn geometries of the top extrusion tool. Different scales are shown to highlight either material gained or material lost. Figure 3-6 shows that 0.5mm of material has been lost at the parting line at the location of the flashing damage.

The material gain measured from the 3D scan may be caused by either plastic deformation or adhesive wear. The difference in microstructure between the workpiece and tool material and the lack of pitting marks associated with adhesive wear indicate that the material gain is caused by plastic deformation(Chattopadhyay 2001). Material lost may be caused by the removal of material through wear or plastic deformation.

The following sections go into further detail exploring the different defects that fail the tooling. "Scoring" damage is investigated by examining the tool surface at the location of the extrusion radius. The "flashing" damage is investigated by examining the tool surface at the parting line.
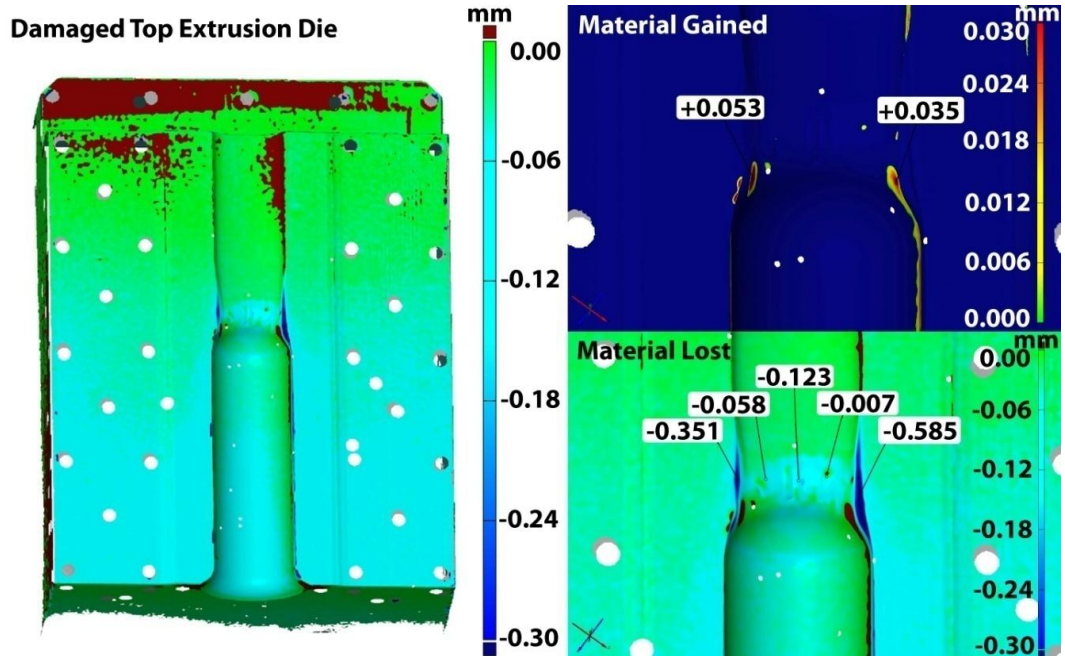
FIGURE 3-6: DIFFERENCE IN GEOMETRY BEFORE AND AFTER A PRODUCTION RUN/

3.2.1.1.1 The "scoring" damage

The scoring damage describes the scoring marks that occur along the extruded stem of the workpiece. Similar scoring marks are observed upon the worn extrusion tool.

A cross section of the 3D scan data was created to examine the geometrical deviation along the extrusion radius aligned with the direction of extrusion. The location of the cross section is illustrated in Figure 3-7.

a) Sectioned isometric   **b) Close up of extrusion radius**

Top of radius

Bottom of radius
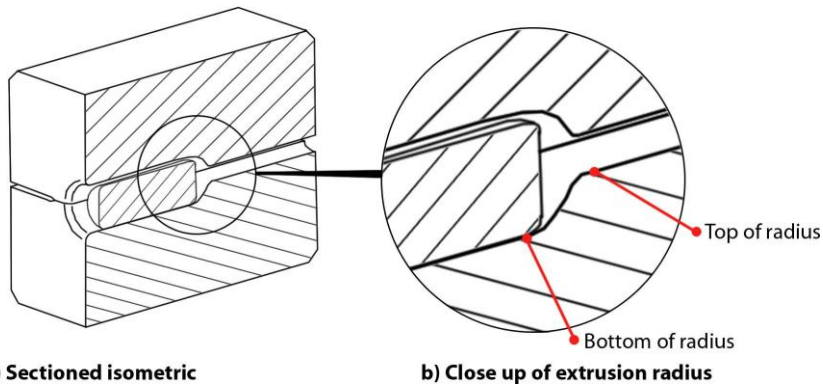
FIGURE 3-7: LOCATION OF EXTRUSION RADIUS

Figure 3-7 displays the location of the extrusion radius. The difference in tool geometry, measured before and after a production run, at the location highlighted in Figure 3-7 b), is shown in Figure 3-8.
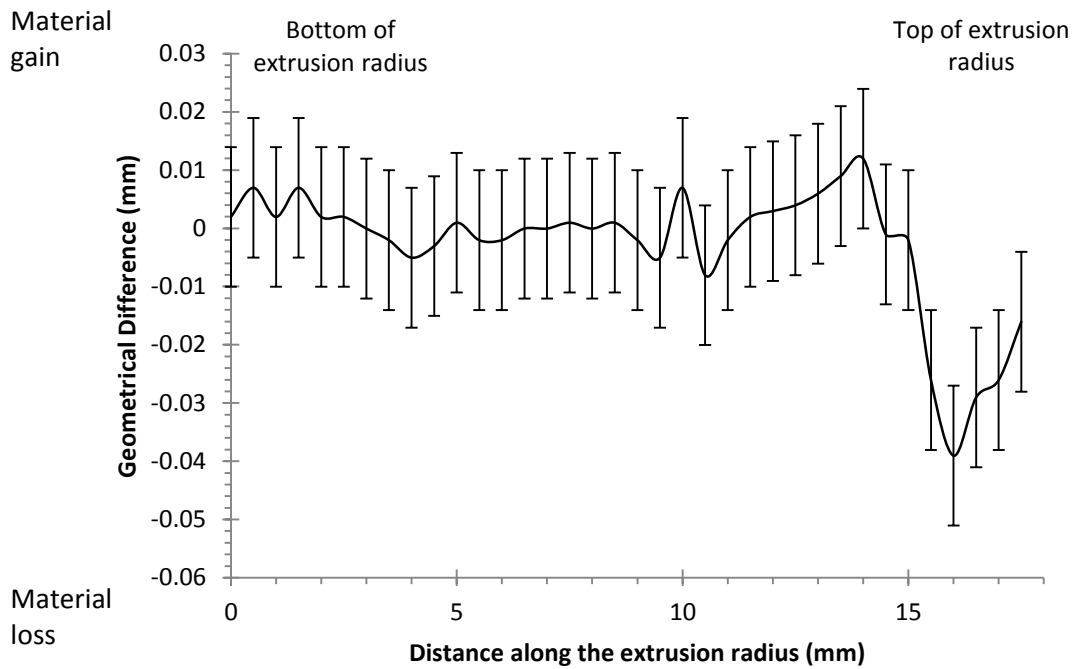
FIGURE 3-8: GEOMETRICAL DEVIATION CROSS SECTIONS ALIGNED WITH THE EXTRUSION DIRECTION

The measured surface is reflective of the heat checking observed upon the tool surface. The scan shows small geometrical deviation with the largest deviation measured near the top of the extrusion radius. This finding corresponds well with the nitride depths measured along the extrusion radius as shown in Figure 3-10.

The surface layers of the worn tool have been examined using light microscopy. Figure 3-9 shows a metallurgical sample taken to examine the surface layers along the extrusion radius.

The most damage is observed around two thirds up the extrusion radius. Regular cracks are observed along the extrusion radius. As the cracks get closer to the area of most damage, the cracks start to penetrate the substrate. A delaminated layer is observed along the bottom of the extrusion radius but not at the region of most damage. The nitride thickness varies in depth with the least amount of nitride at the location of damage. Portions of the nitride layer are missing at the location of most damage. Figure 3-10 shows the reduction in nitride depth measured from the sample.
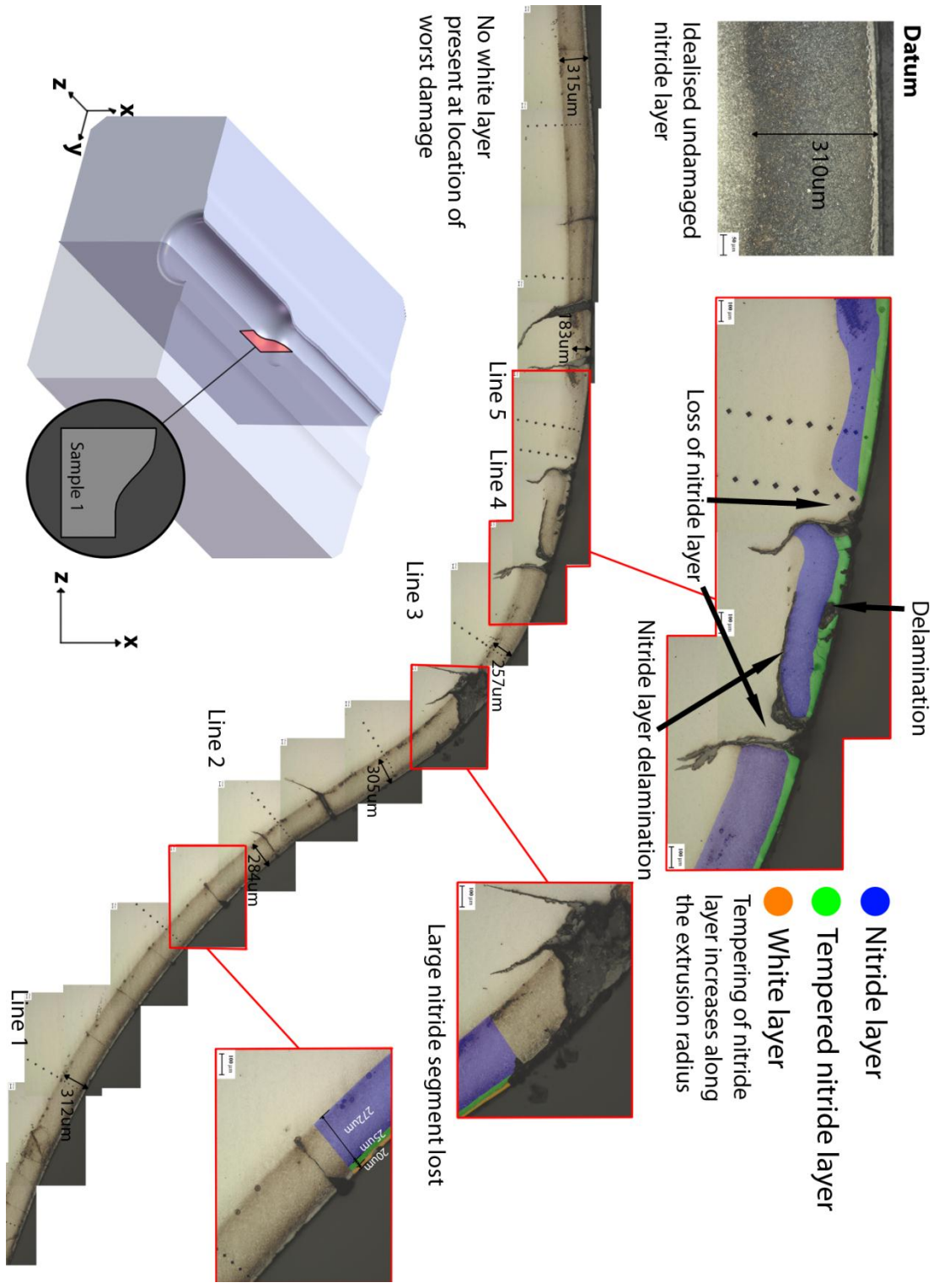
FIGURE 3-9: LIGHT MICROSCOPY AND LOCATION OF HARDNESS MEASUREMENTS.
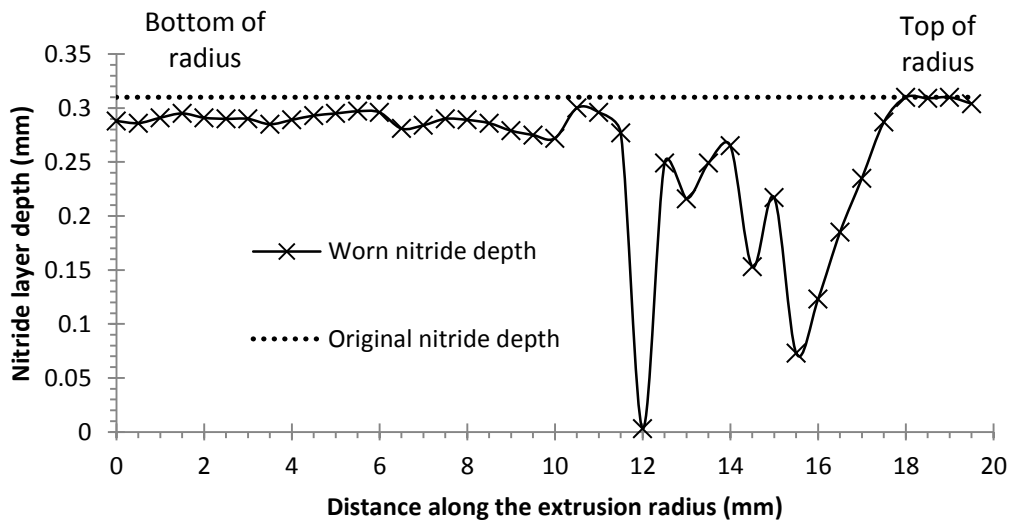
FIGURE 3-10: NITRIDE DEPTH ALONG THE EXTRUSION RADIUS.

Figure 3-9 also highlights a heat affected zone as well as a white layer. The white layer is formed during nitriding. The presence of the white layer suggests that little material has been lost from the die surface at these locations.

Figure 3-11 shows large plastic deformation of the substrate from a similarly failed die as shown in Figure 3-9. The tooling had the same heat treatment and surface treatment.

The graphite lubrication or "dag" was identifiable as the graphite could be seen out of plane from the polished surface. The white layer in the nitride is not evident in the nitride regions of shorter depth than the undamaged locations. This is proof that the nitride layer is being removed at these locations. The substrate shows severe plastic deformation.

An explanation for the observed surface condition is that the nitride is fractured into segments. The plastic deformation of the substrate results in the collision of the nitride segments. Protruding segments of the nitride layer is removed through abrasive wear with the workpiece. Further evidence of plastic deformation of the substrate is shown in Figure 3-12.

In Figure 3-12 the micro-segregation banding is used to highlight the amount of plastic deformation observed near the surface. The micro-segregation is formed during the manufacturing of the die material. The banding is normally aligned in

72

the rolling direction and the change in direction of the banding is indicative of plastic deformation. The micrograph has been digitally enhanced to show the deviation in the direction of the micro segregation. The cracks present in the material are not influenced by the banding, similar to the observations made by Castro et al (2007) and Summerville et al (1995).
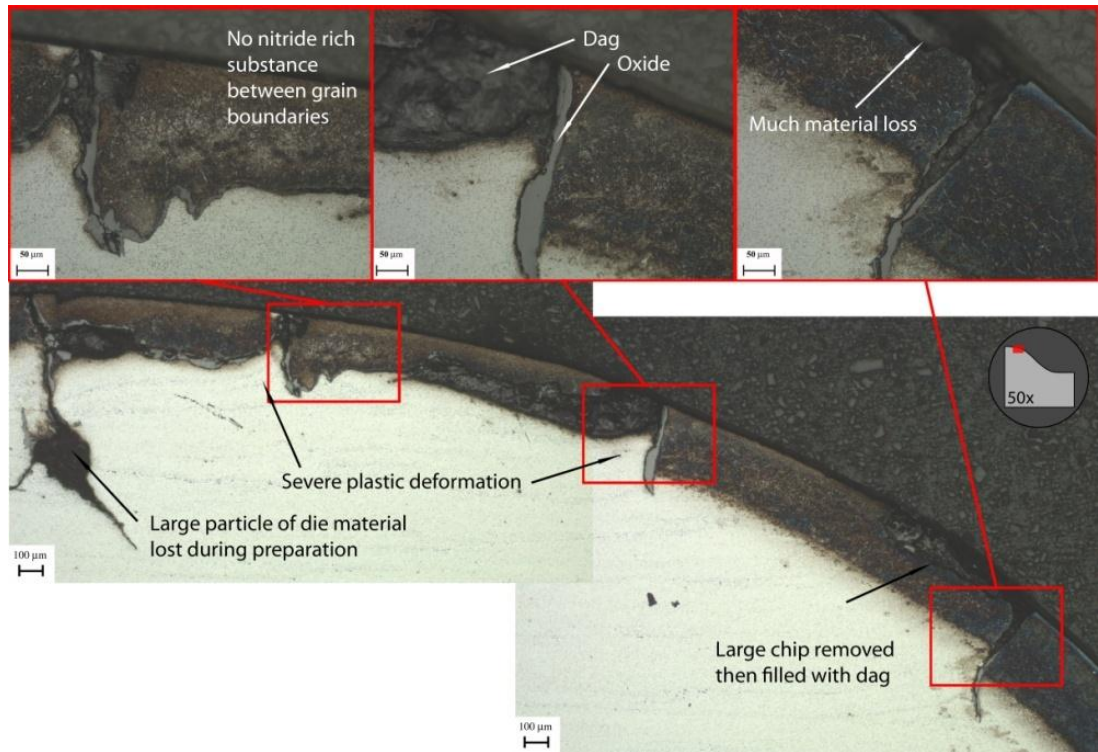
FIGURE 3-11: LIGHT MICROSCOPY OF A WORN EXTRUSION DIE.
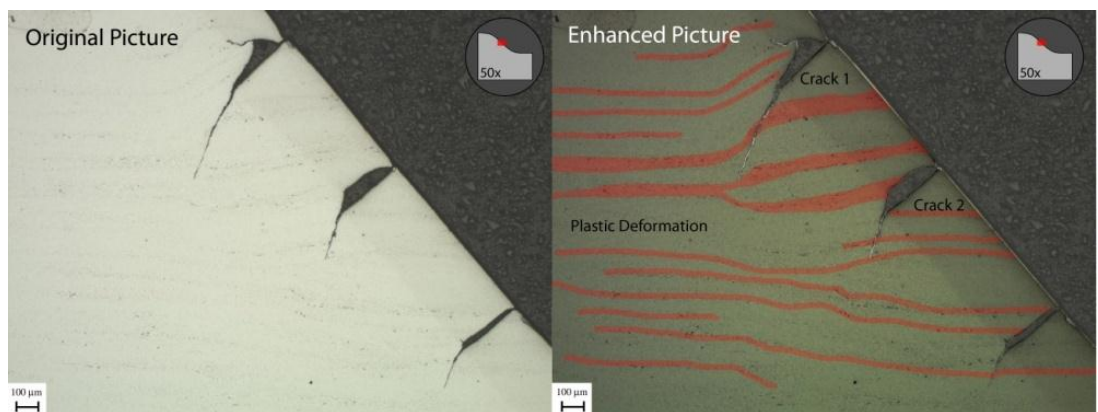
FIGURE 3-12: CRACKING AND PLASTIC DEFORMATION OF THE EXTRUSION RADIUS AT X50 MAGNIFICATION.

Microhardness measurements have been taken in a line normal to the surface at the locations shown in Figure 3-9. The microhardness measurements are

compared to a datum sample of similarly heat treated and nitrided H13 tool steel. The results are shown in Figure 3-13.
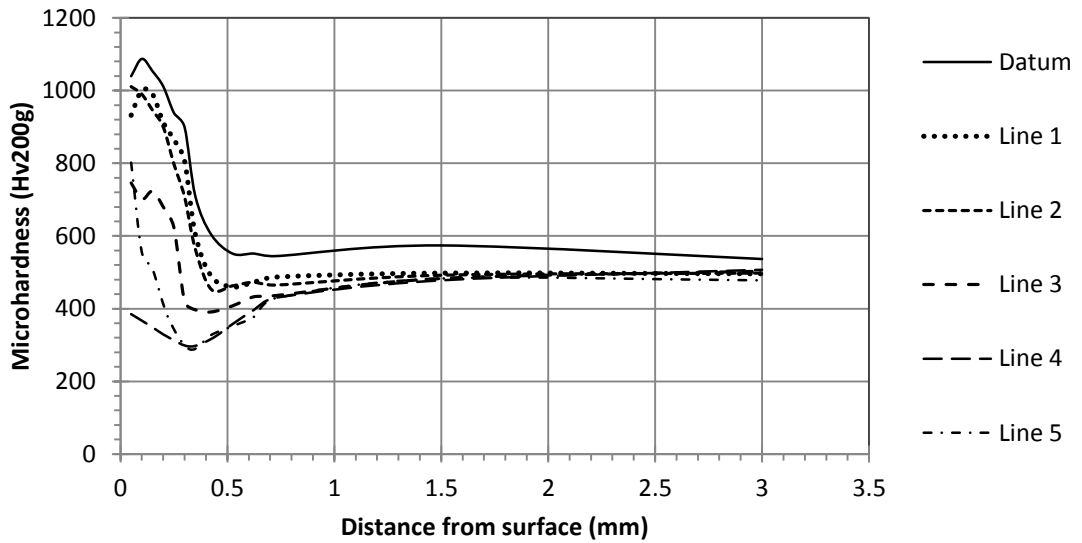
FIGURE 3-13: MICROHARDNESS MEASUREMENTS.

The core hardness of the tool is lower than the datum. Localised reductions in hardness are observed in the surface layers at the regions of damage. The lowest hardness measured is 320HV near the surface where most damage has been observed. Changes in hardness relate to a change in mechanical response from the tool material. Possible explanations of the change in hardness include surface fractures, thermal softening and plastic deformation (Summerville, Venkatesan et al. 1995).

The core hardness has reduced from ~600HV to ~500HV. The tooling in question is nitrided for 48 hours before service. A failed tool is re-cut and re-used. The reduction in core hardness has been found to be caused by repetitive nitriding operations. Over-tempering tests were performed with the aim of determining the hardness of the substrate as a result of repeated nitriding operations. AISI H13 specimens were heated in a furnace for times equivalent to the nitriding time applied to dies used in the forge. The results are shown in Figure 3-14.

$$y = -0.3656x + 562.09$$
$$R^2 = 0.9738$$
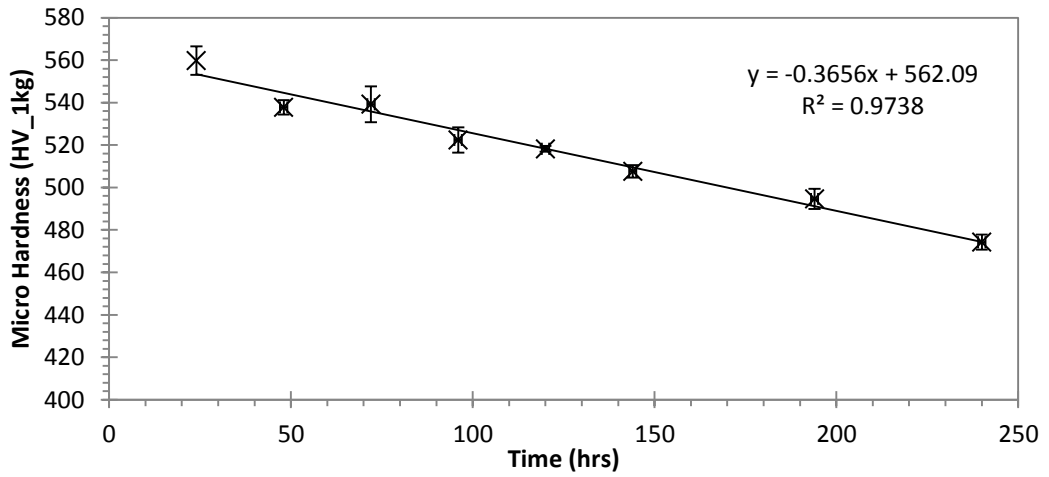
FIGURE 3-14: CORE SUBSTRATE HARDNESS FROM RE-PEAT NITRIDING AT A TEMPERATURE OF 525°C

A linear equation has been fitted to the data to allow the prediction of the substrate hardness as a result of repeated nitriding operations. This equation has been applied to interpolate the core hardness of different cuts of dies considering 24 or 48 hour nitriding. The results are shown in Table 3-2. The reduction in core hardness of the extrusion and upsetting tooling has been explained by the repeated nitriding operations. The failed extrusion tooling examined was a C cut with 48hour nitriding.

TABLE 3-2: SUBSTRATE MICROHARDNESS RESULTING FROM OVER-TEMPERING AS A RESPONSE FROM NITRIDING

24 hour nitriding		48 hour nitriding	
Die Cut	Core hardness (HV_1Kg)	Die Cut	Core hardness (HV_1Kg)
A	553	A	545
B	545	B	527
C	536	C	509
D	527	D	492
E	518	E	474
F	509	F	457
G	501	G	439

The core hardness of the die material has reduced due to repeated nitriding operations. The change in hardness near the damaged surface has been caused as a result of forging.

The following observations have been made when investigating the worn extrusion tooling at the location of the "scoring" defect:

- Regular cracking of the nitride layer with cracks penetrating the substrate at the top of the extrusion radius. The cracks may be caused by mechanical fatigue, thermal fatigue or the plastic deformation of the substrate.

- The substrate is observed to be extruded between cracks in the nitride at the top of the extrusion radius.

- The nitride layer is different depths along the extrusion radius. The difference is indicative of material removal through abrasive wear.

- The nitride layer remains intact at most locations of the tool surface except at the location of most damage where the substrate is observed at the tool surface. The exposed substrate is much more prone to abrasive wear than the nitrided regions.

- The white layer remains at certain locations of the die surface suggesting the wear at these locations is minimal.

- Plastic deformation of the substrate has been identified through the change in the direction of the segregation bands.

- A reduction in hardness has been measured within the nitride layer with largest reductions at the location of most damage. A change in hardness may be explained through microstructural change, the reduced size of the case hardened layer and plastic deformation.

- A reduction in hardness localised to the nitride-substrate interface has been measured with hardness measurements as low as 320HV.

3.2.1.1.2 The "flashing" damage

The "flashing" damage describes the phenomena where the workpiece has flowed in between a gap at the parting line of the extrusion tooling. Figure 3-15 shows the surface layers when examining the material loss of the tool at this location. The location of the sample from the worn tool is shown in the figure. A cross section of the 3D scan has been overlaid upon the micrograph to allow comparison. A depth of 924μm of material has been lost at the parting line.

The nitride and part of the substrate is missing at the parting line. A high amount of plastic deformation is observed in the neighbouring nitride and substrate. Plastic deformation of the nitride is surprising as the nitride has mechanical properties more similar to a ceramic than a metal.

Large non-tangential cracks are noticeable (Figure 3-15a). Figure 3-15b shows an example where the white layer has suffered brittle fracture under compressive load.

In Figure 3-15c) different surface layers have been identified within the nitride layer. The figure highlights an oxidised layer, a white layer, a visibly coarsened nitride layer and the nitride layer.

Figure 3-15d) shows the content of a large crack at the surface. The microstructure of this debris differs to the nitride, the tool steel and the graphite lubrication. It is likely that the debris consists of workpiece material which has been removed due to abrasive contact with the die surface.

Figure 3-15e) shows severe plastic deformation of both the martensitic tool steel and the nitride layer. The nitride layer normally exhibits mechanical properties more similar to a ceramic than a metal and this amount of plastic deformation in the nitride plasticity layer indicates high temperature and high pressure localised to this region. The small gap between the parting lines would act as a stress raiser due to the sharp radii.

Figure 3-15f) shows no white layer. This means that the white layer must have been removed through either continuous abrasion or delamination at this region. Figure 3-15g shows the relatively undamaged nitride layer for comparison with the other micrographs.

In Figure 3-15A) the substrate is observed to be forced through gaps in the nitride layer. High stress and temperature is required to make hot work tool steel this ductile. Image B) shows the damaged parting line where a section of the tool material has been lost during preparation. The nitride is missing at this location. The substrate makes direct contact with the workpiece. The rate of abrasive wear is much higher due to the lack of the high hardness nitride layer.

The observations made from examining the worn tool are listed below.

- Both nitride and substrate is missing at the parting line of the tool.
- The substrate is present at the tool surface at the parting line.
- The substrate extruded between cracks in the nitride.
- Plastic deformation has also been observed within the nitride layer.
- The white layer is not present along the nitride surface that makes contact with the workpiece.

A likely explanation for the loss of material from the parting line is brittle fracture of the nitride layer followed by abrasion of the relatively soft substrate. The sharp angle of the parting line may act as a stress raiser. Any misalignment in the top and bottom dies causes the protrusion of this material into the path of the workpiece.

Figure 3-16 shows a close up of regions showing plastic deformation of the substrate.
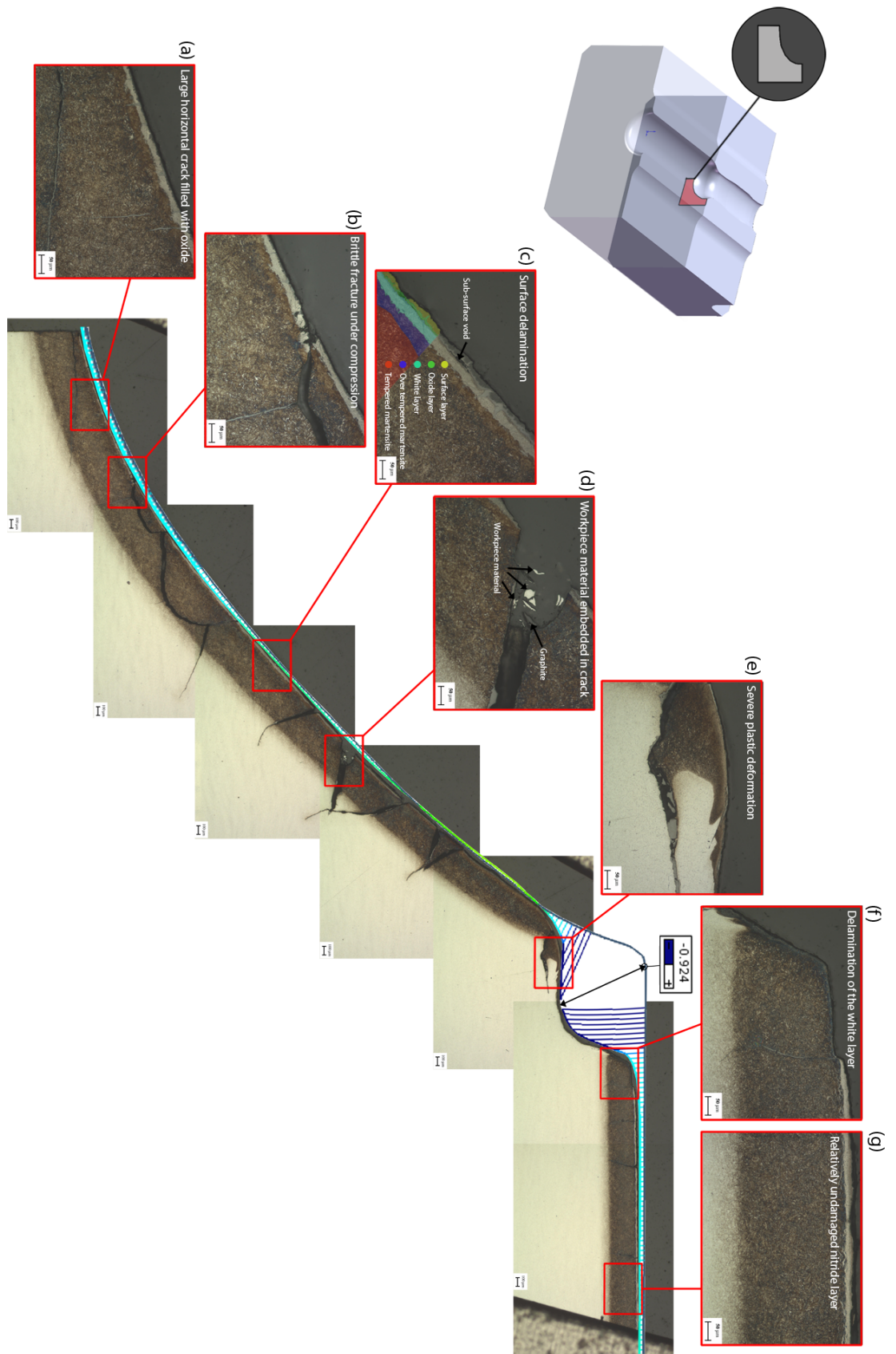
FIGURE 3-15: LIGHT MICROSCOPY OF THE DAMAGE SEEN AT THE PARTING LINE

(a) Large horizontal crack filled with oxide

(b) Brittle fracture under compression

(c) Surface delamination
- Sub-surface void
- Surface layer
- White layer
- Oxide layer
- Over tempered martensite
- Tempered martensite

(d) Workpiece material embedded in crack
- Workpiece material
- Graphite

(e) Severe plastic deformation

(f) Delamination of the white layer

(g) Relatively undamaged nitride layer

-0.924

FIGURE 3-16: IMAGE A - EXTENSIVE PLASTIC DEFORMATION OF THE SUBSTRATE AT (X50 MAGNIFICATION). IMAGE B - THE CORNER OF THE EXTRUSION PROFILE (X50 MAGNIFICATION).

3.2.1.2 INVESTIGATION OF THE THERMO-MECHANICAL LOADING

The thermo-mechanical loading at the location of "scoring" and "flashing" damage has been approximated using finite element analysis applying the assumptions outlined in section 3.3.

The punch moves the workpiece into the die cavity to form the aerofoil blade preform geometry. The press measures a punch load of approximately 30 tonnes during the extrusion operation. The simulated forging load is shown in Figure 3-17. The simulation shows reasonable agreement with the measured load of the forging press.
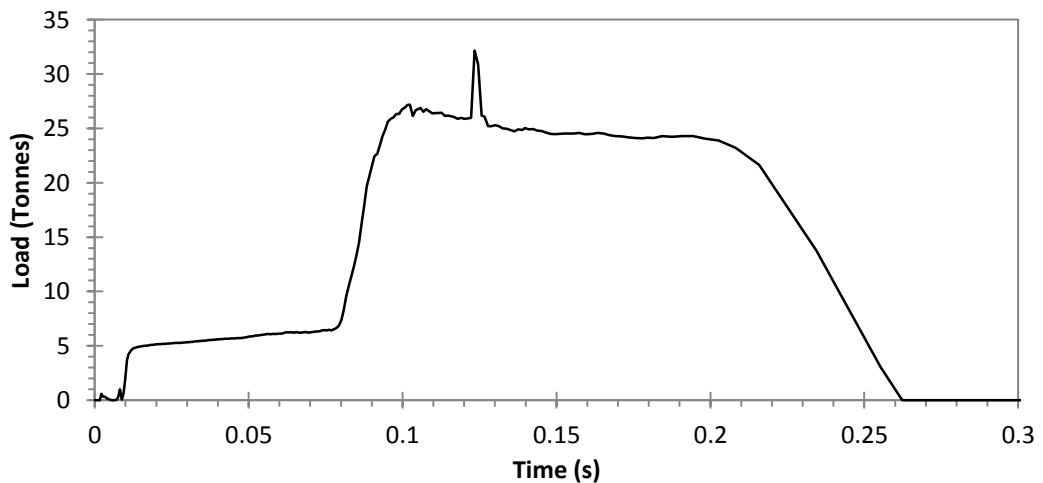
FIGURE 3-17: SIMULATED FORGING LOAD

3.2.1.2.1 FE simulation of the conditions at the location of "scoring"

The thermal gradient at the extrusion radius, at the end of the forming operation is shown in Figure 3-18. The figure also shows the thermal history at points taken at intervals into the tool surface.

A) MAXIMUM THERMAL GRADIENT IN TOOL

B) TEMPERATURE AT SELECT LOCATIONS
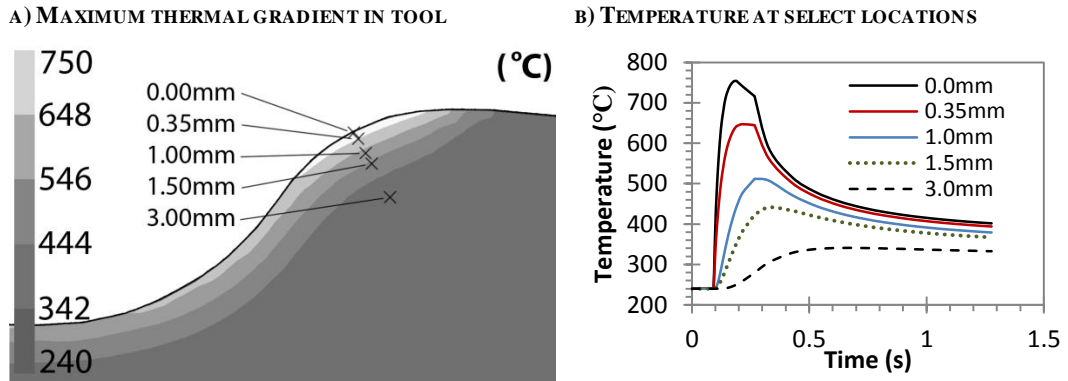
FIGURE 3-18: PREDICTED TEMPERATURE OF THE TOOL

Figure 3-18a) shows the thermal gradient at the end of deformation. The image also highlights locations of interest. The temperature during the forging operation is shown in image b). The highest predicted temperature is 742°C at the tool surface. The simulation suggests that die temperatures exceed 500°C to a depth less than 1mm.

Figure 3-19a) shows the effective stress at peak loading and the location of five points of interest. The temperature dependent 0.2% proof stress has been compared with the von Mises stress in figures b) to d) at the locations highlighted in figure a).

The approximated stress and temperature dependent proof strength suggests that plastic deformation occurs at the extrusion radius. The largest stresses are predicted near the base of the extrusion radius. The lowest proof strength has been predicted at location 3 which aligns with the region of most observed surface damage upon worn tooling.

The comparison of the von Mises stress and temperature dependent proof stress indicates that the tool is prone to plastic deformation during service.
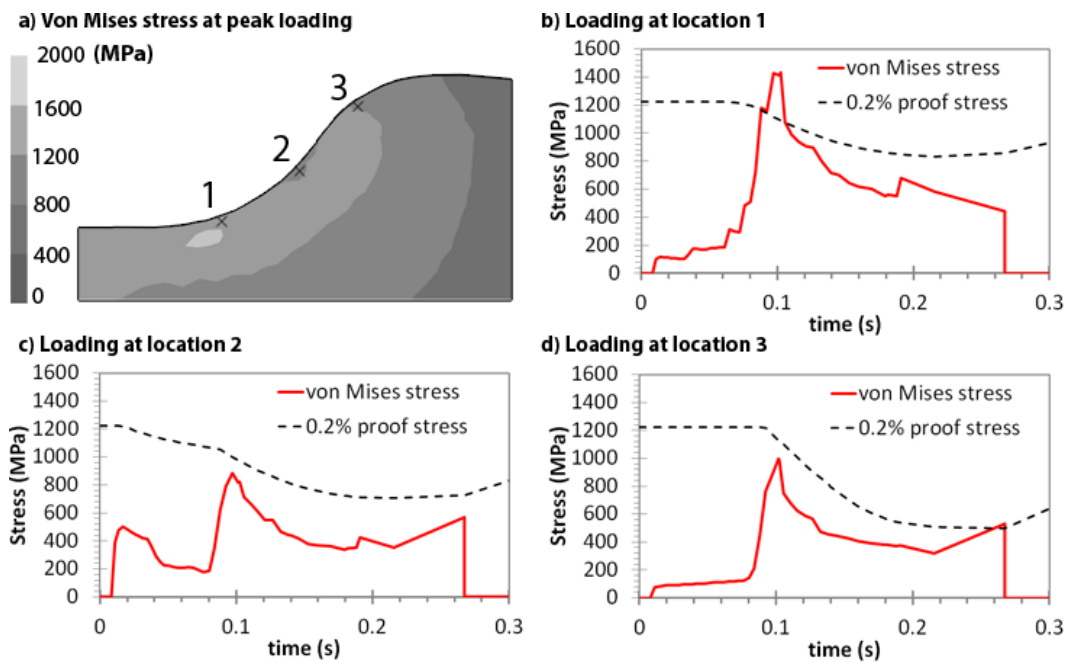
FIGURE 3-19: DIE STRESS PREDICTIONS AT PEAK LOADING AND POINTS OF INTEREST

3.2.1.2.2   FE simulation of the conditions at the location of "flashing"

Figure 3-20 shows the temperature at the parting line at the end of the extrusion operation. Lower temperatures have been predicted at this location in comparison to the extrusion radius where scoring occurs.

A) PEAK TEMPERATURE AND POINT LOCATIONS   B) TEMPERATURE AT POINT LOCATIONS
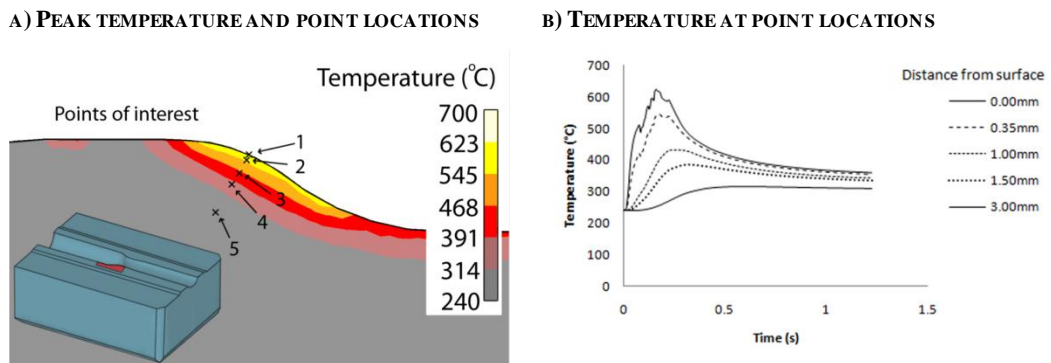
FIGURE 3-20: APPROXIMATED TEMPERATURES AT THE END OF THE CYCLE AT THE EXTRUSION RADIUS

A depth of approximately 0.45mm reaches a temperature above 500°C. The simulation suggests higher temperatures are observed at the extrusion radius where scoring occurs. The simulation does not take into account the change in the die geometry and surface condition with die degradation. Higher friction

82

would be incurred as the workpiece is forced between the parting lines causing the flashing damage.

Figure 3-21a) shows the approximated von Mises stress at the moment of peak loading at the parting line and the location of specific points of interest. The approximated von Mises stress at these locations are shown in figures b) to d). The approximated proof stress and von Mises suggest that the tool is prone to plastic deformation with shock loading.
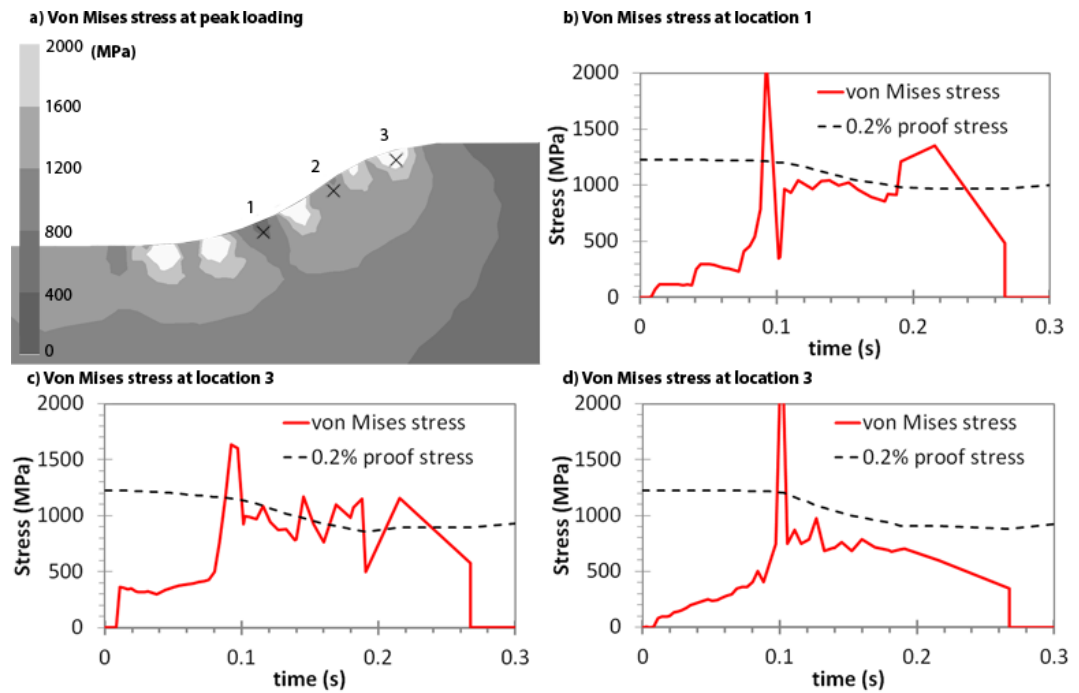
FIGURE 3-21: APPROXIMATE VON MISES STRESS AND PROOF STRESS AT THE PARTING LINE

3.2.2   THE UPSETTING TOOLING

This extruded workpiece is upset to form the root block geometry of the single ended compressor blade. The die material, heat treatment and nitriding are the same as the extrusion operation. The tooling excluding the top die can be seen in Figure 3-22. The geometry of the upsetting tooling is shown in Figure 3-23.
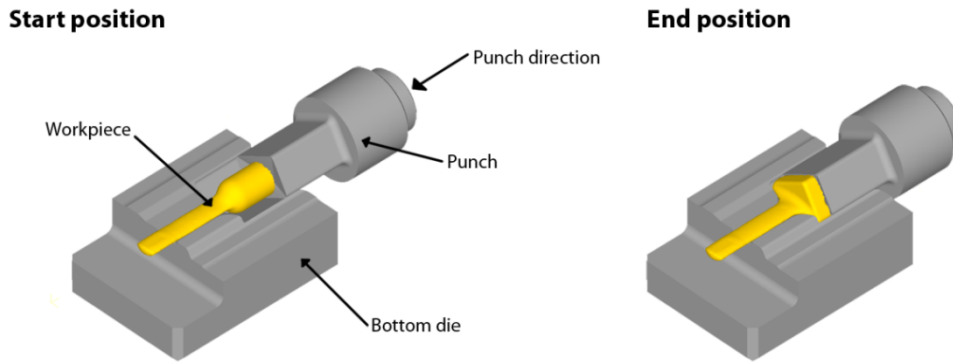
FIGURE 3-22: DIE SET UP EXCLUDING TOP DIE.

Plan

Isometric

Elevation

End elevation
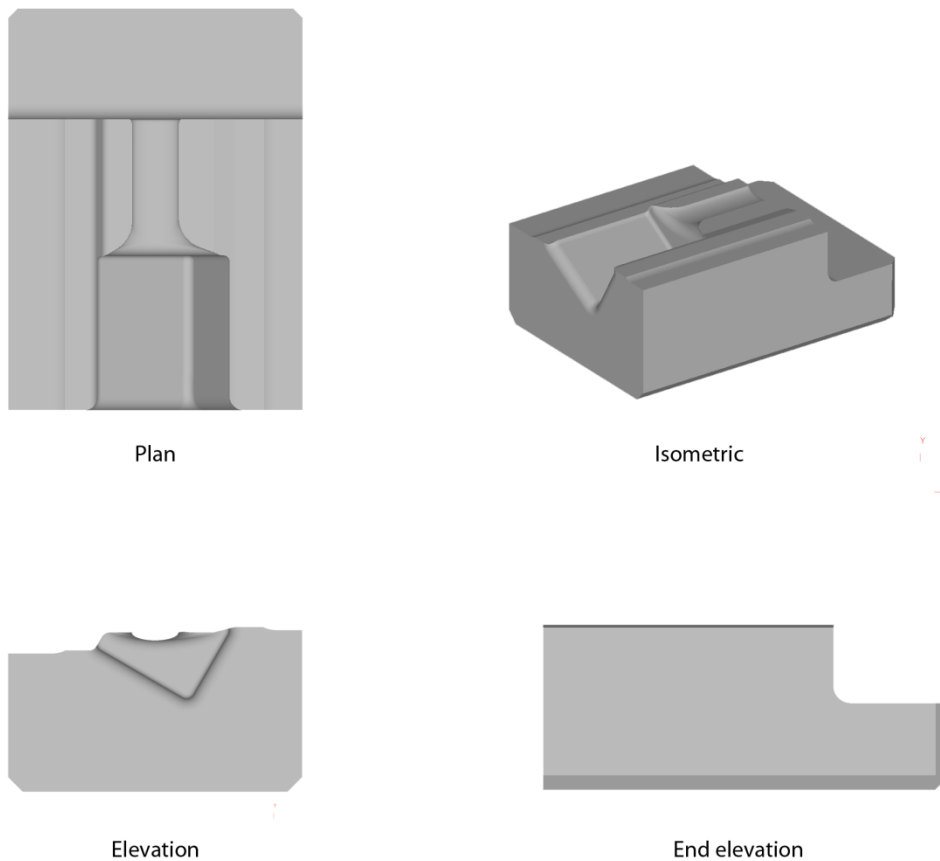
FIGURE 3-23: GEOMETRY OF UPSETTING TOOLING

The most common part defects which fail the upsetting tooling are termed as either "smiley faces" or "crimping". The location of these part damage modes can be seen in Figure 3-24.

FIGURE 3-24: PART DAMAGE FROM THE UPSETTING OPERATION.

The "smiley face" defect describes an indentation which forms upon the root block of the workpiece near the stem. Figure 3-24 highlights this defect in red. The "smiley face" part defect results in die failure when the indentation formed upon the workpiece becomes tactile during part inspection.

The "crimping" part defect describes the scoring marks observed upon the workpiece at the interface between the stem and the root block. These scoring marks are observed on both the workpiece and the tool surface. The "crimping" defect is similar to the "scoring" defect in the extrusion operation in that the forge operator determines the allowable extent of part damage before failing the tool.

3.2.2.1 EXAMINATION OF THE FAILED TOOLING

The worn tooling from the upsetting operation has been examined. The tooling failed through the formation of a "smiley face" part defect; however the "crimping" defect was also evident. Figure 3-25 shows the geometrical deviation of the failed header die compared with the initial as-machined geometry.

There is noticeable geometric deviation in the fillet radius that connects the workpiece stem to the root block. The scan indicates that this radius has collapsed with material protruding on the surface that forms the root block. The

85

geometric deviation measured from the 3D scan aligns with the defect observed upon the formed part.
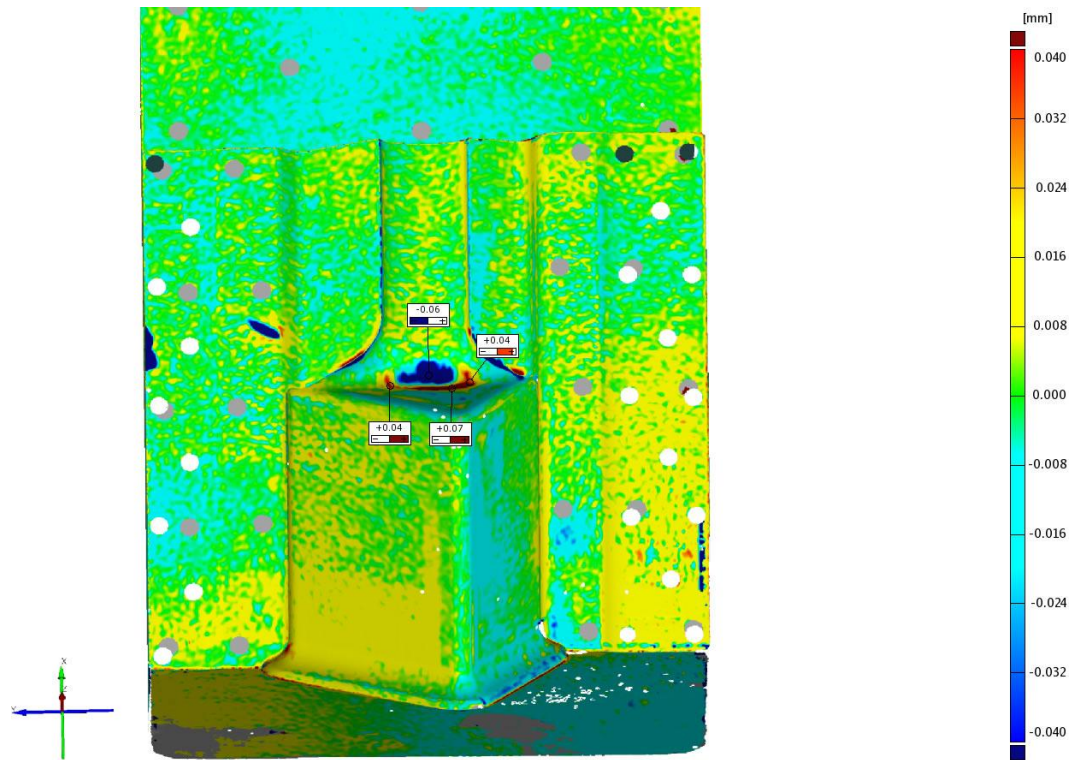
FIGURE 3-25: GOM IMAGE OF THE BOTTOM HEADER DIE. BLUE = MATERIAL LOST. RED = MATERIAL GAINED.

The surface condition has been examined using light microscopy at the locations of the "smiley face" and "crimping" damage. Figure 3-26 shows the sample locations.
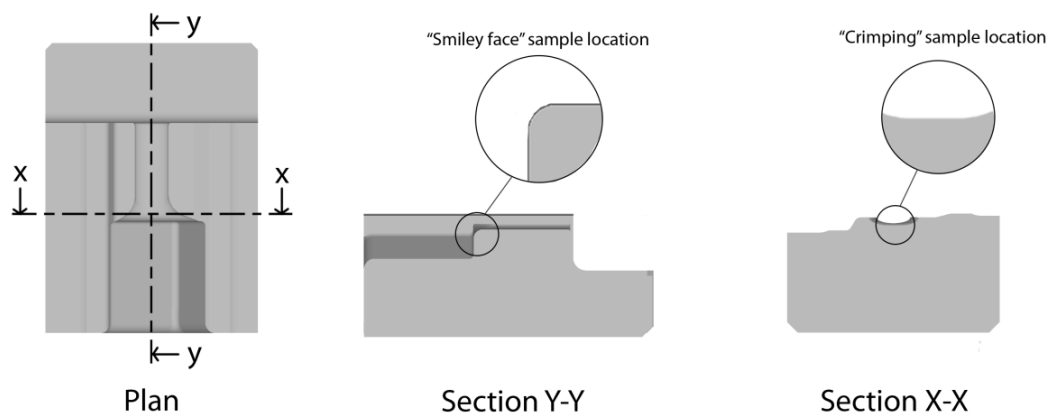
FIGURE 3-26: METALLURGICAL SAMPLE LOCATIONS FROM UPSETTING DIE

3.2.2.1.1   The "smiley face" defect

Figure 3-27 shows a section taken from a 3D scan which aligns with the defect "smiley face". The cross section shows greater material lost in comparison to the material gained. It can be seen that material is lost from above and below the protrusion which forms the "smiley face" on the workpiece.

A metallurgical sample was taken to examine the cross section shown in Figure 3-27. This allowed the examination of the "smiley face" damage. The micrographs are shown in Figure 3-28. In the top right of Figure 3-28 the location of the metallurgical sample is shown. This sample was taken from the top die. The geometric deviation in the surface profile is most noticeable in Figure 3-28 f).

The datum hardness measurements were taken from a sample of similarly heat treated H13. Similar to the extrusion tooling, the reduction in core hardness was a result of over-tempering caused by repeated nitriding operations. Localised softening was measured at the start of the substrate at lines 2, 3 and 4. This aligns with the collapsed region measured from the 3D scan.

Material Gained: 115163um^2
Material Lost: 481905um^2
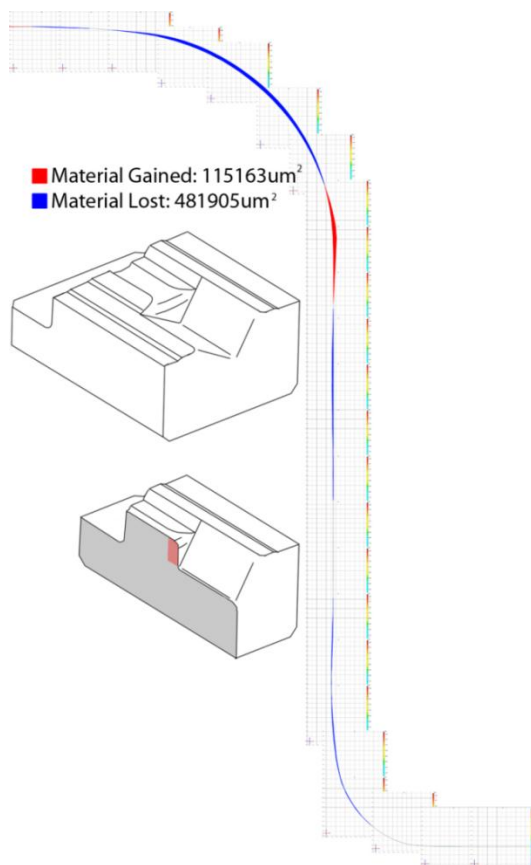
FIGURE 3-27: CROSS SECTION EXAMINING 2D AREA OF GEOMETRIC DEVIATION.

Figure 3-28a) shows the relatively undamaged microstructure. The nitride layer is present at all of the surface, indicating minimal material loss. The geometric deviation shown in Figure 3-27 and Figure 3-25 must be a result of plastic deformation. The hardness depth profile at location 1 shows high hardness within the nitride layer. Nitride precipitates can be seen in the nitride layer. The white layer is observed upon the die surface. Regular cracking is noticeable in the white layer. Figure 3-28h) shows a similar relatively undamaged microstructure.

Figure 3-28b) shows a perpendicular crack through the nitride layer which is retarded by the increased toughness of the substrate. Figure 3-28c) highlights the white layer where evidence of fracture-delamination is observed. Figure 3-28d) shows a part of the nitride where the white layer has been removed and graphite is visible in its place.
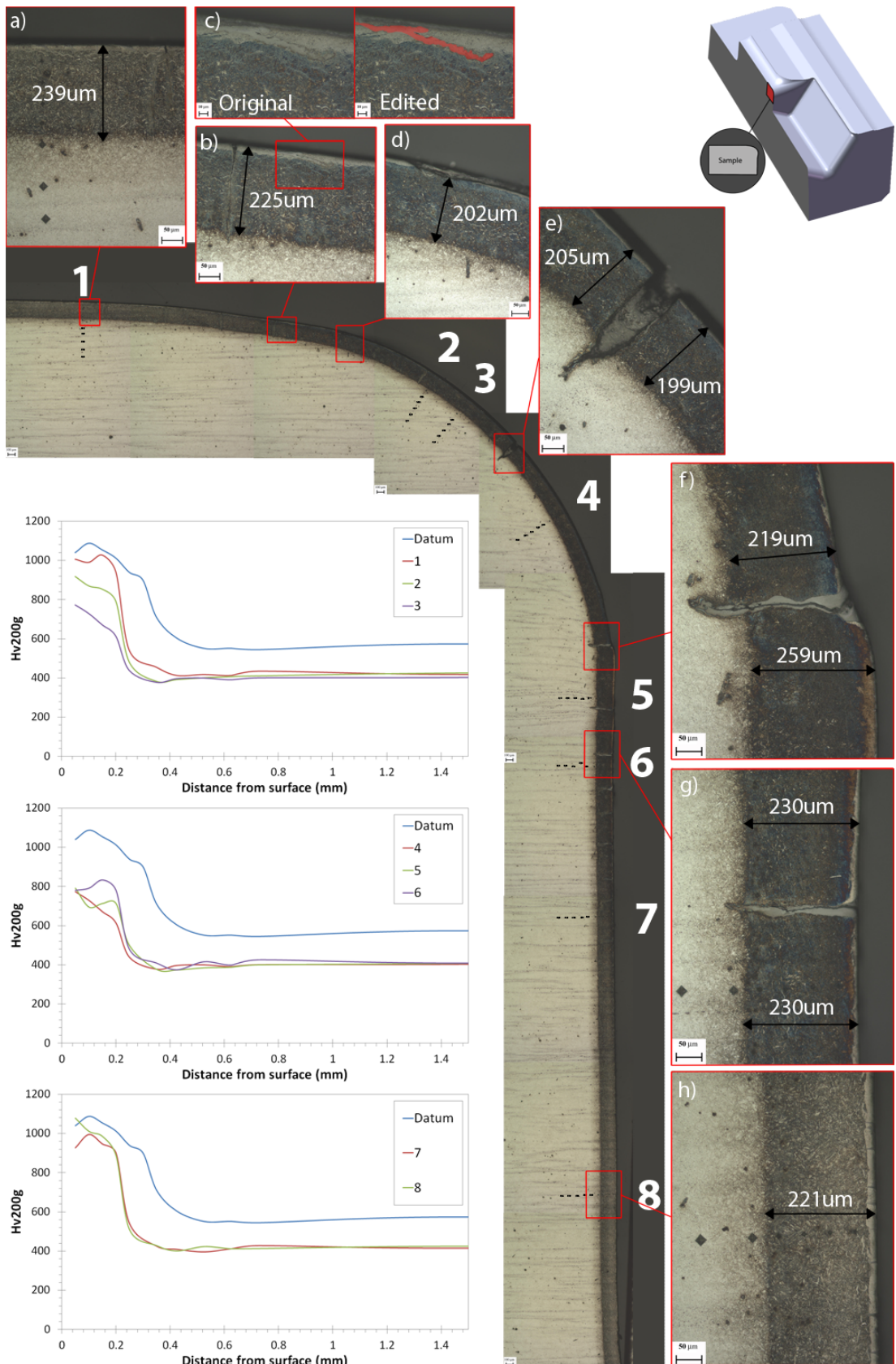
FIGURE 3-28: LIGHT MICROSCOPY & HARDNESS MEASURES EXAMINING THE ROOT BLOCK – STEM RADIUS.

Figure 3-28e) highlights a large hole in the nitride layer which is filled with graphite with cracks penetrating the substrate. The two sections of the nitride layer seem to have been moving in opposing directions.

Figure 3-28f) shows a step in the nitride thickness located at a crack which penetrates the substrate. The difference in depth of the nitride and the lack of the white layer indicate that a portion of the nitride next to the fracture has been abraded. The micrograph suggests that the nitride is divided by the regularly occurring fractures with nitride segments colliding against each other.

Figure 3-29 shows light microscopy images taken from the bottom die from the same tooling as Figure 3-28. The segregation banding is observed to change direction indicating the direction and extent of plastic deformation within the tool.
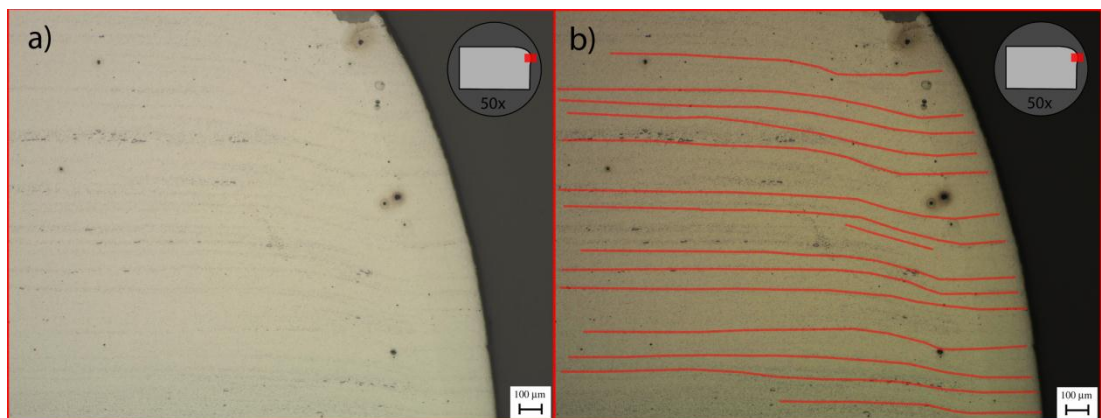
FIGURE 3-29: LIGHT MICROSCOPY OF UPSETTING BOTTOM DIE AT THE LOCATION OF THE "SMILEY FACE" DAMAGE.

The findings of the investigation into the failed upsetting tooling are summarised below:

- The collapse of the radius that forms the platform of the compressor blade.
- The retention of the nitride layer indicating that abrasive wear is not significant.
- Regular cracks have been observed in the nitride layer. Possible causes for the nitride to crack include thermal fatigue, mechanical fatigue and the plastic deformation of the substrate.

- The white layer remains at most locations suggesting that the rate of material loss from the surface is low relative to other failure modes.
- Nitride segments have been observed to either collide with each other or move away from each other indicating the direction of plastic deformation of the tool.
- The nitride segments which have been observed to collide show different depths of nitride. This suggests that one of the colliding nitride segments is forced into the path of the deforming workpiece and suffers abrasive wear.

It can be seen that the radius has plastically deformed due to the applied loading and high temperature of the tool. The resultant protrusion of the tool imparts a defect that is unacceptable and fails the tooling.

3.2.2.1.2   The "crimping" defect

To analyse the part damage "crimping" as shown in Figure 3-24 a cross section is taken perpendicular to that shown in Figure 3-28 and Figure 3-29. Figure 3-30 shows a representative sample of the surface that imprints the surface defect "crimping" upon the formed workpieces.
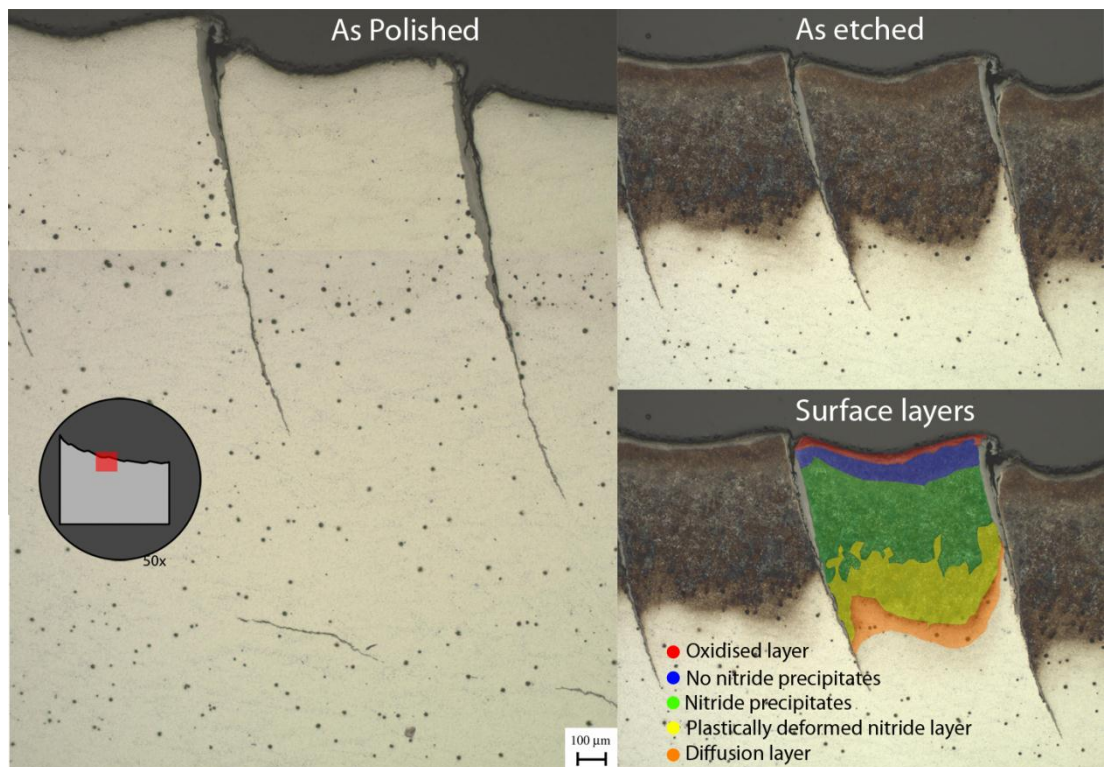
FIGURE 3-30: EXAMINATION OF THE "CRIMPING" DAMAGE

There are regular cracks into the nitride. The cracks penetrate the substrate and there are signs of plasticity in both the substrate and nitride. Multiple distinct layers are observable at the surface. The white layer has been removed and an oxide layer is observed in its place. The oxide is also observed within the cracks. The second layer identified is part of the nitride layer where no nitride precipitates are observed. The following layer contains nitride precipitates. The next layer shows severe plastic deformation of the nitride layer with a high density of pores. The content of the pores is unknown; the pores may be voids or may have contained soft, loose particles which have been removed during sample preparation. Such features have been observed in the extrusion samples but less frequently. The features have not been observed in AISI H13 in the as-heat treated condition. The final layer is the deformed nitride-substrate interface.

Figure 3-30 shows horizontal cracks. These cracks may be explained by the location of the cross section being examined. The nitride is fractured into segments connected by horizontal and vertical fractures. The sample has been taken at such an angle that both horizontal and vertical fractures have been captured.

The failure modes identified at the location relevant to "crimping" damage are listed below.

- Plastic deformation of the substrate and nitride layers.
- The substrate plastically deforming between cracks in the nitride layer.
- Different depths of nitride suggesting abrasive wear.
- The loss of the white layer.
- The corrosion of the surface layer.

The damage observed at the location of "crimping" on the upsetting tool shows similarity with the "scoring" damage observed upon the extrusion tooling. A high amount of plastic deformation is observed in the substrate with nitride present at the tool surface. The different depths of nitride at either side of the cracks suggest that the nitride segments have forced their neighbours to protrude into the path of the incoming deforming workpiece. The protruding material is removed through abrasive wear.

3.2.2.2 INVESTIGATION OF THE THERMO-MECHANICAL LOADING

To approximate the die stress and temperature of the upsetting tooling the operation has been simulated applying the assumptions outlined in section 3.1.3. The punch force peaks at approximately 70tonnes at the end of the operation. The simulated load for the punch in the upsetting operation is shown in Figure 3-31.
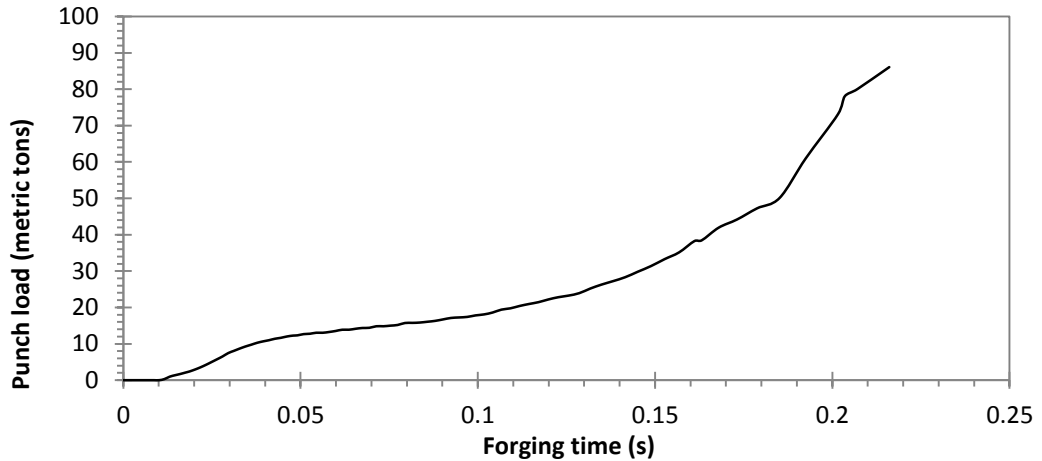
FIGURE 3-31: PUNCH LOAD

The simulation predicts higher forging loads than measured in the forging press however the trend is similar.

3.2.2.2.1   FE simulation of the conditions at the location of "smiley face"

The approximated thermo-mechanical loading of the tooling has been assessed at a cross section that examines the "smiley face" protrusion as illustrated in Figure 3-32. The points have been offset from the surface to account for the nitride layer.
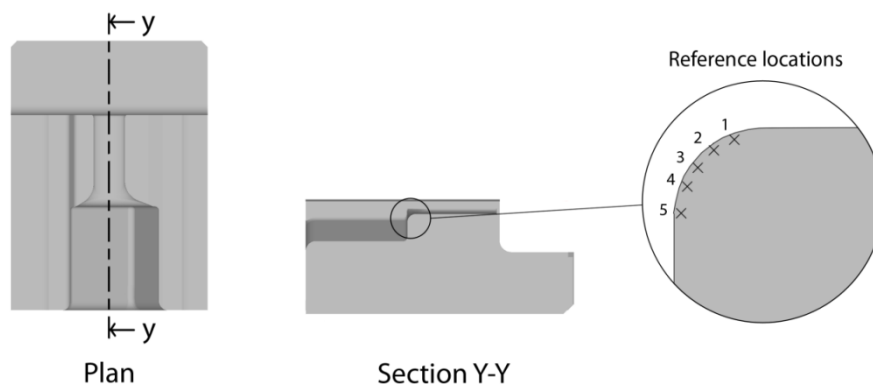
FIGURE 3-32: POINT LOCATIONS

Figure 3-33a) shows the approximated die temperature at the end of the deformation of the workpiece. Figure 3-33b) highlights the temperature changes at the locations shown in Figure 3-32. The highest tool temperature is predicted at the radius which collapses.

A) THE APPROXIMATED TEMPERATURE AT THE END OF FORGING
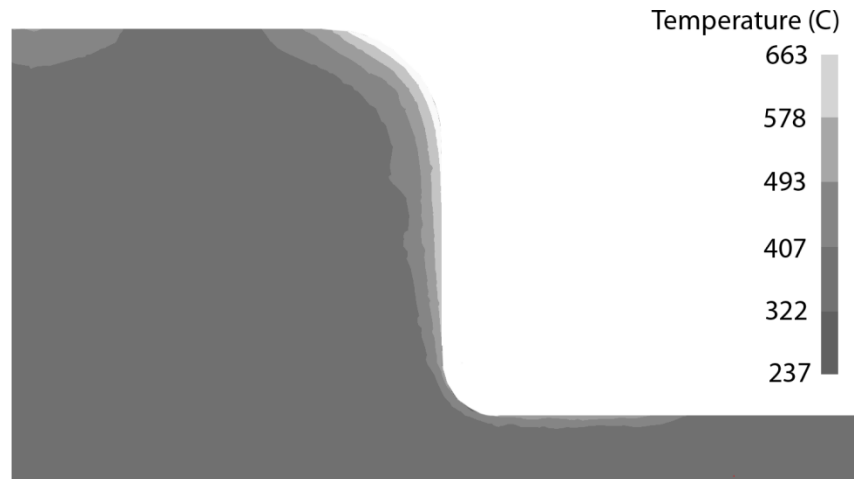
B) THE APPROXIMATED TEMPERATURE AT LOCATIONS OF INTEREST
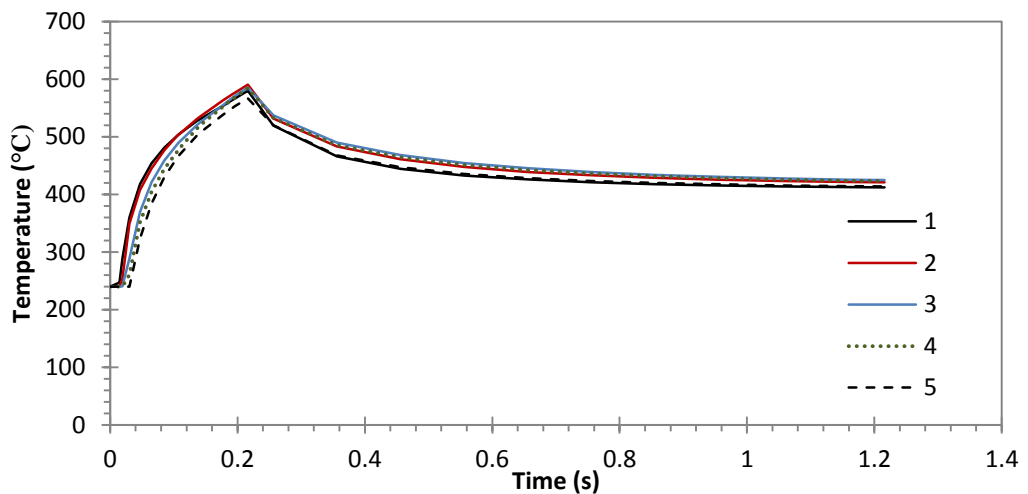
FIGURE 3-33: MAXIMUM TEMPERATURE AT THE LOCATION OF THE SMILEY-FACE

The approximated von Mises stress has been compared against the 0.2% proof stress at locations along the collapsed radius in Figure 3-34b) to f). The temperature dependence of the 0.2% proof stress of AISI H13 is shown in equation 2-1. The simulation suggests that this radius plastically deforms at all

the locations highlighted in Figure 3-32. The simulation suggests greatest plastic deformation at the top of the collapsed radius. The 3D scan measured most material lost at this region as shown in Figure 3-25.

A) EFFECTIVE STRESS AT PEAK LOAD
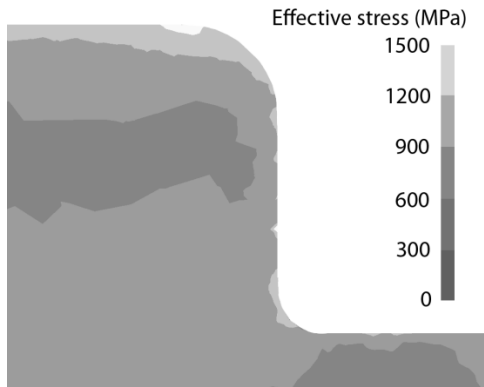
B) LOCATION 1
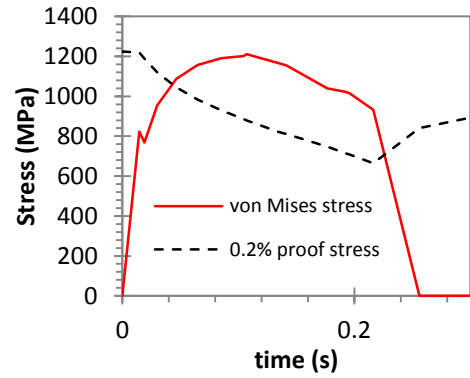
C) LOCATION 2
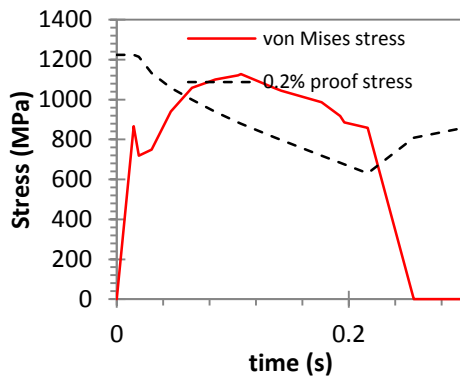
D) LOCATION 3
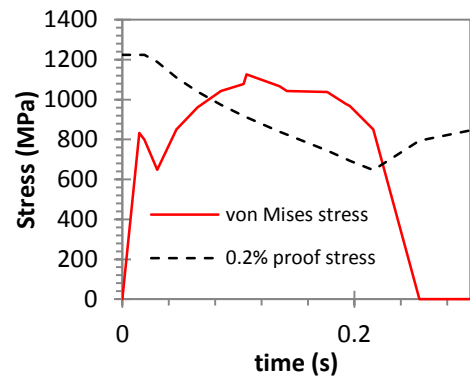
E) LOCATION 4
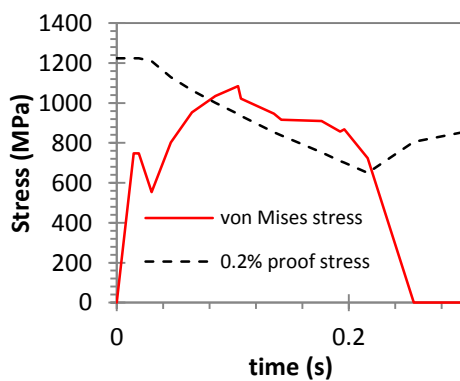
F) LOCATION 5
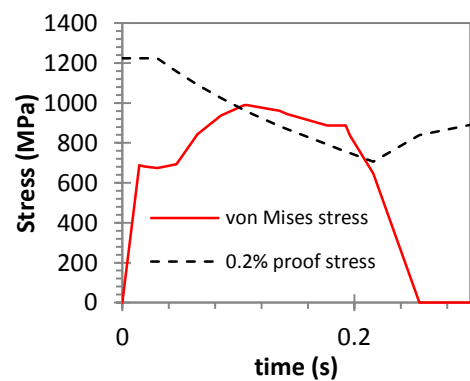
FIGURE 3-34: VON MISES STRESS AND YIELD STRENGTH AT THE RADIUS

3.2.2.2.2 FE simulation of the conditions at the location of "crimping"

Figure 3-27 shows the cross section used to evaluate the thermo-mechanical loading relevant to the "crimping" defect. The approximated temperature of the die at the end of forging is shown in Figure 3-35a). Figure 3-35b) shows the approximate temperature at locations of interest, which are highlighted in figure a).

A) THE APPROXIMATE TOOL TEMPERATURE AT THE END OF FORGING
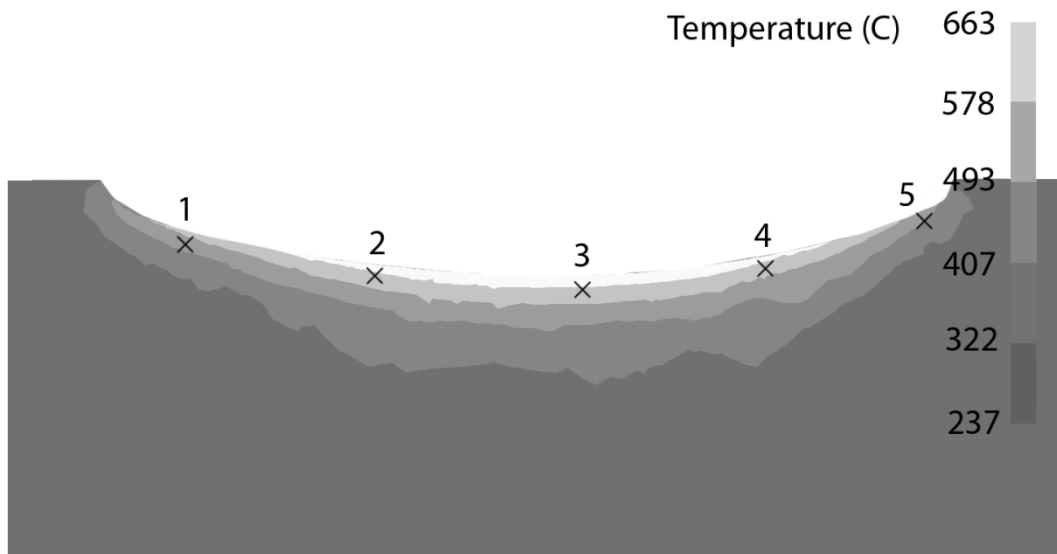
B) THE APPROXIMATE TEMPERATURE AT LOCATIONS OF INTEREST DURING FORGING
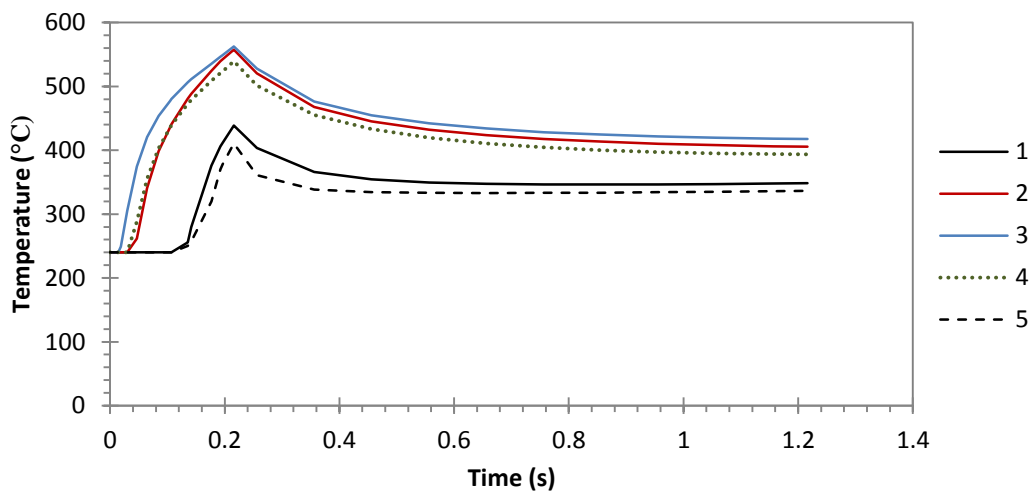
FIGURE 3-35: APPROXIMATED TEMPERATURE AT THE LOCATION OF "CRIMPING".

The simulation approximated a maximum temperature of 663°C at the tool surface and a maximum temperature of 562°C at the substrate.

Figure 3-36a) shows the approximated effective stress at the moment of peak loading. Figure 3-36b) to e) compares the approximated von Mises stress and 0.2% proof stress at select points shown in figure a). At locations 2, 3 and 4 the predicted von Mises stress is higher than the 0.2% proof stress of the material. This aligns with the region of crimping damage where significant plasticity is observed in the substrate. This region also grossly plastically deforms resulting in the "smiley face" defect. It can be seen that damage occurs on two scales; the collapse of the radius forming the smiley face and the localised preferential wear of the surface resulting in "crimping" damage.
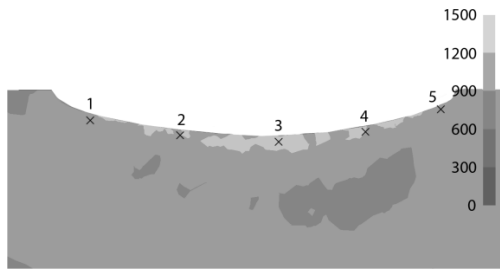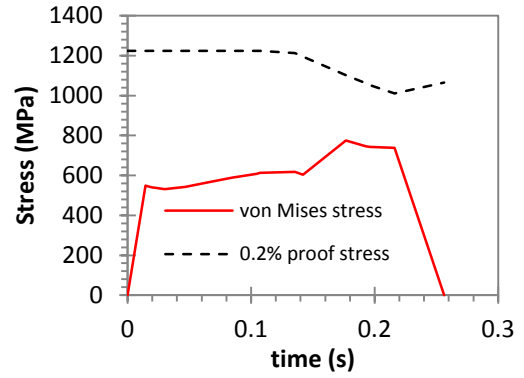
B) POINT 1

B) POINT 2
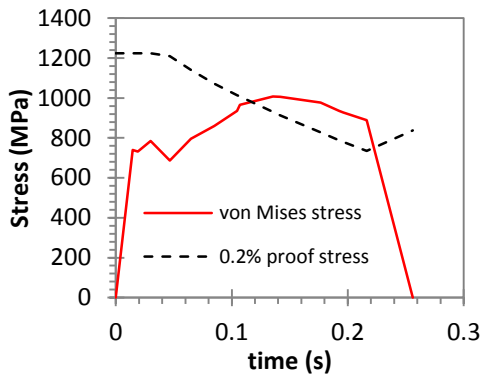
C) POINT 3
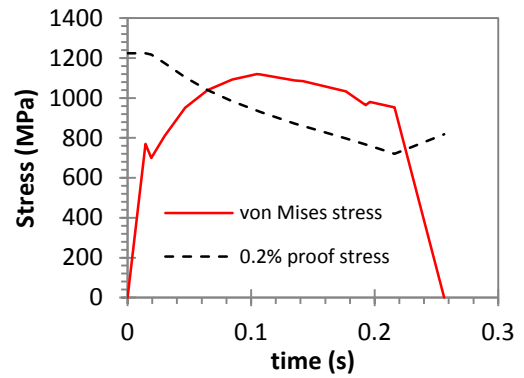
D) POINT 3
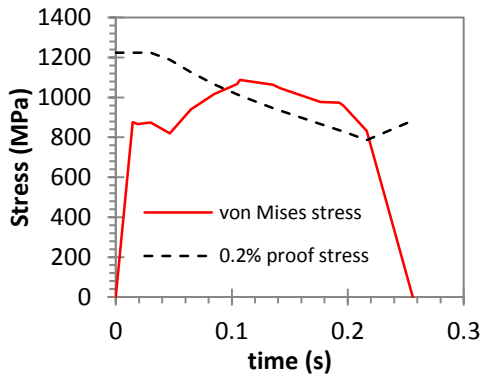
E) POINT 4
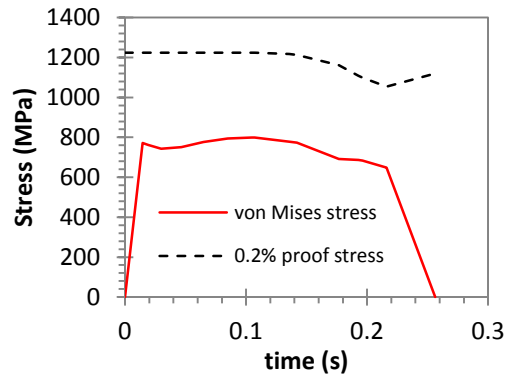
FIGURE 3-36: EFFECTIVE STRESS AND TEMPERATURE DEPENDENT YIELD STRENGTH AT LOCATION OF CRIMPING

3.2.3 THE THERMAL CYCLE

The temperature of the upsetting tooling has been measured during production using a thermal camera. This approach allows for the examination of the tool temperature over the tool's lifetime. A limitation is that the temperature of the

tooling during forming operations is not known. Thermocouples are required to measure tool temperature during deformation however was not pursed to avoid disruption to production. The temperature of the tool during deformation has been approximated from finite element analysis.

The thermal cycle of the tooling needs to be measured to determine whether the tool temperature increases due to repeated forging operations. The thermal cycle is of interest when analysing the role of thermal fatigue and over-tempering. The steady state thermal cycle of the tooling is of interest when determining the mechanical response of the tool.

Thermal images describing the events during an upsetting cycle is shown in Figure 3-37. Accurate measurement of the die surface is only possible once the workpiece is out of the field of view. It was necessary to remove measurements that exceeded 500°C to remove interference from the workpiece.

The press blocks the view of the upsetting die during deformation of the workpiece. To remove the temperature readings of the press the results of average temperature below 150°C were removed. This value was chosen as it distinguished the low temperature of the press from the low temperature of the tool during the application of lubrication.

The tool temperature representative of service conditions is shown in Figure 3-38. The time scale has been normalised to describe a representative time period of production. The peaks in the tool surface temperature correspond to the forging cycles where heat is transferred from the workpiece. Heat is also generated by the friction of the mating bodies and from adiabatic heating of the workpiece.

A) DIES AT REST

B) DIES BEING LUBRICATED

C) WORKPIECE INSERTION

D) FORGING

E) WORKPIECE REMOVAL

F) CYCLE COMPLETE
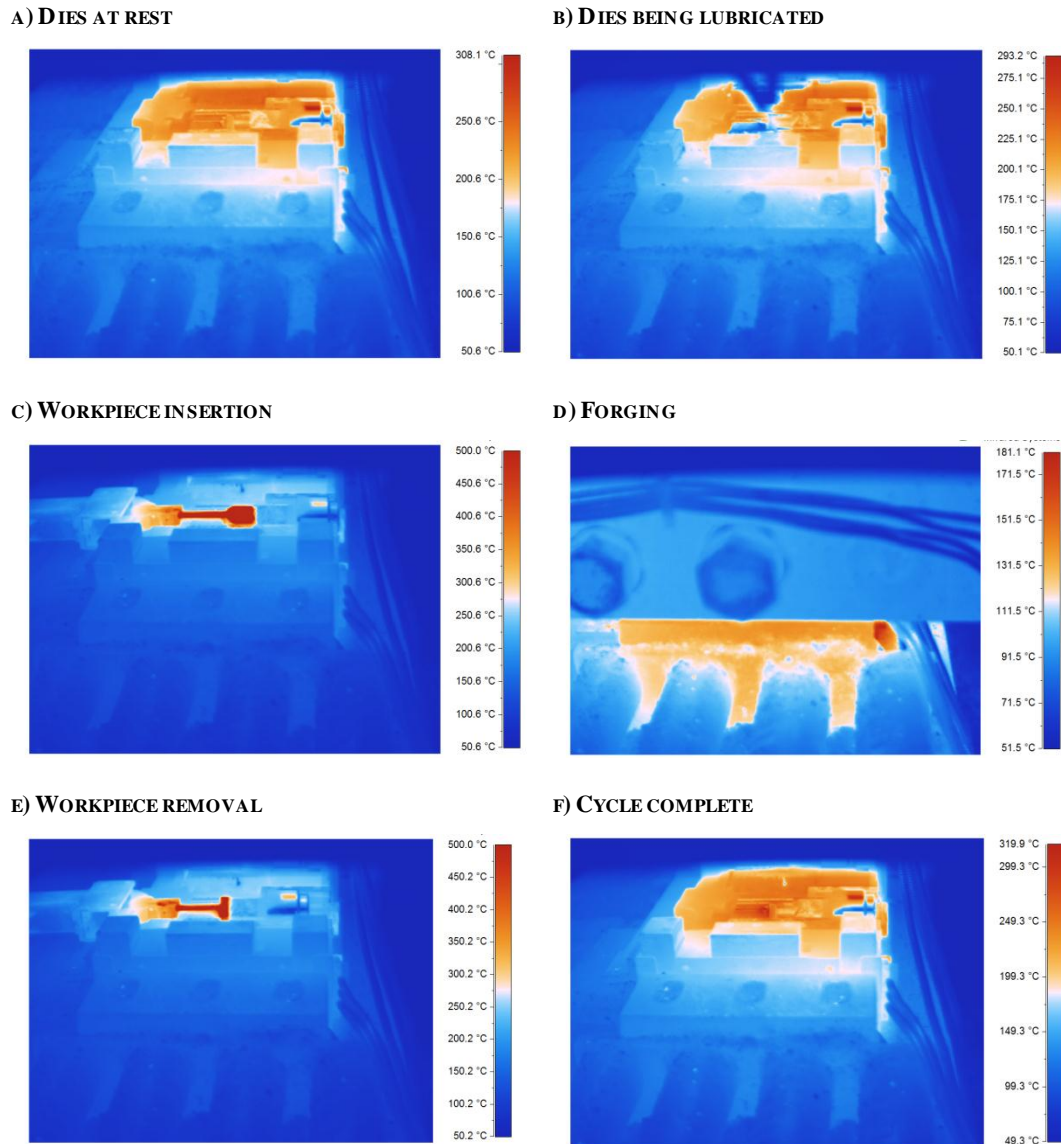
FIGURE 3-37: THERMAL IMAGES OF A UPSETTING CYCLE

By the time the workpiece is removed from the field of view of the camera, the tool temperature measured by the thermal camera is 350°C. Simulation has predicted tool surface temperatures of as high as 700°C during deformation of the workpiece however the heat quickly dissipates throughout the tooling and heat is lost from the surface from convection and radiation.

The valleys correspond to the heat lost from spaying lubrication onto the tool surface. The lubricant is suspended in water which evaporates on contact with the hot tool surface resulting in the observed temperature reduction. On average the surface temperature drops from 250-280°C to 150-200°C. No trends are

noticeable in the amount of heat lost from application of lubricant over the lifetime of this tooling.
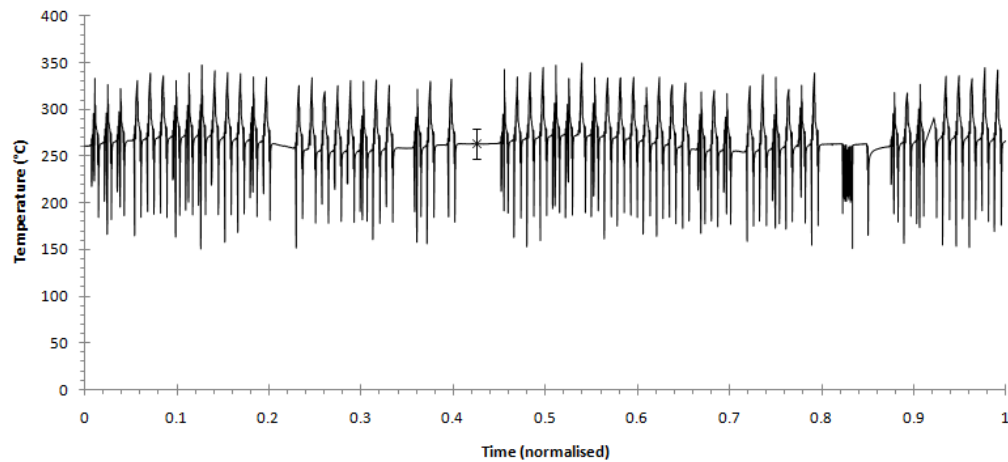
FIGURE 3-38: UPSETTING DIE TEMPERATURE

The temperature of the tool after the forming cycle varies between a minimum of 250°C and a maximum of 280°C. The drift is observed as a sinusoidal waveform which may be explained by the control system used to heat the dies. The thermocouple that controls the heating elements takes time to correct low tool temperature.

From Figure 3-38 it can be seen that the tool temperature does not increase as a result of repeated forging operations.

The thermal cycle of the tooling may be examined through the combination of measured and approximated data from finite element analysis. Finite element analysis was performed to determine the tool temperature when the camera does not have line of sight of the tool surface. Figure 3-39 reports the combination of approximated tool surface temperature, measured tool surface temperature data and interpolated tool surface temperature. The tooling is not visible during the extrusion operation which is performed prior to the operation of interest on the same press. The tool temperature has been interpolated during this period.
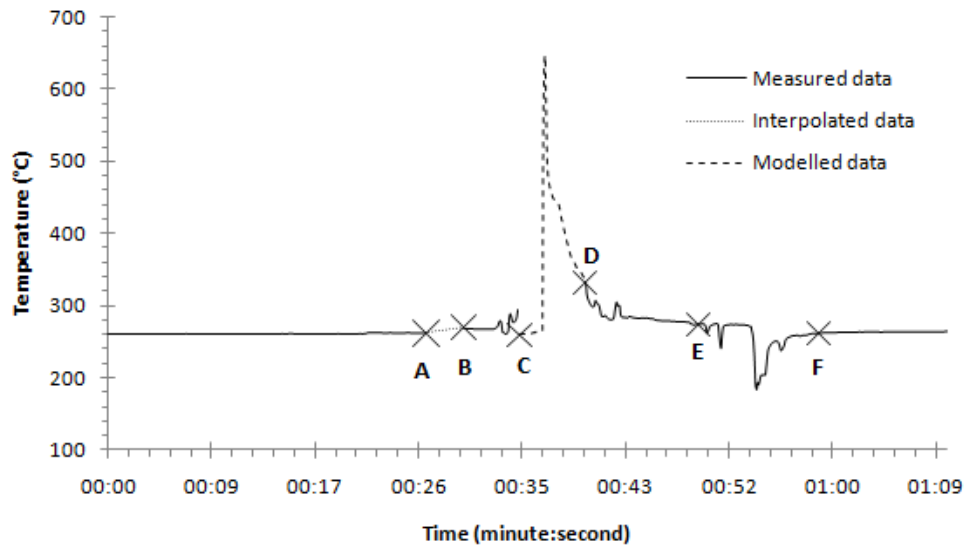
FIGURE 3-39: TOOL TEMPERATURE DURING A FORGING CYCLE

The modelled and measured data show agreement. The key events shown in Figure 3-39 are highlighted using letters. These key events are explained in Table 3-3.

TABLE 3-3: THE FORGING CYCLE

Step	Description
A-B	The extrusion operation temporarily blocks the thermal camera's view of the upsetting tool. A linear interpolation has been used to describe the change in tool surface temperature during this time.
B-C	The press is inactive during the movement of the workpiece from the first operation to the operation being recorded.
C-D	The workpiece is placed upon the upsetting tool and the thermal camera's view of the upsetting tool is blocked. Finite element analysis has been used to predict the tool surface temperature during contact with the workpiece.
D-E	Press inactivity after the forging operation.
E-F	Application of water based graphite to the tool surface.
F-A	Press inactivity until the next forging cycle.

The thermal imaging showed that the tool temperature did not increase as a response of repeated forming operations. It was assumed that the temperature of the tooling between forgings could be approximated from FEA. A database was created that consisted of the entire thermal camera measurements and FEA

102

approximations of the tool temperature during the production run. Figure 3-40 shows a dot plot representative of the approximated and measured tool temperature during service.

From the data used to produce Figure 3-40 it was calculated that the tool surface experiences a temperature above 500°C for a total of 42 seconds during the production of 100 parts. The tool temperature on average is around 250-280°C.

It has been found that the heat generated during forging and transferred from the workpiece quickly dissipates throughout the tool after forging. The temperature of the tooling does not rise as a result of repeated forgings. These findings may also be applicable to the extrusion tooling which operates under similar working conditions. It was not possible to position the thermal camera in a suitable position to measure the temperature of the extrusion tooling.
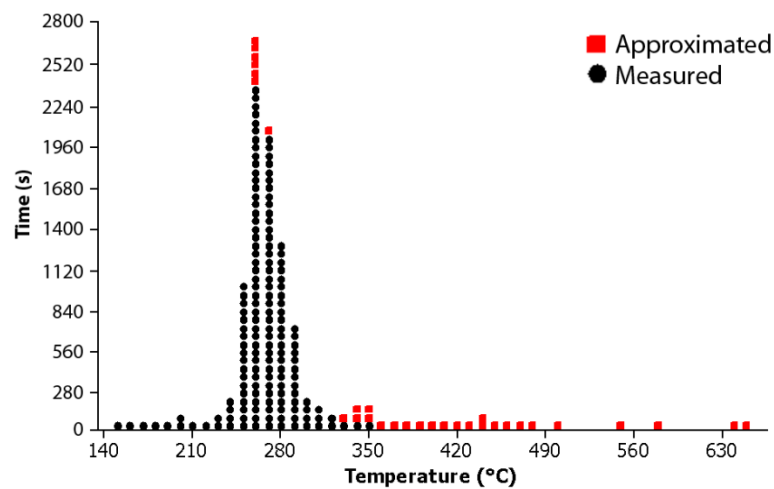
Each symbol represents up to 670 observations made at a frequency of 12Hz.

FIGURE 3-40: A DOT PLOT SHOWING THE TOOL SURFACE TEMPERATURE DISTRIBUTION DURING SERVICE

Thermal softening\ over-tempering is known to reduce the mechanical response of hot work tool steel resulting in increased rates of plastic deformation and wear. The impact of thermal softening has been evaluated through hardness measurements.

The hardness measurements from the failed tooling are shown in Figure 3-13 and Figure 3-28 for the extrusion and upsetting tooling respectively. The

measurements have shown a reduction in core hardness of the tooling and localised reductions in hardness near the damaged regions of the tool surface. The thermal softening behaviour has been examined to investigate the cause of the drop in hardness in the failed tooling.

The thermal softening behaviour of the tool steel was examined through microhardness measurement of over-tempered specimens. Five microhardness measurements were taken of each sample using a Zwick/Roell Indentec hardness measurement machine with an automated stage and automated measurement.
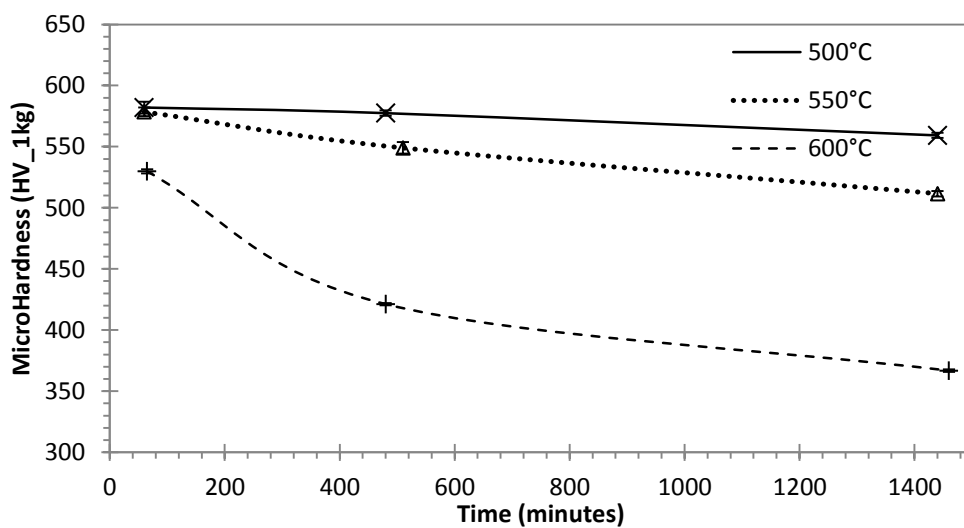
FIGURE 3-41: THERMAL SOFTENING BEHAVIOUR OF AISI H13

Linear softening is observed when exposed to temperatures of 500°C and 550°C however the specimen quickly reaches the annealed hardness of ~360Hv under this time scales when exposed to a temperature of 600°C. The annealed hardness is higher than the softest micro-hardness measurement taken from the worn tooling indicating that surface cracks and damage have influenced the hardness measurements taken from the sample at regions close to the surface damage.

Figure 3-41 shows that the rate of thermal softening is negligible until temperatures exceed 500°C. FEA has approximated that the tool temperature exceeds this temperature for a small depth of less than 1mm for short time scales.

The examination of the thermal cycle has found that the tool temperature is operating at temperatures applicable to over-tempering for small time scales. This finding reduces the likelihood that the reduction in hardness measured near the regions of damage can be explained entirely by thermal softening. Plastic deformation of the substrate and cracking has been observed at these locations. Tempered martensitic tool steel is known to soften under fatigue loading (Bernhart, Moulinier et al. 1999).

3.3 DISCUSSION

The following explanations have been developed from the investigation into the worn tooling and tool conditions.

3.3.1 THE "SCORING" DEFECT

The active damage modes identified include the fracture of the nitride surface, the removal of the nitride layer and the plastic deformation of the substrate. Finite element analysis has approximated die stresses higher than the yield strength of the material.

Two processes have been observed that may explain the formation of the scoring marks. The first is the preferential wear of the substrate that is exposed to the deforming workpiece. The second is the plastic deformation of the substrate.

3.3.1.1 PREFERENTIAL WEAR OF THE SUBSTRATE

In Figure 3-9 and Figure 3-16the tempered martensitic substrate is extruded between cracks and gaps in the nitride layer. This allows for direct contact between the exposed substrate and the harder workpiece, resulting in preferential wear at these locations. The substrate lost at the surface is replaced by the substrate deforming under the nitride layer as illustrated in Figure 3-42
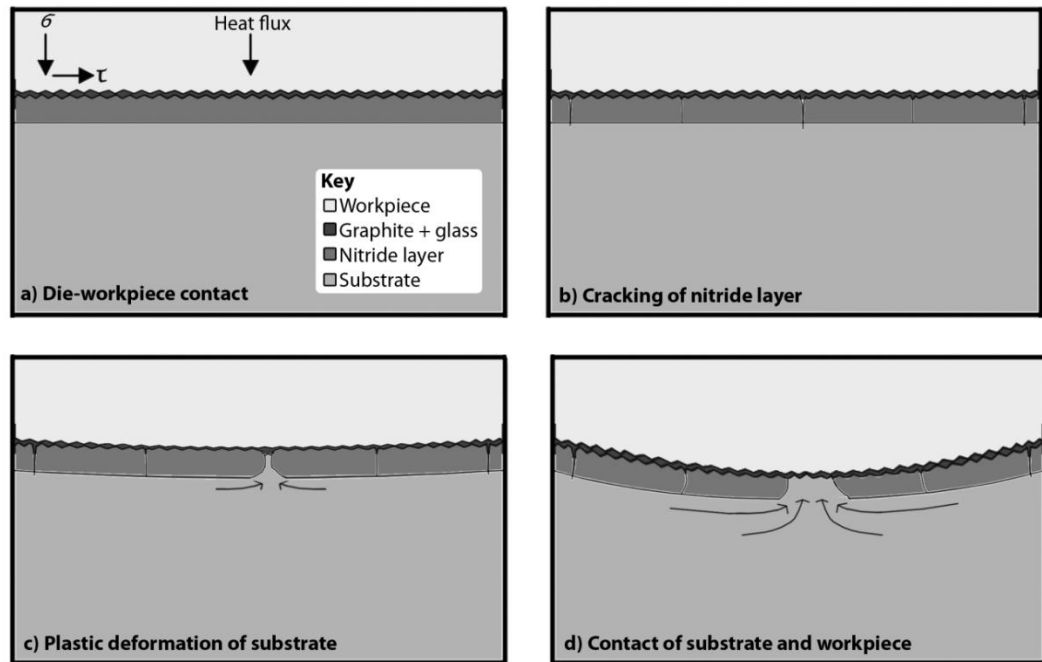
FIGURE 3-42: SCORING MARKS FORMED THROUGH THE PREFERENTIAL ABRASIVE WEAR OF THE SUBSTRATE.

Figure 3-42a) shows a cross section of the workpiece and the tool surface during the forming operation. The lubricant and nitride layer are highlighted in different shades of grey. The deformation of the workpiece exerts a normal stress, shear stress and a heat flux into the tool. In Figure 3-42b) the nitride layer fractures due to a combination of thermal fatigue, mechanical fatigue, and elastic deflection of the tool. In Figure 3-42 c) the substrate is extruded into a crack in the nitride. The substrate comes into direct contact with the workpiece. The relatively soft substrate is removed through abrasive contact with the workpiece. The material removed through preferential abrasive contact may result in the formation of the scoring marks which fail the component, as illustrated in Figure 3-42d).

3.3.1.2 PLASTIC DEFORMATION OF THE SUBSTRATE

The deformation of the substrate may be the cause of the scoring marks that fail the tool. In Figure 3-11 the depth of the nitride layer varies between the nitride segments. The substrate is seen to plastically deform beneath the nitride segments, forcing nitride segments into the path of the workpiece. The formation of half a waveform of the scoring marks is illustrated in Figure 3-43.

106
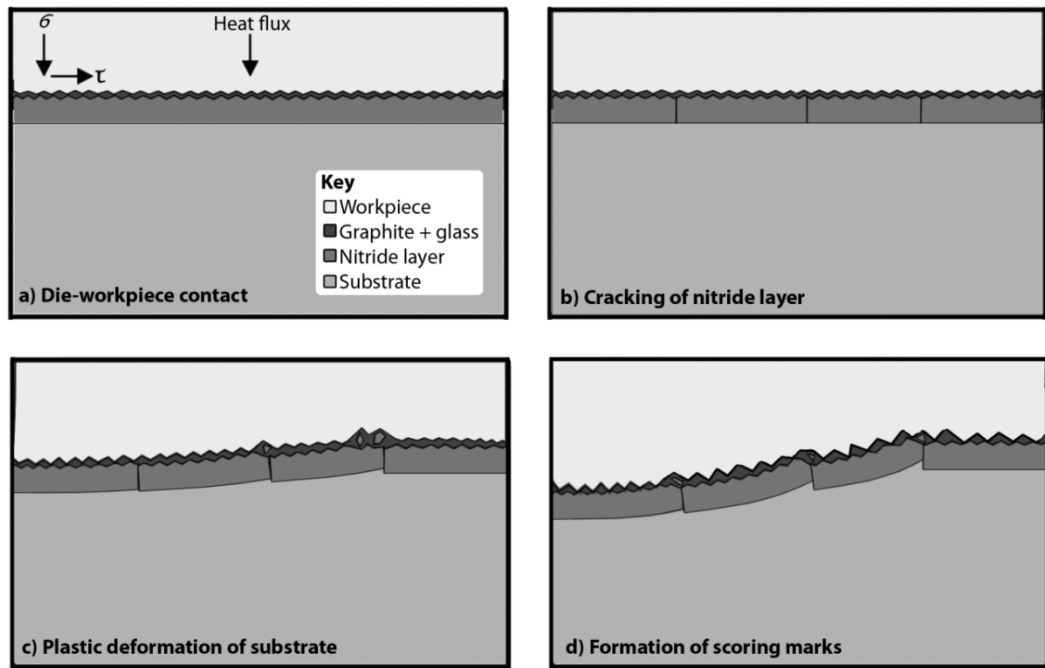
FIGURE 3-43: SCORING MARKS FORMED THROUGH THE PLASTIC DEFORMATION OF THE SUBSTRATE.

Figure 3-43 shows a cross section of the workpiece and die interface, including the nitride layer and lubricants as shown in the legend in figure a). In Figure b) the nitride layer has cracked into segments due to a combination of thermal fatigue, mechanical fatigue and to accommodate the plastic deformation of the substrate. In figure c) the substrate deforms plastically causing the start of the scoring mark and the collision of nitride segments. The protruding nitride is removed by the deforming workpiece and becomes abrasive debris. This process continues until the scoring mark becomes unacceptable as shown in figure d).

3.3.1.3   THE DOMINANT WEAR PROCESS

Both of the observed mechanisms may contribute to the formation of the scoring marks, which fail the tooling. The difference between the observed mechanisms is that the preferential wear of the tool surface illustrates how the scoring marks could be formed through localised material loss. The plastic deformation of the substrate mechanism illustrates how a nitrided surface may plastically deform to create the scoring marks.

To determine the most probable cause of the scoring marks, the extent of plastic deformation and material removal may be assessed. The 3D scan of the worn tooling shows material gain, which without the possibility of adhesive wear, may be explained by plastic deformation.

Figure 3-8 shows the measured difference in geometry along this cross section from the 3D scan. A total area of $0.079mm^2$ of material has been lost from the cross section shown in Figure 3-7. This compares with an area of $0.030mm^2$ that has been gained.

Figure 3-10 shows the measured nitride depth measured at increments along the cross section of interest. An area of $0.99mm^2$ of nitride has been lost in the worn die. A greater amount of nitride has been removed than material lost at the cross section examined. This indicates that the change in shape caused by removal of the nitride layer is offset by the plastic deformation of the tool. This finding suggests that the plastic deformation of the substrate is the dominant cause for the scoring marks.

3.3.2 THE "FLASHING" DEFECT

The observed damage mechanisms at the location of the parting line include the loss of the nitride layer, the delamination of the white layer and the plastic deformation of both the substrate and the nitride layer. The finite element model has approximated higher stresses than the yield strength of H13 tool steel considering the temperature of the tool.

Any misalignment between the top and bottom dies cause part of the nitride layer to protrude. The sharp corner of the parting line acts as a stress raiser. It is likely that the nitride at the parting line experiences brittle fracture. This results in the direct contact between the workpiece and the relatively soft substrate. The reduced hardness of the substrate results in an increased rate of abrasive wear at this location. Due to the loading conditions on the die, the substrate flows plastically between gaps in the nitride. Continued production causes further abrasion at the parting line with the increase in flashing damage. Once the flashing on the workpiece has reached a critical value the parts can no longer be accepted and the die is failed.

Solutions to mitigate this problem include locally reducing the nitride depth at the parting line and ensuring alignment of the top and bottom dies. The rate at which the flashing damage progresses may be reduced by reducing the die stress through redesigning the geometry of the tool.

3.3.3   THE "SMILEY FACE" DEFECT

The cause of the "smiley face" defect is explained by the plastic deformation of the tool. The 3D scan shows how the collapse of the tool has resulted in the protrusion of material that imprints the "smiley face" defect upon the formed workpieces.

Finite element analysis has predicted high stresses that are above the 0.2% proof stress of the material. The yield strength of the tool reduces with prolonged exposure to temperature. The material is known to cyclical soften under fatigue loading (Bernhart, Moulinier et al. 1999).

The life of the tooling may be approximated by determining the number of cycles until the substrate deforms to form the protrusion that causes the "smiley face" defect.

This failure mode may be addressed through redesign of the tooling to reduce die stress. Redesign of the tool would affect the amount of work required from the proceeding forming operation. Another approach is the use of a die material of higher strength. Die life may be improved through increasing the nitride depth however the substrate over-tempers during nitriding.

3.3.4   THE "CRIMPING" DEFECT

There is similarity in the "crimping" defect and "scoring" defect observed in the extrusion tooling. The nitride layer has been observed to fracture into segments as a response to the thermo-mechanical loading. The nitride segments have been forced against each other, resulting in one segment to protrude into the path of the deforming workpiece. The formation of the "crimping" marks may be cause by degradation in surface condition resulting from the plastic deformation of the substrate.

109

Reducing the die stress is one approach to improving die life. The substrate is not capable of supporting the nitride layer. Increasing the strength of the substrate is another approach to mitigating "crimping" damage.

3.4 THE DOMINANT FAILURE MODE

The active failure modes identified in the extrusion and upsetting case studies are listed below:

- plastic deformation of the substrate,
- the plastic deformation of the nitride layer,
- the fracture of the nitride layer with cracks extending into the substrate,
- abrasive wear,
- corrosion,
- fracture delamination of the compound layer.

The time scales for thermal softening to occur during service have been found to be too small to be significant in the extrusion and upsetting operations of interest. The tool steel softens as a result of repeated nitriding operations.

The plastic deformation of the substrate has been observed in the "scoring" damage in the extrusion tool, the "crimping" damage in the upsetting tool and the "smiley face" damage in the upsetting tool. It is likely that the brittle fracture of the nitride layer initiates the "flashing" damage.

The plastic deformation of the substrate of the die has been observed when analysing each forging defect. The inability of the substrate to support the nitride is related to the degradation of the tool surface, resulting in die failure. It has been concluded that the dominant failure mode is the plastic deformation of the substrate.

The life of the tooling may be predicted by modelling the deformation behaviour of the substrate under thermo-mechanical loading. To model the relevant deformation behaviour of the substrate, it is necessary to know the uniaxial flow behaviour of the tool under the temperatures, strain rates and loading conditions relevant to the extrusion and upsetting tooling. The following chapter characterises the mechanical properties and microstructure of the grade of tool steel of interest.

4   DIE MATERIAL CHARACTERISATION

This chapter reports the plastic flow behaviour and microstructural examination of AISI H13 hot work tool steel. To develop the life prediction model, it is necessary to know the plastic flow behaviour under relevant conditions.

The tensile testing followed BS EN ISO 6892-2:2011. Fatigue tests were performed to ASTM E606. The test procedures for tensile testing, fatigue testing and metallographic preparation are found in the section 11.1 of the appendix.

The process simulations conducted in chapter 3 were used to determine the representative temperatures, cyclical loading and strain rates applicable to the plastic deformation of the substrate. This work is documented within section 11.2 of the appendix.

The mechanical testing was funded by the industrial members of the Advanced Forming Research Centre (AFRC). The flow behaviour has been normalised against suitable values to allow for the comparison and examination of behaviour without publishing privately owned information. Information regarding the material flow behaviour is contained within the report "Material characterisation and modelling of AISI H13". Access to this report may be requested from the AFRC.

Uniaxial tensile tests have been performed to examine the work hardening and yield behaviour. Tensile tests of over-tempered specimen have been performed to measure the impact of thermal softening on flow stress. Tensile tests have been performed with step changes in temperature for the purpose of model validation.

Isothermal strain controlled fatigue tests have been performed to measure the cyclical softening behaviour of the tool steel. Fatigue tests have been performed to measure the impact of test temperature and strain amplitude. A fatigue test has been performed upon an over-tempered specimen for the purpose of model validation.

The microstructure of AISI H13 has been evaluated with the aim of measuring microstructural features that relate to material properties. The microstructural features have been assessed using scanning electron microscopy and electron back scatter diffraction. AISI H13 specimens have been examined that have

experienced different extents of plastic deformation or thermal exposure. The microstructural features examined include the particle phases and the martensitic lath structure.

4.1 TENSILE FLOW BEHAVIOUR

Tensile tests have been performed on H13 specimen at temperatures between 20°C and 600°C and at the strain rate range of either $0.1s^{-1}$ or $0.01s^{-1}$ for conditions where the material displays strain rate sensitivity. Interrupted tests have been performed to measure martensitic lath spacing as a response to plastic strain.

Tensile tests have been performed upon over-tempered specimen. For the purpose of model verification, tests have been performed to determine the impact of prior strain on flow behaviour.

Measurement error from the tensile testing was determined through examining the 0.1% proof stress for room temperature tensile testing at strain rate of 0.001/ s. From four tests, an absolute error of 11.8MPa from the average was measured.

4.1.1 TEMPERATURE SENSITIVITY

The temperature dependence of the flow behaviour from tensile testing is shown in Figure 4-1 for different strain rates. The flow behaviour shows significant softening with an increase in temperature. The temperature dependence is more easily observed when examining the 0.1% proof stress, shown in Figure 4-2 a). The temperature dependence of the ultimate tensile strength (UTS) is shown in Figure 4-2 b) which shows similar temperature dependence to the 0.1% proof stress.
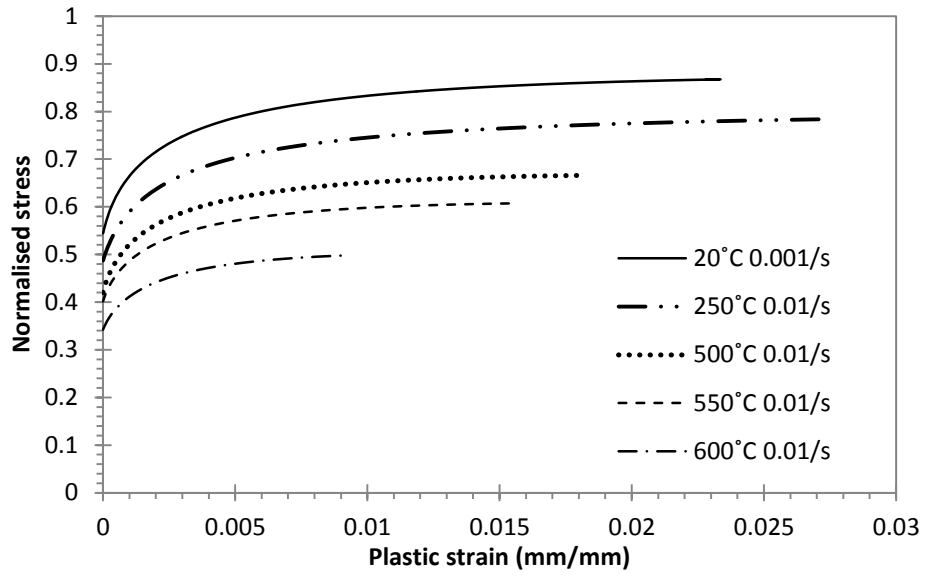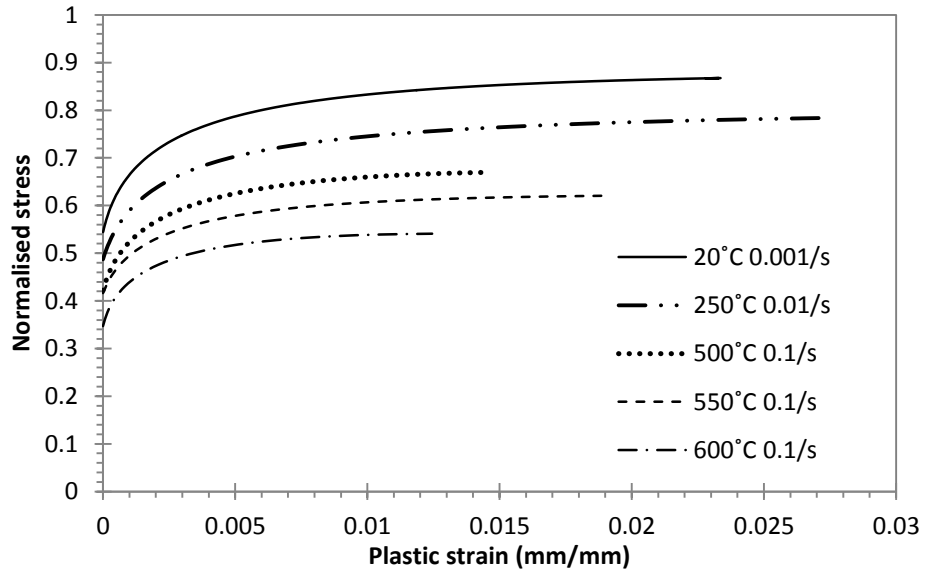
FIGURE 4-1: TEMPERATURE SENSITIVITY OF TENSILE FLOW
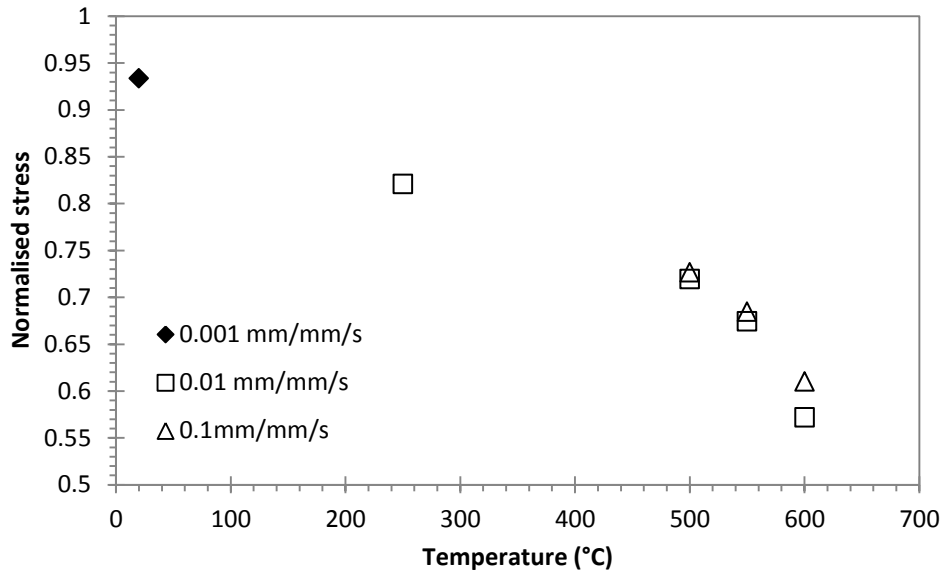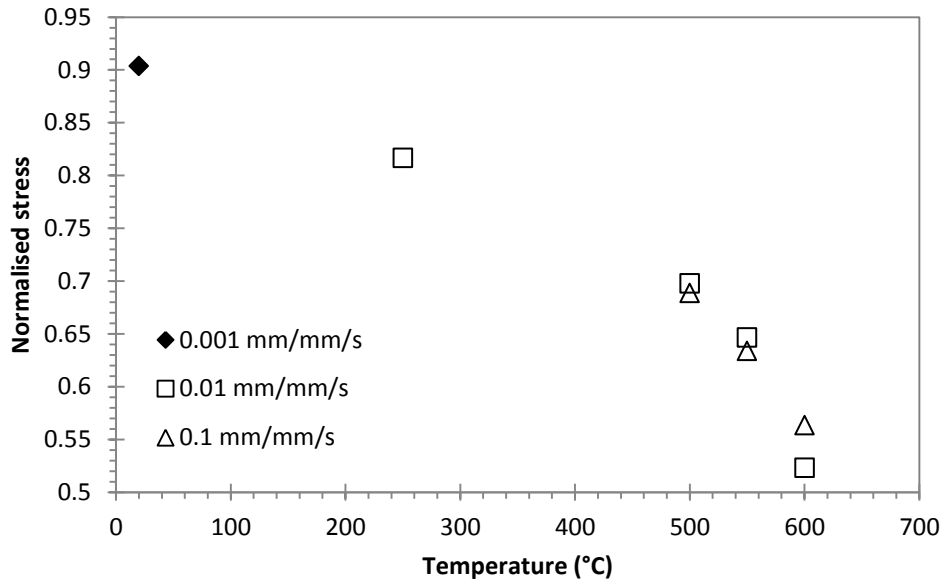
FIGURE 4-2: 0.1% PROOF STRESS AND UTS OF AS-HEAT TREATED H13

4.1.2 STRAIN RATE SENSITIVITY

Figure 4-3 compares the strain rate sensitivity of the material at different temperatures. The material displays no strain rate sensitivity at 500°C, a small amount at 550°C and a significant amount at 600°C. From Figure 4-3 it can be concluded that strain rate sensitivity is insignificant at temperatures below 500°C.

114

A) **TENSILE FLOW BEHAVIOUR AT 500°C**
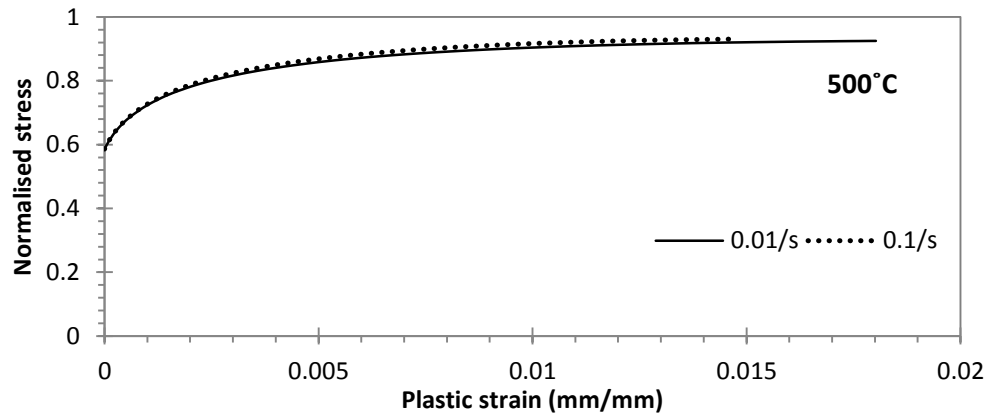
B) **TENSILE FLOW BEHAVIOUR AT 550°C**
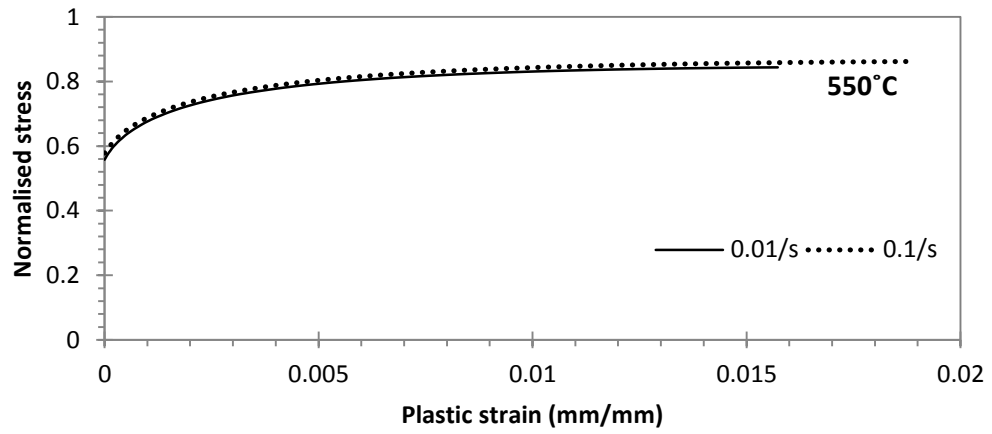
C) **TENSILE FLOW BEHAVIOUR AT 600°C**
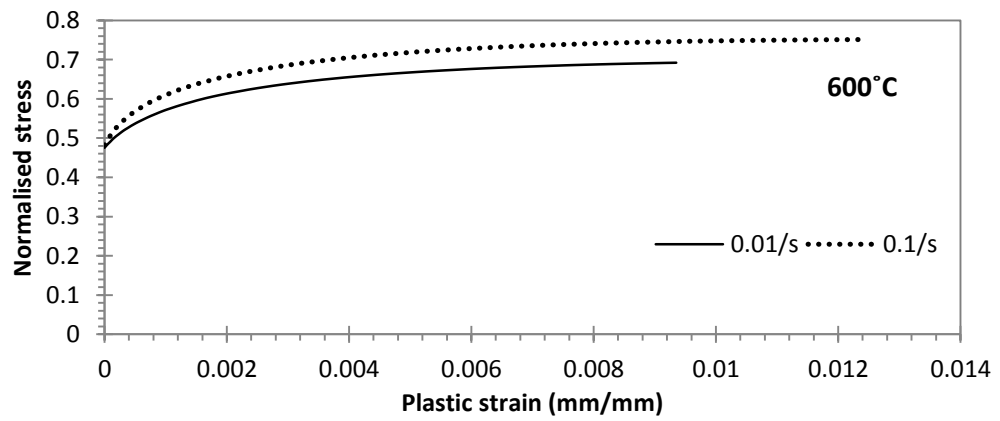
FIGURE 4-3: STRAIN RATE SENSITIVITY

4.1.3 OVER-TEMPERING

Tensile specimens have been over-tempered. The tensile tests have been performed at 500°C at a strain rate of 0.01s^{-1}. A calibrated K type thermo-couple was used to measure the specimen temperature during over-tempering. Each sample was pre-heated to 500°C and given half an hour to reach a uniform temperature before increasing the temperature.

Table 4-1 shows the heat treatment and normalised 0.1% proof stress and UTS for these tests. The proof stress and UTS have been normalised against the as-heat treated behaviour. The fraction of UTS divided by 0.1% proof stress reduces with over-tempering, indicating that work hardening behaviour is affected by over-tempering. The flow behaviour is shown in Table 4-1.

TABLE 4-1: DESCRIPTIVE DATA OF THE TENSILE FLOW BEHAVIOUR OF OVER-TEMPERED SPECIMEN

Specimen	Temperature (°C)	Time (hrs)	0.1% Proof stress (Normalised)	UTS (Normalised)	UTS / 0.1% proof stress
1	550	7	0.94	0.91	1.24
2	600	2	0.86	0.81	1.21
3	600	4	0.72	0.67	1.19
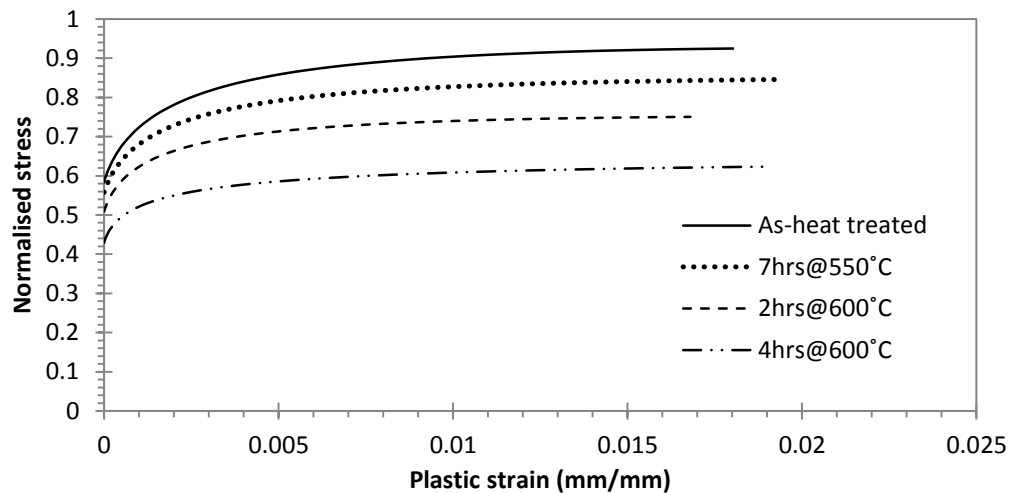
FIGURE 4-4: FLOW BEHAVIOUR OF OVER-TEMPERED SPECIMEN AT 500°C AND A STRAIN RATE OF 0.01/S

116

It is possible to approximate yield stress from hardness measurements. The over-tempering behaviour shown in Figure 3-14 and Figure 3-41 may be expressed in terms of yield stress. Yan et al (2007) measured the relationship between hardness and yield strength within AISI H13. The measurements have been converted from Rockwell scale C to Vickers hardness measurements, for application to the hardness measurements taken within this work. The approximated yield strength from hardness obtained from Yan et al (2007) is shown in Figure 4-5.

Pavlina and Van Tyne (2008) measured an error of 102MPa when converting hardness measurements to yield stress in steels. This error is included when approximating yield strength from hardness measurements. Equation 4-1 has been fit to the data shown from Figure 4-5

$$y_s = +2.7492 H_v - 17.006 \qquad\qquad \textbf{4-1}$$

Where;

y_s Yield strength (MPa)

H_v Hardness (Hv)
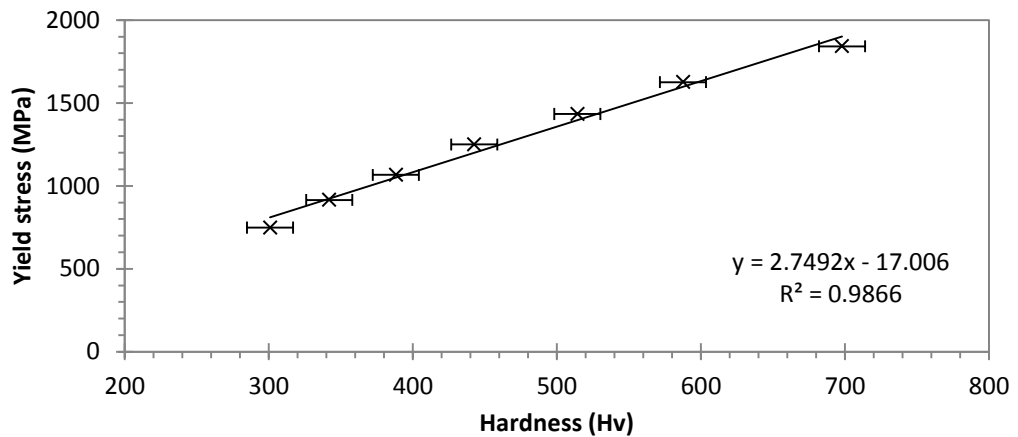
FIGURE 4-5: YIELD STRENGTH OF AISI H13 FOR DIFFERENT HARDNESS

The over-tempering behaviour shown in Figure 3-41 has been expressed in terms of yield strength opposed to micro-hardness utilising equation set 4-1. This is shown in Figure 4-6.
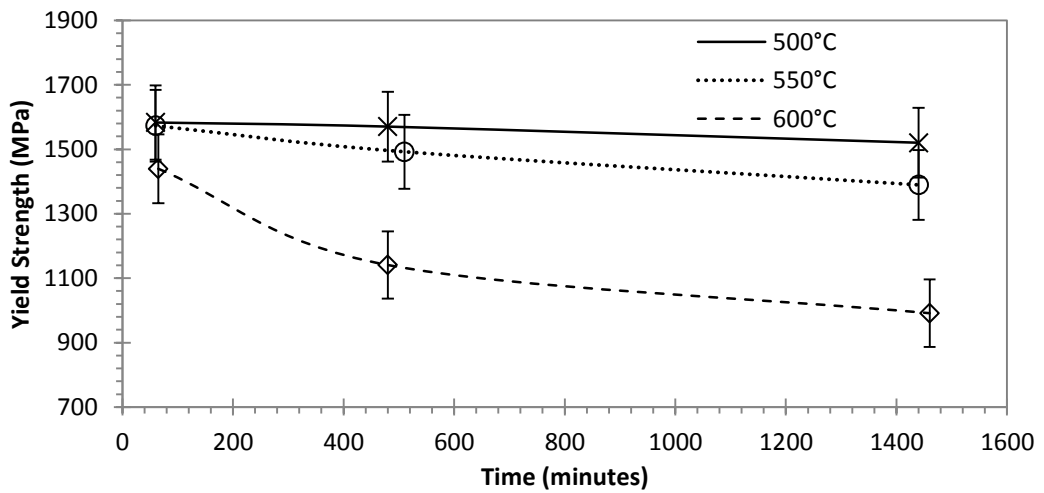
FIGURE 4-6: APPROXIMATED REDUCTION IN YIELD STRENGTH FROM OVER-TEMPERING

The reduction in yield strength of AISI H13 as a result of over-tempering during repeated nitriding operations, may be approximated by applying equation 4-1 to the micro-hardness measured from over-tempered specimen. This is shown in Figure 4-7.
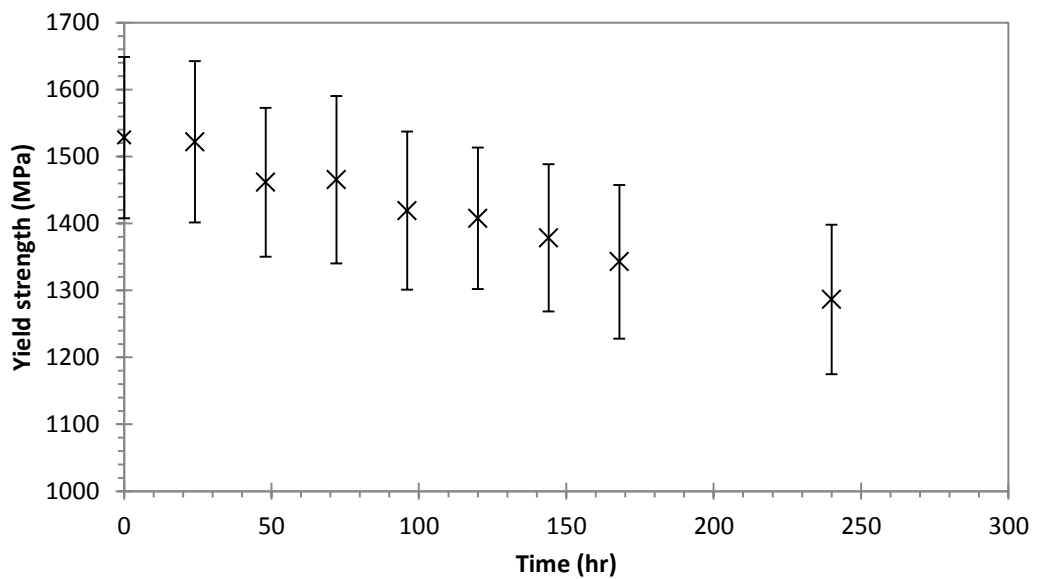
FIGURE 4-7: APPROXIMATED REDUCTION IN YIELD STRENGTH FROM OVER-TEMPERING AT 525°C

The error bars in Figure 4-6 and Figure 4-7 include the error arising from the hardness measurement and from the hardness to yield stress conversion.

4.1.4 STEP CHANGES IN TEST CONDITIONS

To further understand the work hardening behaviour of the alloy, tensile tests have been pre-strained to approximately 1% plastic strain at room temperature with the test continued at either 500°, 550°C or 600°C. At low temperature, the material displays insignificant strain rate sensitivity. The room temperature tests have been performed at a strain rate of 1E-3/s. The strain rate at high temperature was 1E-2/s.

Figure 4-8 shows the measured flow behaviour from these tests. The continued deformation behaviour is compared to behaviour without pre-strain in Figure 4-9. It can be seen that the yield strength of the material after pre-straining has increased in comparison to the flow behaviour without pre-strain. The impact of the room temperature pre-strain upon 0.1% proof stress and UTS in continued deformation is compared in Table 4-2.

TABLE 4-2: DIFFERENCE IN 0.1% PROOF STRESS AND ULTIMATE TENSILE STRENGTH

Room temperature pre-strain (mm/mm)	Post pre-strain test temperature (°C)	0.1% proof stress % difference	UTS % difference
0.0082	500	+26.8%	-2.14%
0.0097	550	+23.1%	-2.30%
0.0070	600	+18.7%	-0.03%

Table 4-2 shows that the increase in yield strength from room temperature pre-strain is temperature dependent. The ultimate tensile strength is not significantly affected by the pre-strain.
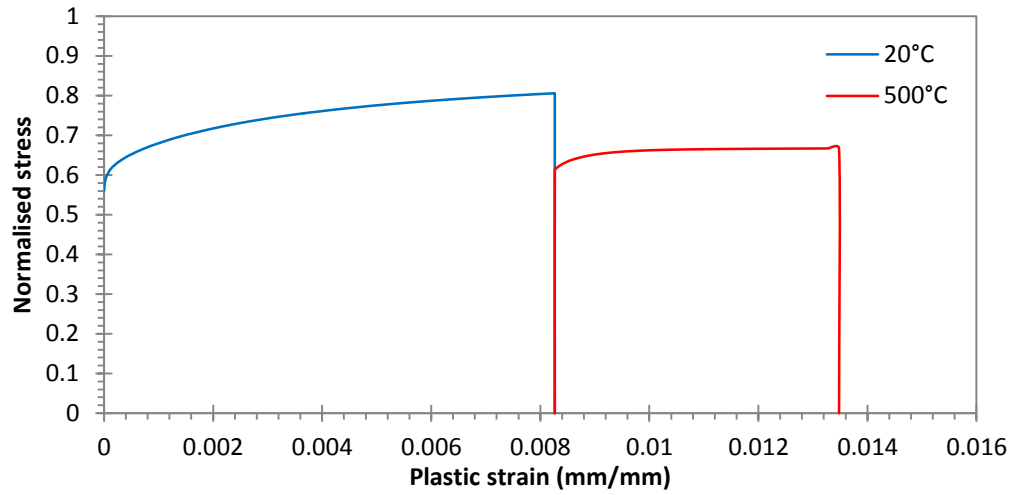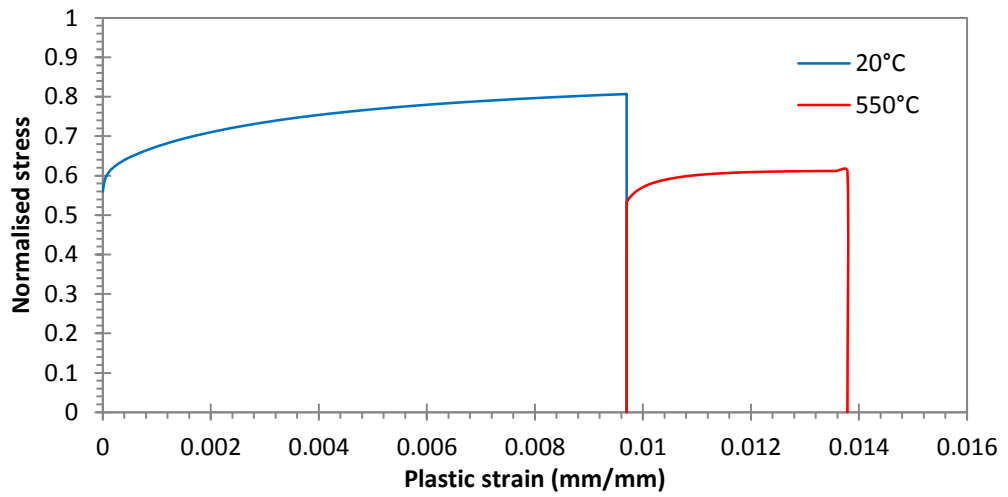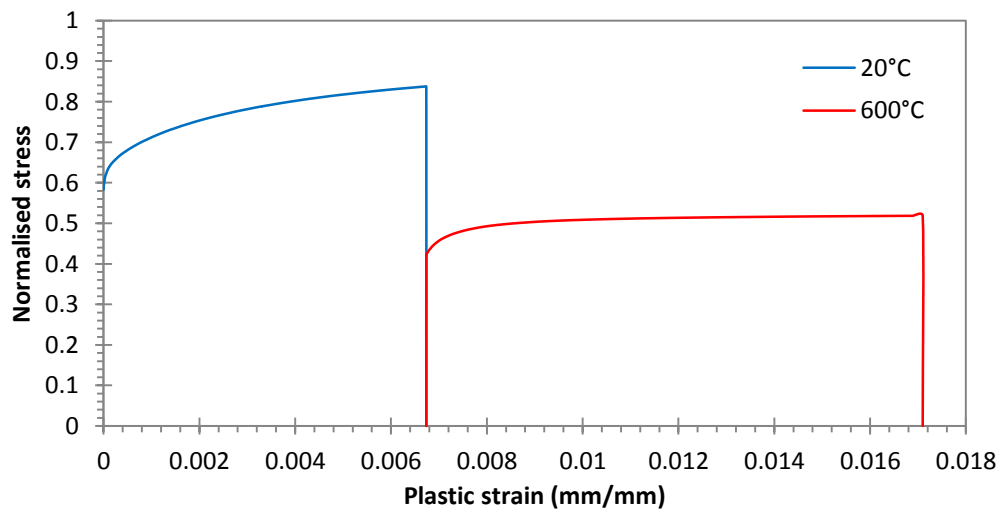
FIGURE 4-8: THE IMPACT OF PRE-STRAIN ON ELEVATED TEMPERATURE FLOW BEHAVIOUR
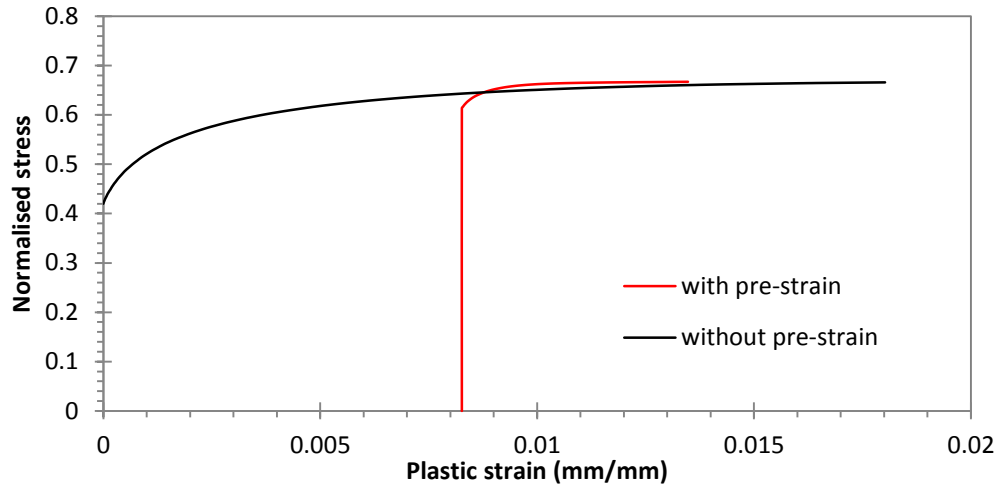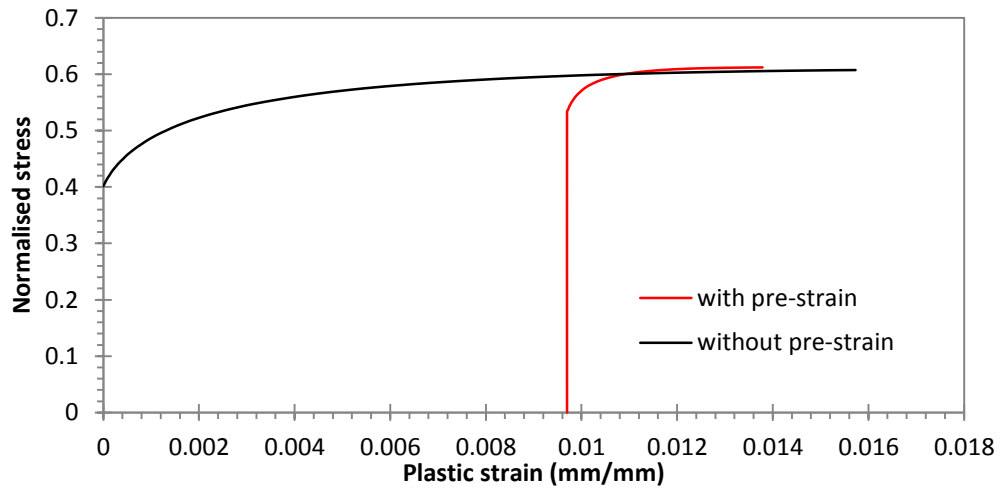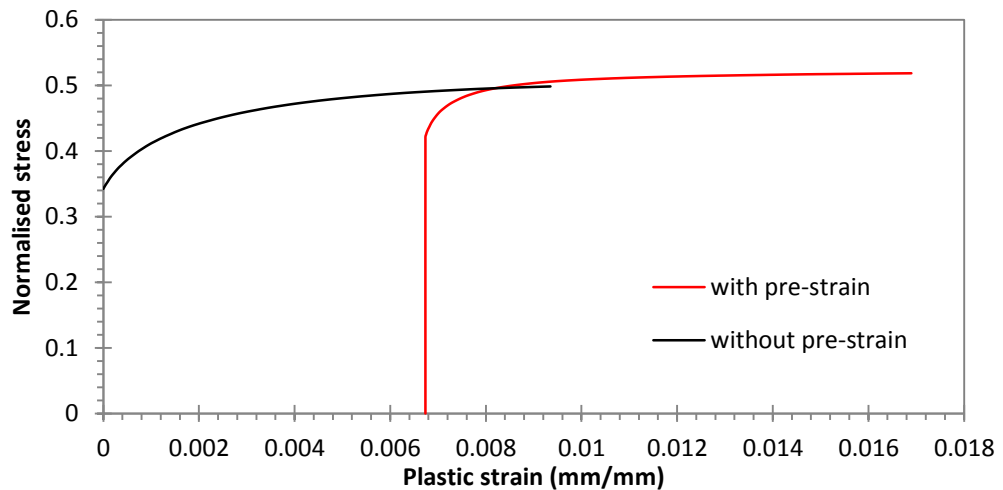
FIGURE 4-9: COMPARISON OF FLOW BEHAVIOUR WITH AND WITHOUT PRE-STRAIN

4.2 FATIGUE BEHAVIOUR

The isothermal fatigue behaviour of AISI H13 hot work tool steel has been measured at temperatures of 500°C, 550°C and 600°C. The strain amplitude varied between ±1% to ±0.6% at a strain rate of $0.01s^{-1}$. Isothermal strain controlled fatigue tests have been performed using symmetrical tension-compression loading conditions with a triangular waveform.

The following sections compare measured tensile and fatigue flow behaviour, examine the strain amplitude sensitivity of fatigue behaviour and the temperature sensitivity of fatigue behaviour.

4.2.1 FATIGUE AND TENSILE BEHAVIOUR COMPARISON

The tensile behaviour measured in the fatigue tests and tensile tests have been compared. One contribution to the differences in flow behaviour measured from these tests is the variation in soak times used in the test procedures. Fatigue tests include a soak time followed by the additional time needed to stabilise the control program.

Figure 4-10 compares the tensile flow behaviour against the measured tensile behaviour during the first loop of fatigue tests, at different temperatures. These tests were performed at a strain rate of 0.01/ s.

The flow behaviour at 500°C and 550°C is similar however the measured behaviour at 600°C differs between the fatigue test and tensile test. At this temperature it is believed that the difference in soak times has a large impact on flow stress.

a) 500°C 0.01/s
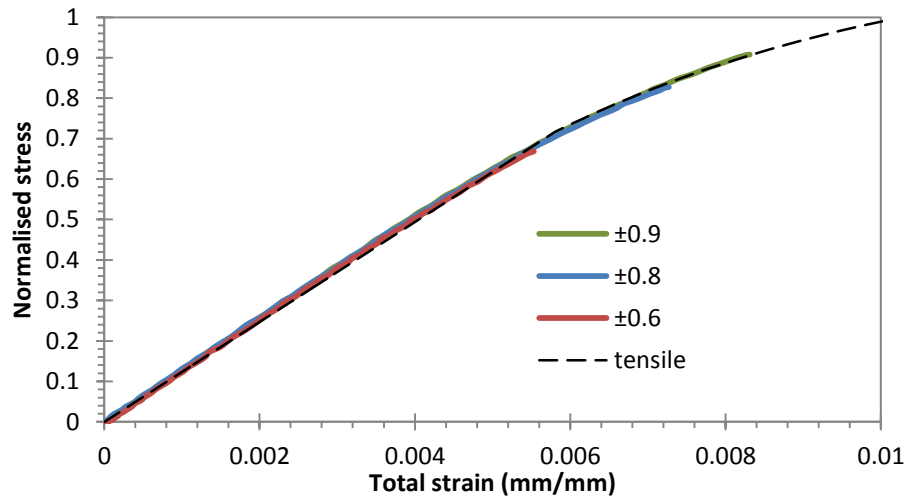
b) 550°C 0.01/s
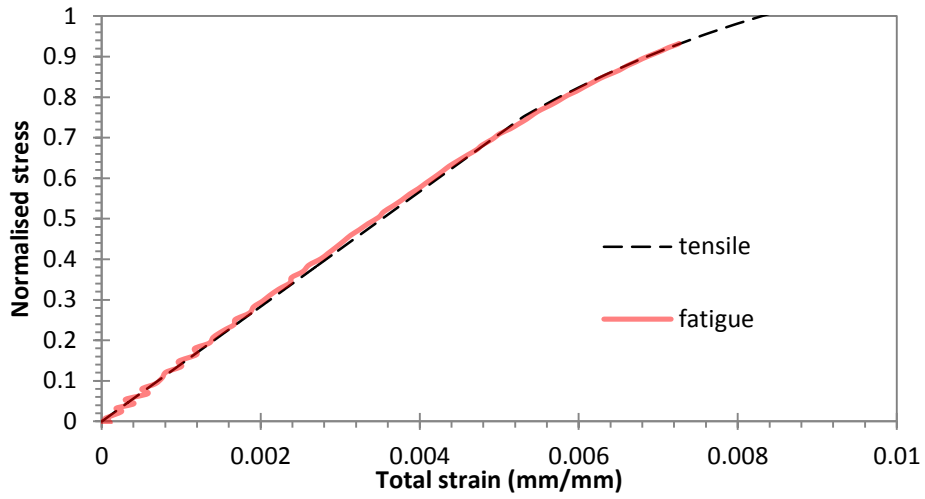
c) 600°C 0.01/s
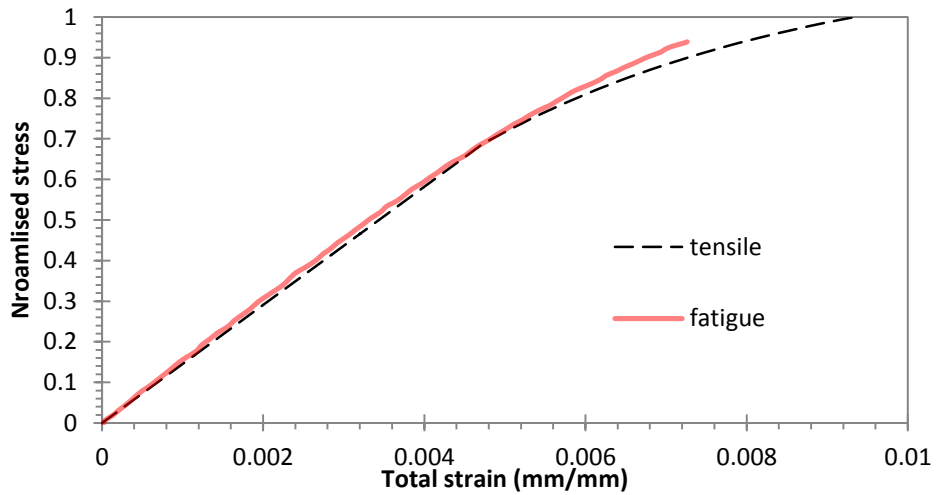
FIGURE 4-10: COMPARISON OF TENSILE LOADING CURVES

4.2.2 STRAIN AMPLITUDE SENSITIVITY

The impact of the strain amplitude upon fatigue behaviour has been investigated for flow behaviour at 500°C and at a strain rate of 0.01/ s. The halved peak stress is shown in Figure 4-11.
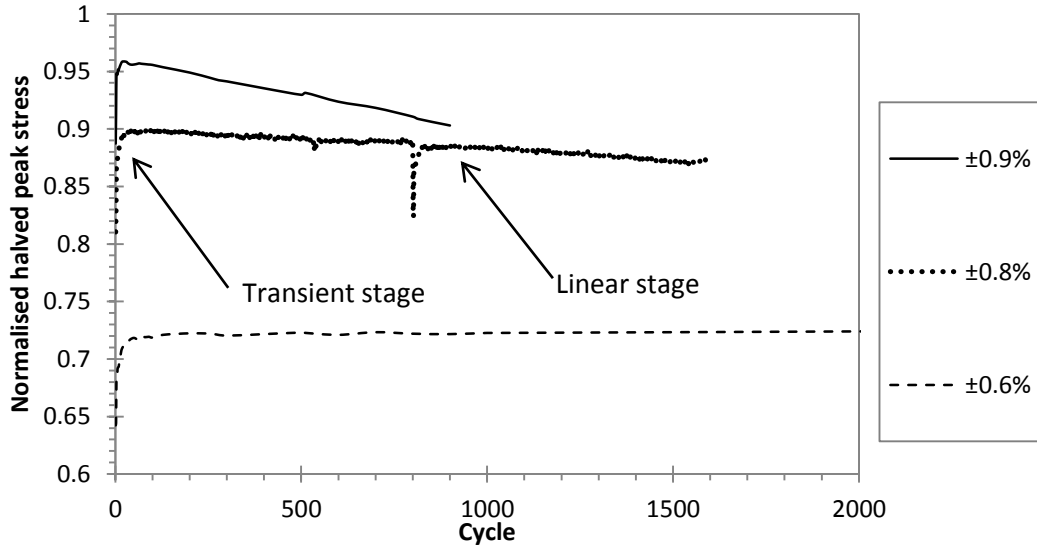
FIGURE 4-11: STRAIN AMPLITUDE SENSITIVITY OF FATIGUE BEHAVIOUR AT 500°C, 0.01/S.

A load drop occurred during the ±0.8% test; however it was possible to continue the test. The test results show a transient cyclical hardening stage followed by linear cyclical softening. This differs to the behaviour observed by Bernhart et al (1999), where the initial behaviour softened opposed to hardened. The initial transient softening behaviour was also reported by Sauzay et al (2008) when examining the fatigue behaviour of 9% Cr tempered martensitic steel.

The hardening behaviour is be explained by the increase in the strain amplitude during the cycles taken to stabilise the control of the strain amplitude at the desired settings. The number of cycles taken to increase the strain amplitude to the desired value coincides with the hardening behaviour measured from the fatigue specimen. An example of this is shown in Figure 4-12 which compares the halved peak strain with the halved peak stress.

124
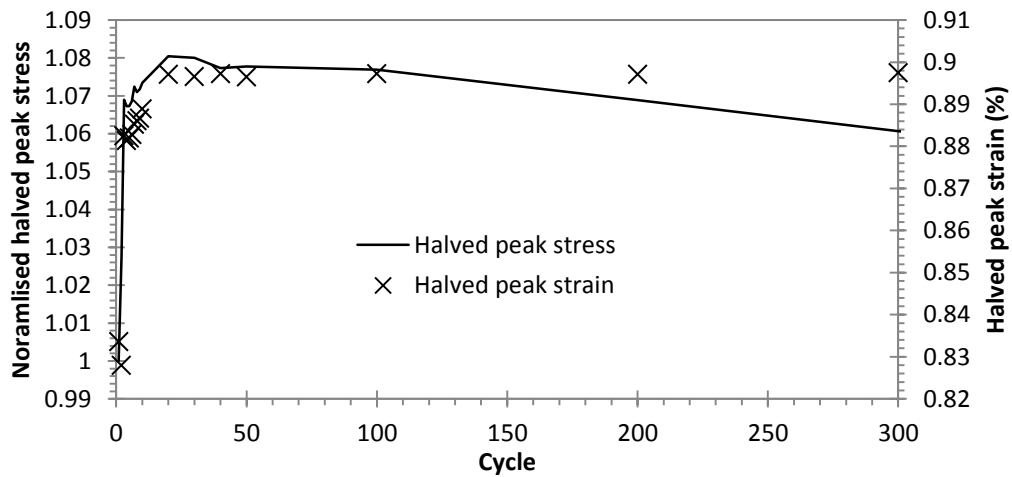
FIGURE 4-12: COMPARISON BETWEEN HALVED PEAK STRAIN AND HALVED PEAK STRESS OF H13

Figure 4-12 reports flow behaviour taken at 500°C, with a strain rate of 0.01/ s and strain amplitude of ±0.9%. It takes approximately 25 cycles for the control program to stabilise the peak strain to the desired value. The initial cycle has a 7.2% error in strain amplitude. The hardening observed corresponds with the number of cycles taken to reach the desired strain amplitude.

The transient cyclical softening behaviour was observed in the fatigue loading of an over-tempered specimen. In this test the strain amplitude slightly overshot the desired value and decreased to stabilise at the required amplitude. The halved peak stress and strain are compared in Figure 4-13.
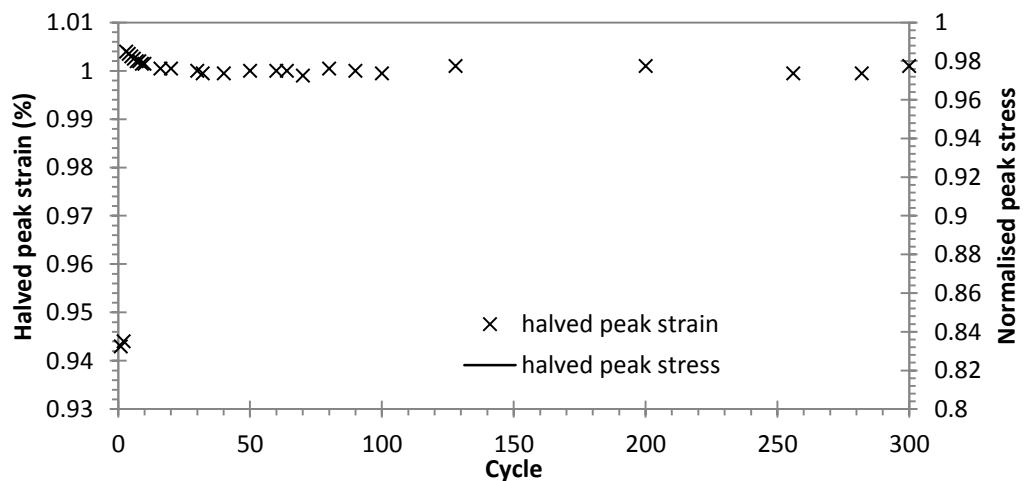
FIGURE 4-13: COMPARISON BETWEEN HALVED PEAK STRAIN AND HALVED PEAK STRESS OF H13

Figure 4-13 shows that the strain amplitude is 0.005% higher for the second cycle which would contribute to the softening behaviour observed but cannot explain the continued transient softening that occurs after stabilisation of the strain amplitude.

Figure 4-14 compares select hysteresis loops descriptive of each test. Many hysteresis loops are shown on the same graph with a strain offset. The cycle number is shown above the hysteresis loop. The ratchetting effect is observed in the ±0.8% test which is not observed under other conditions. This behaviour was caused by failure of the fatigue test tooling.

The impact of the cyclical loading on flow behaviour may be examined by comparing the tensile loading from different hysteresis loops. This is shown in Figure 4-15 for the fatigue behaviour obtained at 500°C at a strain rate of 0.01/ s with strain amplitude of ±0.9%. The flow behaviour is displayed up to the peak stress of the cycle. It can be seen that the yield strength reduces as a response to cyclical loading.

a) ±0.6%
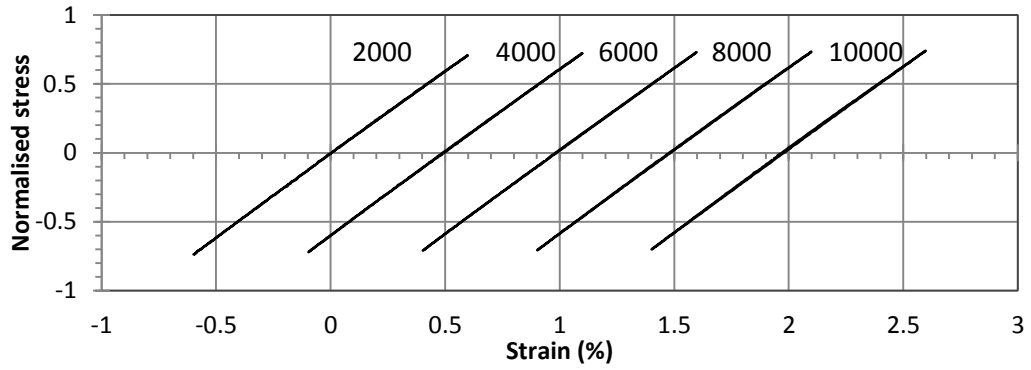
b) ±0.8%
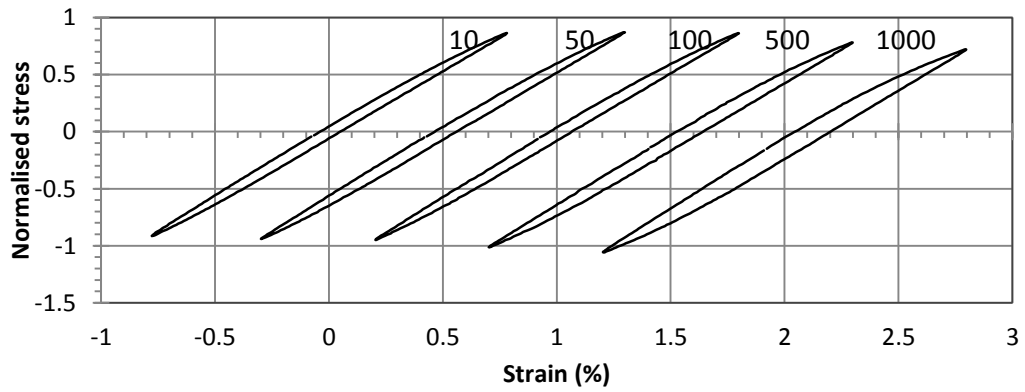
c) ±0.9%
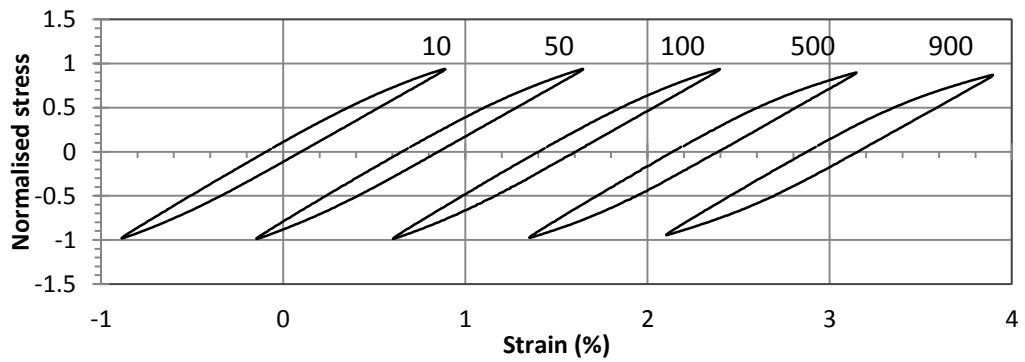
FIGURE 4-14: STRAIN AMPLITUDE SENSITIVITY AT 500°C, 0.01/S
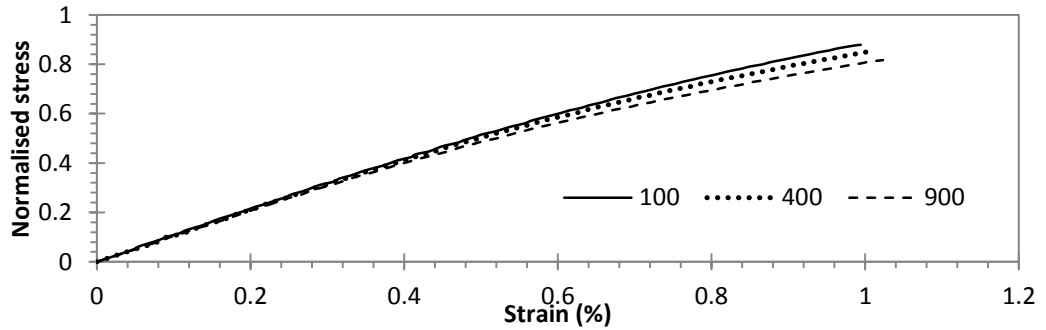
FIGURE 4-15: COMPARISON OF TENSILE LOADING CURVES WITHIN SELECT HYSTERESIS LOOPS

4.2.3   TEMPERATURE SENSITIVITY

The temperature sensitivity of the fatigue behaviour has been examined at a strain rate of 0.01/ s and strain amplitude of ±0.8%. The linear cyclical softening behaviour for different temperatures is compared in Figure 4-16.
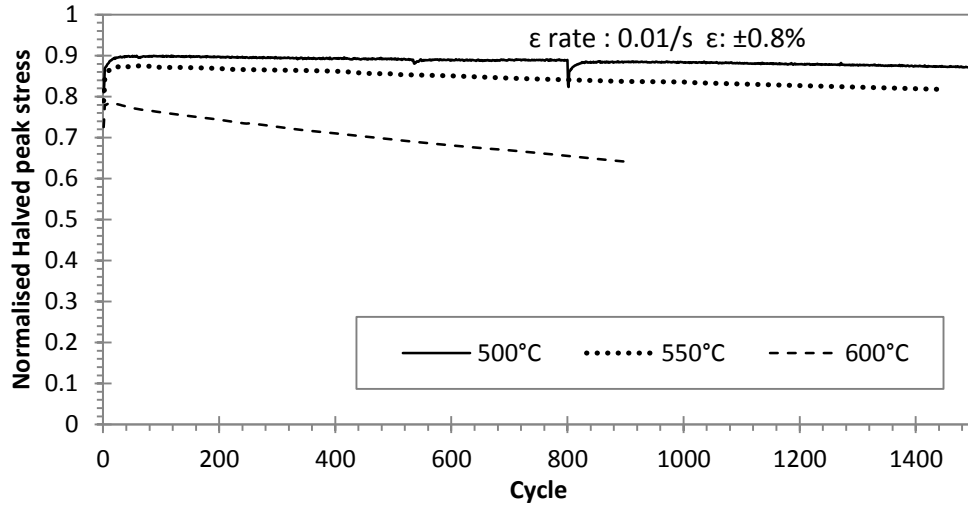
FIGURE 4-16: HALVED PEAK STRESS AT DIFFERENT TEMPERATURES

The softening behaviour is a result of both thermally induced behaviour and strain induced behaviour (Zhang, Bernhart et al. 2008). The hysteresis loops from these conditions are shown in Figure 4-17.

a) 500°C
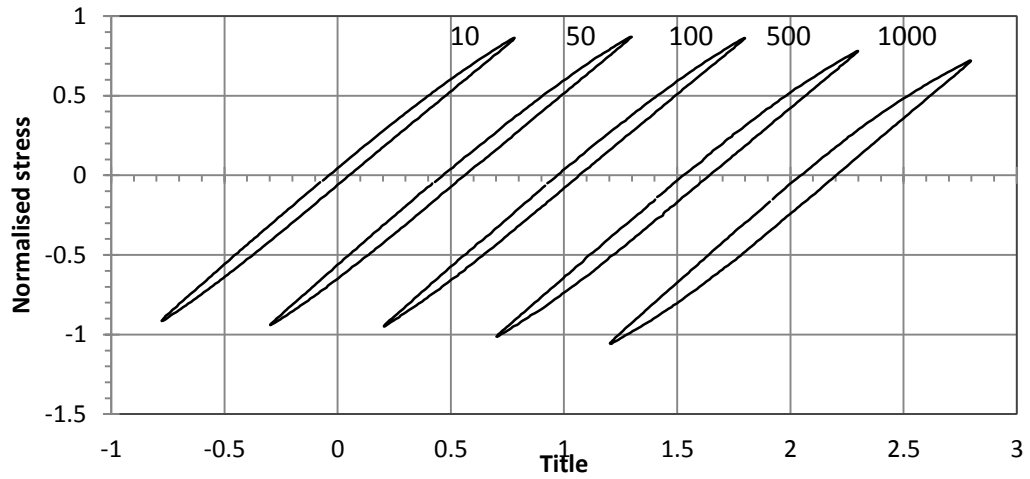
b) 550°C
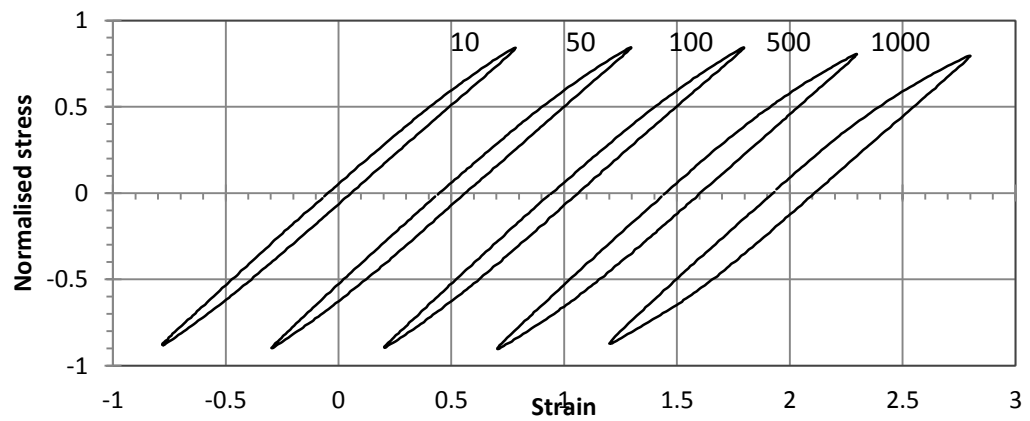
c) 600°C
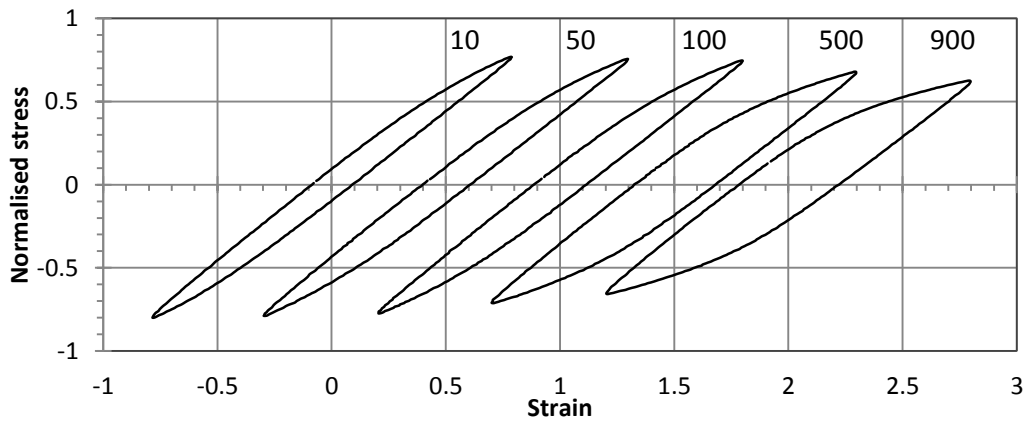
FIGURE 4-17: HYSTERESIS LOOPS AT 0.01/S WITH A STRAIN AMPLITUDE OF ±0.8%.

4.2.4   PRIOR OVER-TEMPERING

A test specimen was over-tempered prior to fatigue testing. The specimen was heated at 600°C for 3 hours. The specimen was tested at 500°C, at a strain rate of 0.01/ s and with strain amplitude of ±1%. Figure 4-18 reports both the halved peak stress and select hysteresis loops.

A) HALVED PEAK STRESS
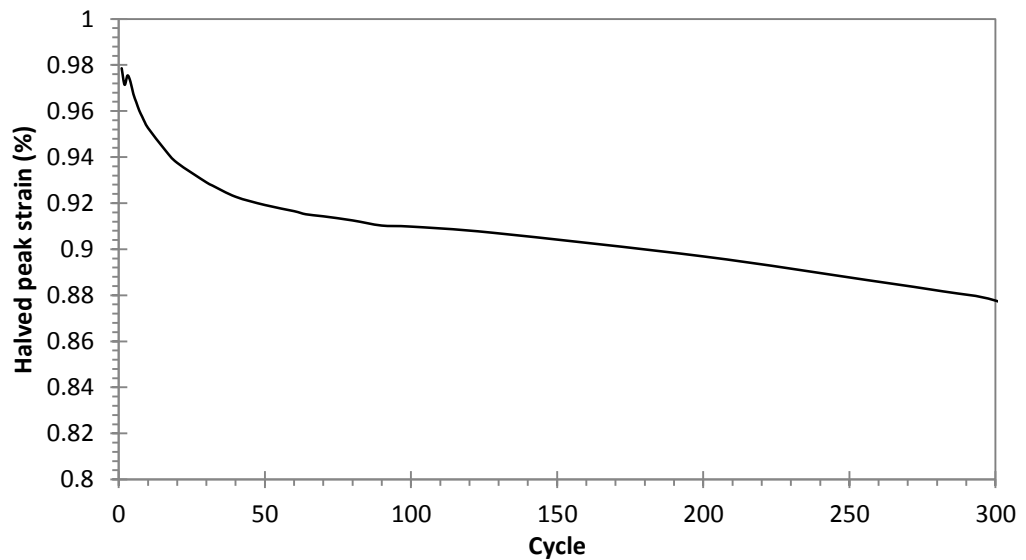
B) SELECT HYSTERESIS LOOPS
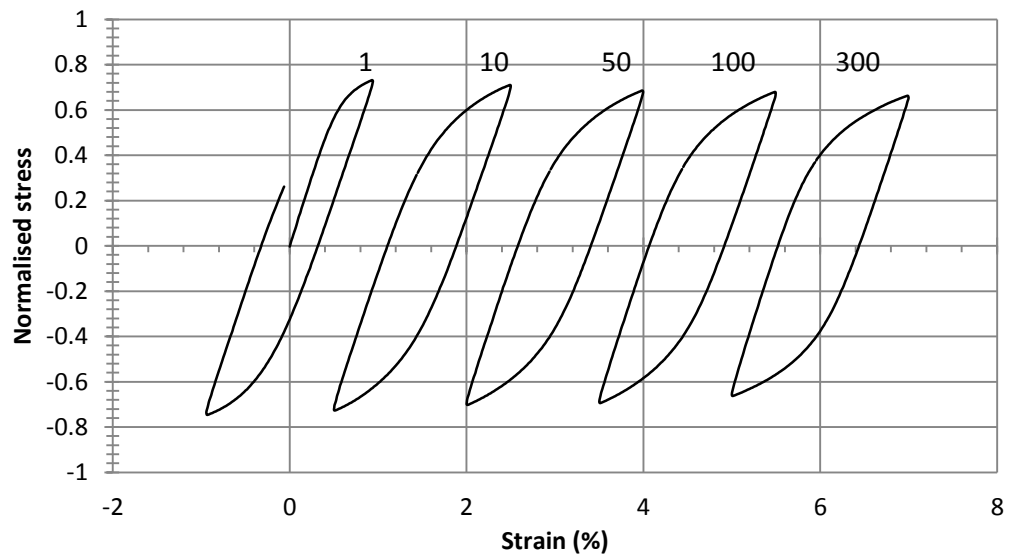
FIGURE 4-18: HALVED PEAK STRESS AND HYSTERESIS LOOPS OF THERMALLY SOFTENED SPECIMEN

In this test the control program quickly reached the desired peak strain after 2 cycles. The initial transient cyclical softening behaviour reported by Bernhart et al (1999) is observed. The UTS and proof strength measured from the hysteresis loops have been measured in both compression and tension. These values are compared in Figure 4-19.
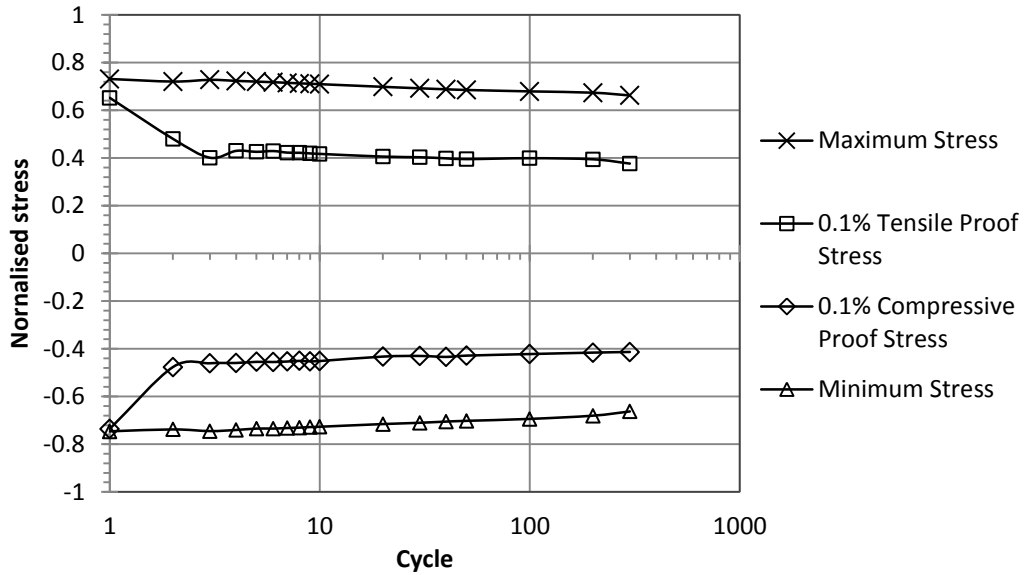
FIGURE 4-19: FATIGUE FLOW BEHAVIOUR ANALYSIS.

Figure 4-19 shows a reduction of 40% in 0.1% proof stress as a response to 3 cycles of fatigue loading. Only a small linear reduction in peak stress is observed. This suggests that the transient cyclical softening affects the yield strength of the material however the softening competes against significant work hardening.

4.3 MICROSTRUCTURAL EXAMINATION

The particle and martensitic laths within specimens of AISI H13 have been examined. The impact of over-tempering upon particles has been assessed. Interrupted tensile and fatigue testing has been performed to evaluate the impact upon the lath spacing.

4.3.1 EXAMINATION OF PARTICLES

Quantitative image analysis has been applied to scanning electron micrographs. The particle size and area fraction has been measured. The specimens have been electro-etched for ten seconds at a voltage of 8V. A Quanta 250 FEI electron microscope with Oxford Instruments detectors was used to take images of the etched surface. A threshold was applied to the image and then the particles of all circularity and of area greater than 0.001 μm^2 were measured. The image process performed is shown in Figure 4-20.

A) RAW IMAGE   **B) BINARY IMAGE**   **C) PARTICLE ANALYSIS**
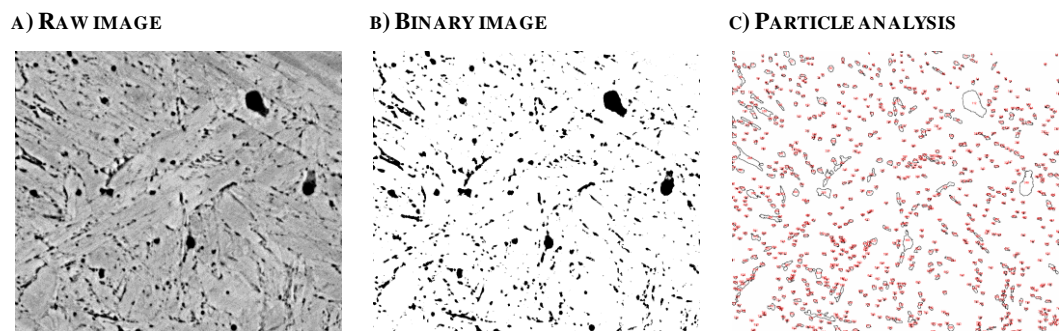
FIGURE 4-20: IMAGE PROCESSING TO MEASURE PARTICLES

The image processing shown in Figure 4-20 has been applied to ten images taken of H13 tool steel at a magnification of 10,000. This corresponds to measuring the particles within an area of 1958μm^2 per condition examined.

The thresholding process incurs error in the measurement. This error has been determined by comparing two extremes of threshold values that may be used to process the micrographs. The minimum threshold ensures no lath boundaries are present in the measurement but risks removing particles from the measurement. The second threshold value has been chosen to maximise the number of particles

captured within the measurement but at the cost of including lath boundaries within the measurement. Descriptive statistics describing the area fraction of particles in the as-heat treated condition are shown in Table 4-3 for the minimum and maximum threshold values.

TABLE 4-3: DESCRIPTIVE STATISTICS DESCRIBING THE AREA FRACTION OF PARTICLES IN THE AS-HEAT TREATED CONDITION

Threshold	min	max
average	5.0%	6.2%
max	7.7%	8.7%
min	3.0%	4.5%
St. dev.	1.4%	1.2%

There is a difference of 1.2% in average area fraction of particles resulting from the thresholding process. It is assumed that the area fraction of particles lies between these values at 5.6±1.4%.

The Feret diameter has been used to measure the diameter of the particles. The distribution of measurements taken from the minimum and maximum thresholding is shown in Figure 4-21.

From Figure 4-21 the most frequently measured diameter of particle is between 60-90nm which is similar to the upper range in measurements taken from Zhang et al (2004). Descriptive statistics regarding the measured particles are given in

Table 4-4.

The mean particle diameter measurements do not vary significantly as a result of the thresholding process. It is not possible to measure particle of diameter less than 40nm using this approach. The implication is that the fine intra-lath particles that impact the mean free path of dislocation glide cannot be measured using scanning electron microscopy. Transition Electron Microscopy is required to measure these particles (Zhang, Delagnes et al. 2004; Bischof, Staron et al. 2008; Medvedeva, Bergström et al. 2009).

FIGURE 4-21: THE FREQUENCY DENSITY AND ACCUMULATIVE PROBABILITY OF FERET DIAMETERS

TABLE 4-4: DESCRIPTIVE STATISTICS DESCRIBING PARTICLE DIAMETERS

Threshold	min	max
average (µm)	0.185	0.191
min (µm)	0.046	0.046
max (µm)	2.755	2.752
1st quartile (µm)	0.091	0.091
mean (µm)	0.136	0.137
3rd quartile (µm)	0.219	0.226
st. dev (µm)	0.165	0.170
count	6479	7624
error (µm)	0.002	0.002

4.3.1.1 IMPACT OF OVER-TEMPERING

H13 specimens in the as-heat treated condition have been over-tempered at temperatures of 500°C, 550°C or 600°C for time scales of either 1 hour, 8 hours or 24 hours. The reduction in microhardness is shown in Figure 4-22.
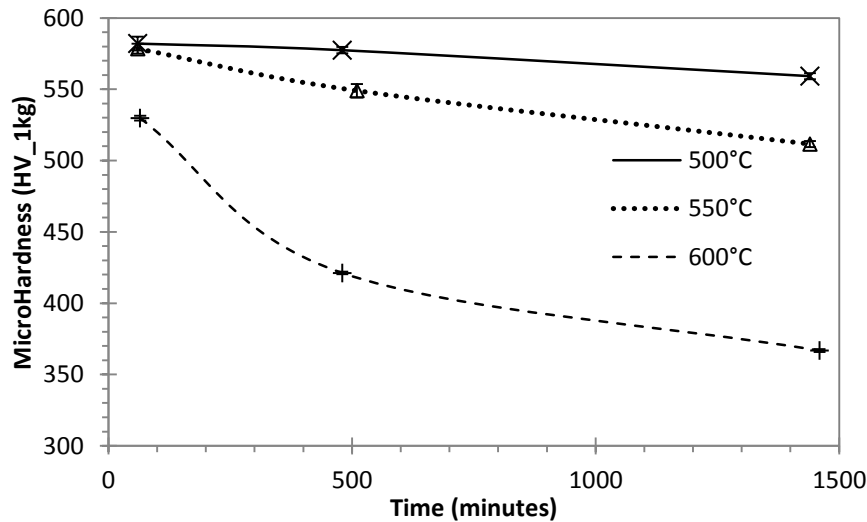
FIGURE 4-22: HARDNESS MEASUREMENTS TAKEN FROM OVER-TEMPERED SPECIMENS.

The specimens were electro-etched using 10% Oxalic acid for ten seconds using 8V. Ten SEM images were taken at 10,000 and 30,000 times magnification. The impact of aging on the particles observed at these scales is shown in Figure 4-23 and Figure 4-24.

Two scales of particles have been observed in each sample. The larger particles have an average diameter of around 0.6 μm whilst the smaller particles have a diameter less than 0.2μm.

Figure 4-24 shows that with over-tempering, more particles are observed under SEM which is noticeable when comparing the initial structure to the fully annealed structure. Quantitative image analysis of these micrographs indicates an increase in particle density as a result of aging however it was not possible to measure small particles of diameter less than 40nm using this approach.
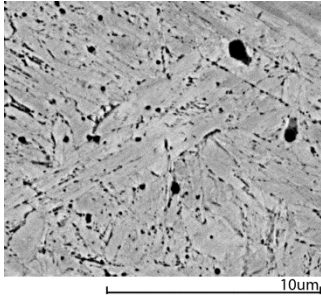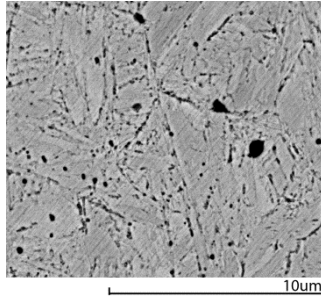
135

A) 500°C FOR 1 HOUR

B) 550°C FOR 1 HOUR
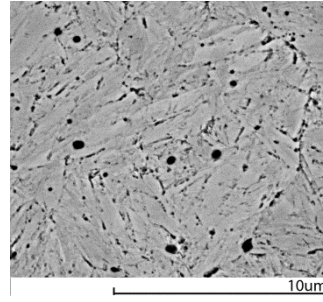
C) 600°C FOR 1 HOUR
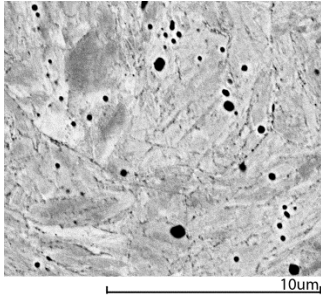
D) 500°C FOR 8 HOURS
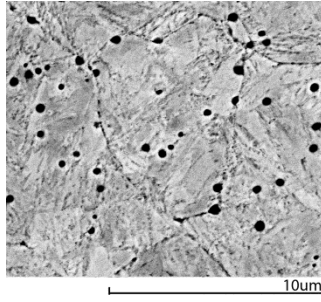
E) 550°C FOR 8 HOURS
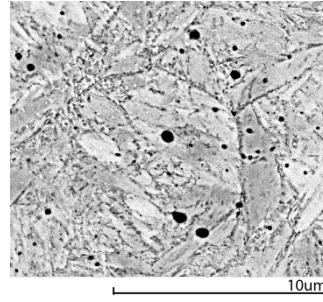
F) 600°C FOR 1 HOUR
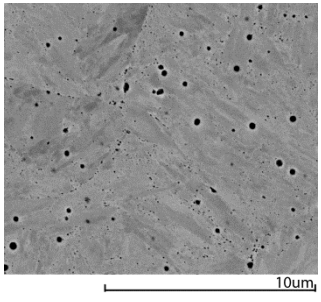
G) 500°C FOR 24 HOURS
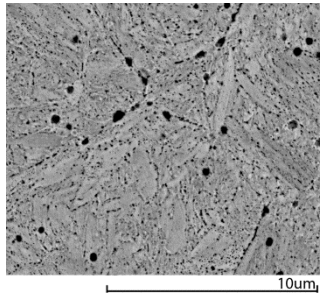
H) 550°C FOR 24 HOURS
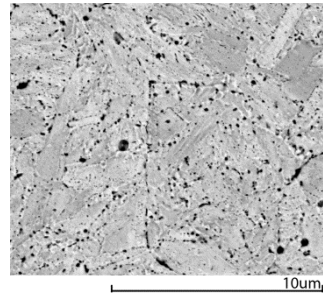
I) 600°C FOR 1 HOUR

FIGURE 4-23: BACK SCATTER IMAGES TAKEN AT 10,000 TIMES MAGNIFICATION DURING AGING
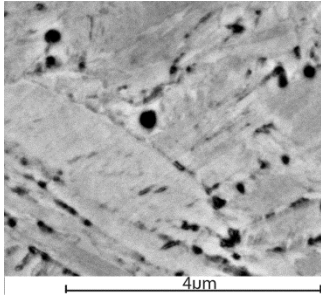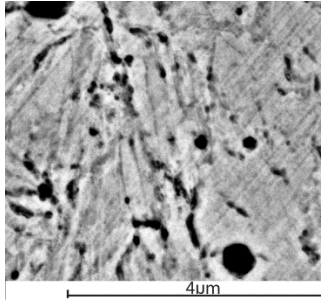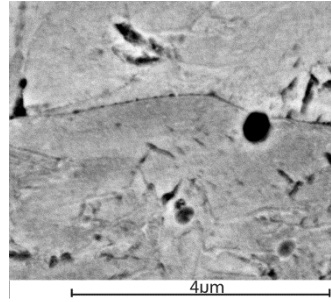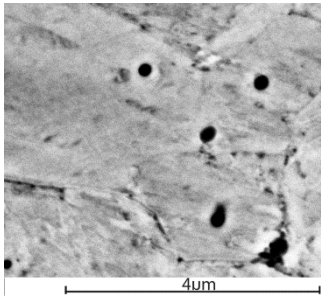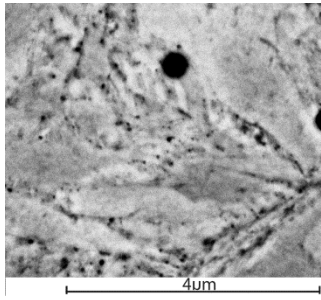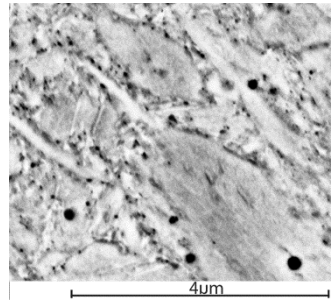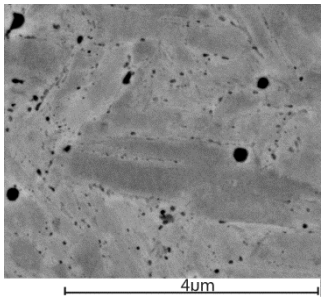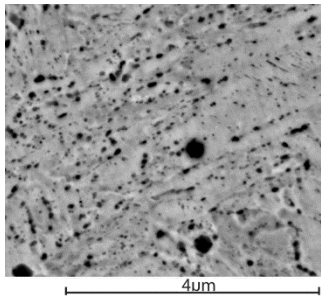
A) 500°C FOR 1 HOUR
B) 550°C FOR 1 HOUR
C) 600°C FOR 1 HOUR
D) 500°C FOR 8 HOURS
E) 550°C FOR 8 HOURS
F) 600°C FOR 1 HOUR
G) 500°C FOR 24 HOURS
H) 550°C FOR 24 HOURS
I) 600°C FOR 1 HOUR
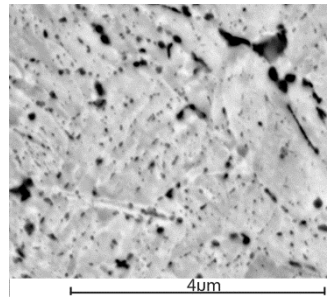
FIGURE 4-24 : BACK SCATTER IMAGES TAKEN AT 30,000 TIMES MAGNIFICATION DURING AGING

4.3.2 MARTENSITIC LATHS

The grain structure of tempered martensitic steel has been evaluated by examining electron back scatter diffraction (EBSD) maps and scanning electron micrographs. To measure the martensitic lath boundary spacing, the line intercept method has been applied to EBSD maps. Attempts to apply the technique to scanning electron micrographs proved unsuccessful.

Figure 4-25 shows the martensitic structure and intra-lath particles at the nitride-substrate interface within AISI H13. The tempered martensitic structure is clearly visible at this location. The sample was etched with 5% Nital to reveal the martensitic structure.

A) 4000x MAGNIFICATION
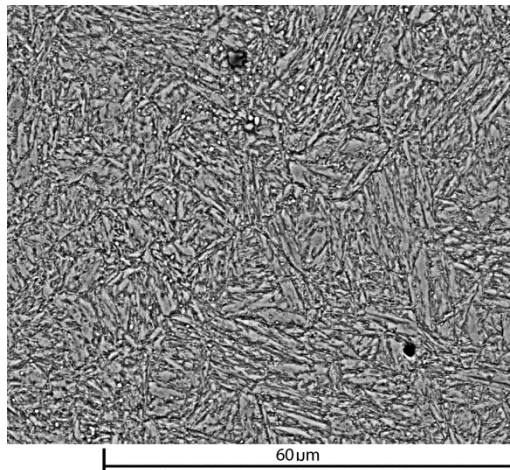
B) 32 000x MAGNIFICATION
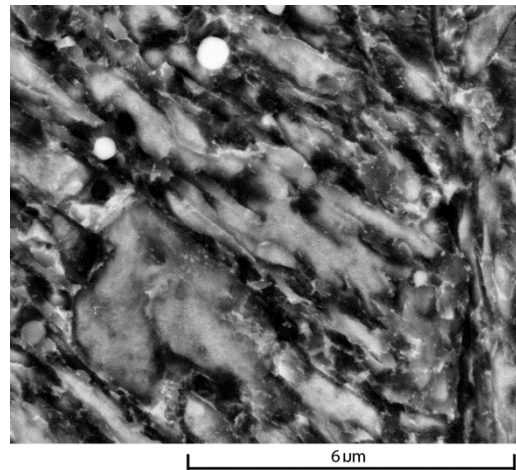
FIGURE 4-25: TEMPERED MARTENSITIC STRUCTURE

Figure 4-26 shows an Eular EBSD map taken from an as-heat treated specimen of AISI H13. The software Channel 5 was used to process the EBSD map and for measuring martensitic lath spacing using the line intercept method. The maps were processed following the procedure outlined by Sun et al (2010). This process consists of removing spikes caused by poorly indexed EBSD patterns and then an iterative process of extrapolating the orientation of un-indexed pixels based upon the orientation of neighbouring pixels. The first iteration extrapolates the average orientation of neighbouring pixels if there are 8 neighbouring pixels that have been successfully indexed. The second iteration reduces this number to

7 neighbouring pixels of known orientation. This process is repeated until the orientation of un-indexed pixels with 5 neighbouring pixels of known orientation is approximated by the mean orientation of these pixels. Further extrapolation based on a lower number of known orientations of neighbouring pixels produces unacceptable error.

The line intercept method has been applied to the EBSD maps to measure boundary spacing. The step size of the EBSD maps was 0.2µm creating an error of ±0.1µm.

200 µm
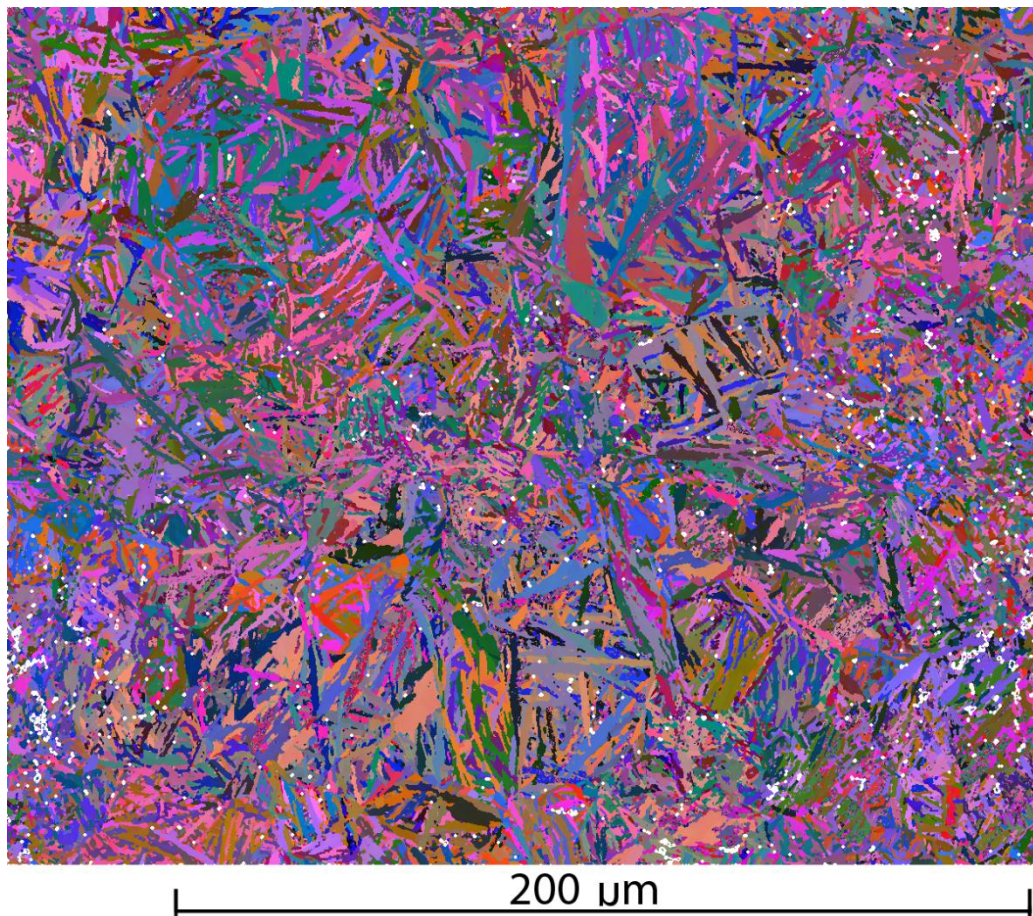
FIGURE 4-26: EULER MAP

The lath spacing measured from the analysis is shown in Figure 4-27. Statistical data of the lath spacing measurements is shown in Table 4-5.
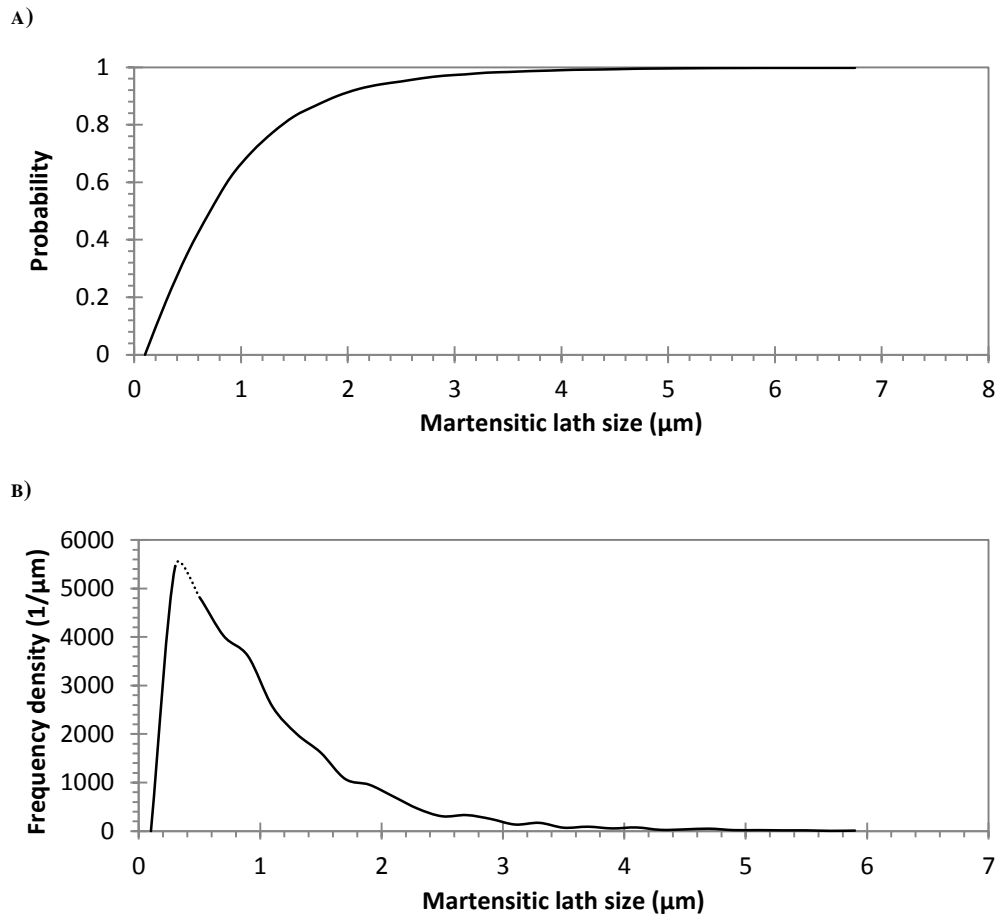
FIGURE 4-27: LATH SIZE MEASUREMENTS FROM EBSD MAPS

TABLE 4-5: STATISTICAL DATA DESCRIBING LATH SPACING MEASUREMENTS

HT	EBSD
Count	5584
Average (μm)	0.93
St. Dev (μm)	0.84
Error (μm)	0.01
Min (μm)	0.20
1st quartile (μm)	0.40
Median (μm)	0.70
3rd quartile (μm)	1.20
Max (μm)	11.60

The lath spacing may be approximated from the median lath spacing measured from the EBSD map. Accounting for the error from the step size, the lath spacing is 0.7±0.1μm.

4.3.2.1 IMPACT OF PLASTIC STRAIN

Interrupted mechanical tests have been performed to examine the impact of plastic strain upon the martensitic structure. Interrupted tensile tests were performed at a strain rate of 0.01/ s and at temperatures of 500C°C and 600°C. The flow behaviour of each test is shown in Figure 4-28.

Lath spacing has been measured from BS images in back scattered (BS) mode taken from samples that have been plastically deformed at a strain rate of 0.01/ s and at temperatures of 500°C or 600°C. Example micrographs from each condition are shown in Figure 4-29.

No significant difference in tempered martensitic spacing was measured when applying the line intercept method to the SEM micrographs. Similar results were found when examining fatigued specimen. Isothermal fatigue tests were performed at a temperature of 500°C, a strain rate of 0.01/ s and a strain amplitude of ±0.8%. One test was interrupted after 150 cycles for examination. The halved peak stresses from the fatigue tests are shown in Figure 4-28.

A) INTERRUPTED TENSILE TESTS AT 500°C   B) INTERRUPTED TENSILE TESTS AT 600°C
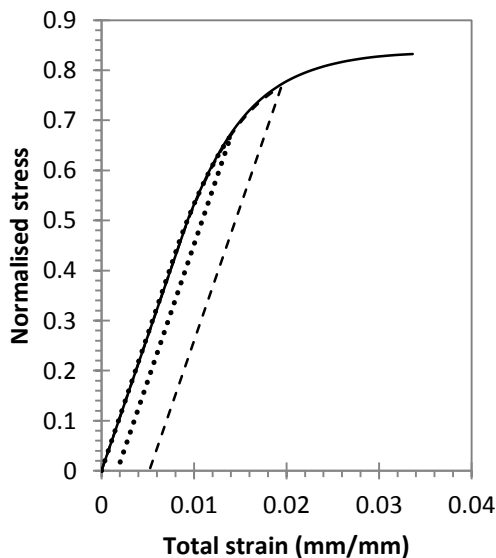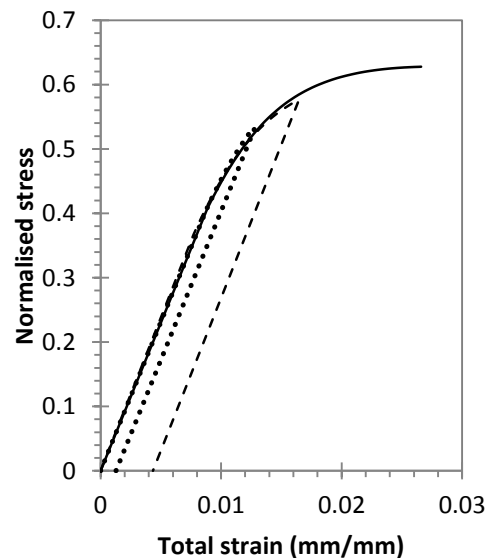
FIGURE 4-28: INTERRUPTED TENSILE TESTS AFTER DIFFERENT AMOUNTS OF PLASTIC STRAI
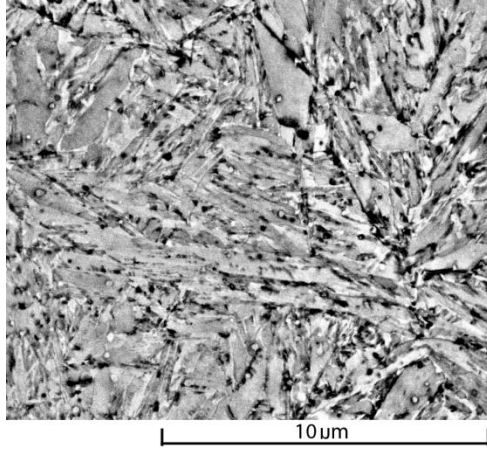
A) 500°C $\varepsilon_p = 0.0020$

B) 600°C $\varepsilon_p = 0.0014$
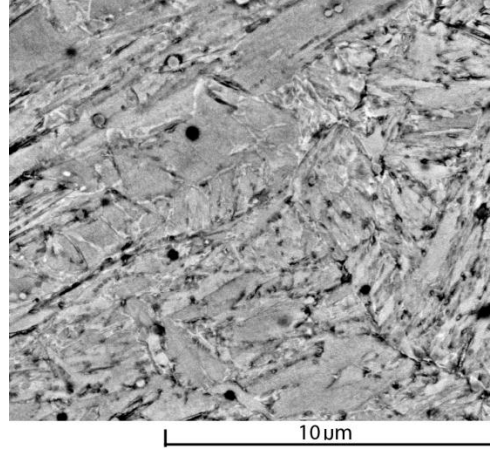
C) 500°C $\varepsilon_p = 0.0060$
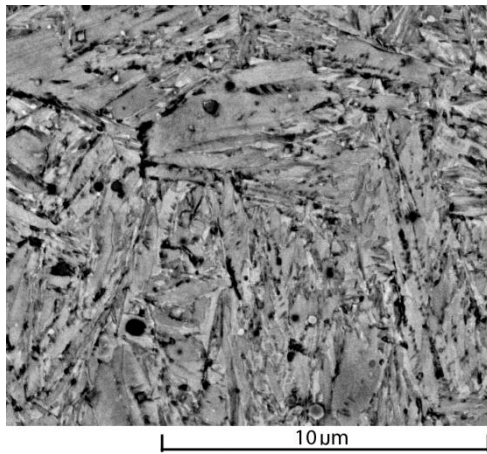
D) 600°C $\varepsilon_p = 0.0044$
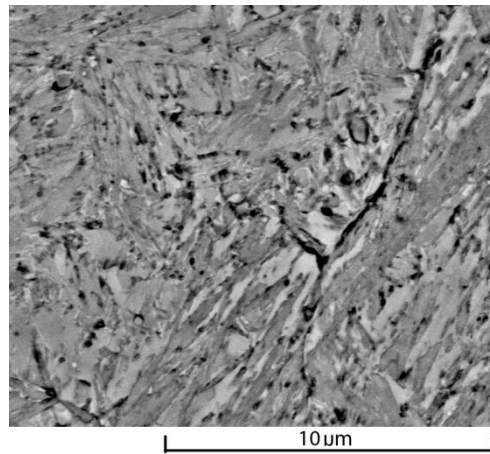
E)) 500°C $\varepsilon_p = 0.021$
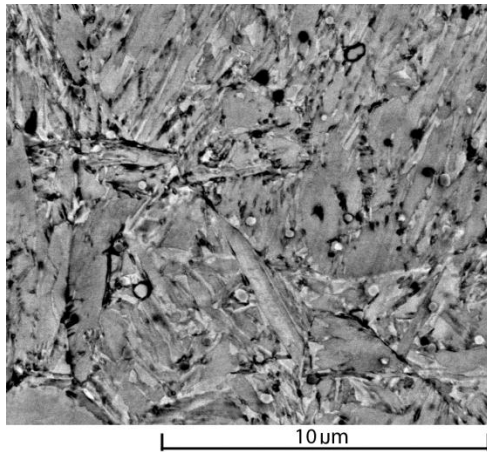
F) 600°C $\varepsilon_p = 0.016$
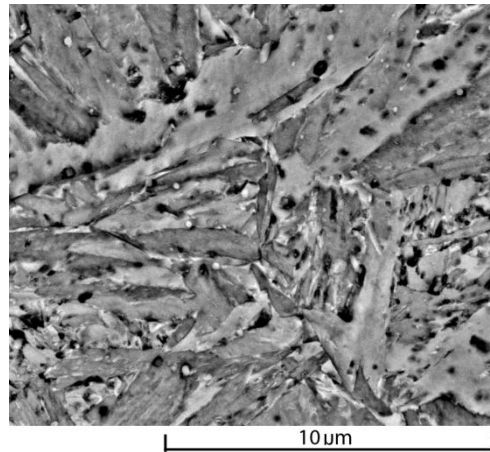
FIGURE 4-29: IMPACT OF PLASTIC DEFORMATION FROM TENSILE LOADING ON TEMPERED MARTENSITE
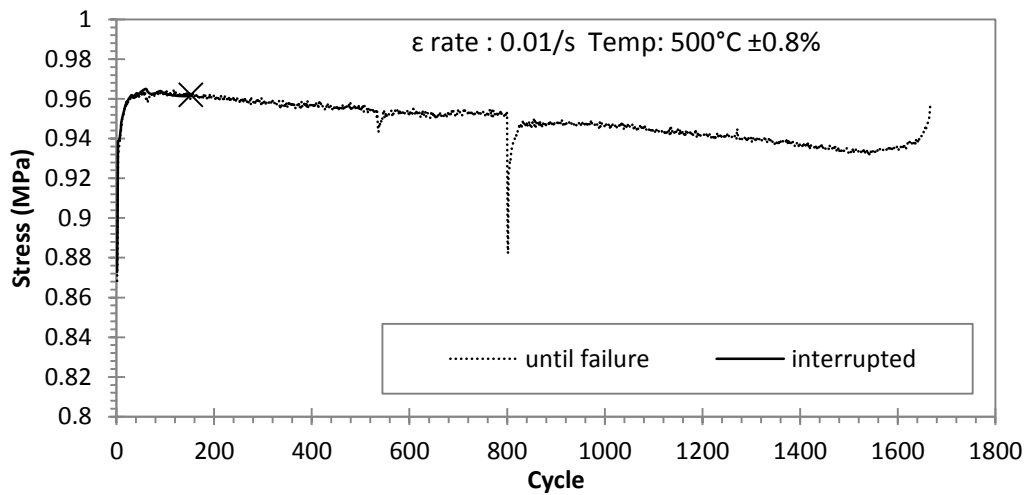
FIGURE 4-30: HALVED PEAK STRESSES OF FATIGUED SPECIMEN

Back scatter images taken from the as-heat treated condition are compared to fatigued specimens in Figure 4-31.

A) AS-HEAT TREATED   B) AFTER 150 CYCLES   C) AFTER FAILURE
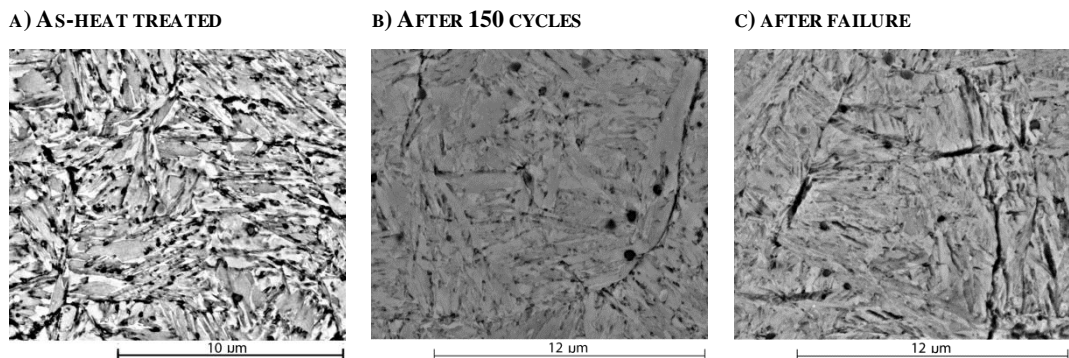
FIGURE 4-31: COMPARISON OF MICROSTRUCTURE THAT HAVE EXPERIENCED DIFFERENT AMOUNTS OF CYCLICAL LOADING

It was not possible to measure changes in lath width as a result of plastic strain using quantitative image analysis of SE back scatter images.

4.4 MATERIAL CHARACTERISATION SUMMARY

Tensile tests have determined the following behaviour of AISI H13. The tests evaluated the following material behaviour:

- Temperature sensitivity of yield behaviour
- Strain rate sensitivity of yield behaviour
- Work hardening
- The impact of pre-strain upon flow behaviour
- The impact of over-tempering upon flow behaviour

Over tempering behaviour has also been analysed from hardness measurements of over-tempered specimens.

Similar to other tempered martensitic steels, the material has been observed to cyclically soften under symmetrical tension-compression fatigue loading. This behaviour was measured for different temperatures and at different strain amplitudes. For the purpose of model verification, a fatigue test has been performed upon an over-tempered specimen.

The over-tempering behaviour of AISI H13 may be explained by particle coarsening and the annihilation of dislocations. It was not possible to measure the intra-lath particles of interest using SEM.

The cyclical softening behaviour may be explained by the change in dislocation structure as a response to cyclical loading. The subgrain diameter may be approximated from the average lath spacing. The lath spacing in the as-heat treated condition has been measured at 0.7±0.1μm from applying the line intercept method to EBSD maps.

5 DIE MATERIAL MODELLING APPROACHES

The purpose of this chapter is to review modelling approaches and identify the most appropriate approach for modelling the plastic flow behaviour of hot work tool steel for use in die life prediction. The approaches covered focus on life prediction where failure is caused by plastic deformation or low cycle fatigue.

The flow behaviour for the tool steel of interest has been presented in chapter 4. Different approaches may be taken to model this behaviour. The approaches have been categorised into empirical damage mechanics, phenomenological models and physical based models. Several empirical damage mechanics models have been developed for fatigue life prediction of hot work tool steels. These models have been developed to predict life as a function of the process parameters that describe the thermo-mechanical loading of the tooling. These models are of interest in how they describe the flow behaviour of the tool steel and how they account for change in material condition.

Phenomenological models have been developed to capture the complex flow behaviour of tempered martensitic hot work tool steels during fatigue loading. Although numerous modelling approaches exist, only the Lemaitre and Chaboche approach is examined as this modelling approach has been applied to modelling tool steel flow behaviour.

Physical based models have been developed to describe the creep behaviour of 9-12% Cr tempered martensitic steels. These approaches are examined to determine how they can be applied to describe the fatigue behaviour of tempered martensitic tool steels under hot forging tooling conditions.

5.1 EMPIRICAL DAMAGE MECHANICS

Damage mechanics is a useful method for modelling material behaviour and predicting life. The term "damage" refers to the reduction in load bearing capacity caused by the formation of cavities during creep (Kachanov 1958). The growth and nucleation of cavities result in the coalescence of voids, forming a macro-scale crack, resulting in failure (Lin et al. 2005).

The thermo-mechanical fatigue damage models examined in this section are based upon the method proposed by Lemaitre and Chaboche (1990). A flow rule is developed to calculate the plastic strain resulting from the cyclical loading conditions. A damage evolution equation is then developed, which describes the progression of damage until failure.

In Kachanov's (1958) original modelling approach, the damage was decoupled from the plastic strain rate. In this approach, the predicted life is not impacted by the flow rule. Rabotnov (1969) addressed this by coupling the plastic strain rate in the damage evolution equation. An increased rate of plastic flow results in reduced life. A further improvement was to fully couple damage, with damage being present within the flow rule. The presence of damage reduces the strength of the material, which increases the rate that plastic strain is accumulated and thus the rate of damage progression. This may be used to describe the final material behaviour, leading to failure (Basoalto et al. 2002). The coupling of damage rate and the plastic strain rate may be used to distinguish Rabotnov (1969) based damage evolution opposed to Kachanov (1958) based damage evolution.

The damage mechanics approaches proposed by Lemaitre and Chaboche (1990) have been adapted to include TMF conditions by Berti and Monti (2009), Fang et al (2002) and Velay et al (2005). Berti and Monti (2009) used two empirical continuum damage models to determine the combined impact of creep and fatigue damage on the fatigue life of hot forging tooling. The creep model was not made an explicit function of temperature, with damage decoupled from the flow rule. It was assumed that creep damage and fatigue damage accumulate linearly.

Table 5-1 shows the origin of the model and the proposed model by each author.

TABLE 5-1: TMF DIE LIFE PREDICTION MODELS – ORIGINAL APPROACHES

Berti and Monti (2009): TMF

Flow rule	$\dot{\varepsilon}_p = \dfrac{\sigma_{max} - \sigma_l(\bar{\sigma})}{\sigma_u - \sigma_{max}}\left(\dfrac{\sigma_{max} - \bar{\sigma}}{M(\bar{\sigma})}\right)^{\beta}$	$\rightarrow$	$\dot{\varepsilon}_p = \dfrac{\sigma_{Tmax} - \sigma_l(T_{max})}{\sigma_u(T_{max}) - \sigma_{Tmax}} \times \left(\dfrac{\sigma_{Tmax}}{\left(1 - \phi(\nabla T_{T_{max}})\right)M_0(T_{max})}\right)^{\alpha \frac{T_{min}}{T_{max}}\beta(T_{max})}$	
Damage rate	$dD_f = \dfrac{(1-D_f)^{-k}}{k+1}.\dot{\varepsilon}_p dN$	$\rightarrow$	$dD_f = \dfrac{(1-D_f)^{-k}}{k+1}.\dot{\varepsilon}_p dN$	

Berti and Monti (2009): Creep

Flow rule	$\dot{\varepsilon}_p = \left(\dfrac{\sigma_0}{A_0}\right)^r$	$\rightarrow$	$\dot{\varepsilon}_p = (r+1)\left(\dfrac{\sigma(t)}{A_o}\right)^r$
Damage rate	$dD_c = (1-D_c)^{-k}.\dot{\varepsilon}_p dN$	$\rightarrow$	$dD_c = \dfrac{(1-D_c)^{-k}}{k+1}.\dot{\varepsilon}_p dN$

Fang et al (2002): TMF

Flow rule	$\dot{\varepsilon}_p = \left[\dfrac{\sigma_{max} - \bar{\sigma}}{\hat{M}(\bar{\sigma})(1-D_f)}\right]^{\beta}$	$\rightarrow$	$\dot{\varepsilon}_p = \left[\dfrac{\sigma_{max}}{M_0(T_{max})(1-D_f)}\right]^{\beta(T_{Max},\Delta T)}$
Damage rate	$dD_f = \left[1-(1-D_f)^{\beta+1}\right]^{A(\sigma_{max},\sigma_u,\sigma_l)}.\dot{\varepsilon}_p dN$	$\rightarrow$	$dD_f = \left[1-(1-D_f)^{\beta(T_{Max},\Delta T)+1}\right]^{A(\sigma_{max},\sigma_u,\sigma_l)}.\dot{\varepsilon}_p dN$

Velay et al (2005): TMF

Flow rule	$\dot{\varepsilon}_p = \left(\dfrac{\frac{\Delta\sigma}{2M_0(1-b\bar{\sigma})}}{(1-D)}\right)^{\beta}$	$\rightarrow$	$\dot{\varepsilon}_p = \left(\dfrac{\frac{\Delta S}{2M_0}}{\frac{(1-D)}{\sigma_u}}\right)^{\beta}$
Damage rate	$dD_f = (1-(1-D)^{\beta+1})^{A(\sigma_{max},\sigma_u,\sigma_l)}.\dot{\varepsilon}_p dN$	$\rightarrow$	$dD_f = \left(1-(1-D)^{\beta+1}\right)^{A(\sigma_{max},\sigma_u,\sigma_l)}.\dot{\varepsilon}_p dN$ Where; $\alpha = \alpha(\sigma_M,\sigma_l,\sigma_U)$ or $\alpha = \alpha(\sigma_M)$

Where;

σ_{max} Maximum stress

$\bar{\sigma}$ Mean stress

$M(\bar{\sigma})$ Coefficient that depends upon the cumulative damage effects (Berti and Monti 2009)

M_0 Material parameter (Fang, Jiang et al. 2002):

$\dot{M}$ Fatigue model parameter (Velay, Bernhart et al. 2005)

σ_u Ultimate tensile strength

σ_l Fatigue limit

β Coefficient that depends upon the cumulative damage effects

α Coefficient that depends upon the fatigue damage accumulation

A Damage rate exponent

A_o Creep damage coefficient

r Creep damage coefficient

k Damage rate coefficient

$\sigma(t)$ Stress evolution in a single cycle

$\Delta\sigma$ Mid-life stress range

σ_M Mid-life maximal stress

ΔS Reduced mid-life stress range

b Fatigue model parameter

$\nabla T_{T_{max}}$ Thermal gradient perpendicular to the load application direction

T_{max} Maximum temperature during thermal cycle

σ_{Tmax} Stress value at the point in time of maximum temperature

ϕ Thermal gradient damage coefficient

γ Exponential coefficient relevant to the damage caused by thermal fatigue

ΔT Temperature range

In all the models reported, the authors have simplified the problem to focus on symmetrical tension-compression loading so that the impact of the mean stress can be ignored. This simplification reduces the ability to apply the models to different loading conditions.

All models, apart from Velay et al (2005), have made the resistance to plastic deformation term a function of temperature, capturing the temperature sensitivity of the yield stress. Only Berti and Monti (2009) have addressed the strain rate sensitivity of yield by including creep damage. The creep damage has

been assumed to accumulate linearly with the fatigue damage. The creep model was not made an explicit function of temperature, with damage decoupled from the flow rule.

These models do not account for the work hardening behaviour of hot work tool steels. The models do not directly account for thermal softening or cyclical softening. The Rabotnov based models that couple damage within the flow rule capture the tertiary behaviour leading to rupture of the fatigue specimen.

Berti and Monti (2009) accounted for the thermal cycle in two ways; making the flow rule exponent include a ratio describing the temperature range and a thermal gradient factor softening the resistance to plastic flow term. Fang et al (2002) also made the exponent β a function of the maximum temperature and the temperature range to describe the impact of the thermal cycle during TMF conditions.

It can be seen that the models developed by Lemaitre and Chaboche have been altered to include parameters descriptive of the thermal cycle in addition to the mechanical cycle.

5.1.1   SUMMARY OF EMPIRICAL DAMAGE MECHANICS

The purpose of these models is to predict die life for given process parameters. The damage mechanics models proposed by Lemaitre and Chaboche (1990) have been adapted to include process conditions that describe thermo-mechanical fatigue conditions.

The models are useful in predicting the impact of thermo-mechanical loading for the conditions used to develop the model. The models cannot be safely extrapolated to other conditions.

The following section examines phenomenological models that have been developed to capture the plastic flow behaviour of hot work tool steels.

5.2 PHENOMENOLOGICAL MODELLING APPROACHES

Phenomenological plastic deformation models have been developed to capture the material flow behaviour that reflects knowledge of deformation and hardening/ softening mechanisms. These models utilise internal state variables that are used as a mathematical representation of the material condition, which is linked indirectly to the microstructure. The types of behaviour include isotropic hardening, kinematic hardening, the Baushinger effect, cyclic softening, cyclic hardening, the shakedown effect and the ratchetting effect (Lemaitre and Chaboche 1990).

Phenomenological models are useful in reliably predicting known material behaviour. The internal state variables are useful when accounting for strain history. Without state variables, it is possible to use the plastic strain as a model parameter to determine the continued flow behaviour. The problem with this approach is that any loading condition may have been taken to reach the same amount of plastic strain, impacting the microstructure, and thus resulting in different material properties. The use of state variables allows for the impact of strain history to be included within the model prediction.

Although other modelling approaches exist, only the yield surface approach proposed by Lemaitre and Chaboche has been reviewed, as this approach has been used to model the cyclical flow behaviour of martensitic tool steel (Bernhart, Moulinier et al. 1999; Zhang, Delagnes et al. 2002; Zhang et al. 2007; Zhang, Bernhart et al. 2008; Krumphals, Reggiani et al. 2012).

Lemaitre and Chaboche (1990) replaced the classical yield surface with an equipotential surface, which allows for the characterisation of flow behaviour through scalar or vector changes to the yield surface. Vector changes are described using kinematic hardening terms whilst scalar changes are made using isotropic terms.

To describe uniaxial plastic deformation, the potential yield surface may be described as a function of stress σ, the isotropic internal variable R, and the kinematic internal variable X. An example of this approach using a power law is given below:

$$\dot{\varepsilon}^p = \left(\frac{|\underline{\sigma} - \underline{X}| - R - k}{K} \right)^n \qquad \textbf{5-1}$$

Where;

σ_0 Stress based material parameter describing resistance to plastic flow

σ Applied stress

k Initial yield strength

n Flow rule exponent

The stress required for deformation to occur is given in equation 5-2. Multiple kinematic and isotropic terms may be used with rate equations to model complex flow behaviour.

$$|\underline{\sigma} - \underline{X}| - R - k > 0 \qquad \textbf{5-2}$$

Bernhart et al (1999) used two kinematic hardening terms to describe the transient and linear work hardening behaviour of H11 hot work tool steel under uniaxial compression.

The cyclical softening behaviour of the material was captured within the isotropic hardening terms. The physical basis for determining such evolution equations is not explicitly accounted for in such models, but is usually linked to a microstructure change during deformation.

Zhang et al (2002) extended the model, capturing the temperature sensitivity of the flow behaviour and modelling the strain amplitude dependence of initial cyclical softening behaviour.

The isotropic hardening material parameters varied linearly with temperature. A quadratic relationship with temperature was required to fit the temperature dependence of material parameters used to describe the initial transient work hardening behaviour and the yield stress.

A strain memorisation term was introduced to capture the dependence of the transient cyclical softening behaviour and the strain amplitude of the fatigue test. Zhang et al (2002) used the accumulated plastic deformation to determine whether to deactivate the transient softening state variable, ending the transient

softening phase. The critical accumulated plastic strain was a function of the strain amplitude.

A third iteration of the model improved upon the strain rate sensitivity of the model predictions as well as introducing thermally induced damage (Zhang, Bernhart et al. 2008). The over-tempering behaviour was determined through hardness measurement and microstructural characterisation (Zhang, Delagnes et al. 2004). A state variable was used to describe the change in hardness from the as-heat treated condition to the annealed condition as shown in equation 5-3.

$$\tau_v = \frac{(HV - H_0)}{(H_\infty - H_0)}$$

5-3

Where;

τ_v Tempering parameter

HV   The current hardness

H_0 The hardness after quenching ($776HV_{0.2}$ for H11)

H_∞ The hardness completely annealed ($210HV_{0.2}$ for H11)

The tempering kinetic law is of Johnson-Mehl-Avrami type and is shown below:

$$\tau_v = 1 - \exp(-(D_o . t)^m)$$

$$D_o. = D_{o,i}. \exp\left(-\frac{Q}{RT}\right)$$

5-4

Where;

t   The tempering time

m   A material dependent (and heat treatment dependent) thermal softening exponent (0.0518 for H11)

$D_{o,i}$ A pre-exponential constant ($2.7 \times 10^8 s^{-1}$ for H11)

Q   The activation energy of the tempering transformation ($231 kJmol^{-1}$)

R   The gas constant

T   The Tempering temperature

The impact of over-tempering upon fatigue behaviour was reported by Zhang et al (2007). Zhang et al (2008) then went on to develop the model to include this behaviour through a tempering dissipation potential that combines with a visco-

plastic dissipation potential to capture strain rate sensitivity. An alternative approach would have been to include the over-tempering behaviour within the yield stress term of the model. The model successfully reproduced the flow stress behaviour.

5.2.1 SUMMARY OF PHENOMENOLOGICAL MODELLING

A phenomenological model has been developed to describe the cyclical plastic flow behaviour of AISI H11 for use in die life prediction. The development of the model has shown that the work hardening may be captured with two variables to describe the transient and linear behaviour. The parameters required a quadratic relationship with temperature. Two state variables were also required to capture the transient and linear cyclical softening behaviour. A linear temperature dependence was required from these parameters. The transient cyclical softening behaviour was related to the accumulated plastic deformation. A single state variable was capable of capturing the over-tempering behaviour of the material.

Phenomenological models are advantageous in their ability to accurately reproduce measured behaviour and thus accurately predict tool life within the conditions used to develop the model.

A disadvantage of phenomenological models is ensuring the suitability of the expressions used to capture behaviour when extrapolating the model. Extrapolation is necessary when applying models developed from isothermal strain controlled fatigue tests to the thermo-mechanical stress controlled fatigue loading descriptive of hot forging tooling.

5.3 PHYSICAL BASED MODELLING APPROACHES

Physical based models provide the potential for increased understanding of material behaviour and for improved extrapolation. The understanding of the material behaviour may guide material selection and heat treatment. Linking material behaviour to microstructural features allows for the description of the scatter in material behaviour resulting from variation in the microstructure. Such variation may include differences in size, shape, or orientation of a key microstructural feature. The difficulty in deriving physical based models is identifying the key microstructural feature and the manner in which the microstructural feature impacts flow behaviour.

The flow rule describes the mechanism which dictates the rate that dislocations flow through the microstructure. In tempered martensite, there are multiple obstacles that impede the motion of dislocations. When determining the mechanism that dictates the behaviour of the material, the frequency in which the obstacle is encountered is considered along with the manner in which dislocations escape the obstacle.

Possible explanations of the work hardening behaviour include plastically hard regions, dislocation pile ups or dislocation multiplication. The mechanism chosen to account for work hardening has implications upon how the fatigue and thermal softening behaviour may be included within the model.

The over-tempering and fatigue behaviour is a result of microstructural instability. Relevant microstructural instabilities that occur in the conditions of interest include particle coarsening, subgrain formation and subgrain coarsening.

Physical based models have been developed to describe creep behaviour of 9-12%Cr tempered martensitic steel used in power generation. It has been shown that physical based creep models may be applied to low cycle fatigue life prediction (Basoalto, Dyson et al. 2002). Krumphals et al (2009) are in the process of applying the physically based model developed by Ghoniem et al (1990) to the thermo-mechanical fatigue life prediction of tempered martensitic under forging tooling conditions.

This section covers potential modelling approaches to capturing the flow behaviour, the work hardening behaviour and key microstructural instabilities.

5.3.1 THE FLOW RULE

Physical based flow rules connect the flow of dislocations through a matrix to the shear strain rate. In such a formulation it is possible to express the plastic strain rate to the material microstructure through identification of the dislocation-structure interactions.

Ghoniem et al (1990) used the Orowan-Bailey relationship to determine the shear strain rate. This requires the explicit calculation of the mean velocity of gliding dislocations. Ghoniem et al (1990) used an empirical approximation of the velocity of glide, accounting for the impact of solute atoms. The yield stress of the material was captured using Orowan, Taylor and frictional threshold stresses. The possibility of dislocation glide being dictated by the cutting of particles was discussed, however doubt exists over whether the particles present are coherent.

Semba (2003) proposed that the rate limiting mechanism in the creep behaviour of tempered martensitic steels is the rate that dislocations climb over subgrain interior particles. Dyson's precipitate strengthening model was applied to tempered martensitic steel to describe this behaviour.

Basoalto (2012) developed an athermal model utilising threshold stresses. The model describes dislocation flow considering dislocation annihilation and dipole formation. These models are now examined in more detail.

5.3.1.1 THE DYSON FLOW RULE

Dyson (2000) modelled the simultaneous climb and glide of dislocations through a two phase system consisting of a plastically soft matrix and non-shearable particles. This model was developed to describe the creep behaviour of precipitate strengthened materials and has been applied to describe the creep behaviour of 9-12% Cr tempered martensitic steels by Semba (2003).

Basoalto (2011) developed an approach for constructing physical based flow rules through considering the continuity equation describing the rate of generation, annihilation and gradients of the dislocations within a representative volume element.

It is possible to construct the Dyson model of precipitate strengthened materials following this approach, assuming the gradient in dislocation density is negligible. The continuity equation is shown in equation 5-5.

$$\frac{\partial \rho_g}{\partial t} = G(\tau, T, \mu) - \rho_g \frac{\bar{v}_g}{\lambda} \qquad \text{5-5}$$

Where;

ρ_g The density of gliding dislocations (m^{-2}).

$G(\tau, T, \mu)$ The rate that dislocations escape the rate limiting obstacle ($\text{m}^{-2}\text{s}^{-1}$).

$\bar{v}_g$ The mean velocity of gliding dislocation (m/ s).

λ The mean free path of gliding dislocations (m).

The steady state condition of equation 5-6 is shown below:

$$\rho_g \bar{v}_g = G(\tau, T, \mu)\lambda \qquad \text{5-6}$$

Multiplying equation 5-6 by the Burger's vector allows the equation to be expressed in terms of the Orowan shear strain rate.

$$\dot{\gamma} = G(\tau, T, \mu)\lambda b \qquad \text{5-7}$$

The rate that dislocations overcome the rate limiting obstacle may be calculated by multiplying the frequency of escape events by the probability of escape events with the potential density of escape events. The potential density of escape events may be approximated by the mobile dislocation density.

$$G(\tau, T, \mu) = \rho_m . P_{[unpinned]} \Gamma_{release} \qquad \text{5-8}$$

Where;

$P_{[unpinned]}$ The probability of escape

$\Gamma_{release}$ The frequency of escape events (1/ s)

The frequency that dislocations are released from particles is given by the velocity of climb divided by the jog spacing. The jog spacing may be approximated by the Burger's vector.

$$\Gamma_{release} = \frac{\bar{v}_c}{b} \qquad \text{5-9}$$

Where;

$\bar{v}_c$ The mean velocity of climbing dislocations (m/ s)

b Burger's vector (m)

The probability of a dislocation encountering a particle may be given by the volume fraction of particles. The probability of the pinned dislocation being in a position ready for escape is given by the fraction of pinned mobile dislocations that are in a position where they can escape. This fraction is described by the jog spacing divided by the particle radius. The jog spacing may be approximated from the Burger's vector.

$$Probability\ of\ a\ mobile\ dislocation\ interacting\ with\ a\ particle = \ \phi_p \qquad \textbf{5-10}$$

$$Probability\ of\ a\ pinned\ dislocation\ being\ in\ a\ favourable\ location\ for\ escape = \frac{b}{r_p} \qquad \textbf{5-11}$$

Where;

ϕ_p Particle volume fraction

r_p Particle radius (m)

The multiplication of these probabilities determines the likelihood that a mobile dislocation is pinned by a particle and in a position where it may escape through climb.

$$P_{[unpinned]} = \phi_p.\frac{b}{r_p} \qquad \textbf{5-12}$$

The mean velocity of climb, $\bar{v}_c$, is proportional to the process of diffusion, the jog density and the work required to move the dislocation past the obstacle as shown in equation 5-13.

$$\bar{v}_c \propto D_d c_j \left\{ exp\left(\frac{\tau b^2 \lambda_p}{kT}\right) - 1 \right\}$$

$$D_d.C_j = D_{di0}.c_{ji0}\, exp\left(-\frac{Q_{j,i}}{RT}\right) \qquad \textbf{5-13}$$

Where;

D_{di0} Volume diffusion coefficient (m^2s^{-1})

c_{ji0} Jog density (m^{-2})

k Boltzmann constant ($m^2kgs^{-2}K^{-1}$)

$Q_{j,i}$ Activation energy for diffusion and jog formation ($kJmol^{-1}$)

R Gas constant (JK-1mol-1)

Considering that a dislocation may jump away from the escape location or jump towards the escape location, equation 5-13 may be expressed as shown in equation 5-14.

$$\bar{v}_c = \frac{D_d C_j}{b} \sinh\left(\frac{\tau b^2 \lambda_p}{kT}\right)$$ **5-14**

$$D_d . C_j = D_{di0} . c_{ji0} \, exp\left(-\frac{Q_{j,i}}{RT}\right)$$ **5-15**

The mean free path is given by the particle spacing. The particle spacing differs depending upon the particle shape. The MX particles within the subgrain interior may be assumed to be spherical. This assumption is not entirely accurate; Bischof et al (2008) describe the subgrain interior MX particles as oblate and the M_2C particles as prolate in shape. The spacing may be approximated assuming lattice square spacing as shown in equation 2-6.

The flow rule may now be derived from substituting equations 2-6, 5-14 and 5-12 into equation 5-7.

$$\dot{\gamma} = \rho_m . \phi_p . D_{di0} . c_{ji0} \, exp\left(-\frac{Q_{j,i}}{RT}\right) \sinh\left(\frac{\tau b^2 \lambda_p}{kT}\right) 2\sqrt{2/3}\left(\sqrt{\frac{\pi}{4\phi_p}} - 1\right)$$ **5-16**

The Taylor factor may be used to scale up equation 5-16 to describe macro-scale strain. The Taylor relationships between macro-stress with shear stress and macro-strain and shear-strain are shown in equation set 5-17.

$$\tau = \frac{\sigma}{M}$$

$$\dot{\varepsilon}_p = \frac{\dot{\gamma}}{M}$$ **5-17**

Where;

M Taylor factor

τ Internal shear stress (MPa)

σ External stress (MPa)

Applying this relationship to equation 5-16 gives the following flow rule.

$$\dot{\varepsilon}_p = \frac{1}{M} \cdot \rho_m \cdot \phi_p \cdot D_{di0} \cdot c_{ji0} \, exp\left(-\frac{Q_{j,i}}{RT}\right) \sinh\left(\frac{(\sigma - \sigma_k)b^2\lambda_p}{MkT}\right) 2\sqrt{2/3}\left(\sqrt{\frac{\pi}{4\phi_p}} - 1\right)$$ **5-18**

This equation may be simplified by grouping terms shown in equation set 5-19.

$$\dot{\varepsilon}_p = \dot{\varepsilon}_0^i \sinh\left(\frac{\overline{\sigma}}{\sigma_0}\right)$$

$$\dot{\varepsilon}_0^i = \frac{1}{M} 2\rho_m\sqrt{2/3}\left(\sqrt{\frac{\pi}{4\phi_p}} - 1\right)\phi_p \cdot D_{di0} \cdot C_{ji0}\, exp\left(-\frac{Q_{j,i}}{RT}\right)$$ **5-19**

$$\sigma_0 = \frac{MkT}{b^2\lambda}$$

Where;

ε_0 Stress independent term

$\overline{\sigma}$ The effective stress considering back stresses (MPa)

σ Applied stress (MPa)

σ_k Kinematic back stresses (MPa)

σ_0 Orowan resistance to obstacle bypass (MPa)

M Taylor factor

ρ_m Mobile dislocation density (m^{-2})

r_p Average MX and M$_2$X particle radius (m)

ϕ_{pmx} Volume fraction of MX and M$_2$X particles

D_{di0} Diffusion constant of the matrix (m^{2}s^{-1})

C_{ji0} Jog density coefficient (m^{-2})

$Q_{j,i}$ Activation energy for diffusion and jog formation (kJmol^{-1})

R Gas constant (JK^{-1}mol^{-1})

T Temperature (K)

k Boltzmann constant (m^{2}kgs^{-2}K^{-1})

λ_{MX} Spacing of MX and M2X particles (m)

b Burgers vector (m)

The temperature dependence of in the σ_0 term is complicated. The parameter is a function of if the spacing of the pinning obstacle. The spacing of the pinning obstacle must increase with temperature to describe the observed temperature sensitivity of the material. Semba et al (2005) estimated the value of σ_0 from analysing the minimum creep rate from experimental data using equation 5-20.

$$\sigma_0 = \frac{1 - H^*}{2.3 \frac{d\dot{\varepsilon}_{min}}{d\sigma}}$$
     5-20

Dyson (2000) gives the following empirical relationship that may be used to capture the temperature dependence of the term σ_0.

$$\sigma_0 = \sigma_{0,m} \left[1 - \left(exp\left(\frac{T_s}{T} - 1 \right) \right) \right]$$
     5-21

Where;

$\sigma_{0,m}$ Maximum σ_0 (MPa)

T_s Solvus temperature (K)

T Temperature (K)

Dyson (2009) proposed an alternative approach that explicitly models the temperature dependence of the volume fraction of particles. This approach is shown in equation set 5-22.

$$C_e = exp\left(\frac{dS}{R}\right) \times exp\left(-\frac{dHs}{RT}\right)$$

$$C_o = exp\left(\frac{dS}{R}\right) \times exp\left(-\frac{dHs}{RT_s}\right)$$ **5-22**

$$\phi_p = \frac{(C_o - C_e)}{(C_\# - C_e)}$$

Where;

T_s The solvus temperature (K)

dS Entropy of mixing (J/ mol)

dHs Enthalpy of solute (J/ mol)

C_o Concentration of precipitate forming elements (m^{-3})

C_e The equilibrium concentration of precipitate forming elements for a given temperature (m^{-3})

$C_\#$ A material constant (~0.25)

The volume fraction of particles and particle radii are related as shown in equation 5-23.

$$\phi_{pmx} \propto r_p{}^3$$ **5-23**

The volume fraction of particles and average radii of particles for room temperature and high temperature may be expressed using a coefficient, k_*.

$$\phi_{p,rt} = k_* r_{p,rt}{}^3$$ **5-24**

$$\phi_{p,ht} = k_* r_{p,ht}{}^3$$ **5-25**

Where;

$r_{p,rt}$ Average particle radius at room temperature

$r_{p,ht}$ Average particle radius at high temperature

$\phi_{p,rt}$ Volume fraction of particles at room temperature

$\phi_{p,ht}$ Volume fraction of particles at high temperature

The relationship relating the volume fraction of particles and the average radii of particles may be determined by dividing equation 5-24 by equation 5-25 and

rearranging for the particle radii at elevated temperature. This is shown in equation 5-26.

$$r_{p,ht} = r_{p,rt} \left(\frac{\phi_{p,ht}}{\phi_{p,rt}} \right)^{\frac{1}{3}}$$

5-26

Kadoya et al (2002) used the software Thermo-Calc to estimate the volume fraction of MX particles with temperature. Figure 5-1 shows the result of fitting equation set 5-22 to this behaviour.

The temperature of interest regarding tooling ranges from between 240°C to 650°C. In this temperature range the volume fraction of MX particles does not change significantly when examining Kadoya et al's (2002) data.

This model is useful for describing the flow behaviour of a material that consists of a plastically soft matrix and non-shearable particles. The model is applicable to the situation where it is more preferable for dislocations to escape particles through climbing over the particles opposed to Orowan bowing around the particles.

FIGURE 5-1: TEMPERATURE DEPENDENCE OF THE VOLUME FRACTION OF MX PARTICLES
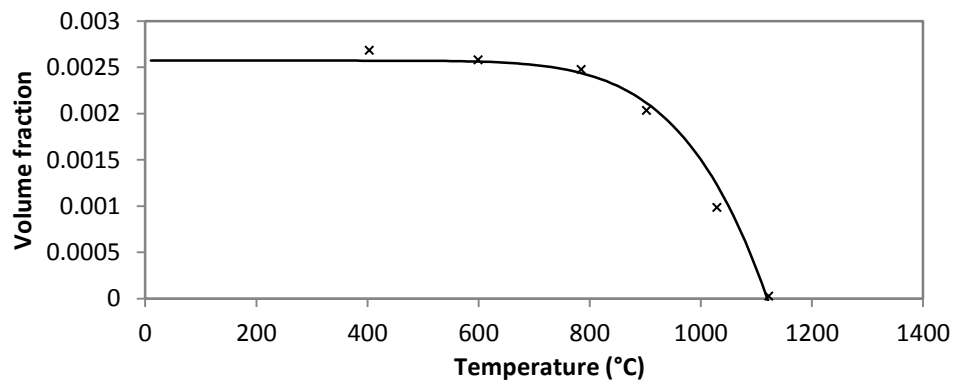
dS	dHs	C#	Co
25	108000	0.7	0.0018

5.3.1.2 THE GHONIEM, MATTHEWS AND AMODEO FLOW RULE

Ghoniem et al (1990) used the Orowan-Bailey relationship to calculate the plastic shear rate. This approach requires the explicit calculation of the average velocity of gliding dislocations. An empirical description of the gliding velocity considering solute atom interference is given in equation 5-27.

$$\bar{v}_g = a_1 exp\left(-\frac{W_g}{kT}\right)\frac{\sigma_c\Omega}{kT}$$
                                                              5-27

Where;

W_g, a_1 Calibration parameters

σ_c The effective stress (MPa)

Ω Atomic volume ($1.19 \times 10^{-19} m^3$)

Q_g Thermal activation energy ($kJmol^{-1}$)

This approach assumes that the velocity of dislocation glide is given by the interaction between mobile dislocations and solute atoms.

Ghoniem et al (1990) use threshold stresses to predict appropriate yield stress from the model. An Orowan bypass stress is used to account for the combined spacing of particles and dislocations. A Taylor stress is used to account for mobile dislocation interaction. A frictional resistive threshold stress is also included. Equation 5-28 shows the effective stress within the model.

$$\sigma_{eff} = \sigma - \sigma_{Oro} - \sigma_{Tay} - \sigma_0$$
                                                              5-28

Where;

σ_{eff} The effective stress

σ The applied stress

σ_{Oro} The internal Orowan stress of obstacle bypass

σ_{Tay} The internal Taylor stress of dislocation interaction between mobile and pinned dislocations

σ_0 A frictional stress that is fitted to the model based upon the resistance measured in a fully annealed microstructure

The microstructural instabilities of interest change the magnitude of these threshold stresses, describing the behaviour of interest. Work hardening is captured through the increase in the Taylor back stress resulting from dislocation pile ups. It is difficult to predict strain rate sensitivity utilising threshold stresses to obtain yield behaviour.

5.3.1.3 THE BASOALTO FLOW RULE

The athermal flow behaviour of bcc or fcc materials may be described using an approach developed by Basoalto (2012). The flow rule is reached considering the steady state of dislocation multiplication and annihilation, without requiring the explicit calculation of the mean velocity of gliding dislocations. The change in mobile dislocation density for a given increment of plastic strain is shown in equation 5-29 (Kocks et al. 1975).

$$\dot{\rho}_m = \dot{\rho}^+_{mobile} - \dot{\rho}^-_{DP} \qquad\qquad \textbf{5-29}$$

Where;

$\dot{\rho}^+_{mobile}$ The rate of dislocation multiplication

$\dot{\rho}^-_{DP}$ The rate of dislocation annihilation

Dislocations are assumed to multiply through Frank-Read sources. There are many length scales that Frank-Read sources may operate. Greater stress is required to activate smaller sources, due to the increase in dislocation line tension. It may be assumed that the majority of generated dislocations are formed from larger scale sources. The likely length scales for Frank-Read sources to operate upon in tempered martensitic materials include subgrain boundaries and the mobile dislocation network.

The rate that dislocations are generated through Frank-Read sources is given by the number of sources operating multiplied by the frequency in which they produce dislocations.

$$\dot{\rho}^+_{mobile} = \rho_s \frac{\bar{v}}{L} \qquad\qquad \textbf{5-30}$$

Where;

$\bar{v}$ The mean velocity of mobile dislocations (ms^{-1})

ρ_s The density of Frank-Read sources operating (m^{-2})

L The length scale at which the Frank-Read sources operate (m)

It may be assumed that the majority of generated dislocations arise from Frank-Read sources that act upon the mobile dislocation network. The fraction of the mobile dislocation network acting as a source is given in equation 5-31.

$$\rho_s \approx k_a . \rho_m \qquad \textbf{5-31}$$

Where;

k_a A constant describing the fraction of sources operating

The length scale that the Frank-Read source operates may be estimated by the spacing of the total dislocation network.

$$L = \frac{1}{\sqrt{\rho_m}} \qquad \textbf{5-32}$$

The stress fields of neighbouring dislocations may either increase or reduce the length scale at which the source operates. A coefficient β is used to account for this affect.

$$L = \frac{\beta}{\sqrt{\rho_m}} \qquad \textbf{5-33}$$

The generation of dislocations through a Frank-Read source may be approximated by substituting equations 5-31 and 5-33 into equation 5-30 to reach the following equation, as shown by (Weertman and Weertman 1980).

$$\rho_{mobile}^{+} = k_a \rho_m^{3/2} \frac{\bar{v}}{\beta} \qquad \textbf{5-34}$$

The work hardening rate of hot work tool steels is observed to reduce with continued plastic strain. If the work hardening behaviour arises from dislocation multiplication, there must be a recovery process limiting the dislocation density. This may be described through dislocation annihilation.

The impact of dislocation annihilation may be taken into account through modelling the rate that dislocation dipole pairs are formed from mobile dislocations. It is assumed that potentially all mobile dislocations may form a dipole attraction. The frequency that a dipole attraction may be formed is given by the rate that mobile dislocations pass neighbouring mobile dislocations with opposite Burgers vector. This is shown in equation 5-35 (Weertman and Weertman 1980).

$$\bar{\rho_{DP}} = \rho_m \frac{\bar{v}}{\lambda_m}$$

5-35

Where;

λ_m The distance between dislocations of opposing Burger's vector travelling upon the same slip system

The separation between the passing dislocations determines whether the dipole attraction is sufficient to pin the dislocations and allow for dislocation annihilation. The spacing between two mobile dislocations of opposing Burgers vector that are gliding upon similar slip systems may be considered. Figure 5-2 illustrates the dislocations.
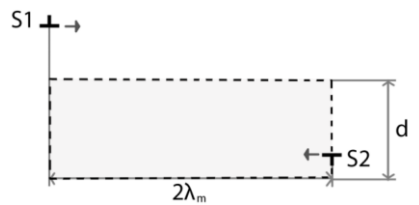
FIGURE 5-2: DISLOCATION DIPOLE FORMATION

The distance between the two dislocations is given by $2\lambda_m$ and the separation between the two dislocations is given by d. The area that captures dislocation annihilation is given by $2\lambda_m d$. The distance of d is determined by the mobile dislocation density so that the area of consideration captures the kinetics of a single dislocation whilst forming a dipole.

$$\rho_m(2\lambda_m d) = 1$$

5-36

The internal stress from a dislocation dipole is given in equation 5-37 (Hull and Bacon 2001).

$$\tau_{dipole} = \frac{Gb}{2\pi(1-v)}\frac{1}{d}$$

5-37

For the dipole to exist for long enough for annihilation to occur the dipole stress must be greater than the effective shear stress of the matrix.

$$\tau_{dipole} \gg \tau - \tau_k$$

5-38

Equation 5-36 may be rearranged for the distance d, and substituted into equation 5-37. Equation 5-38 may also be substituted into this expression.

$$\tau - \tau_k \ll \frac{Gb}{\pi(1-v)}\rho_m\lambda_m$$

5-39

The minimum spacing for a dipole to form may be expressed by rearranging equation for λ_m.

$$\lambda_m \gg \frac{(\tau - \tau_k)\pi(1-v)}{Gb\rho_m}$$

5-40

The Taylor factor may be introduced to scale up equation 5-40 so that it is in terms of macro-stress. This expression may be substituted into equation 5-35 to determine the rate of dislocation annihilation considering the formation of dislocation dipoles.

$$\rho^-_{DP} = \bar{v}\rho_m{}^2\frac{GbM}{(\sigma - \sigma_k)\pi(1-v)}$$

5-41

The change in mobile dislocation density considering dislocation generation and annihilation is given in equation 5-42.

$$\dot{\rho}_m = k_a\rho_m{}^{3/2}\bar{v} - \pi(1-v)\rho_m{}^2\frac{GbM}{\bar{\sigma}}\bar{v}$$

5-42

The steady state condition may be examined where the rate of dislocation generation balances the rate of dipole formation. This expression may be rearranged for the mobile dislocation density as shown in equation 5-43.

$$\rho_m = \left(\frac{k_a}{\pi(1-v)}\frac{\bar{\sigma}}{GbM}\right)^2$$

5-43

Basoalto (2012) developed a flow rule considering the steady state of dislocation multiplication and annihilation. Equation 5-44 was multiplied by the velocity of dislocation glide and the Burger's vector. The Orowan-Bailey shear strain relationship was then used to obtain an equation in terms of the shear strain rate. The Taylor factor was used to scale up to macro-strain resulting in equation 5-44.

$$\dot{\varepsilon}_{p,a} = \frac{b}{M} \left(\frac{k_a}{\pi(1-v)} \frac{\bar{\sigma}}{GbM} \right)^2 \bar{v} \qquad\qquad \textbf{5-44}$$

The velocity of dislocation glide may be approximated from the drag coefficient as shown in equation 5-45 with a drag coefficient of 4.5×10^{-5}Pas descriptive of dislocation kink motion in a BCC lattice (Cai et al. 2001).

$$\bar{v} = \frac{b\tau}{B} \qquad\qquad \textbf{5-45}$$

The shear stress in Equation 5-45 may be replaced with the effective shear stress and scaled up using the Taylor factor. This equation may be substituted into equation 5-44 to obtain the following athermal flow rule:

$$\dot{\varepsilon}_{p,a} = \frac{b^2}{M^2 B} \left(\frac{k_a}{\pi(1-v)} \frac{\bar{\sigma}}{GbM} \right)^2 \bar{\sigma} \qquad\qquad \textbf{5-46}$$

The effective stress accounts for the relevant threshold stresses. This equation may be used to describe the athermal flow behaviour of tempered martensitic steels. The model includes threshold stresses that may arise from precipitates, subgrains, solute atoms and\ or dislocations (Abe 2008).

5.3.1.4 SUMMARY OF PHYSICAL BASED FLOW RULES

The flow rule is obtained through consideration of the rate limiting process that dictates the flow of dislocations resulting in plastic strain. The flow rules reported have been developed to describe the creep behaviour of tempered martensitic steels. The approaches taken differ significantly.

Semba (2003) modelled the rate limiting process of dislocation flow as the rate that dislocations climb over the subgrain interior particles. Climb driven flow behaviour is not suitable for describing low temperature behaviour of tempered martensitic steel. It is likely that a different mechanism dictates this behaviour.

Ghoniem et al (1990) modelled the rate limiting mechanism as the velocity of dislocations gliding through the matrix. Threshold stresses are required to describe the measured yield behaviour.

The Dyson and Ghoniem flow rules have been developed to describe creep behaviour. To describe athermal behaviour, the model outlined by Basoalto (2012) is relevant.

The appropriate flow rule captures the mechanism that restricts the flow of dislocations for the conditions of interest. The mechanism may change over the conditions of interest.

5.3.2 WORK HARDENING

Tempered martensitic hot work tool steels significantly work harden during plastic deformation. The work hardening is observed to plateau and is temperature sensitive.

There are numerous approaches that may be adopted to describe work hardening within a physical based model. Possible approaches include plastically hard regions, dislocation multiplication and dislocation pile ups. These approaches are examined in the following section.

5.3.2.1 PLASTICALLY HARD REGIONS

The work hardening may be explained through the presence of plastically hard regions found within a heterogeneous microstructure. Sources of heterogeneity include different phases and differently orientated grains. The difference in mechanical response between regions results in stress transfer from the soft region to the hard region.

Examples of hard regions include hard phases, subgrain boundaries, and differently orientated grains. Within a polycrystalline material the distribution in grain orientations results in a distribution in Schmidt factors. The grains of low Schmidt factor require greater stress for deformation to occur, compared to grains better orientated with the loading direction.

The work hardening results from the additional stress required to deform the plastically hard grains to achieve compatible deformation. The limit to the work

hardening may be caused by the hard region deforming plastically, or through plastic punching.

The two-bar composite model may be used to model the rate that stress is transferred from the soft region to the hard region. Potential plastically hard regions within a tempered martensitic microstructure include the non-deforming particles, misaligned subgrains/laths and the subgrain/lath boundaries, as illustrated in Figure 5-3.
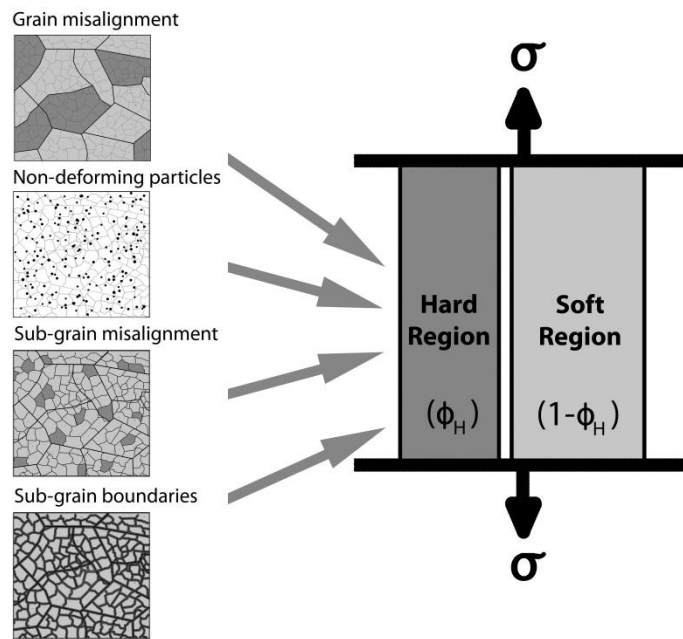
FIGURE 5-3: HARD REGIONS WITHIN A TEMPERED MARTENSITIC MICROSTRUCTURE

The rate of work hardening may be formulated considering the stress transfer between hard and soft regions of different elastic modulus. The Young's modulus of the material is described as shown in equation 5-47.

$$E_S \phi_S + E_H \phi_H = E \qquad \text{5-47}$$

Where;

E_S, E_H, E The elastic modulus of the soft region, hard region and bulk respectively (Pa).

ϕ_S, ϕ_H The volume fraction of soft and hard regions.

170

It may be assumed that the effective stress rate applied to the material is the sum of the contribution of local stress rate experienced within each region.

$$\dot{\sigma}_S \phi_S + \dot{\sigma}_H \phi_H = \dot{\sigma} \qquad \text{5-48}$$

The total strain rate within the regions may be expressed as the sum of elastic and plastic contributions.

$$\dot{\varepsilon}^T = \frac{\dot{\sigma}}{(E_S \phi_S + E_H \phi_H)} + \frac{E_S}{(E_S \phi_S + E_H \phi_H)} \dot{\varepsilon}^{P,S} \phi_S \qquad \text{5-49}$$

This allows for equation 5-49 to be simplified as shown below:

$$\dot{\varepsilon}^T = \frac{\dot{\sigma}}{E} + \frac{E_S}{E} \dot{\varepsilon}^{P,S} \phi_S \qquad \text{5-50}$$

A simple approach may be taken to account for the difference in elastic modulus between a hard and soft region. A constant may be used to express the difference between the elastic modulus in the soft region and the Young's modulus. This constant is given by K_E as shown below:

$$E_S = K_E E \qquad \text{5-51}$$

Substituting equation 5-51 into equation 5-47 obtains the following equation:

$$E_H = \frac{E(1 - K_E \phi_S)}{\phi_H} \qquad \text{5-52}$$

Substituting equation 5-52 into equation 5-50 results in the following equation that may be used to calculate total strain:

$$\dot{\varepsilon}^T = \frac{\dot{\sigma}}{E} + K_E \dot{\varepsilon}^{P,S} \phi_S \qquad \text{5-53}$$

The local stress of the soft region is given by the sum of the internal stresses applied to the hard regions subtracted from the effective stress.

$$\sigma_S = \sigma - \sigma_H \qquad \text{5-54}$$

There is a limit to the stress that may be transferred to the hard region, as shown in Figure 5-4.
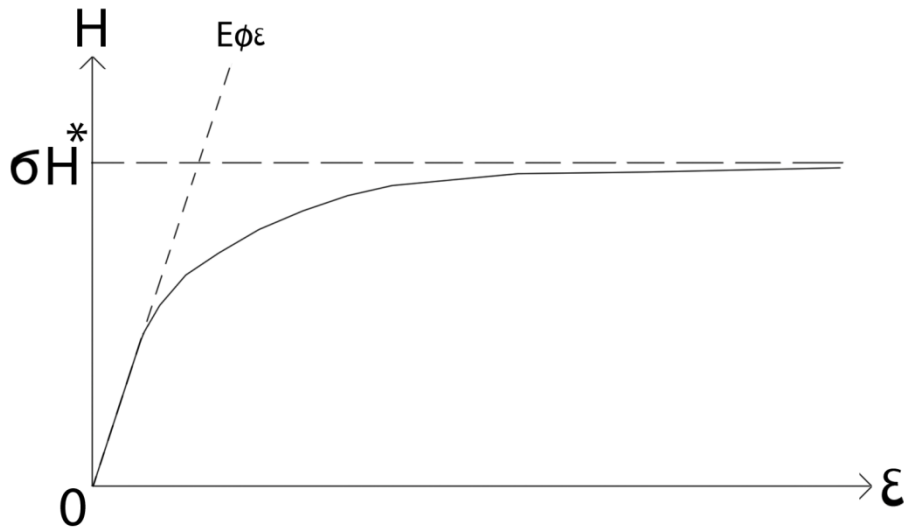
FIGURE 5-4: THE EVOLUTION OF THE KINEMATIC BACK STRESS ARISING FROM HARD REGIONS

A recovery mechanism limits the stress that may be transferred to plastically hard regions. This recovery term may be described as shown in equation 5-55.

$$\dot{\sigma}_k = E_H \phi_H \dot{\varepsilon}_p - \sigma_k A_p \dot{\varepsilon}_p \qquad \text{5-55}$$

Where;

A_p Recovery rate constant (s^{-1})

σ_k Kinematic back stress (Pa)

The first part of equation 5-55 is the internal stress caused by the elastic deflection of the hard region for a given increment of plastic deformation of the soft region. The second part describes the rate at which the stress limit of the hard region is reached. This equation may be rearranged as shown below:

$$\dot{\sigma}_k = E_H \phi_H \left(1 - \frac{A_p \sigma_k}{E_H \phi_H} \right) \dot{\varepsilon}_p \qquad \text{5-56}$$

The limit to the stress that may be transferred to the hard region may be given by equation 5-57.

$$\sigma_{k,max} = \frac{E_H \phi_H}{A_p} \qquad \text{5-57}$$

The maximum stress transferred to the hard region may be normalised against the applied stress, as shown below:

$$H^* = \frac{\sigma_{k,max}}{\sigma} \qquad \text{5-58}$$

Substituting H^*, equations 5-58 and 5-57 into 5-56 gives the following equation: This may be described with the following expression (Dyson 2000):

$$\dot{\sigma}_k = E_H \phi_H \left(1 - \frac{\sigma_k}{\sigma H^*}\right) \dot{\varepsilon}_p \qquad \text{5-59}$$

Semba (2003) describes the limit for stress transfer through the mechanism of plastic punching around spherical shaped obstacles. This is shown in equation 5-60.

$$H^* = \frac{2\phi_H}{1 + 2\phi_H} \qquad \text{5-60}$$

This equation has been derived from the observed behaviour where the stress in a hard region cannot be greater than three times the stress in the soft region. The impact of the kinematic back stress may be included within the effective stress describing the stress within the plastically soft matrix phase.

Semba (2003) proposed that the work hardening in tempered martensitic steels is caused by plastically hard subgrain boundaries and that the limit to stress transfer to these boundaries is limited by plastic punching of spherical particles. This modelling approach is shown in equation set 5-61.

$$\dot{\sigma}_{sgb} = \acute{h}_{sgb}\left(1 - \frac{\sigma_{sgb}}{\sigma H^{*}_{sgb}}\right)\dot{\varepsilon}$$

$$\acute{h}_{sgb} = E.\phi_{sgb}$$

$$H^{*}_{sgb} = \frac{2\phi_{sgb}}{1 + 2\phi_{sgb}}$$

5-61

$$\phi_{sg} = \frac{2w}{\lambda_{sg}}$$

Where;

ϕ_{sgb} The volume fraction of subgrain boundaries

w The subgrain boundary thickness

λ_{sg} The subgrain boundary spacing

Semba and Dyson (2005) modelled the work hardening of tempered martensitic steel where the subgrain boundaries had a volume fraction of approximately a third. The thickness of the subgrain boundaries was not mentioned.

5.3.2.2 DISLOCATION MULTIPLICATION

The work hardening behaviour may be explained by a rise in dislocation density within the subgrain interior resulting in a greater Taylor back stress. The competing mechanism of dislocation annihilation may explain the reduction in work hardening rate observed in tool steels.

The rate of change in mobile dislocation density may be determined through modelling dislocation multiplication and annihilation, as described in equation 5-42. This equation may be rearranged to obtain equation set 5-62.

$$\rho_{sat} = \left(\frac{(\sigma - \sigma_k)}{G}\frac{\pi(1-v)}{bM}\right)^2$$

5-62

$$\dot{\rho_m} = \frac{M}{b}\rho_m^{1/2}\left(\frac{k_a}{\beta} - \left(\frac{\rho_m}{\rho_{sat}}\right)^{1/2}\right)\dot{\varepsilon}_p$$

This approach allows for the calculation of the change in mobile dislocation density until the rates of generation and dipole formation balance.

5.3.2.3 DISLOCATION PILE UPS

Dislocation pile ups can result in work hardening. Uncertainty exists regarding the precise process describing how mobile dislocations interact with subgrain boundaries. Figure 5-5 highlights the possible flow behaviour.
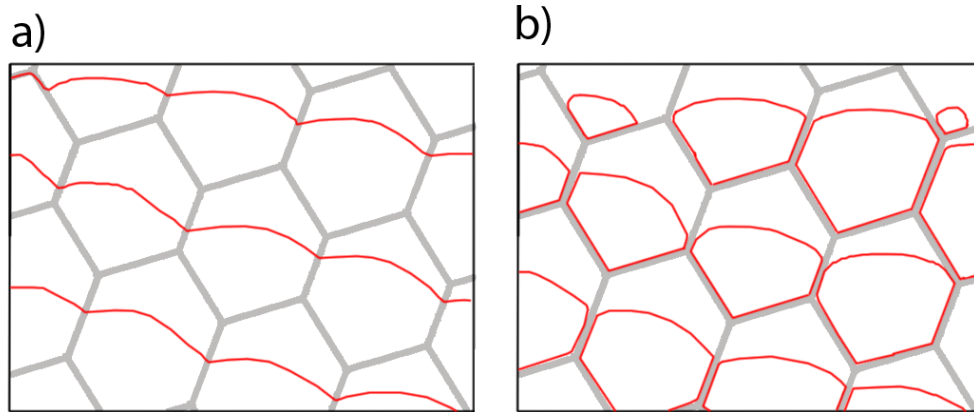
FIGURE 5-5: DISLOCATION GLIDE WITHIN A DISLOCATION STRUCTURE

Figure 5-5 a) is similar to the process described by Mughrabi (1983) and Sedlacek (1995) where mobile dislocations travel through the subgrain boundaries but experience higher resistance due to the higher dislocation density. This approach assumes that the lattice misorientation between neighbouring subgrains is small. The interaction between gliding dislocations and subgrain boundary dislocations is not considered significant.

Figure 5-5 b) shows the case where the travel of mobile dislocations is limited to subgrain interiors. Mobile dislocations are either emitted or generated from subgrain walls. Kuhlmann-Wilsdorf (2001) illustrate this process, as shown in Figure 5-6.
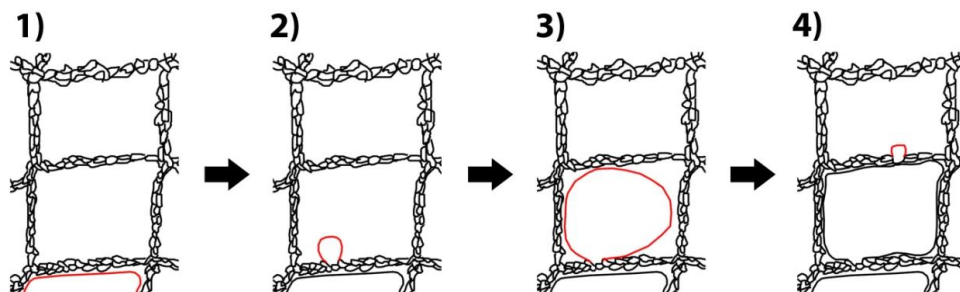
FIGURE 5-6: DISLOCATION GLIDE IN A DISLOCATION STRUCTURE (KUHLMANN-WILSDORF 2001)

Figure 5-6 shows mobile dislocations in red. In step 1 a mobile dislocation becomes immobilised by the subgrain boundaries. In step 2 a dislocation link of the subgrain boundary escapes into the subgrain interior. In step 3 the mobile dislocation has become pinned by the subgrain boundaries. In step 4 the process repeats in an adjacent subgrain.

If dislocation pile ups explain the work hardening behaviour of tool steels, there must be a recovery process that limits the immobilised dislocation density. The rate that mobile dislocations become immobilised by subgrain boundaries may be calculated using equation 5-63.

$$G_{wall}^{+} = \rho_m \frac{\bar{v}_g}{\lambda_{sg}}$$

5-63

Ghoniem et al (1990) modelled static and dynamic recovery of the immobile dislocations, as shown in equation set 5-64.

$$G_{static}^{-} = 8\rho_{pin} \frac{\bar{v}_{cP}}{h}$$

5-64

$$G_{dynamic}^{-} = \delta\rho_m\rho_{pin}\bar{v}_g$$

Where

ρ_{pin} The dislocation density immobilised by subgrain boundaries (m^{-2})

h The dipole spacing (m)

$\bar{v}_{cP}$ The velocity of climb (m/ s)

δ A length parameter related to the separation distance between dislocations resulting in spontaneous annihilation (m)

The dynamic and static recovery of the immobilised dislocation density may explain the reduction in work hardening rate observed in the flow behaviour of tempered martensitic steels.

5.3.2.4   SUMMARY OF WORK HARDENING APPROACHES

Possible approaches to modelling work hardening behaviour include plastically hard regions, dislocation multiplication and dislocation pile ups. To capture the

work hardening behaviour of interest the work hardening rate has to start high and reduce to a steady state. Other considerations include whether the work hardening model captures impact of reversal of loading direction relevant to fatigue loading.

5.3.3 PARTICLE COARSENING

There are numerous ways in which particles have been suggested to act as strengthening features within tempered martensite. Semba (2003) modelled the process where mobile dislocations become pinned by the small MX particles found within subgrain interiors. Ghoniem et al (1990) included an Orowan threshold stress where particles are included when calculating the obstacle spacing. Abe (2008) and Ghoniem et al (1990) suggests that the subgrain boundary particles impede subgrain boundary migration. Ashby (1970) proposed that such particles may be treated as plastically hard regions which do not deform with the rest of the matrix.

The precipitates coarsen through diffusion. Diffusion may occur more quickly at locations with increased density of vacancies, such as grain boundaries or areas of high dislocation density. Semba (2003) reviewed the different mathematical expressions for describing diffusion depending upon the rate controlling mechanism. These models are given in Table 5-2.

Although each mechanism shown in Table 5-2 may be occurring, only one mechanism dictates the rate of diffusion when considering a specific type of particle.

The mechanisms that have been reported to occur within the coarsening of subgrain interior particles in tempered martensitic steel include volume diffusion and dislocation pipe diffusion (Kadoya, Dyson et al. 2002; Semba 2003).

Equation set 5-65 may be used to describe particle coarsening with different exponents for volume diffusion or dislocation pipe diffusion (Semba 2003). An m value of 3 relates to volume diffusion whilst a value of 5 describes dislocation pipe diffusion.

TABLE 5-2: DIFFUSION MODELS EXAMINED BY SEMBA (2003)

Rate controlling mechanism	Model	Author
Volume diffusion	$$r^3 - r_o^3 = \frac{8K_m\gamma CD\Omega}{9RT}t$$ $$D = D_o\exp\left(-\frac{Q_{vd}}{RT}\right)$$ $$C = C_o\exp\left(-\frac{Q_{solute}}{RT}\right)$$	Wagner (1961)
Grain boundary diffusion	$$r^4 - r_o^4 = \frac{8K_mD_gC\omega\gamma\Omega}{32ABkT}t$$ $$A = \frac{2}{3}\frac{\gamma_{gb}}{2\gamma} + \frac{1}{3}\left(\frac{\gamma_{gb}}{2\gamma}\right)^3$$ $$B\sim\ln(L/r)$$ $$D_g = D_{go}\exp\left(-\frac{Q_{bdg}}{RT}\right)$$ $$C = C_o\exp\left(-\frac{Q_{solute}}{RT}\right)$$	Kirchner (1971)
Dislocation pipe diffusion	$$r^5 - r_o^5 = \frac{K_mCD_dq\gamma N\Omega^2}{RT}t$$ $$D_d = D_{go}\exp\left(-\frac{Q_{dpd}}{RT}\right)$$ $$C = C_o\exp\left(-\frac{Q_{solute}}{RT}\right)$$	Ardell (1972)

Where;

r	Particle radius (m)
r_o	Initial radius (m)
K_m	Proportionality constant
γ	Interfacial energy between the particle and the matrix (J)
γ_{gb}	Surface free energy per unit area of the grain boundary (j)
C	The solute concentration (m^{-3})
D, D_o, D_g, D_d	Diffusion coefficient (m^2/ s, m^3/ s, m^4/ s)
Ω	The atomic volume (m^3)
ω	Grain boundary width (m)
L	Grain size (m)
q	Cross sectional area of the dislocation pipe diffusion path (m^2)
N	The total number of dislocations intersecting each particle
R	The perfect gas constant

T Absolute temperature (K)

t Time (s)

K Coefficient describing diffusion

$$\dot{r}_p = \frac{K}{m{r_p}^{m-1}}$$

$$K = K_0 exp\left(\frac{Q_c}{RT}\right)$$

5-65

Where;

r_p The initial average particle radius (m)

K_0 Diffusion based constant (m^{2}s^{-1} or m^{4}s^{-1})

Q_c Activation energy (kJmol^{-1})

Zhang et al (2004) measured intra-lath particle sizes in over-tempered specimen of AISI H11 hot work tool steel. Equation set 5-65 has been applied to predict the rate of coarsening from measurements taken from these studies using different diffusion kinetics. Figure 5-7 shows the modelling results when considering volume diffusion and Figure 5-8 shows the results for dislocation pipe diffusion. Two error bars are included in the results. The smallest describes the 99% confidence level and the largest describes the standard deviation from the measurements.

It is known that the rate of thermal softening when considering the reduction in hardness is small at the temperature of 500°C for the timescales of interest. It is assumed that at this temperature the model should not predict a significant change in particle radius. Reasonable value for the thermal activation of volume diffusion ranges from between 240kJ to 300kJ (Semba 2003). The thermal activation measured for dislocation pipe diffusion has been estimated to be in the region of 160kJ (Kadoya, Dyson et al. 2002). The temperature sensitivity observed in the particle coarsening behaviour is better described by volume diffusion.

Data source: Zhang et al (2004)	r_i	K_0	Q_p	m
Volume diffusion	30	5×10^{-13}	240	3
	nm	$m^2 s^{-1}$	kJ	
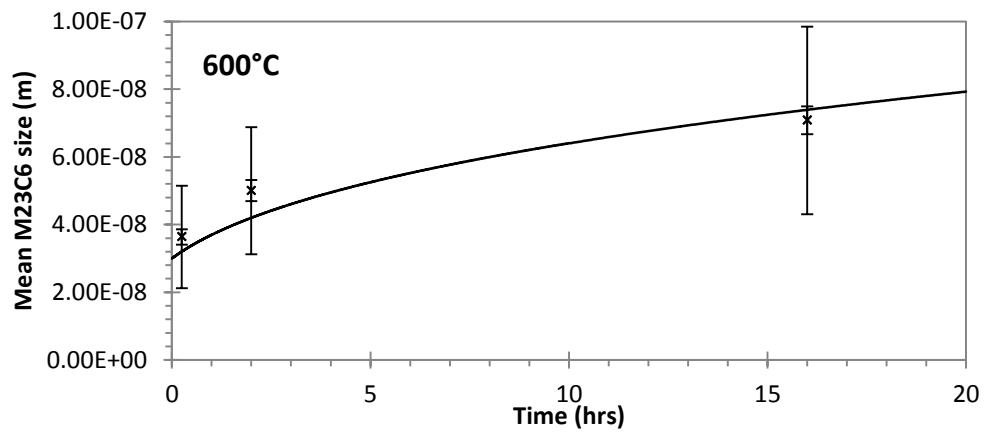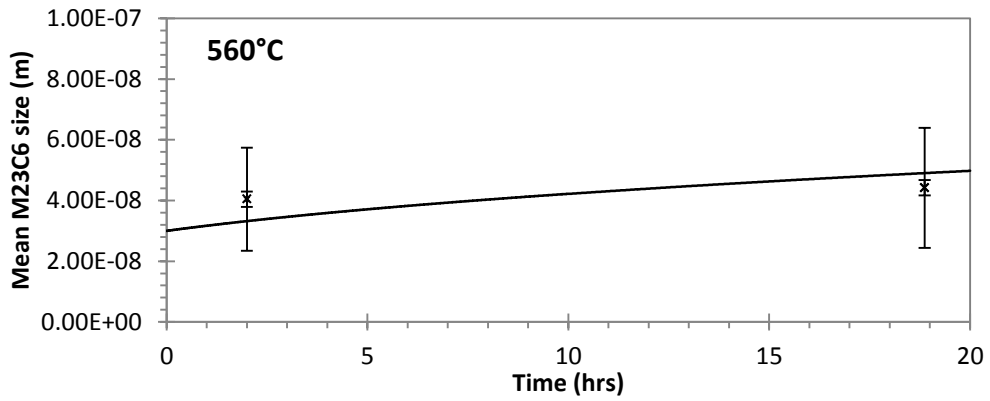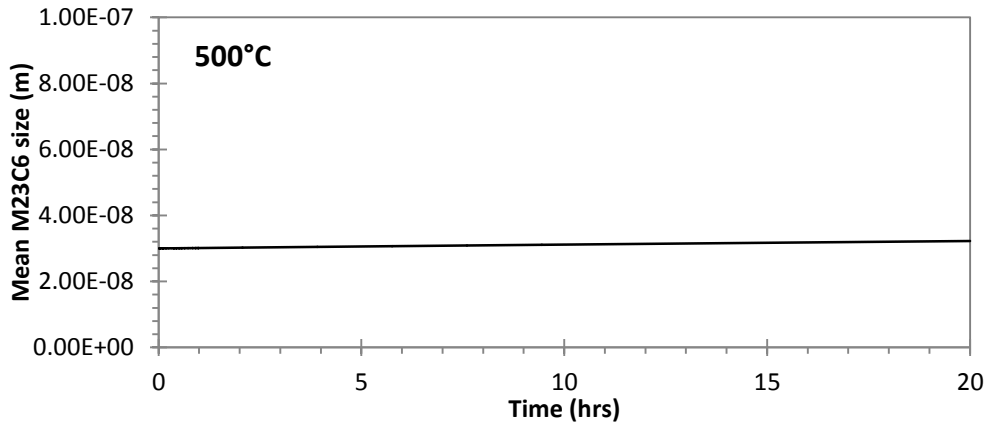
FIGURE 5-7: MODEL PREDICTIONS CONSIDERING VOLUME DIFFUSION AS THE RATE DETERMINING MECHANISM

Data source: Zhang et al (2004)	r_i	K_0	Q_p	m
Dislocation pipe diffusion	30 nm	1×10^{-32} $m^4 s^{-1}$	160 kJ	5
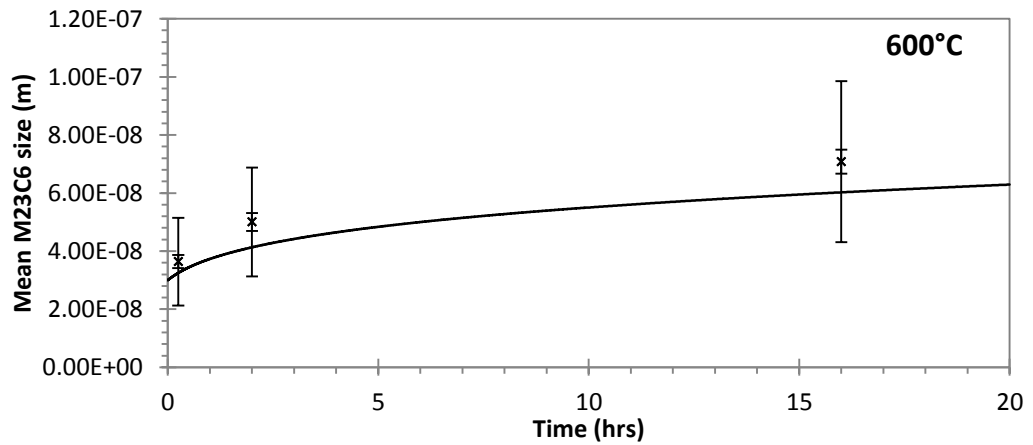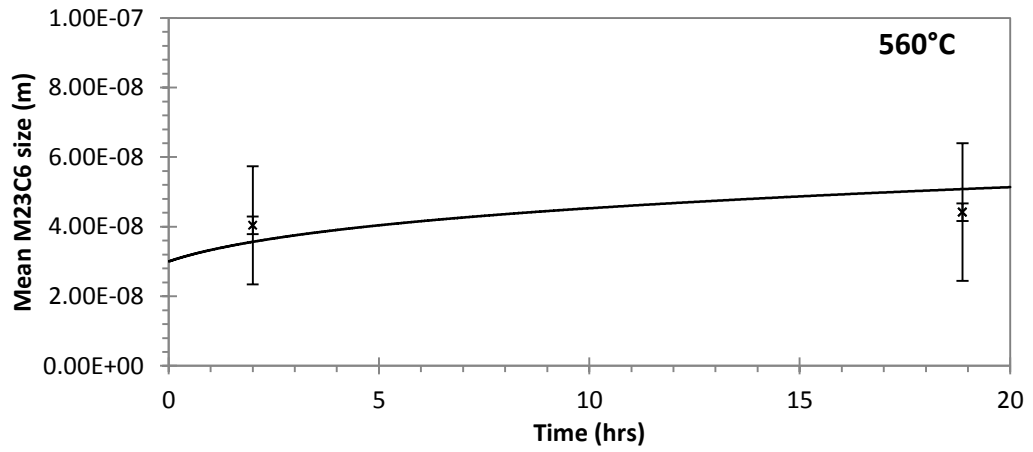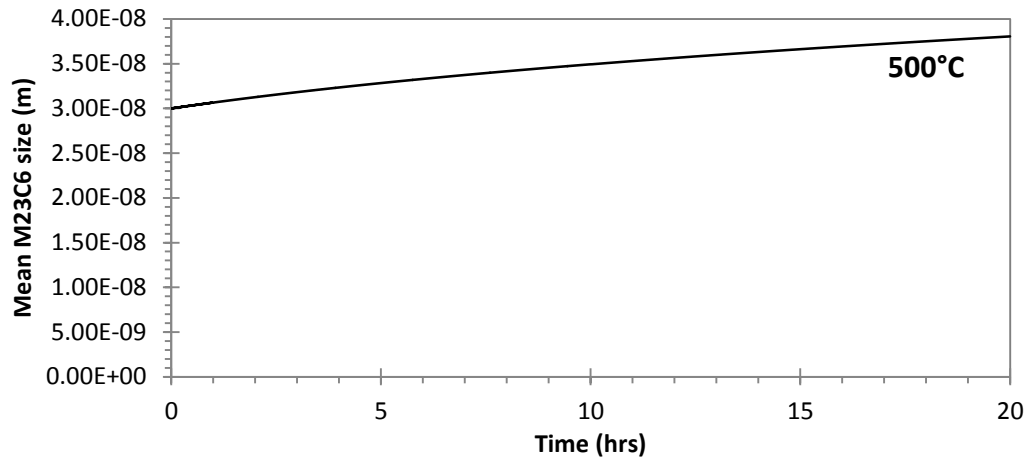
FIGURE 5-8: MODEL PREDICTIONS CONSIDERING DISLOCATION PIPE DIFFUSION AS THE RATE DETERMINING MECHANISM

181

5.3.3.1 SUMMARY OF PARTICLE COARSENING

Particle coarsening occurs during the over-tempering of tempered martensitic steels. The coarsening of particles results in an increase in spacing between the particles and thus a decrease in the Orowan bypass stress.

From examining reported coarsening data describing the subgrain interior particles, it can be seen that volume diffusion best describes the coarsening kinetics within hot work tooling.

The small subgrain interior particles are most frequently encountered by mobile dislocations. The subgrain boundary particles are reported to pin the migration of subgrain boundaries and impede coarsening.

5.3.4 EVOLUTION OF SUBGRAIN STRUCTURE

The cyclical softening behaviour observed in the fatigue loading of tempered martensitic hot work tool steels has been explained by the mechanisms of subgrain formation and coarsening (Zhang, Delagnes et al. 2002). Semba (2003) accounted for the strain induced softening behaviour observed in creep as a response from subgrain coarsening.

The driving force for subgrain formation is the minimisation of free energy (Kuhlmann-Wilsdorf 2002). Sedlacek et al (2002) states that dislocation structures form to allow for compatible deformation of a heterogeneous microstructure. Localised regions within grains re-orientate themselves with the primary slip systems, reducing the number of active slip systems and thus reducing the impact of forest dislocations impeding glide. Kuhlman-Wilsdorf and Hansen (1991) proposed that subgrains may also be formed through the grouping of dislocation dipoles into incidental subgrain boundaries in addition to the geometrically necessary subgrain boundaries described by Sedlacek et al (2002).

During fatigue and/or creep conditions the subgrains have been observed to coarsen as shown in Figure 4 9. It can be seen that the initial structure consists of pockets of high dislocation density. Equiaxed subgrains form as a result of either creep or fatigue.
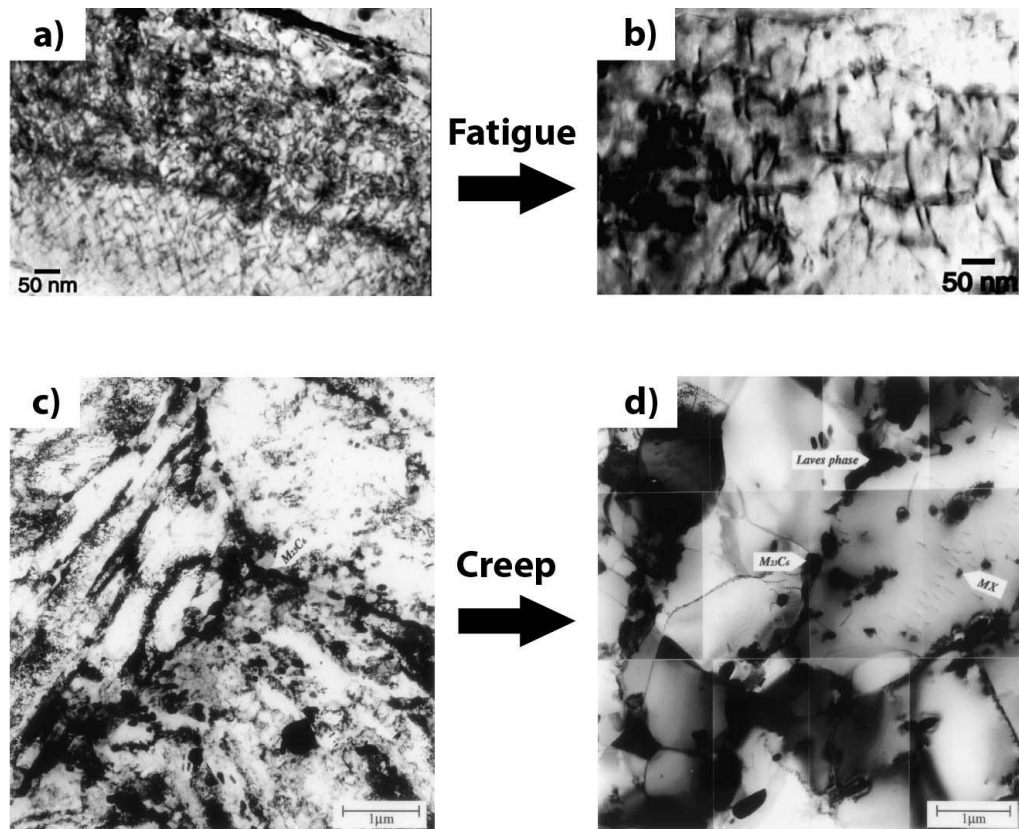
FIGURE 5-9: A) AND B) ARE TEM MICROGRAPHS OF H11 DISLOCATION STRUCTURE BEFORE AND AFTER FATIGUE (MEBARKI, DELAGNES ET AL. 2004). IMAGES B) AND C) ARE TEM MICROGRAPHS OF 9-12%CR MARTENSITIC STEEL DISLOCATION STRUCTURE BEFORE AND AFTER CREEP (KADOYA, DYSON ET AL. 2002).

Bernhart et al (1999) proposed that the initial transient cyclical softening behaviour observed during fatigue loading of hot work tool steel is caused by the formation of subgrains and that the linear cyclical softening behaviour may be explained through subgrain coarsening.

Principles of scaling have been used to describe how the dislocation link length and subgrain wall thickness maintain proportion with varying subgrain diameter (Nes 1997). Nes' (1997) assumptions are listed in equations 5-66 to 5-68.

$$\sqrt{\rho_m} = q_c \frac{1}{\lambda_{sg}}$$ **5-66**   The relationship between the dislocation density in the subgrain interior and the subgrain diameter.

$$h = q_h \lambda_{sg}$$ **5-67**   The relationship between the subgrain boundary thickness and the subgrain diameter

$$\sqrt{\rho_b} = q_b \sqrt{\rho_m}$$ **5-68**   The relationship between the dislocation density in the subgrain boundaries and the dislocation density in the subgrain interiors

Where;

λ_{sg}	Subgrain diameter (m)
h	Subgrain wall thickness (m)
ρ_m	The dislocation density in the subgrain interiors (m^{-2})
ρ_b	The dislocation density in the subgrain walls (m^{-2})
k, q_c, q_h, q_b	Proportionality constants

Semba (2003) used the relationship shown in equation 5-66 to describe the impact of strain-induced subgrain coarsening through the change in mobile dislocation density.

Nes (1997) proposed that the subgrain wall thickness scaled with the subgrain diameter during coarsening of steels whilst Semba (2003) assumed that the wall thickness remained constant.

Equations 5-69 to 5-71 lists different expressions that have been used to estimate the volume fraction of subgrain boundaries which originate from the line intercept method.

(Nes 1995) $$\phi_{sgb} = \frac{k_1 h}{\lambda_{sg}}$$ **5-69**

(Semba 2003) $$\phi_{sgb} = \frac{2h}{\lambda_{sg}}$$ **5-70**

(Orlova 2000) $$\phi_{sgb} = 5.2 \frac{b}{\Theta \lambda_{sg}}$$ **5-71**

Where;

ϕ_{sgb} The volume fraction of subgrain boundaries.

k_1 A geometrical constant.

Θ Subgrain misorientation (degrees\ radians).

Under the conditions of interest, the subgrains have been observed to coarsen, reaching a dynamic equilibrium based upon the loading conditions which may be described as a steady state. A phenomenological relationship between the shear stress and the inverse of the subgrain size has been observed (Nes 1997; Kuhlmann-Wilsdorf 1999). This relationship may be modelled empirically through the Orowan stress equation as shown below (Mughrabi 1987):

$$\tau = \frac{CGb}{\lambda^m}$$ **5-72**

The impact of subgrain coarsening may be accounted for in several ways. A threshold stress may be used describing the strengthening from the subgrain boundaries using a Hall-Petch relationship. Semba (2003) modelled the decrease in volume fraction of hard subgrain boundaries as a result of subgrain coarsening. The rate that dislocations become pinned by subgrain boundaries is also impacted by subgrain coarsening. If the subgrain spacing determines the mean free path of dislocation glide, the coarsening of the subgrains has a direct impact upon the yield strength of the material. Expressions defining the stress dependence of the stabilised subgrain size are shown in expressions 5-73 to 5-77.

| (Kadoya, Dyson et al. 2002) | $\lambda_{sg_{ss}} = A\sigma^n \exp\left(\dfrac{Q}{RT}\right)$ | 5-73 |

$$\lambda_{sg_{ss}} = A\sigma^n \exp\left(\frac{Q}{RT}\right) \qquad \text{5-73}$$

(Semba 2003; Dubey et al. 2005)

$$\lambda_{sg_{ss}} = \frac{10bG}{\sigma} \qquad \text{5-74}$$

(Sedlacek, Blum et al. 2002).

$$\lambda_{sg_{ss}} = \frac{23bG}{\sigma} \qquad \text{5-75}$$

(Polcik et al. 1999)

$$\log\left(\frac{\lambda_{sg}}{\lambda_{sg_{ss}}}\right) = \log\left(\frac{\lambda_{sg_i}}{\lambda_{sg_{ss}}}\right).\exp\left(\frac{-\varepsilon}{k_{dsg}}\right) \qquad \text{5-76}$$

(Agamennone, Blum et al. 2006)

$$\frac{d\log\lambda_{sg}}{d\varepsilon} = \frac{\log\lambda_{sg_{ss}} - \log\lambda_{sg}}{0.12} \qquad \text{5-77}$$

Where;

λ_{sg} The current subgrain size

λ_{sg_i} The initial subgrain size

$\lambda_{sg_{ss}}$ Steady state subgrain size

b Burgers vector

G Shear modulus

σ The applied stress

ε The creep strain

k_{dsg} A constant

Strain induced subgrain coarsening has been observed to occur significantly faster than when thermally induced (Kadoya, Dyson et al. 2002; Semba 2003; Mebarki, Delagnes et al. 2004).

Semba (2003) chose to ignore thermally induced subgrain coarsening and model strain induced coarsening. A phenomenological model was used to describe the coarsening of the subgrain structure to a pre-determined steady state. The relationship between the subgrain interior dislocation density and the subgrain spacing was used to describe subgrain coarsening through the change in

subgrain interior dislocation density. It was assumed that the subgrain interior dislocation density was equivalent to the mobile dislocation density.

Semba (2003) used the phenomenological models given by Kocks and Mecking to determine an expression describing the reduction in mobile dislocation to a steady state. Estrin and Mecking (1984) developed a phenomenological equation describing the change in mobile dislocation density considering the athermal storage of dislocations and dynamic recovery.

Semba (2003) adopted a similar phenomenological approach and applied equation 5-78 to describe the strain induced reduction in mobile dislocation density.

$$\dot{\rho}_m = k_1\sqrt{\rho_m}\left(1 - \frac{k_2}{k_1}\sqrt{\rho_m}\right) \qquad \text{5-78}$$

The model was used to describe the reduction of dislocation density from a value of 2×10^{14}m^{-2} to a steady state of 2×10^{13} m^{-2}. The reduction in mobile dislocation density has a strengthening impact upon the flow rule however this is countered by the coarsening of the subgrains and the reduction in Taylor back stress.

Ghoniem et al (1990) also modelled the coarsening of the subgrain structure which includes the competing mechanisms of subgrain nucleation and recovery. The impact of subgrain boundary particles upon subgrain boundary migration is also included. Equation 5-79 describes the rate of change in subgrain spacing.

$$\dot{\lambda}_{sg} = M_{sb}\left(\rho_{pin} - 2\pi r_p^2 N_p \gamma_{sb}\right) - G\eta_v K_c \lambda_{sg}\left[\left(\rho_m + \rho_{pin}\right)^{1/2} - \frac{K_c}{\lambda_{sg}}\right]\frac{\Omega D_s}{2kT} \qquad \text{5-79}$$

Where;

M_{sb} Subgrain mobility (m/ s)

η_v Sink strength

K_c Constant with a value of 10

Ω Atomic Volume (m^3)

D_s Self diffusion coefficient

The first part of equation 5-79 describes the static recovery of the subgrain structure. The subgrain boundary particles impede subgrain migration. The resistance encountered by these particles must be overcome before the boundary can migrate. Ghoniem et al (1990) propose that the immobilised dislocations drive the mobility of the subgrain boundary.

The second part of this model describes subgrain nucleation. The model describes subgrain nucleation through the formation of incidental subgrain boundaries, as described by Kuhlmann-Wilsdorf (1991). Ghoniem et al (1990) propose that subgrain nucleation only occurs when the value of $\sqrt{\rho_m + \rho_{pin}}$ is greater than K_c / λ_{sg}. The model does not consider the formation of geometrically necessary subgrains caused by lattice rotations.

5.3.4.1 SUMMARY OF SUBGRAIN STRUCTURE EVOLUTION

Subgrains are observed to form within the martensitic lath boundaries during the accumulation of plastic strain. Under fatigue and creep conditions the subgrains are observed to coarsen to a dynamic equilibrium based upon the applied stress.

Empirical relationships have been observed between the shear stress and the inverse of the subgrain diameter. For the process conditions of interest, dynamic recovery is of importance however static recovery may also occur.

The impact of subgrain boundaries have been modelled in different ways. Semba (2003) modelled the work hardening observed in tempered martensitic steels through the plastically hard subgrain boundaries. Ghoniem et al (1990) modelled the subgrains as obstacles to dislocation glide that results in dislocation pile ups. Neither model describes the initiation of the subgrain structure.

Semba (2003) used a phenomenological model to describe the coarsening of the subgrain structure. Ghoniem et al (1990) developed a physically based model describing the growth and nucleation of subgrain boundaries.

5.4 DISCUSSION OF MODELLING APPROACHES

Different approaches may be taken to model the plastic flow behaviour of hot work tool steels. The appropriate type of model is based upon what level of detail is required, the level of understanding required of the material and

whether it is necessary to extrapolate to conditions not tested during material characterisation.

Phenomenological models are useful in accurately predicting material behaviour within known conditions. To allow for safer extrapolation, it is desirable to utilise a physics based model. Physics based models have been developed to describe the creep behaviour of tempered martensitic steel.

Two approaches to physical based modelling have been found that have been developed to describe tempered martensitic steel; describing the material through precipitate strengthening or using a dislocation strengthening model.

The Dyson model describes the creep behaviour of precipitate strengthened materials. The rate of deformation is linked to the rate that mobile dislocations overcome particles through climb. The Semba-Dyson-McLean model applies this model to tempered martensitic steel. In this model, work hardening is attributed to plastically hard subgrain boundaries. Thermal softening behaviour may be captured through particle coarsening. Cyclical softening behaviour may be captured through subgrain coarsening and the reduction in mobile dislocation density.

The Ghoniem-Matthews-Amodeo model assumes that tempered martensite may be best described as a dislocation strengthened material. The model describes the evolution of mobile dislocations, subgrain boundary dislocations, immobilised dislocations and the change in subgrain diameter. The flow behaviour is modelled using the Orowan-Bailey relationship, with yield behaviour captured using multiple mechanical threshold stresses. Work hardening is captured through the increase in immobilised dislocations, increasing the Taylor stress. The thermal softening behaviour is captured through thermally induced dislocation annihilation, lowering the Taylor stress. The cyclical softening behaviour is captured through subgrain coarsening and strain induced dislocation kinetics.

To determine which modelling approach is most appropriate, it is necessary to understand how the different microstructural features impact the plastic shear strain rate. For continuous dislocation glide during athermal plastic flow, the applied stress must overcome the largest threshold stress to allow plastic

deformation. At high temperature, dislocations are able to escape this obstacle, resulting in strain rate sensitivity. The mobile dislocation interaction and Orowan stress of particle bypass may be compared, to determine the most suitable approach.

The upper and lower bounds of mobile dislocation density within tempered martensitic tool steel may be approximated from the range in values reported describing as-heat treated tempered martensite. The upper limit for the mobile dislocation density is given by $5 \times 10^{14} \text{m}^{-2}$ and the lower limit given by $8 \times 10^{11} \text{m-2}$ (Krumphals, Wlanis et al. 2009; Krumphals, Reggiani et al. 2012). Assuming a shear modulus of 80.2GPa considering room temperature behaviour, a Burger's vector of 0.254nm and an alpha of either 0.5 or 0.8, the Taylor stress may vary between 28.2MPa and 1130MPa.

The Orowan mechanical threshold stress describing particle bypass may be calculated considering the measurements taken by Zhang et al (2004) and Bischof et al (2008). Using equation 2-5, the particle measurements shown in Table 2-4, a shear modulus of 80.2Gpa and a burger's vector of 0.254nm, a high or low alpha (0.5 or 0.8 respectively) the Orowan stress may very between 243MPa to 2330MPa.

The room temperature yield strength of AISI H13 varies between 1200 – 1450MPa (Bohler 2010). Only the Orowan stress of particle bypass covers the yield strength of AISI H13, indicating that the mechanical behaviour may be best captured by a precipitate model.

The Dyson flow rule is most suitable for describing such behaviour. Athermal flow behaviour may be captured using the Basoalto model. The microstructural instability may be described by either the Semba-Dyson-McLean model or the Ghoniem-Matthews-Amodeo model.

5.5 CONCLUSION OF MODELLING APPROACHES

The empirical damage mechanics models developed for fatigue life prediction of hot forging tooling do not describe the flow behaviour of tempered martensitic hot work tool steels with sufficient accuracy.

The flow behaviour can be captured accurately using the phenomenological models developed by Lematire and Chaboche (1990), as shown by Zhang et al (2008). To improve confidence in the extrapolation of the model, physical based models are desired.

Two competing approaches have been identified; the Semba-Dyson-McLean and Ghoniem-Matthews-Amodeo models. The models assume the material is either precipitation strengthened or dislocation strengthened, respectively. The mechanical threshold stress for precipitate strengthening better describes the athermal yield behaviour of AISI H13. The work hardening behaviour may be captured by plastically hard regions, dislocation multiplication or dislocation pile ups. Thermally induced softening may be attributed to particle softening and\ or dislocation annihilation. Strain induced softening may be captured through modelling the reduction in dislocation density and the coarsening of subgrains.

6 DIE MATERIAL MODEL DEVELOPMENT

The physical based models developed to describe the creep behaviour of tempered martensitic steels may be applied to the thermo-mechanical fatigue behaviour of tempered martensitic tool steel.

A physical based model is desired to improve the confidence in model predictions when extrapolating the model to describe the thermo-mechanical loading of hot work tooling.

The Dyson-Semba model has been applied to the thermo-mechanical fatigue behaviour of tempered martensitic 5% Cr hot work tool steel. The Basoalto model has been used to describe athermal flow behaviour. The model describes physical mechanisms using microstructural measurements taken from alloys similar to AISI H13.

The problem has been approached assuming that subgrains exist in the as-heat treated condition. It is argued that the subgrain structure is formed during the rolling of the tool steel. The microstructural features being considered are the mobile dislocations, the subgrain boundaries and the subgrain interior particles. A schematic representation of tempered martensite is shown in Figure 6-1.

The Dyson-Semba model assumes that yield behaviour is influenced by precipitation strengthening. Dislocation strengthening has been included within the model through the use of a Taylor stress. The small spacing of the subgrain interior particles results in a large Orowan stress and dictates the mean free path of dislocation glide.

The Dyson model of precipitate strengthened materials has been applied to capture strain rate sensitive material behaviour. The Basoalto model has been applied to capture strain rate insensitive material behaviour utilising an Orowan stress describing particle bypass.
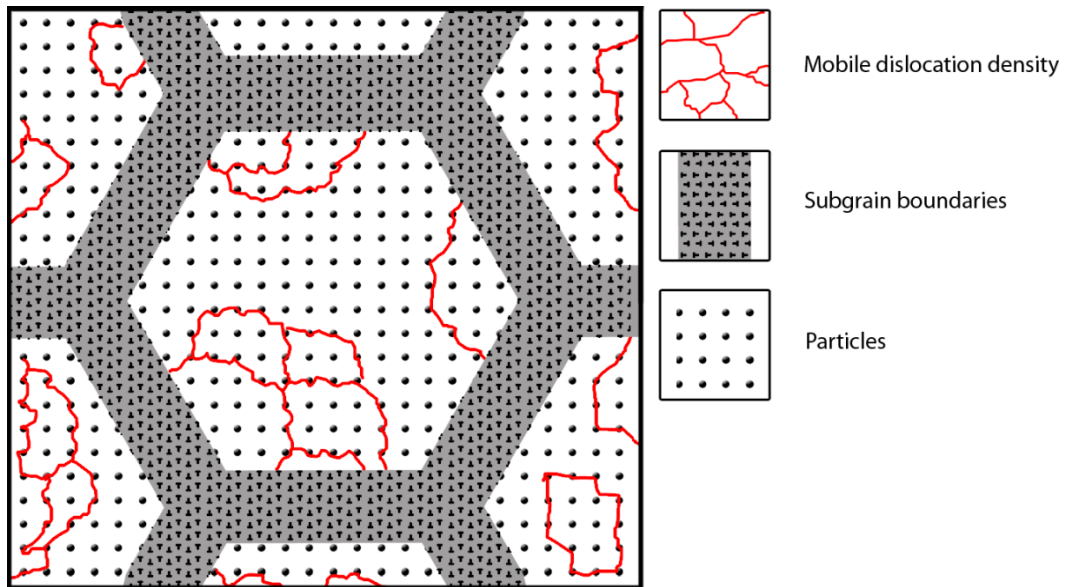
FIGURE 6-1: SIMPLIFIED MICROSTRUCTURE

The work hardening behaviour has been attributed to the presence of plastically hard subgrain boundaries, following the Dyson-Semba model. The model has been adapted to include differing elastic modulus between the hard subgrain boundaries and the subgrain interior.

The microstructural instabilities included within the model are illustrated in Figure 6-2. The thermal softening (over-tempering) behaviour of the alloy has been modelled through particle coarsening as illustrated in figure a). Volume diffusion has been found to better describe the measured softening behaviour.

The cyclical softening measured during fatigue loading has been attributed to subgrain coarsening. The Dyson-Semba model uses a phenomenological model to capture the observed reduction in mobile dislocation density. This is illustrated in figure b).

A linear relationship between the mobile dislocation network spacing and the spacing of the dislocation structure is used to model subgrain coarsening. The coarsening of the subgrains is illustrated in figure c).

A) PARTICLE COARSENING
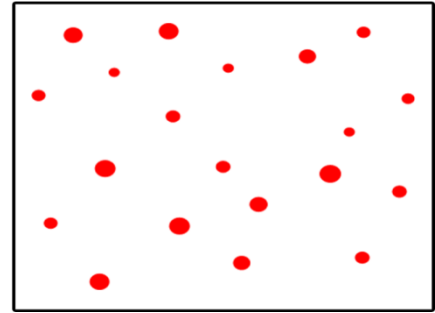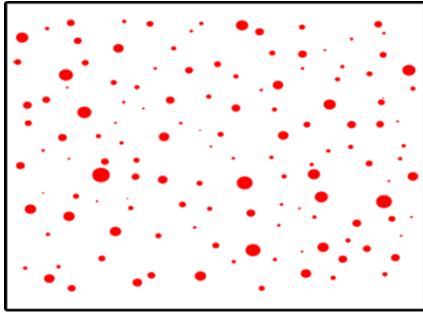
B) SUBGRAIN COARSENING
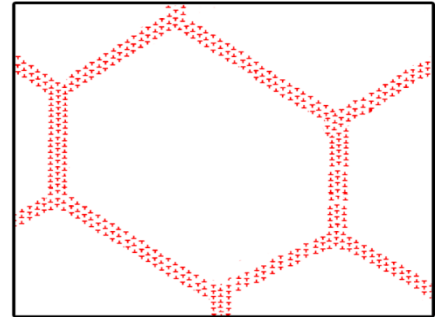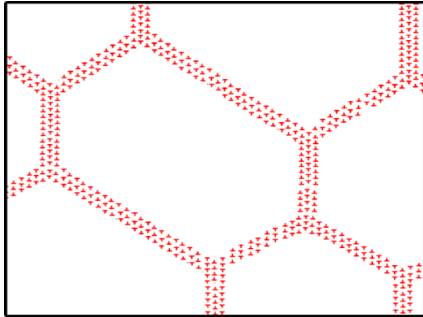
C) REDUCTION IN MOBILE DISLOCATION DENSITY
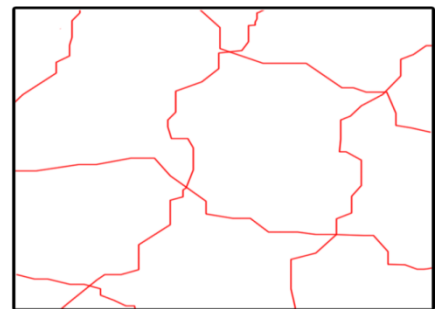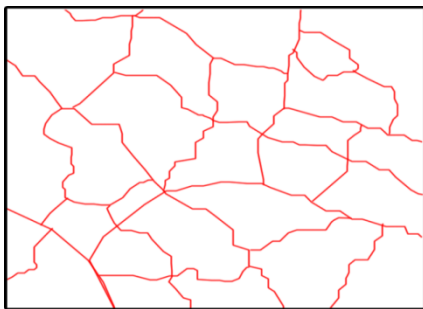
FIGURE 6-2: THE SIMPLIFIED MICROSTRUCTURE AND MICROSTRUCTURAL INSTABILITIES

6.1   THE FLOW RULE

It is proposed that at low temperature, the Orowan particle bypass threshold stress dictates yield behaviour and at higher temperatures, the pinned mobile dislocations are able to climb and escape these obstacles. The Dyson model of precipitate strengthened materials is used to describe the high temperature behaviour, following the work of Semba (2003). An athermal flow rule is used to describe flow behaviour at temperatures showing insignificant strain rate sensitivity. The flow rule which predicts greatest plastic strain for a given time increment is used to determine behaviour.

The following sections outline the two mechanisms that are proposed to govern yield behaviour.

6.1.1   THERMAL YIELD BEHAVIOUR

The Dyson-Semba model has been used to describe the creep behaviour of 9-12%Cr tempered martensitic steels. The Dyson flow rule of precipitate strengthened materials is shown in equation set 5-19. A Taylor stress has been included in the flow rule, as shown in equation 6-1.

$$\bar{\sigma} = \sigma - \alpha_1 GbM\sqrt{\rho_m} \qquad\qquad \textbf{6-1}$$

The Taylor stress is a resistive stress, so cannot result in a negative effective stress, considering loading in either compression or tension.. This is achieved with the condition shown in 6-2, considering the loading in the tensile direction as the positive direction.

$$|\sigma| - \psi\alpha_1 GbM\sqrt{\rho_m} \geq 0 \qquad\qquad \textbf{6-2}$$

Where;

ψ This term is positive 1 when the loading direction is in tension and -1 for compression.

From section 2.3, the mean particle radius measured in similar alloys to AISI H13 in the as heat treated condition vary between 1nm to 30nm (Zhang, Delagnes et al. 2004; Bischof, Staron et al. 2008) with volume fractions varying between 1.9% to 8.2% (Zhang, Delagnes et al. 2004; Bischof, Staron et al. 2008).

The activation energy for volume diffusion through the matrix may vary between 266 kJ.mol^{-1} to 239 kJ.mol^{-1} depending whether using the lower bound of α phase bcc iron or those found to be descriptive of volume diffusion in tempered martensitic steels (Semba 2003; Frost and Ashby 2011).

The rate of diffusion for α phase bcc iron is given at $2 \times 10^{-4} m^2 s^{-1}$ with a slower rate of $1.9 \times 10^{-4} m^2 s^{-1}$ for 1%Cr-Mo-V steel (Frost and Ashby 2011). The value used to describe the volume diffusion coefficient in 9-12%Cr tempered martensitic steels varies between $2 \times 10^{-4} m^2 s^{-1}$ to $2.8 \times 10^{-4} m^2 s^{-1}$ (Ghoniem, Matthews et al. 1990; Semba et al. 2008).

The upper and lower bounds of reported magnitudes of mobile dislocation densities describing tempered martensitic steels vary from $2 \times 10^{14} m^{-2}$ to $8 \times 10^{11} m^{-2}$ (Semba 2003; Krumphals, Wlanis et al. 2009). This difference in mobile dislocation densities has a large impact upon whether the Taylor stress arising from mobile dislocation interaction is significant.

The upper and lower bounds of material parameters reported from the literature are summarised in Table 6-1. The model is highly sensitive to the mean subgrain interior particle radius and volume fraction. The values measured by Bischof et al (2008) descriptive of the as-heat treated condition have been used to describe AISI H13.

Two magnitudes of mobile dislocation densities have been reported that describe tempered martensitic steel; (low) $8 \times 10^{11} m^{-2}$ and (high) $2 \times 10^{14} m^{-2}$ (Semba 2003; Krumphals, Wlanis et al. 2009). The impact of the magnitude of the mobile dislocation density and the diffusion parameters upon the predicted yield behaviour has been examined. The material parameters kept constant are shown in Table 6 2. An α_1 constant of 0.5 is assumed (Abe 2008).

Parameter		Lower limit		Upper limit	
r_p	nm	1.2	(Bischof, Staron et al. 2008)	30	(Zhang, Delagnes et al. 2004)
ϕ_p	%	0.5	(Semba 2003)	8.2	(Zhang, Delagnes et al. 2004)
d_v	m^2s^{-1}	1.9×10^{-4}	(Frost and Ashby 2011)	2.8×10^{-4}	(Semba, Dyson et al. 2008)
Q_{dj}	$kJ.mol^{-1}$	239	(Frost and Ashby 2011)	266	(Semba, Dyson et al. 2008)
ρ_m	m^{-2}	8×10^{11}	(Krumphals, Wlanis et al. 2009)	2×10^{14}	(Semba 2003)

TABLE 6-2: MATERIAL PARAMETERS

M	b	ϕ_{pmx}	r_p	α_1
	m	-	m	-
3.1	2.54×10^{-10}	0.019	1.2×10^{-9}	0.5

To take into account the impact of uncertainty in diffusion parameters upon flow behaviour, these terms have been grouped to produce either a strong or weak diffusion terms. These values are shown in Table 6-3.

TABLE 6-3: UPPER AND LOWER BOUNDS OF VOLUME DIFFUSIVITY AND MOBILE DISLOCATION DENSITY

	d_v	Q_{dj}	ρ_i
	m^2s^{-1}	$kJ.mol^{-1}$	m^{-2}
Weak diffusion	2.8×10^{-4}	239	-
Strong diffusion	1.9×10^{-4}	266	-
High dislocation density	-	-	2×10^{14}
Low dislocation density	-	-	8×10^{11}

Out et al (2008) and Engberg and Larrson (1988) report the temperature dependence of the elastic modulus and shear modulus for AISI H13. The Elastic and shear modulus are shown in equation 6-3, which is in Pascals.

$$E = (0.11T(C) + 30) * 10^9 \qquad \textbf{6-3}$$

$$G = \left(91540 - 38.7T(K)\right) * 10^6$$

Figure 6-3 compares the predicted and measured yield strength of AISI H13. The measured data refers to the stress measured at the onset of yield. The first term refers to the magnitude of the dislocation density whilst the second term refers to the diffusivity parameters, with respect to Table 6-3.
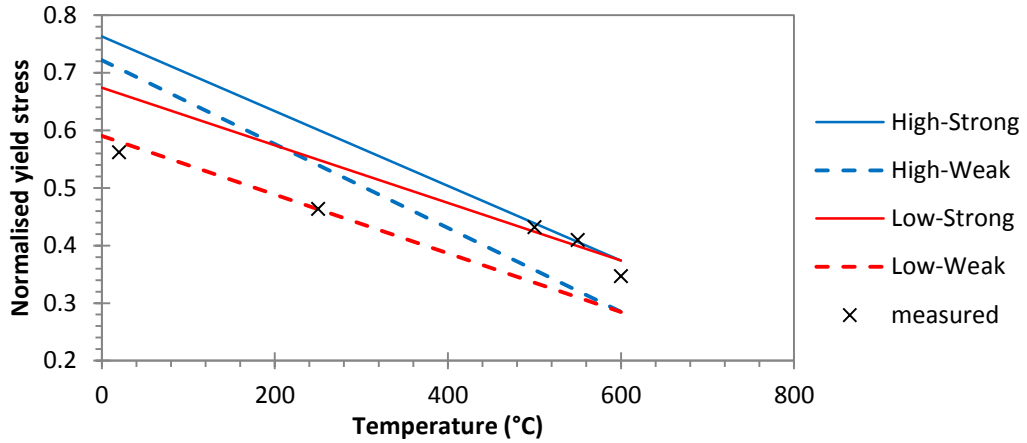
FIGURE 6-3: YIELD STRESS PREDICTIONS AT A STRAIN RATE OF 0.01/S FOR DIFFERENT TEMPERATURES AND MATERIAL PARAMETERS. THE LEGEND SHOWS THE COMBINATION OF BOTH HIGH OR LOW DISLOCATION DENSITY AND EITHER STRONG OR WEAK DIFFUSIVITY PARAMETERS.

The temperature sensitivity predicted by the model is most affected by the magnitude of the mobile dislocation density. A high mobile dislocation density results in a large Taylor back stress and greater temperature sensitivity from the epsilon nought term. The diffusivity parameters have a scalar impact upon the predicted yield stress.

The yield behaviour at temperatures greater than 500°C may be captured using the parameters shown in Table 6-4. The predicted temperature and strain rate sensitivity in yield stress behaviour is shown in Figure 6-4.

TABLE 6-4: CALIBRATED MODEL PARAMETERS

ρ_m m^{-2}	M	b m	d_v m^{2}s^{-1}	Q_{dj} kJ.mol^{-1}	ϕ_{pmx} %	r_p nm	α_1 -
2×10^{14}	3.1	2.54×10^{-10}	1.9×10^{-4}	266	1.9	1.2	0.5

The measured flow data shows insignificant strain rate sensitivity at temperatures below 500°C. For the purpose of comparing the strain rate

sensitivity predicted by the model and the measured behaviour, the results from temperatures lower than 500°C have been assumed to be strain rate insensitive. The extrapolated data is shown in circles whilst measured data is shown with crosses.
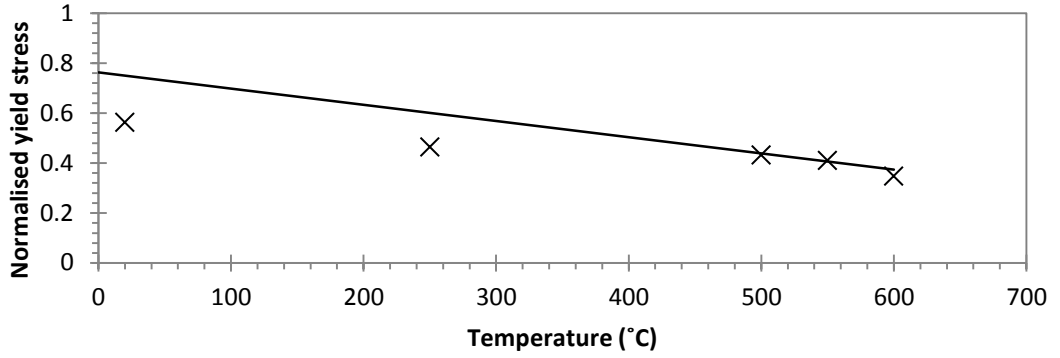
B) STRAIN RATE SENSITIVITY: 20°C
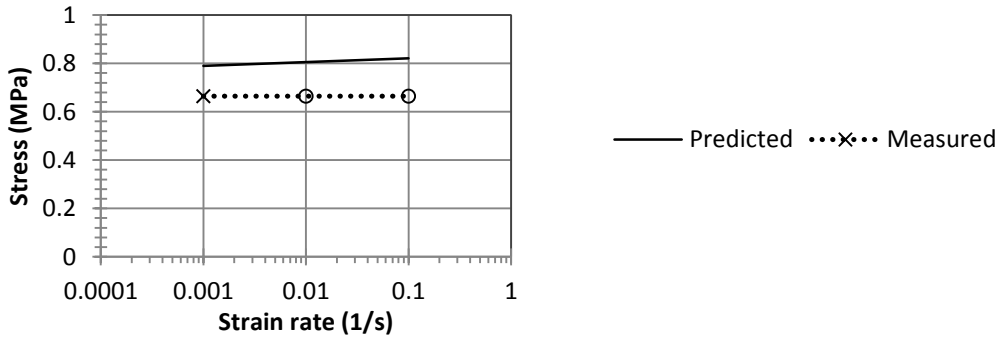
C) 250°C
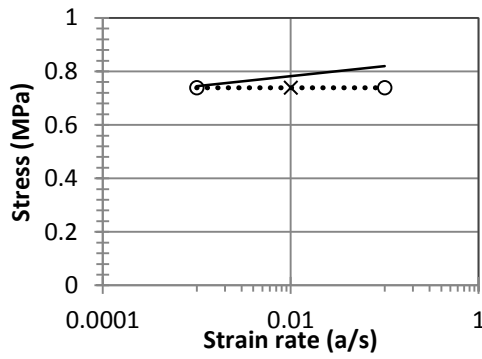
D) 500°C
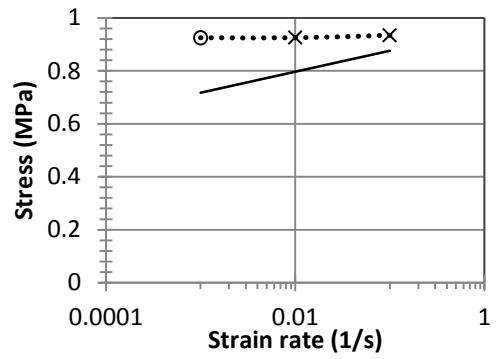
E) 550°C
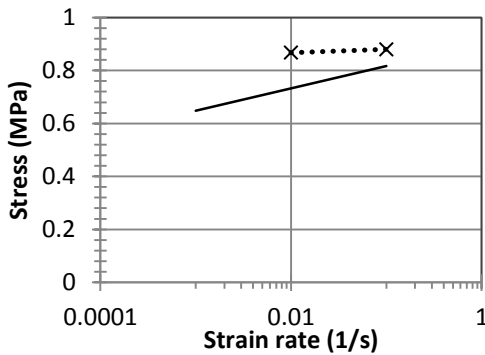
F) 600°C
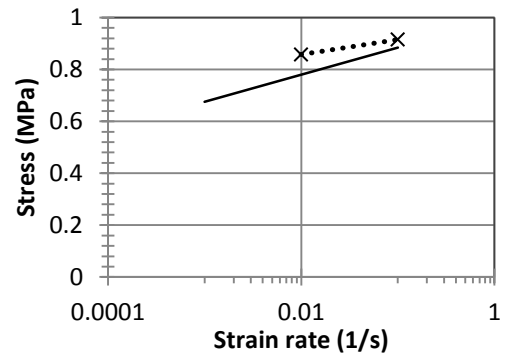
FIGURE 6-4: TEMPERATURE AND STRAIN RATE SENSITIVITY OF THE THERMAL MODEL

The thermal model predicts similar high temperature yield behaviour, but does not capture low temperature behaviour. The model predictions are more strain rate sensitive than the measured behaviour at low temperatures. This is expected, as a creep model is being described to relatively cold temperatures of the material.

6.1.2 PHENOMENOLOGICAL SIGMA NOUGHT

The non-linear reduction in yield stress observed at temperatures greater than 500°C may be captured by including the temperature dependence of the σ_0 term, appearing in equation set 5-19. This temperature dependence is described through modelling the temperature dependence of the particle phase (Dyson 2009). The volume fraction reduces as the temperature reaches the solvus temperature of the particle phase.

Kadoya et al (2002) has approximated the temperature dependence of the volume fraction of MX particles within 9-12%Cr tempered martensitic steel. They predicted a solvus temperature of MX particles in the region of 1100-1200°C. To capture the observed temperature sensitivity of the flow behaviour, it was necessary to use a significantly lower solvus temperature.

An empirical approach has been taken to describe the temperature dependence of the volume fraction and size of subgrain interior particles. Equation set 5-22 applies the rules of mixtures to model phase temperature sensitivity. Equation 5-26 is used to determine the particle radius at elevated temperature.

Equation set 5-22 has been used to fit the temperature sensitivity required from the sigma nought term to describe the measured yield behaviour. The temperature dependence obtained from the calibration is shown in Figure 6-5 using the parameters shown in Table 6-5.

TABLE 6-5: TEMPERATURE DEPENDENCE OF SIGMA NOUGHT

dS	dHs	C#	Co
193	140,000	10500	200
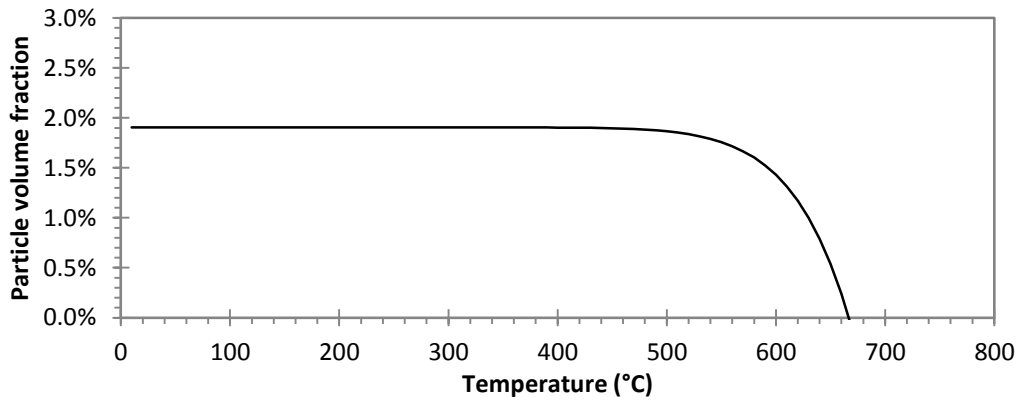
FIGURE 6-5: TEMPERATURE DEPEDENCE OF THE SUBGRAIN INTERIOR PARTICLE PHASE

This temperature sensitivity of yield predicted by the model is compared with and without the phenomenological σ_0 approximation in Figure 6-6. The implication of this assumption is that the model cannot be used to predict behaviour for temperatures higher than 660°C. At such a temperature it is assumed that the particle phase has come out of solution, and a different microstructural feature dictates flow behaviour. The predictions use the material data shown in Table 6-4 and Table 6-5.
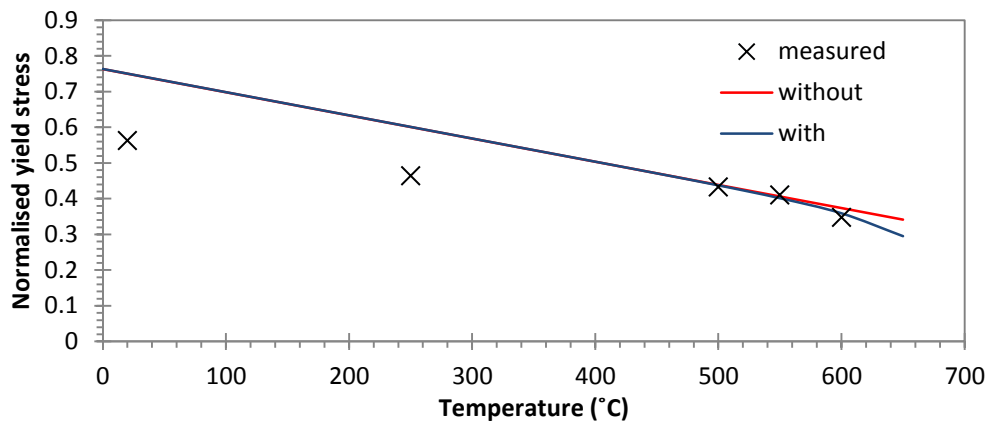
FIGURE 6-6: COMPARISON OF TEMPERATURE SENSITIVITY OF THE YIELD STRESS WITH AND WITHOUT THE PHENOMENOLOGICAL TEMPERATURE DEPENDENCE OF THE SIGMA NOUGHT TERM

The reduction in volume fraction in subgrain interior particle phase with temperature captures the transient drop in yield strength at high temperature measured from the material.

6.1.3 ATHERMAL OROWAN BOWING MODEL

The athermal model developed by Basoalto (2012) described in equation 5-46, has been used to describe the athermal flow behaviour of tempered martensitic steel. The Orowan bowing stress has been included in the model, as outlined in equation set 6-4.

$$|\sigma| - \sigma_{Oro} \geq 0$$

$$\sigma_{Oro} = \frac{\alpha_2 M G b}{2\sqrt{2/3}\, r\left(\sqrt{\frac{\pi}{4\phi_p}} - 1\right)} \qquad \textbf{6-4}$$

The temperature and strain rate sensitivity predicted by the athermal model is shown in Figure 6-7 using the material parameters shown in Table 6-6. The temperature sensitivity of the particle phase is given using equation set 6-4 and Table 6-5.

TABLE 6-6: ATHERMAL MODEL PARAMETERS

ρ_m	k_a	M	b	B	ϕ_{pmx}	r_p	α_1	α_2
m^{-2}			nm	Pa s	%	nm	-	-
2x10^{14}	0.01	3.1	0.254	4.5x10^{-5}	1.9	1.2	0.5	0.236

A) TEMPERATURE SENSITIVITY
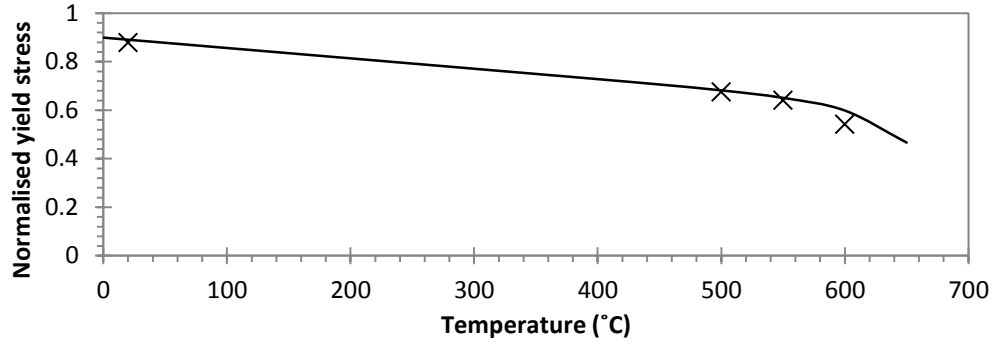
B) STRAIN RATE SENSITIVITY: 20°C
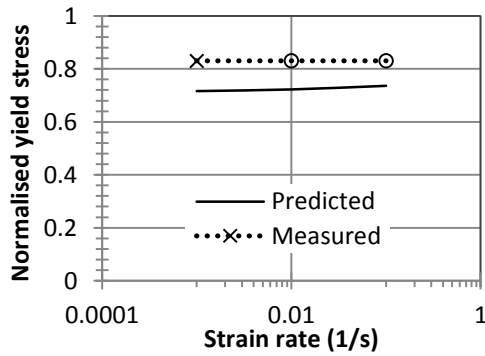
C) 250°C
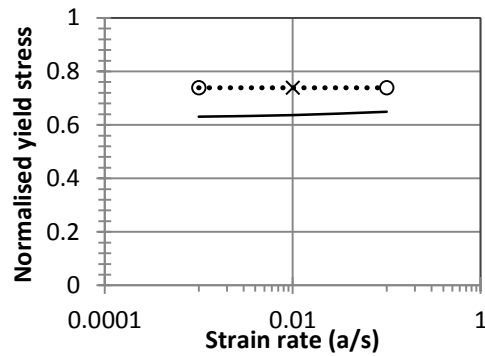
D) 500°C
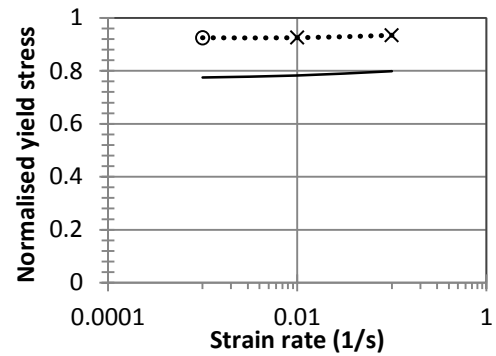
E) 550°C
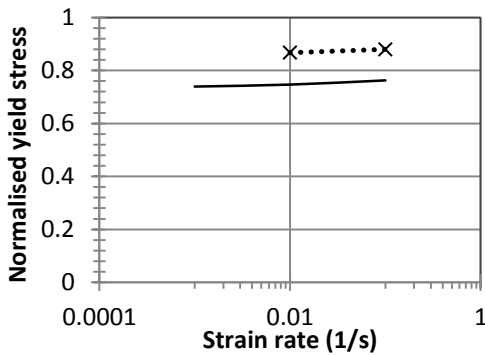
F) 600°C
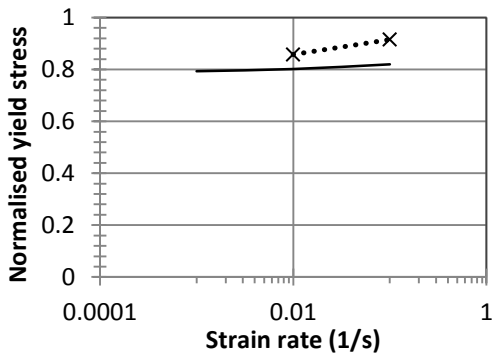
FIGURE 6-7: TEMPERATURE AND STRAIN RATE SENSITIVITY OF THE ATHERMAL MODEL

6.1.4 COMBINED BEHAVIOUR

The athermal and thermal flow rules describe the subgrain interior particles pinning dislocations. The athermal model describes flow behaviour dictated by dislocations escaping particles through Orowan bypass. The thermal model describes the flow behaviour where dislocations are able to escape these particles through climb. The mechanism that allows for greater plastic flow is the dominant mechanism for a given temperature and strain rate. The predicted yield behaviour of the athermal, thermal and combined model is shown in Figure 6-8.
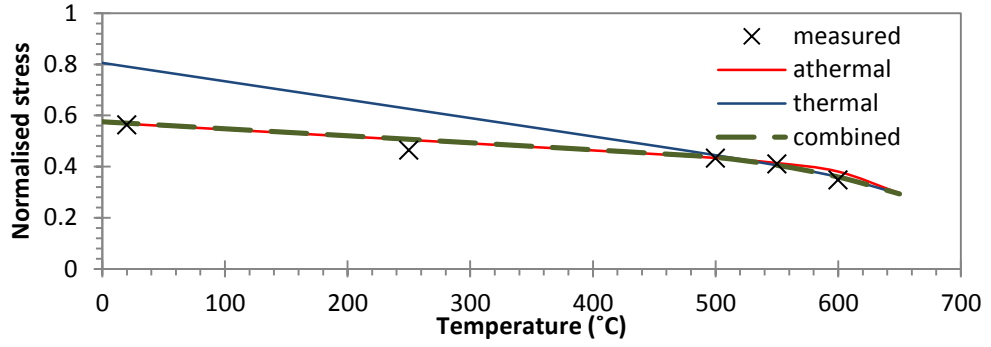
C) 250°C

D) 500°C

E) 550°C

F) 600°C

FIGURE 6-8: TEMPERATURE AND STRAIN RATE SENSITIVTY

6.2 WORK HARDENING

The work hardening behaviour of AISI H13 has been measured in tension and fatigue with symmetrical tensile-compressive loading. The work hardening behaviour of interest includes the plateaux in work hardening, the temperature sensitivity in work hardening, and the work hardening upon reversal of slip direction measured from fatigue loading, as shown in section 4.1.

The flow rule derived by Dyson and Basoalto allow for the description of work hardening through mobile dislocation interaction, dislocation pile ups or plastically hard regions.

Mobile dislocation multiplication and annihilation can describe the increase in dislocation density to a dynamic equilibrium. The increase in the Taylor stress captures the work hardening behaviour. An alpha of 0.8 within the Taylor stress allows for dislocation interaction to capture similar work hardening behaviour.

The Taylor stress may describe the combined dislocation density including mobile and immobile dislocations. The immobile dislocations refer to dislocation pile ups at subgrain boundaries. The reduction in the work hardening rate may be captured through the recovery in immobile dislocation density. The immobile dislocation density may stabilise when the rate of immobilisation of dislocations is balanced by the rate of interaction between immobile dislocations and subgrain boundary dislocations.

The complication incurred in both approaches is modelling the annihilation that must occur upon reversal of slip direction. To predict similar work hardening behaviour during fatigue, the change in dislocation density must rest upon reversal of loading direction.

For the scenario where work hardening is a result of mobile dislocation multiplication, it is necessary to consider the Burger's vector of the mobile dislocations being generated. If mobile dislocation multiplication only occurs in the direction of slip, upon load reversal the newly generated mobile dislocations must annihilate with the high density of mobile dislocations of opposing Burgers vector. The annihilation resulting from reversal of slip direction may capture the observed work hardening behaviour. It is difficult capturing this behaviour and

the observed behaviour where the subgrain interior dislocation density reduces as a response to cyclical loading.

The work hardening behaviour may be modelled through dislocation pile ups. The dislocations immobilised by subgrain boundaries become mobile upon reversal of slip direction. A fraction of these dislocations may join the mobile dislocation population whilst the remaining dislocations annihilate. To model similar behaviour to the measured behaviour, it is necessary that the mobile dislocation density is unaffected by this process. This is possible when the immobilised dislocations that annihilate mobile dislocations is equal to the immobile dislocations that join the mobile dislocations.

The approach chosen to model the work hardening of tempered martensitic steels is based on Semba (2003). The work hardening is attributed to plastically hard regions that result in stress transfer from the plastically soft region. The two-bar composite model is used to model this process. The plateau in work hardening behaviour is explained by the limit to stress transfer to the hard region due to plastic punching.

Semba (2003) proposed that the work hardening in tempered martensitic steels was due to subgrain boundaries acting as hard regions. Semba (2003) made the assumption that the subgrain wall thickness does not change significantly during creep. A similar assumption may be made for the subgrain wall thickness during thermo-mechanical fatigue.

The initial fast rate of work hardening may be explained by a plastically hard region that has significantly greater elastic modulus than the soft region. The approach outlined in section 5.3.2.1 may be applied to the work hardening model developed by Semba. The result is shown in equation set 6-5

$$\dot{\sigma}_k = \acute{h}\left(1 - \frac{\sigma_k}{\sigma H^*}\right)\dot{\varepsilon}_p$$

$$\acute{h} = E(1 - K_E \phi_S)$$

$$H^*_{sgb} = \frac{2\phi_{sgb}}{1 + 2\phi_{sgb}}$$

6-5

$$\phi_{sg} = \frac{2w}{\lambda_{sg}}$$

Figure 6-9 shows the impact of different values of K_E considering a subgrain diameter of 700nm and a subgrain wall thickness of either 100nm or 120nm. This results in a H* value of either ~0.336 or 0.41 respectively. It can be seen that a large difference in elastic modulus between the hard and soft regions is required to describe the fast initial work hardening behaviour when applying Semba's model of plastically hard subgrain boundaries.

For a subgrain diameter of 700nm and subgrain wall thickness of 100nm, the elastic modulus of the hard and soft regions for different values of K_E is shown in Figure 6-10. For low values of K_E the elastic modulus in the soft region reaches become questionable. A reasonable difference between elastic moduli of the hard and soft regions is given by a K_E of 0.6.

The description of the limit for stress transfer may be inaccurate. The limit described by equation 6-5 is descriptive of plastic punching of spherical obstacles. A limit that describes the plastic punching of subgrain boundaries may provide improved work hardening predictions. The plastically hard region may be better described by differently orientated grains.

Figure 6-11 reports the flow behaviour considering different temperatures using the work hardening parameters shown in Table 6-7.

A) *w* 120NM, λ_{sg} 700NM
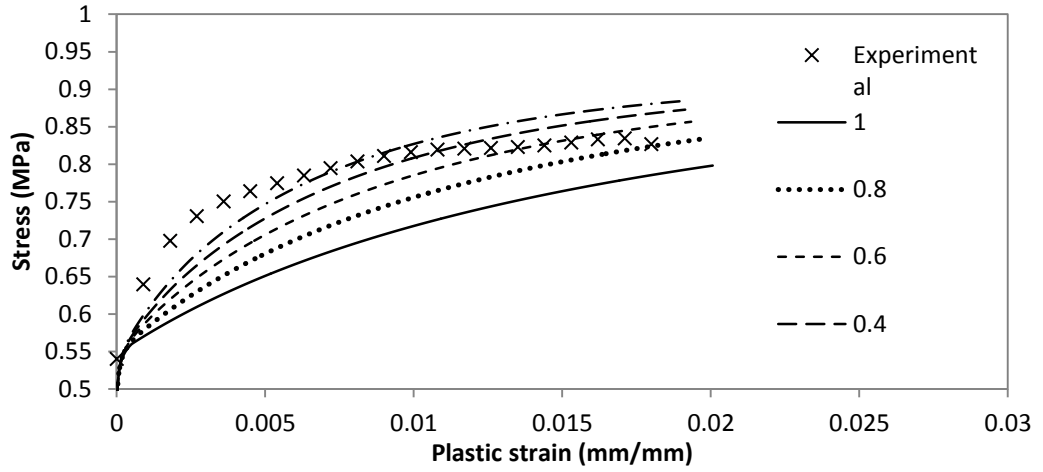
B) *w* 100NM, λ_{sg} 700NM
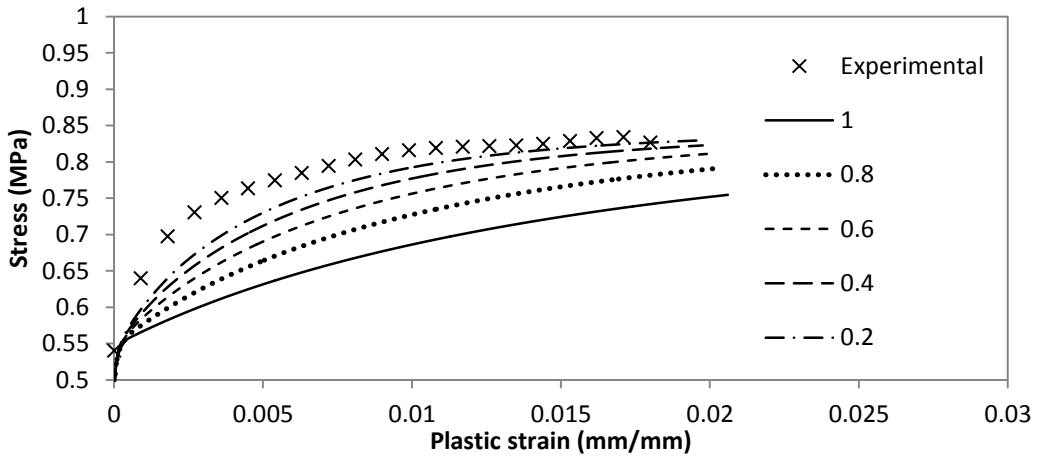
FIGURE 6-9: IMPACT OF COEFFICIENT K_E FOR DIFFERENT WALL THICKNESSES
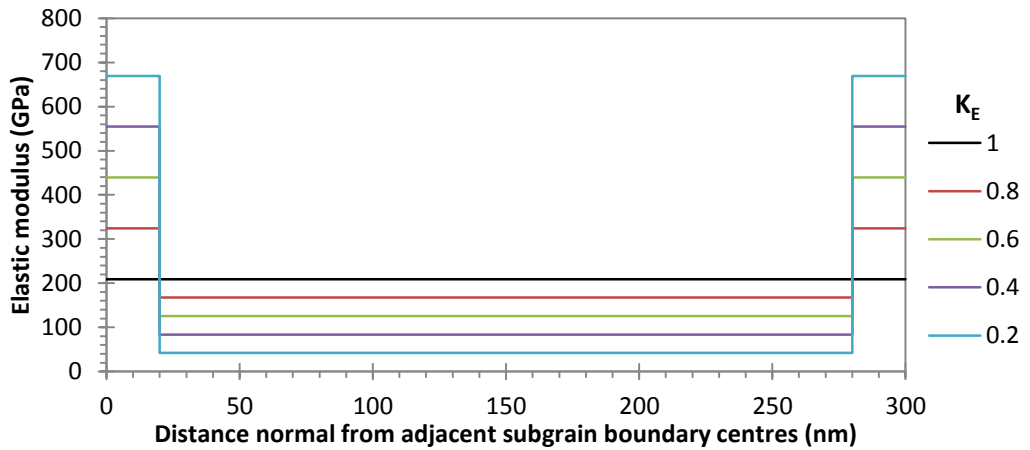
FIGURE 6-10: ELASTIC MODULUS OF HARD AND SOFT REGIONS

A) 20°C @0.001/s
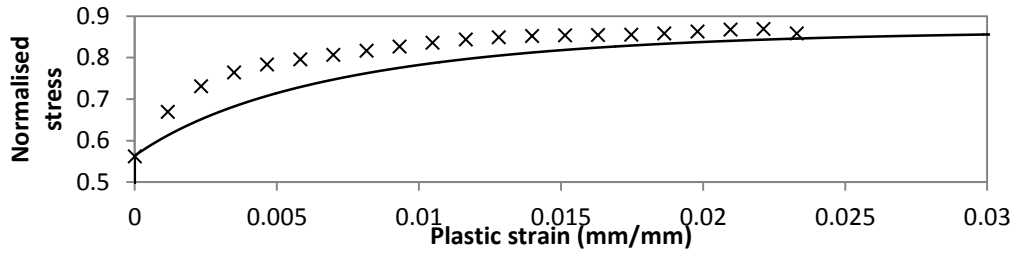
B) 250°C @0.001/s
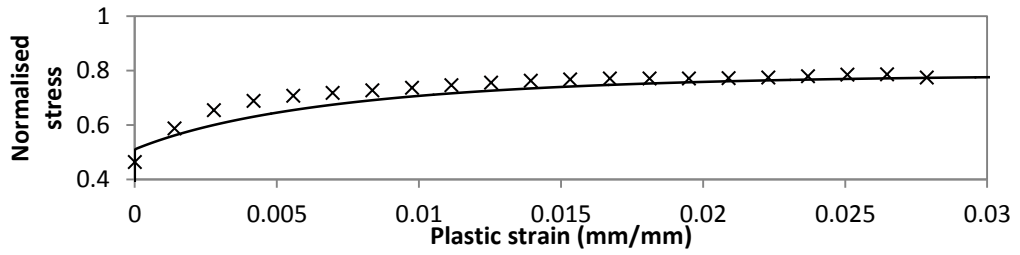
C) 500°C @0.001/s
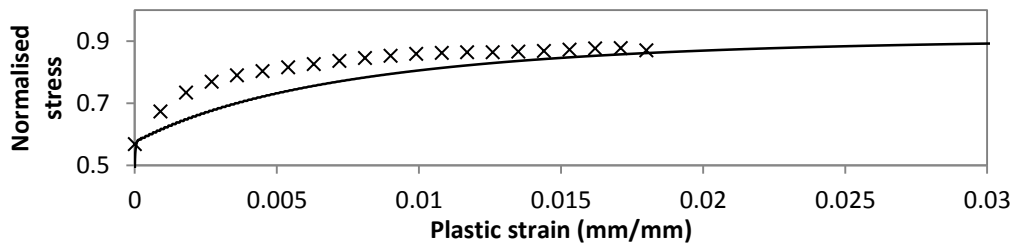
D) 550°C @0.001/s
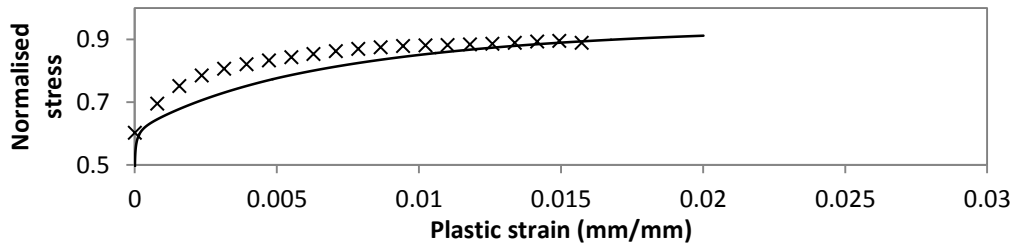
E) 600°C @0.001/s
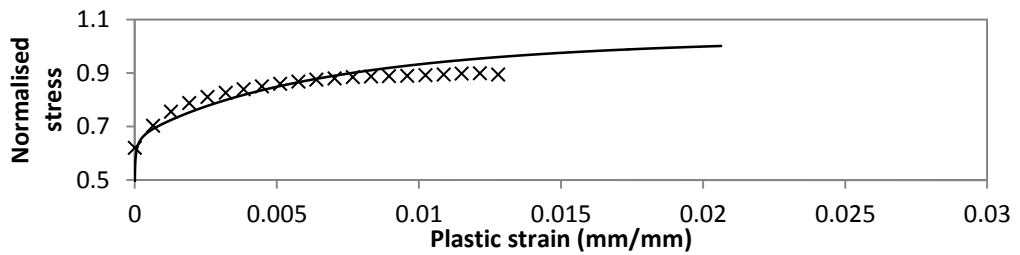
FIGURE 6-11: WORK HARDENING PREDICTIONS

211

Figure 6-12 compares measured and predicted hysteresis loops for isothermal strain controlled fatigue at a temperature of 500°C, a strain rate of 0.01/ s and a strain amplitude of ±0.9%.
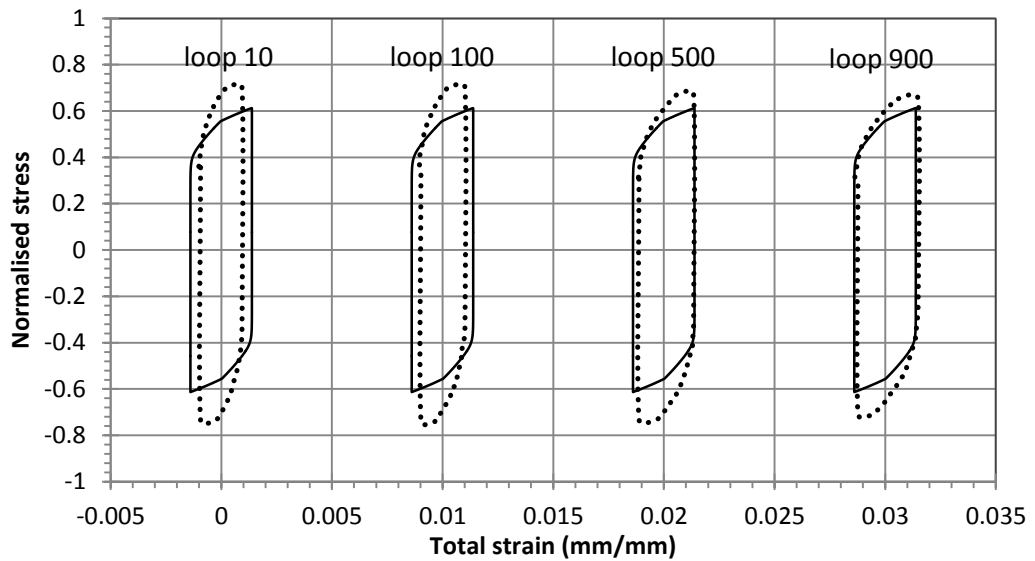
FIGURE 6-12: FATIGUE PREDICTIONS FOR 500˚C, 0.01/S AND ±0.9%

The fast rate of work hardening is not predicted. The implication of this deficiency is that life prediction would be lower than reality when applying this approach. The behaviour in yield strength upon reversal of loading is similar comparing the predicted and measured flow behaviour.

TABLE 6-7: MODEL PARAMETERS FOR PLASTICALLY HARD SUBGRAIN BOUNDARIES

w (nm)	λ_{sg} (nm)	K_E
100	700	0.6

6.3 THERMALLY INDUCED SOFTENING BEHAVIOUR

Tempered martensitic steels over-temper during production due to prolonged exposure to high temperatures reached from heat transferred from the workpiece and heat generated through friction. It is proposed that this behaviour is caused by the coarsening of the subgrain interior particles.

Particle coarsening is a diffusion based process. The diffusion mechanisms relevant to the coarsening of the subgrain interior particles include dislocation pipe diffusion and volume diffusion. Semba (2003) and Kadoya et al (2002) report that dislocation pipe diffusion best captures the particle coarsening behaviour measured in the over-tempering of 9-12% tempered martensitic steel. Particle coarsening may be modelled using equation set 5-65, with an *m* of either 3 or 5 relating to volume diffusion or dislocation pipe diffusion controlled coarsening kinetics.

The particle coarsening parameters have been calibrated to the coarsening behaviour measured by Bischoft et al (2008). The parameters descriptive of dislocation pipe diffusion and volume diffusion are given in Table 6-8.

TABLE 6-8: PARTICLE COARSENING PARAMETERS

Parameter		Dislocation pipe diffusion	Volume diffusion
Q_p	kJ.mol^{-1}	174	266
K_0	m^{4}s^{-1}/ m^{2}s^{-1}	2.5×10^{-38}	8×10^{-16}

The rate of particle coarsening predicted from dislocation pipe diffusion and volume diffusion as a result of aging at 650°C is shown in Figure 6-13.
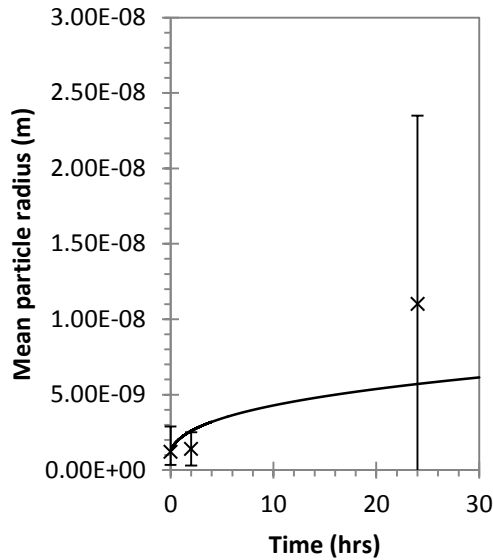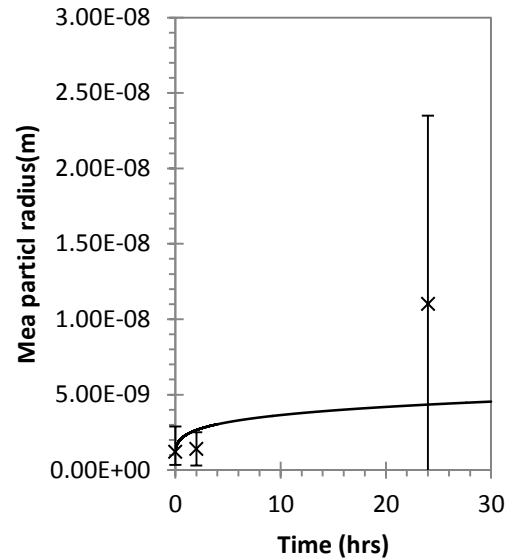
FIGURE 6-13: FITTING PARTICLE COARSENING KINEITCS

Tensile tests have been performed upon over-tempered specimen. Figure 6-14 compares the model predictions to measured behaviour considering particle coarsening dominated by either volume diffusion or dislocation pipe diffusion. The particle coarsening predicted by dislocation pipe diffusion does not capture the temperature sensitivity of the softening behaviour resulting from over-tempering. It is proposed that volume diffusion is the dominant diffusion mechanism in the coarsening of subgrain interior particles within AISI H13.

The 0.1% proof stress has been approximated from hardness measures taken from over-tempered specimens. The results are shown in Figure 6-15. The model predicts similar behaviour.

The 0.1% proof stress has also been approximated from hardness tests taken from over-tempered specimen that examine the softening of the substrate caused by repeated nitriding operations. The model prediction is compared to the measured behaviour in Figure 6-16. The model predicts a faster rate of softening than the measured behaviour. The implication of this deficiency is that the model predicts smaller life when accounting for the total nitriding time of a set of tooling.
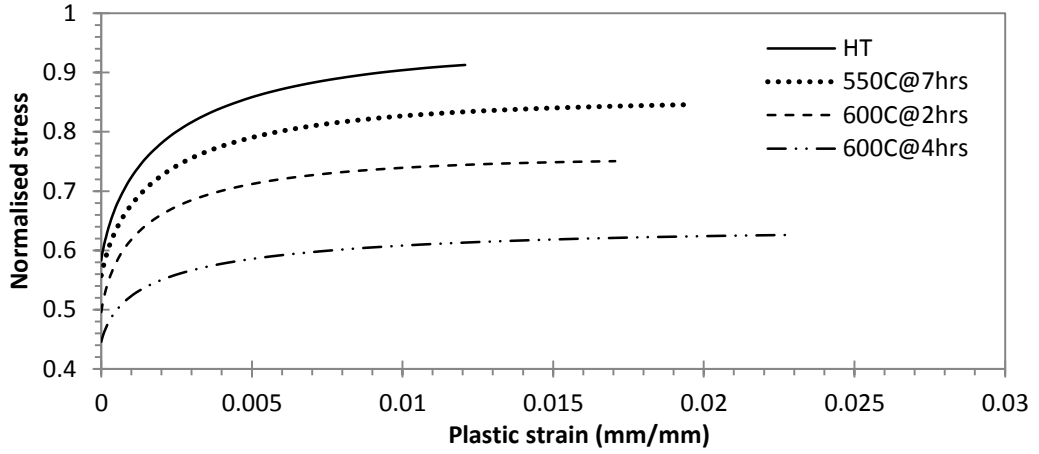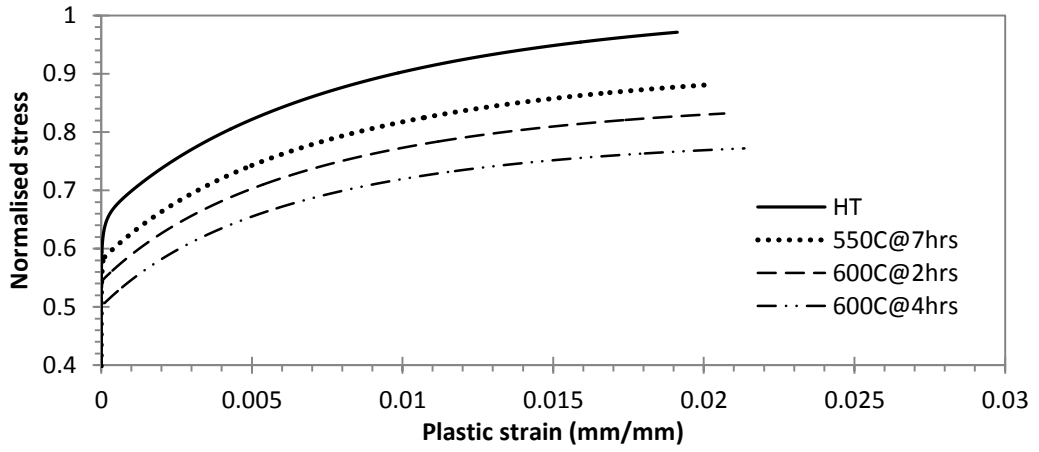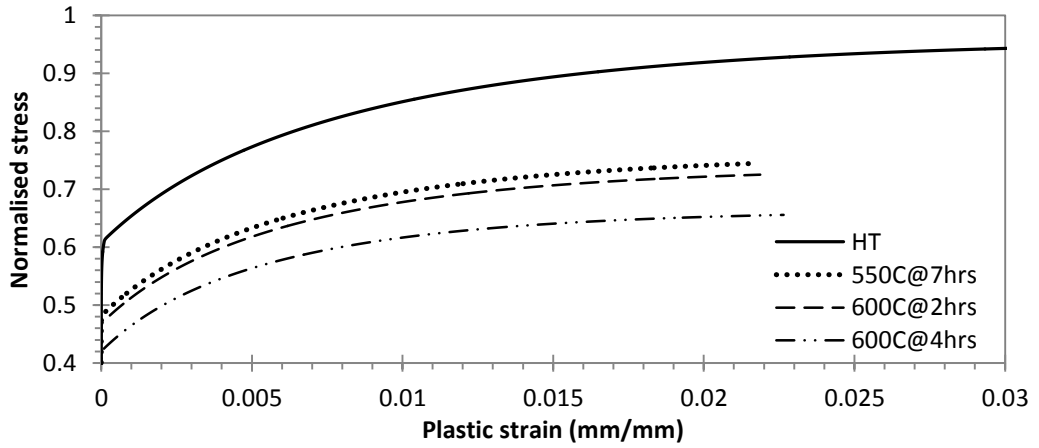
Figure 6-14: 500°C @0.01/s, plastically hard regions of different elastic moduli

A) OVER-TEMPERING AT 500°C
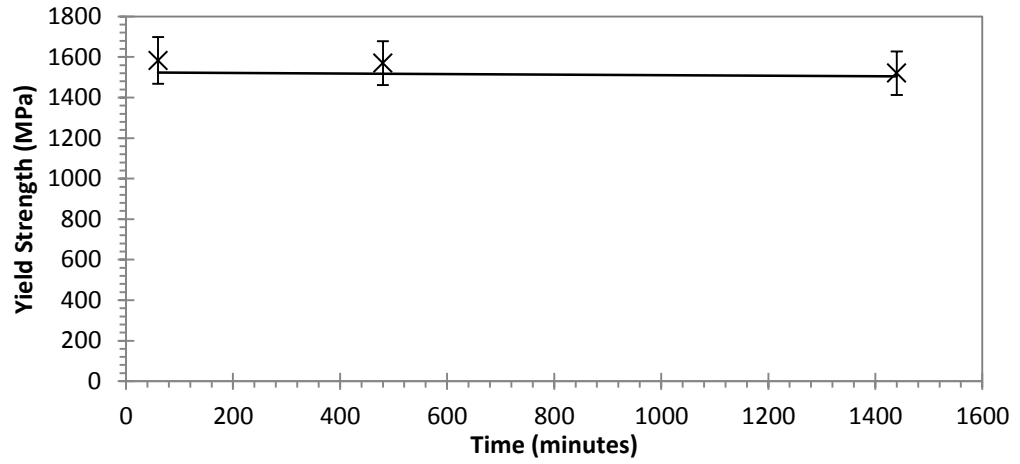
B) OVER-TEMPERING AT 550°C
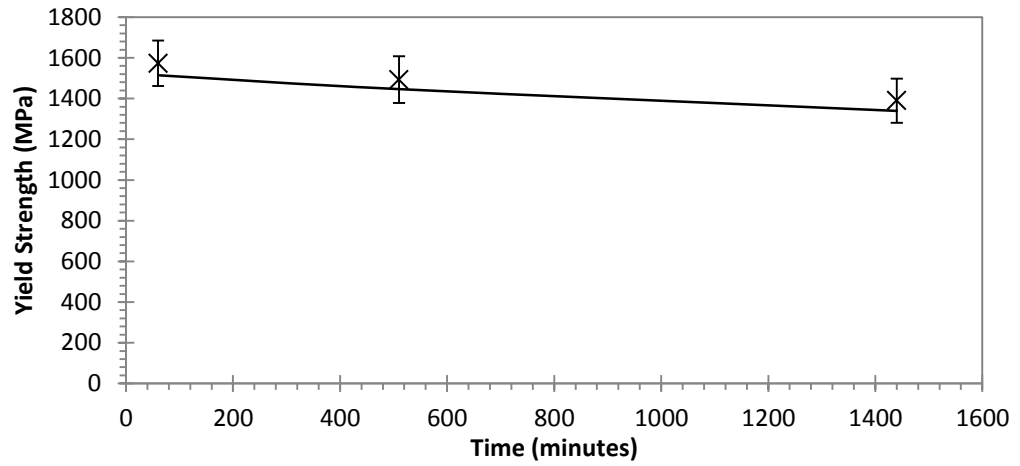
C) OVER-TEMPERING AT 600°C
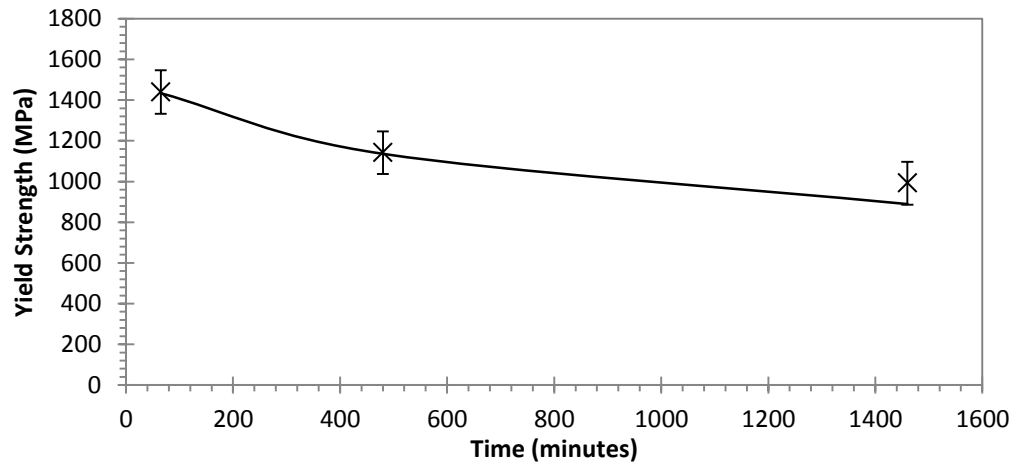
FIGURE 6-15: PREDICTED AND MEASURED OVER-TEMPERING BEHAVIOUR

216
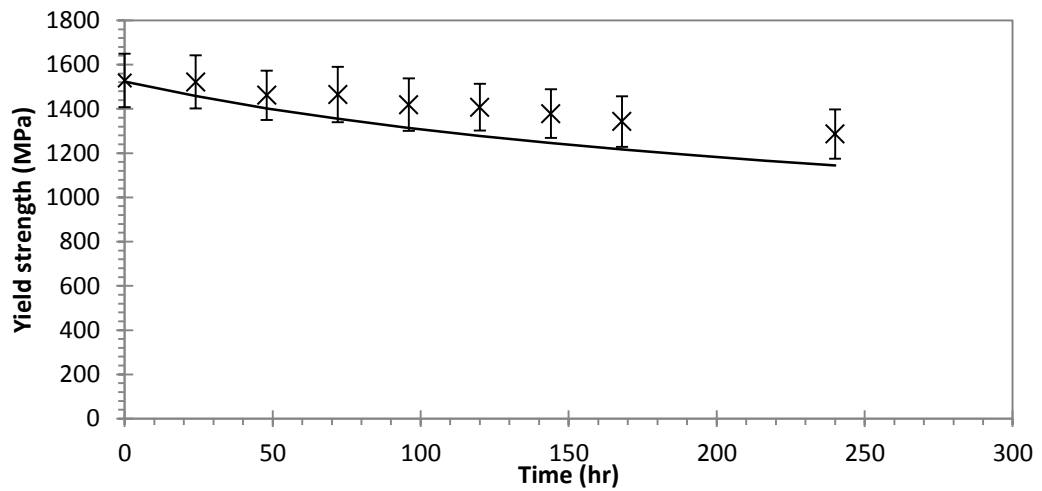
6.4 STRAIN-INDUCED SOFTENING BEHAVIOUR

The relationship observed between the softening behaviour measured during fatigue and the strain amplitude indicates that a strain-induced mechanism is occurring during the cyclical loading of AISI H13. This behaviour may be attributed to changes in the dislocation structure. The dislocation structure is known to coarsen with a reduction in dislocation density within the subgrain interior.

Ghoniem et al (1990) describes the change in mobile dislocaion density in tempered martensitic steel in detail. The mechanisms described include the increase in mobile dislocation density through Frank-Read sources operating upon the mobile dislocaion network and from the subgrain boundary dislocations, climb driven dislocation annihilation, glide driven dislocation annihilation and immobilisation upon encountering a subgrain boundary.

It can be argued that due to the small length scales present in the subgrain boundary dislocations, it is unlikely that Frank-Read sources operate. Dislocations are more likely to be emitted from subgrain boundaries opposed to being generated.

Without more information regarding which mechanisms dictate the change in mobile dislocation density, it is preferable to adopt the phenomenological model applied by Semba (2003).

Semba (2003) used a phenomenological equation to describe the strain-induced reduction in mobile dislocation density observed in the creep of 9-12%Cr tempered martensitic steels. A similar reduction in mobile dislocation was measured by Sauzay et al (2008) in the fatigue loading of 9%Cr tempered martensitic steel. Equation 5-78 was used to describe this behaviour.

Semba (2003) made use of the relationship observed by Kadoya et al (1999) between the mobile dislocation density and the subgrain diameter. This relationship is shown in equation 5-66. The coarsening of the subgrain structure results in the reduction of volume fraction of hard regions, impacting the work hardening behaviour.

Semba et al (2005) used a value of $1.9 \times 10^8 \text{m}^{-1}$ for K_p and a steady state dislocation density of $2 \times 10^{13} \text{m}^{-2}$ for describing the creep behaviour of 9-12%Cr tempered martensitic steels. A lower coarsening rate is required to predict the strain induced softening behaviour measured in the fatigue loading of AISI H13. The parameters used are shown in Table 6-9.

TABLE 6-9: SUBGRAIN\ DISLOCATION KINETICS PARAMETERS

k_{sg}	ρ_{ss}	K_p
-	m^{-2}	m^{-1}
9.9	2×10^{13}	1×10^6

The measured and predicted halved peak stress shown in Figure 6-19 a). The model consistently predicts lower stresses. The cause of the lower than measured prediction of halved peak stress is due to the work hardening model. The initial high rate of work hardening is not captured. This is observed in Figure 6-17 which examines select hysteresis loops.

The model predicts the rate of softening measured at 500°C and 550°C but not at 600°C. The implication of this deficiency is that the model predicts longer die life than reality. The model predictions include the initial variation in strain amplitude that occurred during mechanical testing. The time taken to stabilise the strain amplitude explains the initial increase in halved peak stress.

Figure 6-19 b) shows the predicted particle coarsening and figure c) shows the predicted subgrain coarsening. The predicted subgrain coarsening is similar to the measured subgrain coarsening reported by Sauzay et al (2008) as shown in Figure 6-18.

FIGURE 6-17: SELECT HYSTERESIS LOOPS FROM ISOTHERMAL STRAIN CONTROLLED FATIGUE LOADING AT A TEMPERATURE OF 500°C, A STRAIN RATE OF 0.01/S AND A STRAIN AMPLITUDE OF ±0.9%.

FIGURE 6-18: COMPARISON OF PREDICTED SUBGRAIN COARSENING AND MEASURED SUBGRAIN COARSENING BY SAUZAY ET AL (2008). THE COARSENING IS A RESULT OF STRAIN CONTROLLED FATIGUE LOADING AT A TEMPERATURE OF 550°C, STRAIN AMPLITUDE OF ±1% AND A STRAIN RATE OF 0.01/S.

FIGURE 6-19: PREDICTIONS FOR ISOTHERMAL STRAIN CONTROLLED FATIGUE OF SYMETRICAL STRAIN AMPLITUDE OF ±0.8% AND A STRAIN RATE OF 0.01/S.

6.5   MODEL DEVELOPMENT DISCUSSION

6.5.1   THE FLOW RULE

The flow rule is built on the assumption that the flow behaviour is dictated by the small particles within the subgrain interior. The largest threshold stress predicted by the model is the Orowan bypass of subgrain interior particles. This conflicts with Abe (2008), who proposes that the largest threshold stress in tempered martensitic steels, arises from the subgrain boundaries which, may be modelled using a Hall-Petch relationship. The Orowan and Hall-Petch threshold stresses may be calculated using equation set 6-6.

$$\sigma_{Oro} = \frac{\alpha_2 M G b}{2\sqrt{2/3}\, r\left(\sqrt{\frac{\pi}{4\phi_p}} - 1\right)}$$

$$\sigma_{sg} = \frac{10 G b}{\lambda_{sg}}$$

6-6

Where;

σ_{sg} The Hall-Petch subgrain strengthening threshold stress

The threshold stresses may be compared using the parameters summarised in Table 6-10. For the behaviour at room temperature, the Orowan stress is 1402MPa compared to 291MPa from the subgrain strengthening threshold stress. It is argued that for the microstructure of interest, the Orowan threshold stress dictates yield behaviour.

TABLE 6-10: THRESHOLD STRESS COMPARISON PARAMETERS

b	ϕ_{pmx}	r_p	λ_{sg}	α_2
nm	%	nm	nm	-
0.254	1.9	1.2	700	0.237

Another concern regarding the flow rule is the phenomenological model that has been fit to describe the required temperature dependence from the particle phase. The solvus temperature reported by Kadoya et al (2002) is higher than the calibrated solvus temperature used to describe AISI H13. The super solvus flow

behaviour must be included if the model is to be applied to higher temperatures. A different mechanism must dictate flow behaviour at super solvus temperatures.

The difficulty in describing yield behaviour lies in determining the microstructural feature that dictates the mean free path of dislocation glide. To capture the non-linear reduction in yield strength at high temperature it was necessary that the mean free path increase with temperature. This was achieved through using a phenomenological model of the temperature dependence of the particle phase.

Another possibility is that the mean free path is dictated by the dislocation jog spacing. The jog spacing is related to the dislocation link length and thus the dislocation structure. Basoalto (2011) developed a flow rule describing the viscous drag of jogs in titanium at high temperature. The flow rule is given in equation set 6-7.

$$\dot{\varepsilon}_p = \dot{\varepsilon}_0^i \sinh\left(\frac{\sigma - \sigma_k}{\sigma_0}\right)$$

$$\sigma_0 = \frac{MkT}{b^2\lambda^*}$$
6-7

$$\dot{\varepsilon}_0^i = \frac{1}{M} 2 f_{d,0} \rho_m b^2 exp\left(-\frac{Q_{j,i}}{RT}\right)$$

Where;

λ^* The jog spacing (m)

$f_{d,0}$ The Debye frequency (1/ s)

This modelling approach is based upon the assumption that at high temperature the jog density reduces, resulting in the increase in the mean free path of dislocation glide. Nes (1995) modelled the steady state jog density considering the competing mechanisms of jog formation through dislocation interaction and jog annihilation through the lateral glide of jogs, derived from equation 6-8.

$$\dot{n}_j = k^* \rho_m ds - X n_j{}^2 ds$$
6-8

Where;

n_j Jog density (1/ m)

s   Distance (m)

k^* A constant describing the jogs formed through dislocation cutting.

X   A ratio between the lateral drift velocity of the jogs and the velocity of the screw dislocation.

This approach relies upon capturing the temperature dependence of jog annihilation. Insufficient data was found from published literature regarding jog spacing in similar alloys.

6.5.2   WORK HARDENING

An issue with the developed model is that the initial high rate of work hardening is not captured. To predict the required behaviour following the two-bar composite model approach, a faster rate of stress transfer is required between the hard and soft regions.

One way to increase the rate that stress is transferred to the hard region is to increase the volume fraction of hard regions. Increasing the volume fraction of hard regions results in a too great a Hstar term from equation set 6-5. It is possible that the Hstar expression is incorrect as it describes the plastic punching of spherical shaped obstacles which is being applied to subgrain boundaries. The possibility of elastically hard subgrain boundaries has been proposed however too great a difference in elastic modulus is required to predict the observed behaviour.

The work hardening behaviour may be a result of an increase in the Taylor back stress describing dislocation interaction within the subgrain interior. The dislocation density may increase due to mobile dislocation multiplication or dislocation pile ups at subgrain boundaries. As previously mentioned, these approaches encounter complexity when modelling fatigue behaviour where the slip direction reverses. It is also difficult to model the increase in dislocation density within the subgrain interior when observations reported from the literature indicate that the subgrain interior dislocation density reduces.

6.5.3 MICROSTRUCTURAL INSTABILITY

In the current model the thermally induced softening behaviour is captured entirely through particle coarsening. Over-tempering behaviour cannot be adequately captured if the Taylor back stress is significantly higher. This may be a possibility if the alpha coefficient in the Taylor equation is higher and/or if the dislocation density within the subgrain interior is higher. In this situation it is necessary to model the thermally induced annihilation of subgrain interior dislocations.

The reduction in dislocation density has been measured with no significant coarsening of the subgrains (Bazazi 2009). This suggests that Friedel recovery is not suitable for describing this behaviour. The thermally induced reduction in dislocation density is not linked to the coarsening of the dislocation structure within the time scales of interest. In the Dyson-Semba model, the mobile dislocation link spacing and the subgrain diameter are proportional. This relationship cannot capture this observed behaviour.

One approach is to decouple the mobile dislocation link length and subgrain diameter. The mobile dislocation density may reduce during over-tempering and subgrain coarsening may be modelled through the migration of the subgrain boundaries, as modelled by Ghoniem et al (1990).

Alternatively, the static dislocations that form during the martensitic transformation may be considered. The static dislocations refer to the pockets of high dislocation density as observed by Kadoya et al (2002). The annihilation of these dislocations during over-tempering may contribute to the measured softening behaviour.

The model may be adapted to include this behaviour by distinguishing static and mobile dislocations within the subgrain interior. The Taylor stress describes the dislocation interaction including both the mobile and static dislocation density as shown in equation 6-9.

$$\sigma_{Tay} = \alpha_1 MGb\sqrt{\rho_m + \rho_s}$$

6-9

The annihilation of these dislocations may explain the reduction in dislocation density that occurs without significant coarsening of the dislocation structure. This is illustrated in Figure 6-20. The static dislocations have been highlighted in red.
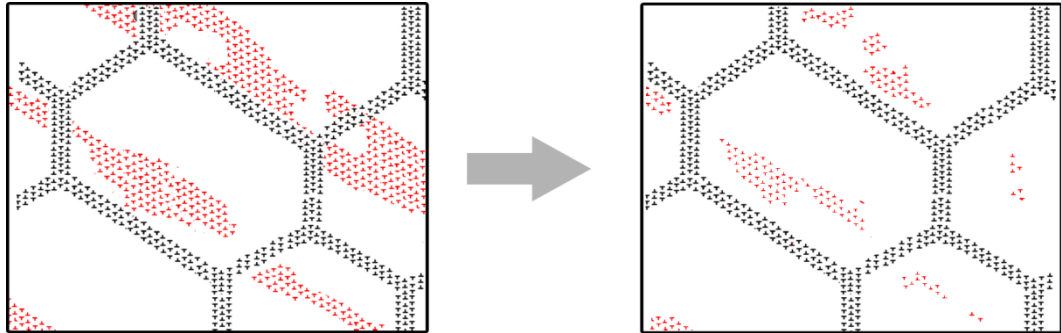
FIGURE 6-20: ANNIHILATION OF STATIC DISLOCATIONS

Equation 6-10 may be used to model the annihilation of static dislocations.

$$\dot{\rho}_s = -\rho_s{}^{3/2}\bar{v}_c \qquad\qquad \textbf{6-10}$$

During plastic deformation the velocity of climb in equation 6-10 is greater. The strain-enhanced annihilation of static dislocations may explain the transient softening behaviour observed in the fatigue loading of tempered martensitic steels. Thermally induced climb would explain the reduction in dislocation density reported by Mebarki et al (2004).

One issue with this approach is that it suggests that the amount of transient cyclical softening would reduce as a result of over-tempering. Zhang et al (2007) observed transient cyclical softening behaviour in over-tempered specimens during strain controlled symmetrical fatigue loading.

The Dyson-Semba model does not predict the initial transient cyclical softening reported in similar tempered martensitic hot work steels. This behaviour may be modelled using a phenomenological model describing the strain induced annihilation of static dislocations as shown in equation 6-11.

$$\dot{\rho}_s = K_{p,s}\sqrt{\rho_s}\left(1 - \sqrt{\frac{\rho_s}{\rho_{ss,s}}}\right)\dot{\varepsilon}_p$$

6-11

The model parameters that differ to the developed model that are required when including the static dislocation density are shown in Table 6-11.

TABLE 6-11: MODEL PARAMETERS INCLUDING THE STATIC DISLOCATION DENSITY

ρ_m	ρ_s	r_p	k_{sg}	$\rho_{ss,m}$	$\rho_{ss,s}$	$K_{p,m}$	$K_{p,m}$	α_2
m^{-2}	m^{-2}	nm	-	m^{-2}	m^{-2}	m^{-1}	m^{-1}	-
8×10^{13}	1.2×10^{14}	1.3	6.26	8×10^{12}	1.2×10^{13}	1×10^{6}	5×10^{7}	0.17

The predicted behaviour and behaviour measured from AISI H11 is compared in Figure 6-21 considering isothermal strain controlled fatigue with a strain amplitude of ±1% and a strain rate of 0.01/ s.

A) PREDICTED BEHAVIOUR OF AISI H13   B) MEASURED BEHAVIOUR OF AISI H11
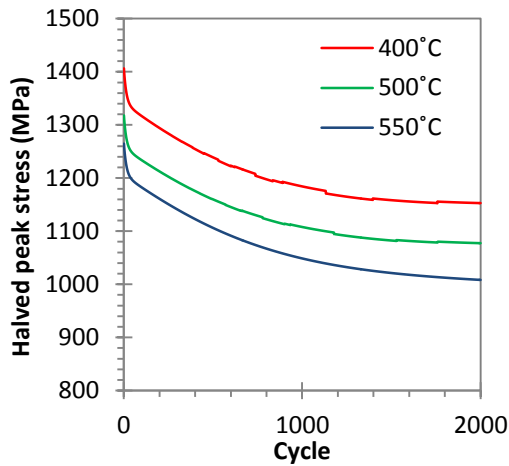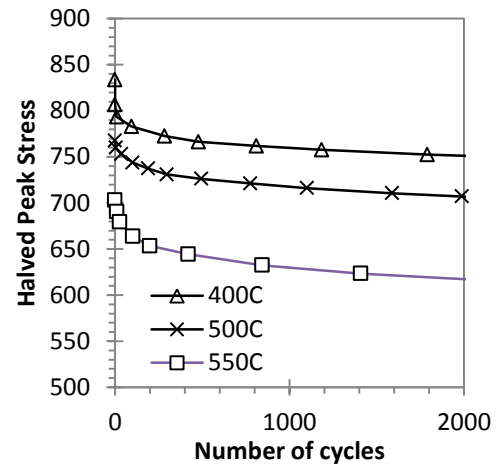
FIGURE 6-21: HALVED PEAK STRESSES PER CYCLE IN ISOTHERMAL STRAIN CONTROLLED FATIGUE WITH A STRAIN AMPLITUDE OF ±1%, AND A STRAIN RATE OF 0.01/S.

The reduction in static dislocation density captures the initial transient softening. The impact of this mechanism upon the predicted work hardening behaviour during fatigue is examined in Figure 6-22 for strain controlled fatigue loading.

It can be seen that to capture the transient cyclical softening behaviour, it is necessary to describe the change in dislocation structure as a response to fatigue. The solution proposed is to include the static dislocations that form during the

martensitic transformation during quench. The rapid annihilation of these dislocations during fatigue may capture the transient softening behaviour.

This approach explains why the reduction in dislocation density observed by Mebarki et al (2004) does not have to relate to Friedel recovery when applying the proportional relationship between the mobile dislocation network spacing and the subgrain diameter. Friedel recovery is still applicable however not under the time scales of interest.

The transient cyclical softening behaviour has not been measured in the as-heat treated condition. To describe the measured behaviour it was not necessary to include this mechanism.
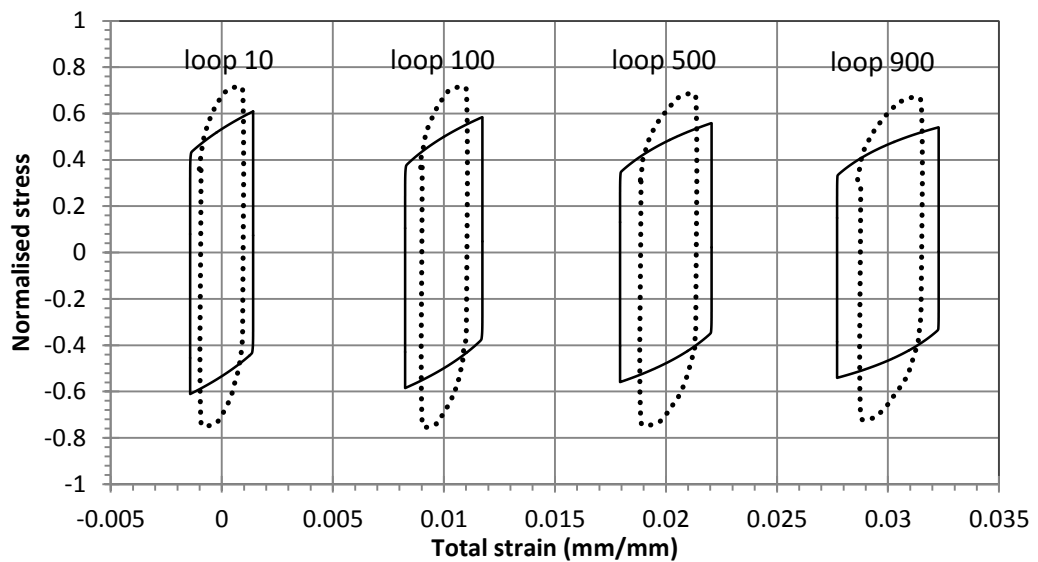
FIGURE 6-22: SELECT HYSTERESIS LOOPS DURING ISOTHERMAL STRAIN CONTROLLED FATIGUE AT 500°C WITH A STRAIN AMPLITUDE OF ±0.9% AND A STRAIN RATE OF 0.01/S.

6.6 MODEL SUMMARY

The complete model developed to describe AISI H13 has been summarised in this section. The temperature dependence of the shear and elastic modulus (Pa) are shown in equation set 6-12. The complete model is shown in equation set 6-13 to equation 6-18. The material model parameters are given in Table 6-12 to Table 6-16.

TEMPERATURE DEPENDENCE OF THE SHEAR AND ELASTIC MODULUS

$$G = \left(91540 - 38.7T(K)\right) * 10^6$$

$$E = \left(216 - 0.11T(°C)\right) * 10^9$$

6-12

6-13

THERMAL FLOW RULE – DYSON-SEMBA MODEL

$$\dot{\varepsilon}_{p,t} = \varepsilon_0 \sinh\left(\frac{\bar{\sigma}_t}{\sigma_0}\right)$$

$$\dot{\varepsilon}_0^i = \frac{1}{M} 2K_E\left(1 - \phi_{sgb}\right)\rho_m \sqrt{2/3} \left(\sqrt{\frac{\pi}{4\phi_p}} - 1\right) \phi_{pmx}. D_{di0}. C_{ji0} exp\left(-\frac{Q_{j,i}}{RT}\right)$$

$$\sigma_0 = \frac{MkT}{b^2 \lambda_p}$$

$$\bar{\sigma}_t = \sigma - \alpha_1 GbM\sqrt{\rho_m} - \sigma_k$$

6-14

ATHERMAL FLOW RULE – BASOALTO MODEL

$$\dot{\varepsilon}_{p,a} = K_E\left(1 - \phi_{sgb}\right)\frac{b^2}{M^2 B}\left(\frac{k_a}{\pi(1-v)}\frac{\bar{\sigma}_a}{GbM}\right)^2 \bar{\sigma}_a$$

$$\bar{\sigma}_a = |\sigma| - \frac{\alpha_2 MGb}{\lambda_p} - \sigma_k$$

6-15

TEMPERATURE DEPENDENCE OF THE SUBGRAIN INTERIOR PARTICLES

$$C_e = \exp\left(\frac{dS}{R}\right) \times \exp\left(-\frac{dHs}{RT}\right)$$

$$C_o = \exp\left(\frac{dS}{R}\right) \times \exp\left(-\frac{dHs}{RT_s}\right)$$

$$\phi_{p,ht} = \frac{(C_o - C_e)}{(C_\# - C_e)}$$

$$\phi_{p,rt} = \frac{C_o}{C_\#}$$

$$r_{ht} = r_{,rt}\left(\frac{\phi_{p,ht}}{\phi_{p,rt}}\right)^{\frac{1}{3}}$$

WORK HARDENING **6-16**

$$\dot{\sigma}_k = h\left(1 - \frac{\sigma_k}{\sigma H^*}\right)\dot{\varepsilon}_p$$

$$\acute{h} = E(1 - K_E\phi_S)$$

$$H^*_{sgb} = \frac{2\phi_{sgb}}{1 + 2\phi_{sgb}}$$

$$\phi_{sg} = \frac{2w\sqrt{\rho_m}}{k_{sg}}$$

PARTICLE COARSENING **6-17**

$$\dot{r}_p = \frac{K}{3r_{p,0}^2}$$

$$K = K_0 Exp\left[-\frac{Q_p}{RT}\right]$$

MOBILE DISLOCATION\ SUBGRAIN KINETICS **6-18**

$$\dot{\rho}_m = K_p\sqrt{\rho_m}\left(1 - \sqrt{\frac{\rho_m}{\rho_{ss}}}\right)\dot{\varepsilon}_p$$

TABLE 6-12: FLOW RULE PARAMETERS

ρ_m m^{-2}	M	b Nm	d_v m^{2}s^{-1}	Q_{dj} kJ.mol^{-1}	ϕ_{pmx} %	r_p nm	α_1 -
2×10^{14}	3.1	0.254	1.9×10^{-4}	266	1.9	1.2	0.5

k_a -	B Pa s	α_2 -					
0.01	4.5×10^{-5}	0.236					

TABLE 6-13: TEMPERATURE DEPENDENCE OF THE PARTICLE PHASE

dS	dHs	C#	Co
193	140,000	10500	200

TABLE 6-14: WORK HARDENING

w	λ_{sg}	K_E
nm	nm	-
100	700	0.6

TABLE 6-15: PARTICLE COARSENING

K_0
$m^2 s^{-1}$
8×10^{-16}

TABLE 6-16: SUBGRAIN COARSENING

k_{sg}	ρ_{ss}	K_p
-	m^{-2}	m^{-1}
9.9	2×10^{12}	1×10^{6}

6.7 MODEL DEVELOPMENT CONCLUSION

The plastic flow behaviour of tempered martensitic hot work tool steel has been described by using an athermal flow rule, a thermal flow rule, particle coarsening, the reduction in dislocation density to a steady state and subgrain coarsening.

The Dyson model has been used to describe the strain rate sensitive flow behaviour of tempered martensitic steel. The athermal behaviour has been captured using the Basaolto model. The approach developed by Semba (2003) has been followed to capture the relevant microstructural instability of hot work tool steel during hot forging.

The model suggests that the intra-lath particles are most important microstructural feature in determining the mechanical properties of AISI H13, followed by the dislocation density and lath\ subgrain spacing.

The model was successful in describing the temperature and strain rate sensitivity in yield behaviour. The model cannot be applied to the subgrain interior particle supersolvus temperature. For the given assumptions, a different mechanism dictates flow behaviour for this regime.

The plateau in work hardening behaviour is captured through plastically hard subgrain boundaries however the initial fast rate of work hardening was not predicted.

The over-tempering behaviour of the alloy is described through particle coarsening which has been calibrated using the data measured by Bischof et al (2008).

The reduction in mobile dislocation density and subgrain coarsening observed in similar alloys is modelled using the phenomenological approach outlined in the Dyson-Semba model. A relationship is assumed between the mobile dislocation network link length and the spacing of the dislocation structure. The rate of subgrain coarsening was calibrated against the measurements given by Sauzay et al (2008).

The model is capable of predicting the material behaviour relevant to hot work tooling under thermo-mechanical loading. The following chapter examines the ability of the model to predict behaviour not used within development.

7 DIE MATERIAL MODEL VERIFICATION

The model developed to describe the plastic flow behaviour of AISI H13 has been tested against conditions not used within the development of the model. This testing is necessary to determine the conditions where the model is applicable and identify deficiencies with the model that may impact the accuracy of life prediction.

The model has been tested with regard to work hardening behaviour, fatigue behaviour and over-tempering behaviour. The purpose of these tests is to determine the suitability of the modelling approaches and assumptions.

Mechanical tests have been performed with a step change in temperature. These test results have been used to examine the work hardening approach.

The suitability of the approach developed to describe thermal softening is tested by comparing the fatigue behaviour of an over-tempered specimen to the predicted behaviour of the model.

The ability of the model to describe the cyclical behaviour displayed by the material is examined through testing the model at different strain amplitudes and comparing against measured behaviour.

7.1 WORK HARDENING BEHAVIOUR

Pre-strained tensile tests have been performed to determine whether the model predicts the observed behaviour upon continuing deformation at a higher temperature.

Figure 7-1 compares the measured and predicted work hardening behaviour for step changes in test temperature. From Figure 7-1 it can be seen that the model predictions are acceptable for continued deformation at 500°C however; at higher temperatures the model does not capture the continued work hardening behaviour. The temperature dependence of the pre-strained increase to yield strength is not captured by the work hardening model.

A) 20°C @0.01/s UNTIL 0.83% PLASTIC STRAIN FOLLOWED BY 500°C @0.01/s
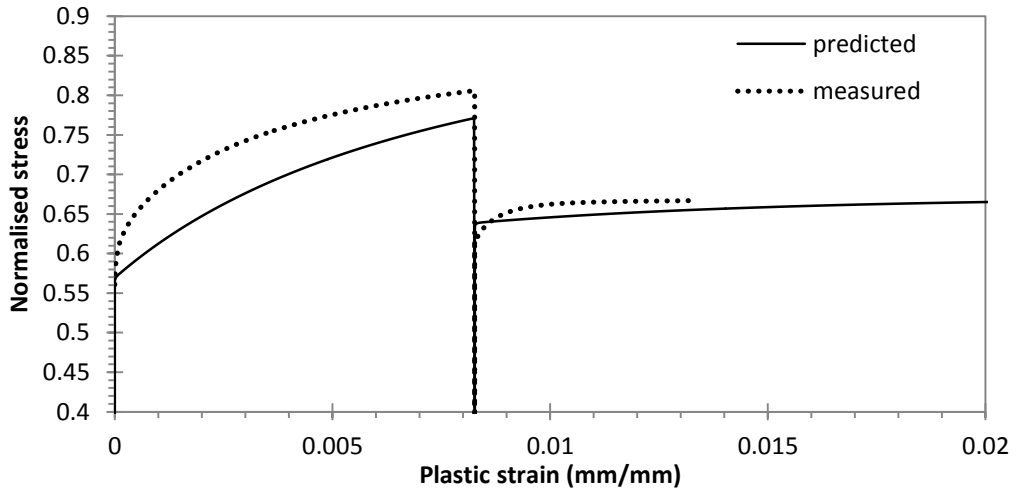
B) 20°C @0.01/s UNTIL 0.97% PLASTIC STRAIN FOLLOWED BY 550°C @0.01/s
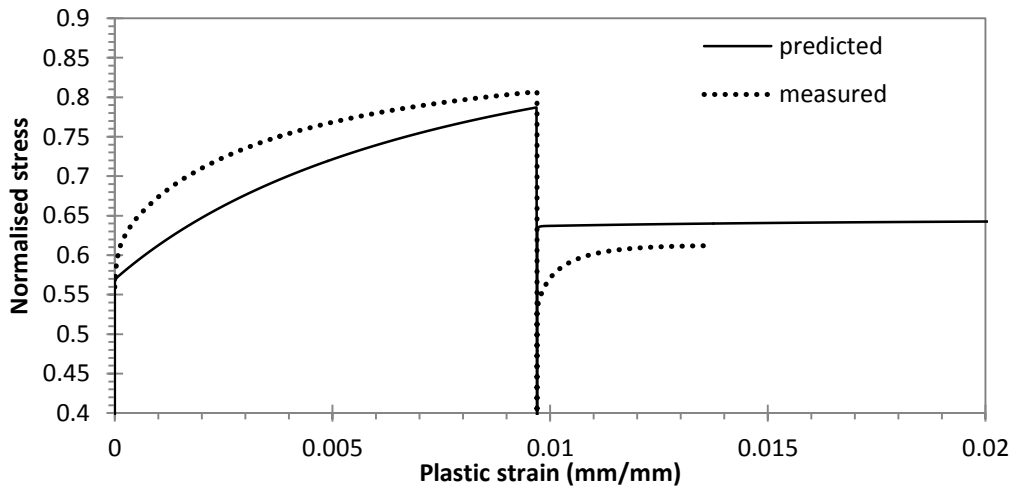
C) 20°C @0.01/s UNTIL 0.70% PLASTIC STRAIN FOLLOWED BY 600°C @0.01/s
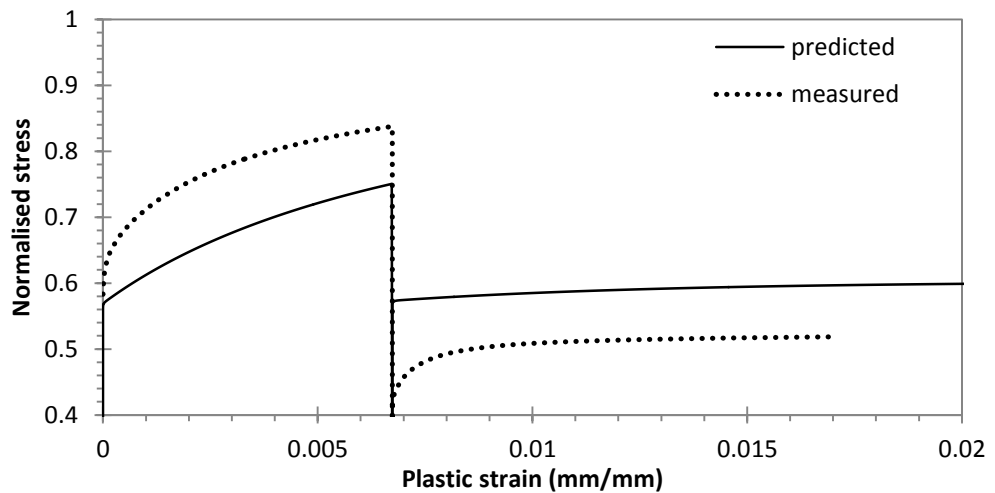
FIGURE 7-1: STEP CHANGE IN TEMPERATURE ASSUMING PLASTICALLY HARD SUBGRAIN BOUNDARIES

It is possible to predict similar behaviour when describing the work hardening as a result from dislocation interaction using a Taylor stress. The temperature dependence of the shear modulus captures the temperature sensitivity of the pre-strain. Mebarki et al (2004) noted high dislocation density near subgrain boundaries from examining TEM micrographs of fatigued hot work tool steel. Ghoniem et al (1990) proposed that the work hardening behaviour of 9-12% Cr tempered martensitic steels is caused by dislocation pile ups at subgrain boundaries. The Taylor back stress may be modified to include the immobile dislocations as shown in equation 7 1.

$$\bar{\sigma} = \sigma - \alpha_1 GbM \sqrt{\rho_m + \rho_{im}}$$

7-1

Where;

ρ_{im} The immobile dislocation density (m^{-2})

Equation 7-2 is a phenomenological equation that may be used to describe the increase in immobile dislocation density which reaches a dynamic equilibrium associated with the interaction between immobile and subgrain boundary dislocations.

$$\dot{\rho}_{pin} = k_1 \rho_m \left(1 - \frac{\rho_{pin}}{\rho_{\max}}\right)$$

7-2

Where;

ρ_{pin} The immobile dislocation density (m^{-2})

ρ_{max} The maximum immobile dislocation density (m^{-2})

k_1 The frequency that mobile dislocations become immobile (s^{-1})

The frequency that mobile dislocations become immobile is given by the equation 7-3.

$$k_1 = \frac{\bar{v}_g}{\lambda_{sg}}$$

7-3

Equation 7-3 may be substituted into equation 7-2. The Orowan-Bailey shear strain rate relationship may be rearranged for the velocity of dislocation glide and substituted into this expression. This obtains equation 7-4.

$$\dot{\rho}_{pin} = \frac{M}{\lambda_{sg} b}\left(1 - \frac{\rho_{pin}}{\rho_{\max}}\right)\dot{\varepsilon}_p \qquad \textbf{7-4}$$

The predicted behaviour considering step changes in test temperature are shown in Figure 7-2 assuming a $\rho_{\max}$ of $1\times10^{15} m^{-2}$. The temperature dependence of the shear modulus allows for the prediction of a temperature sensitive increase in yield strength resulting from cold work.

A higher alpha coefficient in the Taylor stress equation results in predicting similar magnitudes of work hardening behaviour. To predict similar flow behaviour, an alpha coefficient of 0.8 and a mean particle radius of 1.5nm has been used. With an increased Taylor stress, the thermal softening behaviour can no longer be captured through particle coarsening on its own. It is necessary to include thermally induced dislocation annihilation.

The complication involved in this approach is modelling cyclical loading flow behaviour. It is proposed that immobilised dislocations either join the mobile dislocation density or annihilate with mobile dislocations upon load reversal. The fraction of pinned dislocations that annihilate with mobile dislocations may be given by k_{mob}. Assuming that all dislocations pinned by subgrain boundaries escape upon load reversal, the impact upon the mobile dislocation density may be calculated as shown below:

$$\rho_m = \rho_{m,i} + \rho_{pin}(1 - 2k_{mob}) \qquad \textbf{7-5}$$

A k_{mob} of 0.5 results in no change to the mobile dislocation density as a result of the reversal of slip direction. This is desirable to avoid complication in modelling the change in mobile dislocation density during fatigue loading.

A) 20°C @0.01/S UNTIL 0.83% PLASTIC STRAIN FOLLOWED BY 500°C @0.01/S
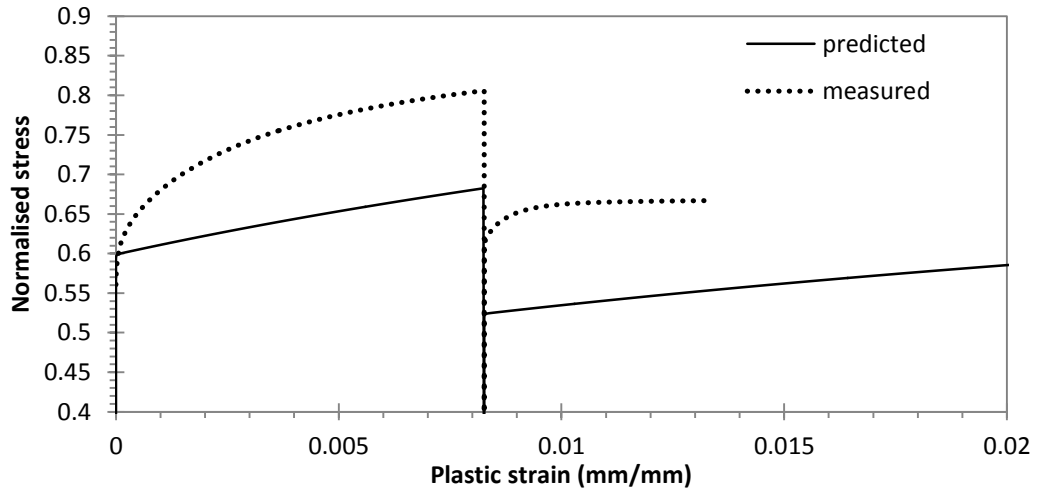
B) 20°C @0.01/S UNTIL 0.97% PLASTIC STRAIN FOLLOWED BY 550°C @0.01/S
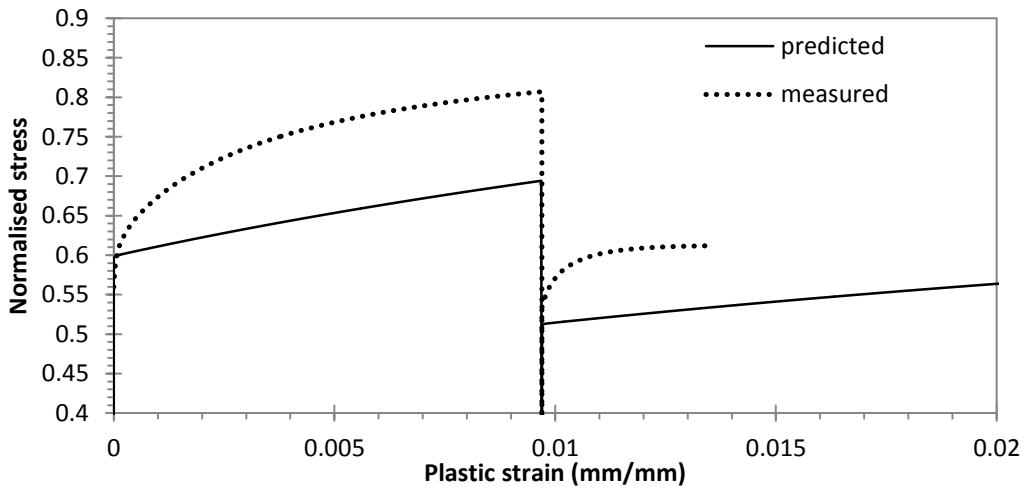
C) 20°C @0.01/S UNTIL 0.70% PLASTIC STRAIN FOLLOWED BY 600°C @0.01/S
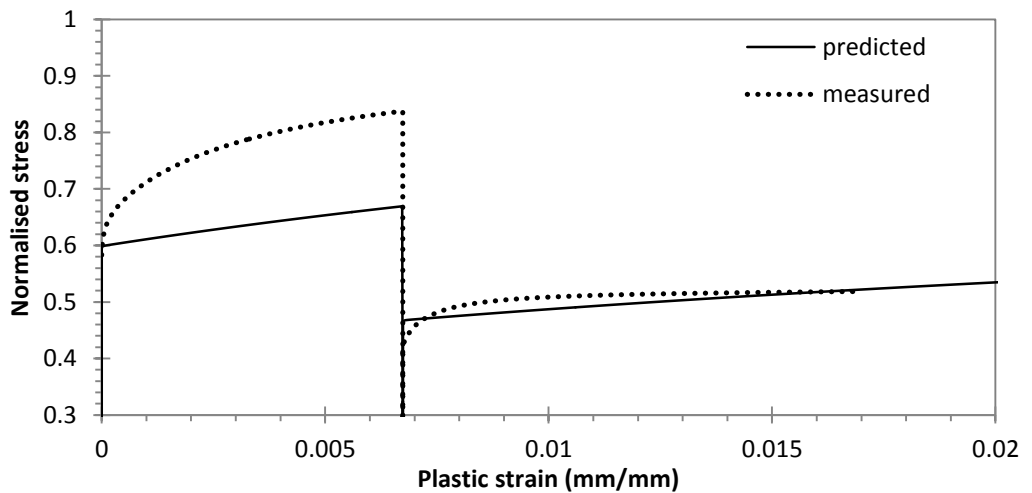
FIGURE 7-2: STEP CHANGE IN TEMPERATURE ASSUMING DISLOCATION PILE UPS

In conclusion, the two-bar composite model developed by Semba (2003) is successful in describing the plateaux in work hardening but does not capture the temperature sensitivity of work hardening.

It is possible that the temperature sensitivity of the work hardening arises from the temperature sensitivity of the shear modulus within the Taylor stress. The increase in Taylor stress may be caused by dislocation pile ups at subgrain boundaries or an increase in mobile dislocation density. The mobile dislocation density has been observed to reduce as a response to fatigue loading, indicating that dislocation pile ups may be a possible explanation for this behaviour. The complication encountered is describing the change in immobilised dislocation density upon load reversal, and including thermally induced dislocation annihilation.

7.2 STRAIN AMPLITUDE SENSITIVITY

Additional fatigue tests have determined the impact of the strain amplitude upon the cyclical behaviour under symmetrical tension-compression loading conditions. The rate of cyclical softening increases with increasing strain amplitude.

Figure 7-3 compares the predicted and measured halved peak stress for isothermal fatigue at 500˚C at a strain rate of 0.01/s and different strain amplitudes. The model predictions include the variation in strain amplitude during the start of fatigue loading.
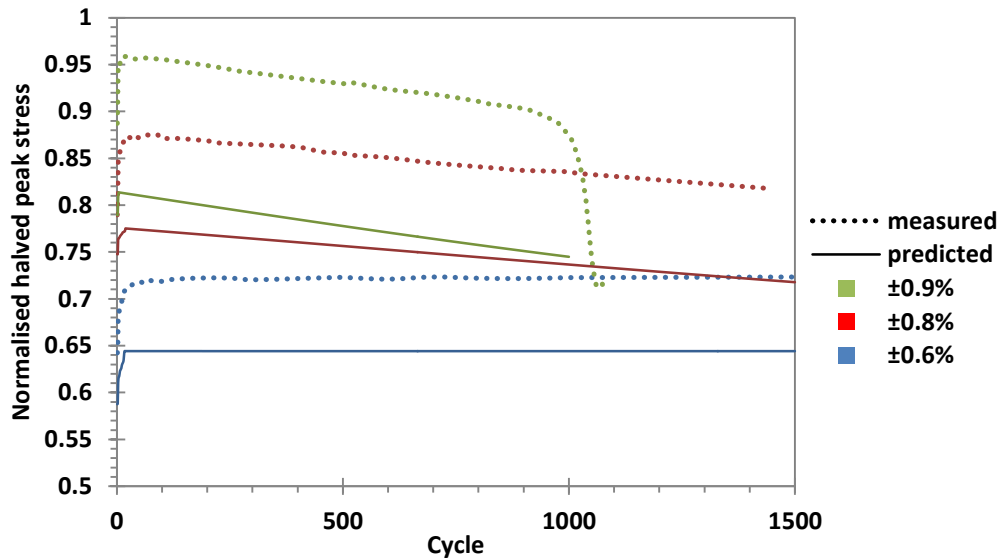
FIGURE 7-3: STRAIN AMPLITUDE SENSTIIVTY FOR STRAIN CONTROLLED ISOTHERMAL

The model predicts similar trends in halved peak stress considering strain amplitude sensitivity however predicts lower magnitudes of halved peak stress due to the inability to capture the initial sharp rise in work hardening.

It can be concluded that the strain amplitude sensitivity of the linear stage of fatigue softening is adequately captured applying the Dyson-Semba model.

7.3 OVER-TEMPERED BEHAVIOUR

A fatigue test specimen was over-tempered for three hours at 600°C. The fatigue test was performed with strain amplitude of ±1%, a strain rate of 0.01/s and a temperature of 500°C. Figure 7-4 compares the predicted and measured behaviour.
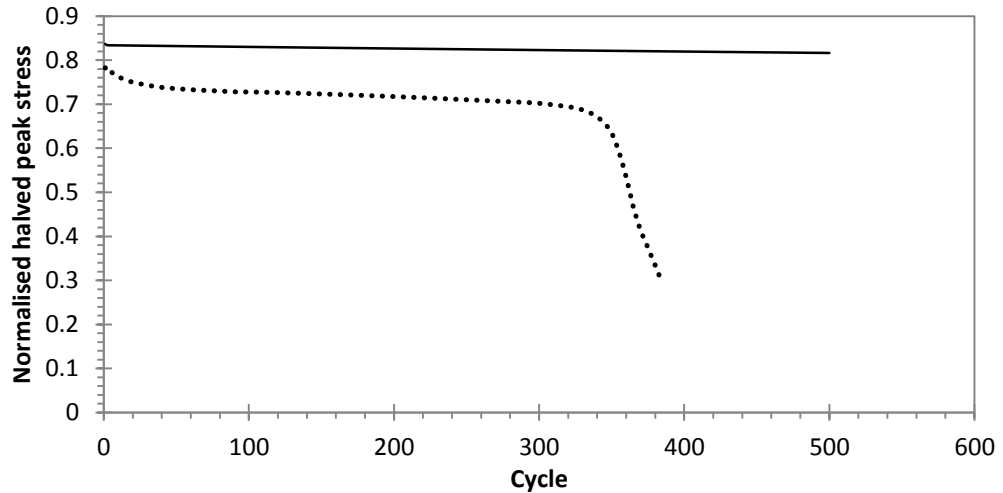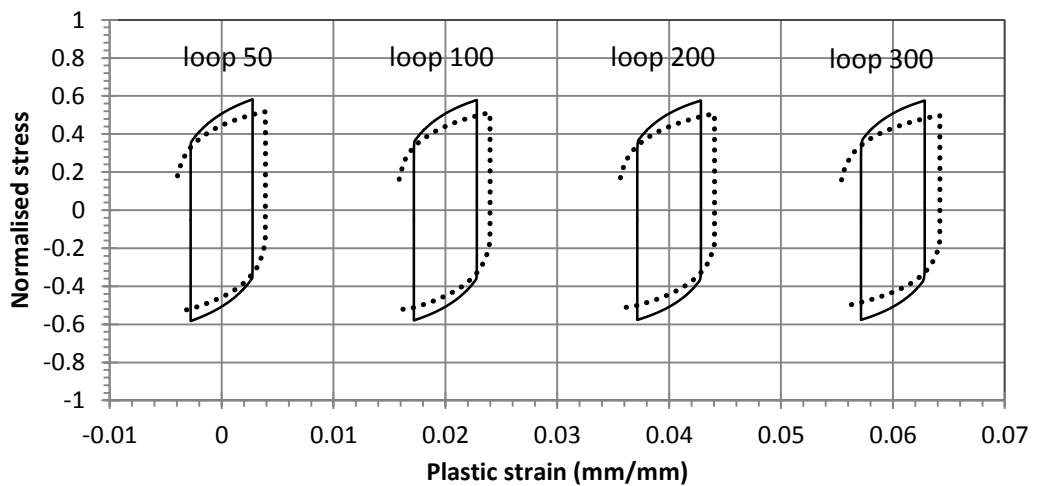
FIGURE 7-4: STRAIN CONTROLLED FATIGUE AT A TEMPERATURE OF 500°C, A STRAIN RATE OF 0.01/S AND A STRAIN AMPLITUDE OF ±0.8% OF A SPECIMEN OVER-TEMPERED BY 3 HOURS AT 600°C.

The model does not predict the same extent in softening as measured from the test specimen. The transient cyclical softening behaviour has not been predicted however the predicted hysteresis loops are similar to the measurements. The particle coarsening model cannot capture the softening of the material at the high temperature of 600°C.

7.4 MODEL VERIFICATION CONCLUSION

The model has been tested in its ability to describe flow behaviour with a step change in temperature, the ability to predict the impact of different strain

239

amplitudes during strain controlled fatigue, and the fatigue behaviour of an over-tempered specimen.

Work hardening: Impact of pre-strain

Tensile specimens have been pre-strained at room temperature with deformation continued at higher temperature. The tests showed that the work hardening is temperature sensitive. The two-bar composite model used to describe work hardening did not capture the temperature dependence observed from work hardening.

The implication of this deficiency is that the model predicts higher yield stresses when the die has undergone cold work. This would result in longer life predictions for loading conditions with significant cold work.

The temperature dependence of the shear modulus within a Taylor back stress can capture such temperature sensitivity. This suggests that dislocation pile ups may be a more suitable explanation for work hardening behaviour. This approach becomes complicated when considering the impact of load reversal and requires the modelling of thermally induced dislocation annihilation to capture over-tempering behaviour.

Strain-induced softening: Strain amplitude in fatigue tests

Strain controlled, symmetrical tension-compression fatigue tests were performed at the same temperature and strain rate but with varying strain amplitudes to measure the impact upon strain-induced softening behaviour.

The model successfully predicts the impact of the strain amplitude upon cyclical softening behaviour during fatigue loading. The cyclical softening behaviour of the material should be adequately captured by the model.

Thermally induced softening: Fatigue behaviour

A fatigue specimen was over-tempered prior to testing. The specimen showed an initial phase of non-linear cyclical softening, not seen in other conditions, but documented in the literature regarding the fatigue behaviour of hot work tool steels.

The impact of over-tempering upon fatigue behaviour has not been captured by the model. The implication of this deficiency is that longer die life than reality

would be predicted considering the impact of thermal exposure to high temperatures.

The initial transient cyclical softening behaviour measured in an over-tempered condition and reported from similar hot work tool steels is not predicted by the model. The implication of not including the transient cyclical softening behaviour in the model is that a stronger material response is predicted during fatigue loading. Longer die life would be predicted as a result of this issue.

8   DIE LIFE PREDICTION

The model has been applied to the life prediction of the "smiley face" defect examined in chapter 3. This defect is chosen as it is an unmistakable example of die failure due to plastic deformation.

A simple approach to life prediction has been adopted where a reference stress and temperature cycle is used to describe the thermo-mechanical loading responsible for die failure. The algorithm used to predict life is illustrated in Figure 8-1.

The advantage of this approach is that it is computationally inexpensive. The disadvantage is that the location of failure must be known prior to life prediction. The impact of tool design alterations requires finite element modelling to determine the difference in the thermo-mechanical cycle at the location of interest. To predict the location of failure or compare competing preform designs, the model needs to be implemented within FEA to predict a relative measure to assess the suitability of die designs

There are different approaches that may be taken to determine the failure criteria for life prediction. One option is to use a critical deviation of a key microstructural feature from the initial condition. Another approach is to determine the plastic strain associated with the formation of the "smiley face" defect. The latter approach has been adopted due to difficulty in adequately measuring important microstructural features when characterising the material.

The thermo-mechanical loading at the location of failure is required as an input into the model. This can be approximated from the FEA model used in chapter 3.
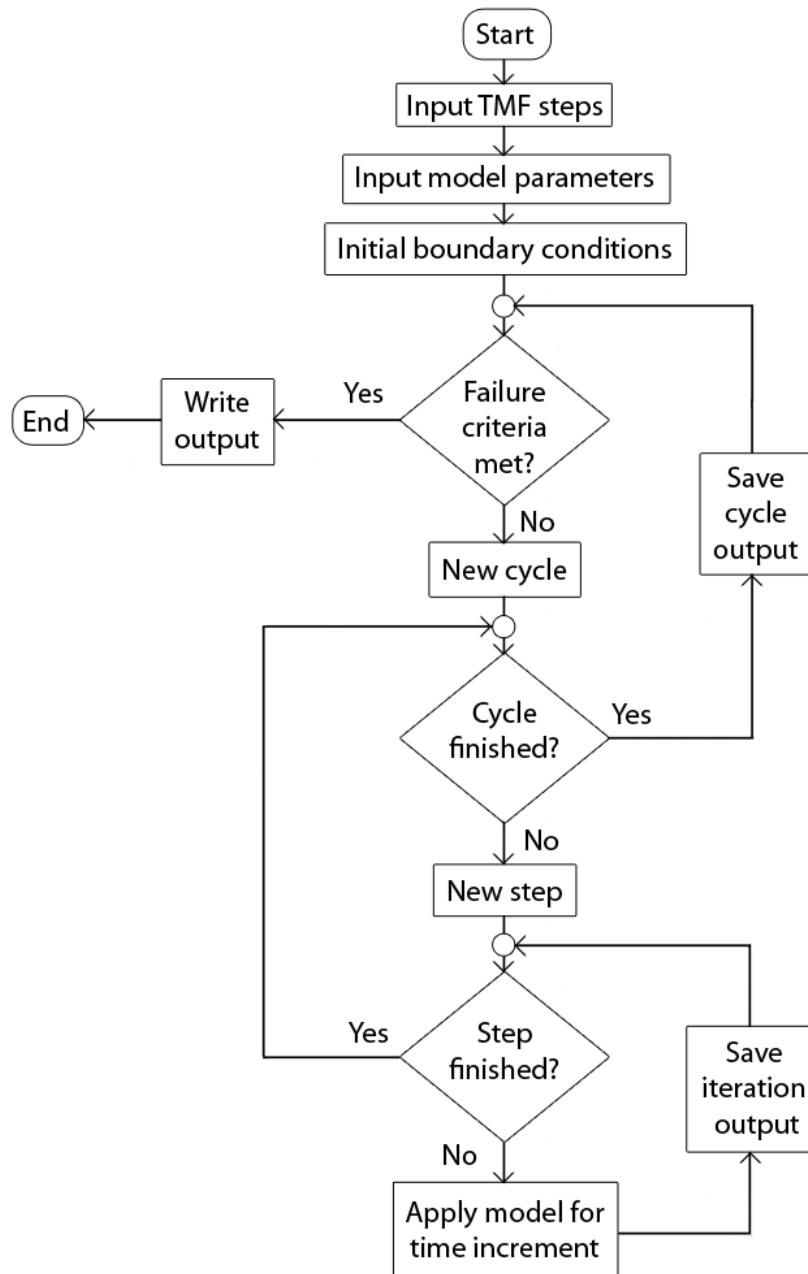
FIGURE 8-1: THERMO-MECHANCIAL FATIGUE LIFING ALGORITHM

The life predictions within this chapter have been normalised against the average die life measured from the forge. The predicted values are available in chapter 12: Appendix B. Access to this information is controlled by the AFRC and the industrial partner to this work.

8.1 THE FAILURE CRITERIA

The failure criteria used in this example is the amount of plastic strain associated with the formation of a smiley face defect. One way to experimentally measure the plastic strain associated with this defect is to measure the change in geometry of the worn tool using a 3D scan. This is shown in Figure 8-2.

The deformation appears to be localised close to the surface of the die. It is possible to estimate the extent of deformation by tracking the changes in phase segregation observed in micrographs. These act as markers to measure displacements experienced by the tooling during forging operations. The error involved in this approximation arises from measuring lengths from 2D micrographs that relate to deformation in a 3D body. To mitigate the impact of this error, the 2D slice has been taken in the region where plane strain is most applicable. Figure 8-3a) highlights the phase segregation and the plastically deformed region. The un-edited micrograph is shown in figure b).
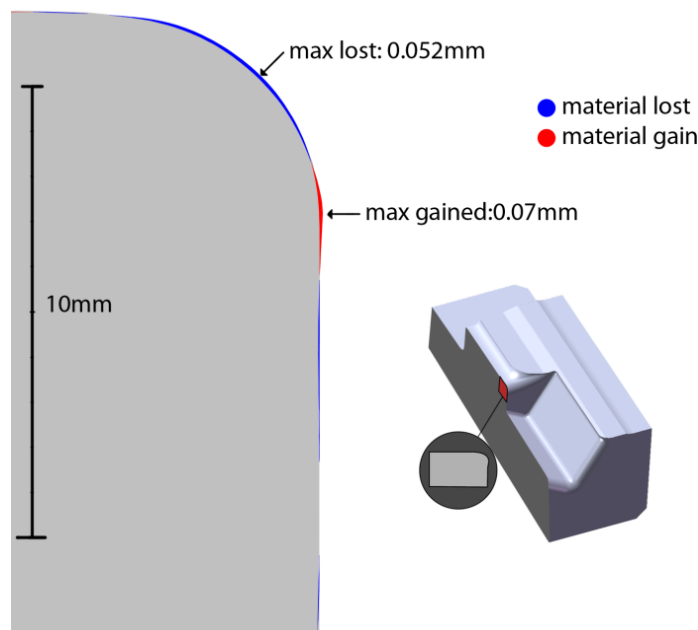
FIGURE 8-2: 3D SCAN MEASUREMENTS OF THE "SMILEY FACE" DEFECT
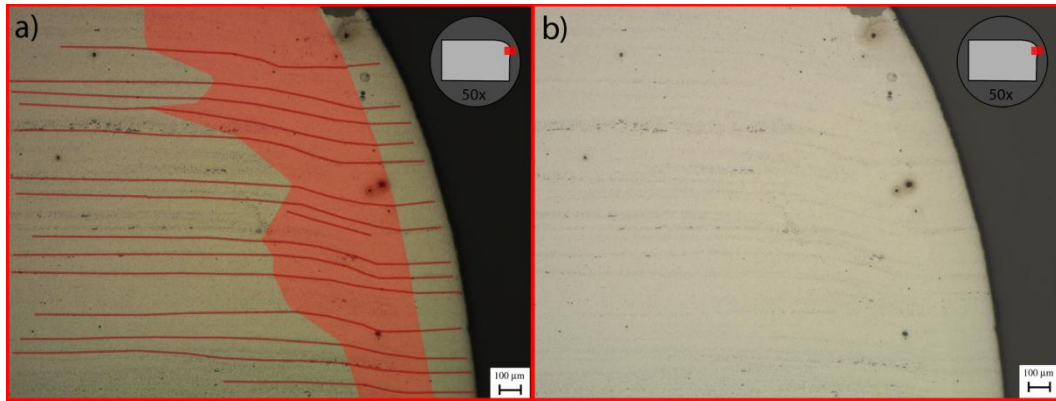
FIGURE 8-3: THE LOCALISED DEFORMED REGION

The longitudinal plastic strain may be approximated by assuming that the length (*L*) of the original phase segregation is the sum of the original length (*L*$_o$) and the displacement measured from the 3D scan, *u*. This is illustrated in Figure 8-4.

$$\varepsilon_p = \ln\left(\frac{L+u}{L_o}\right)$$

FIGURE 8-4: UNIAXIAL PLASTIC STRAIN ESTIMATION

Table 8-1 gives the plastic strain approximations considering the average, upper and lower measurements of the length of deformed substrate.

TABLE 8-1: PLASTIC STRAIN CRITERIA APPROXIMATIONS

	Final length (mm)	Initial length (mm)	True plastic strain
maximum	1.18	1.10	6.13%
average plus st. dev.	1.36	1.29	5.27%
average minus st. dev.	0.989	0.919	7.34%

Depending upon the depth of the deformed region, the plastic deformation at failure may vary between 5.27% and 7.34%. The lower bound plastic strain is used as the failure criterion for failure through the formation of a "smiley face".

245

8.2 THE THERMO-MECHANICAL LOADING

The thermo-mechanical loading of the tool may be approximated by the stress and temperature approximated from FEA at a reference location within the tooling. The die temperature and Von Mises stress approximated by FEA at the collapsed radius is shown in Figure 3-33 and Figure 3-34. Figure 3-32 highlights the locations of interest.

From Figure 3-34, the greatest amount of plastic deformation has been approximated to occur at location 1. The thermo-mechanical loading input into the lifing model is shown in Figure 8-5. The maximum von Mises stress and temperature predicted by FEA at this location is 1200MPa and 580°C respectively.
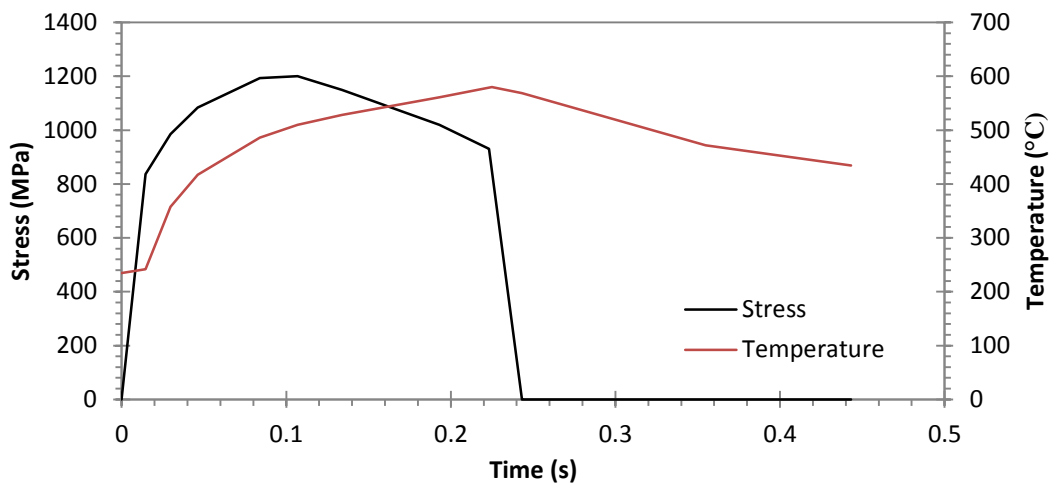
FIGURE 8-5: THERMO-MECHANICAL LOADING

It is assumed that the thermo-mechanical loading is not significantly affected by the progression of wear to the tooling.

8.3 LIFE PREDICTION

The lifetime of upsetting tooling is predicted using the model and parameters shown in section 6.6. The thermo-mechanical loading is given in Figure 8-11. The failure criterion is 5.27% plastic strain.

Figure 8-6 shows the predicted change in plastic strain, particle radius, mobile dislocation density and subgrain diameter where the peak stress is 1200MPa and the peak temperature is 580°C.

The life of hot forging tooling is commercially sensitive, so the predictions have been normalised.

The model over-predicts tool life by a factor of 63.148. The error in the predicted life may arise from numerous factors, relating to assumptions and made within the material model, the boundary conditions and the failure criterion.

The batch size for producing components sets an upper limit to die life, which may contribute to differences between actual die life and measured die life. The tooling is re-cut after forging a batch of components, regardless of the amount of damage present.

The model predicts negligible change in mobile dislocation density and subgrain diameter in the failed die. The timescale for over-tempering to occur is too short for significant particle coarsening, similar to the findings from chapter 3.

The loading is entirely compressive compared to the tension-compression loading used to examine the material behaviour. In the tension-compression loading there is greater accumulated plastic deformation within a cycle. This plastic deformation drives the strain-induced softening mechanisms. This difference explains the small contribution of strain-induced mechanisms in the predicted behaviour.

A) PLASTIC STRAIN

B) MEAN PARTICLE RADIUS

C) MOBILE DISLOCATION DENSITY

D) SUBGRAIN DIAMETER

A) PLASTIC STRAIN
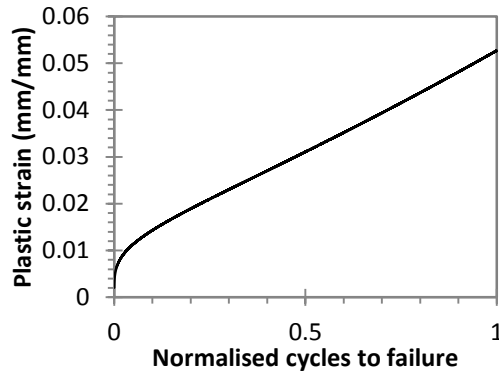
B) MEAN PARTICLE RADIUS
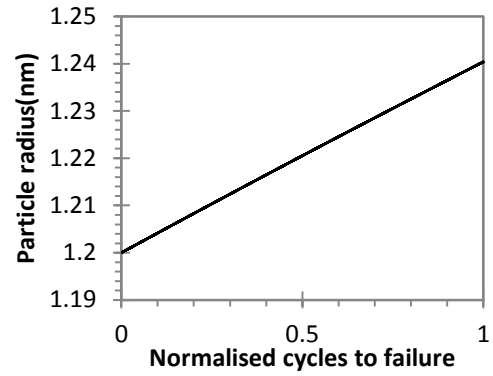
C) MOBILE DISLOCATION DENSITY
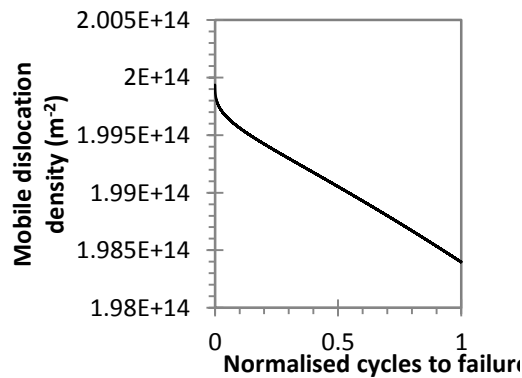
D) SUBGRAIN DIAMETER
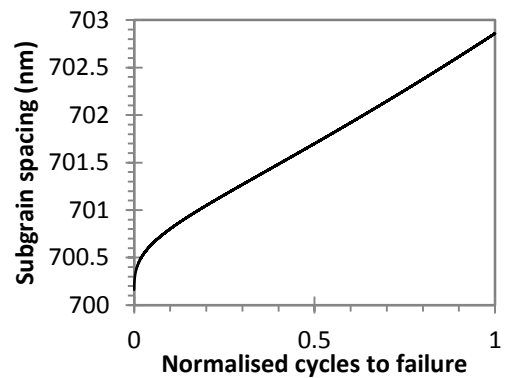
FIGURE 8-6: MODEL PREDICTIONS

The thermo-mechanical loading has been approximated from FEA of the forming process. The assumptions made within the FEA model impacts the thermo-mechanical loading input into the lifing model. Possible causes of error include inaccurate descriptions of friction, heat transfer, press kinetics and\ or workpiece flow stress.

Figure 8-7 shows the sensitivity of die life prediction to the thermo-mechanical loading. The life predicted has been normalised against the die life measured within the forge. In figure a) the maximum temperature is constant at 580°C. In figure b) the maximum die stress is constant at 1200MPa. To predict similar die life applying these model assumptions the peak stress needs to be greater than 1250MPa with a peak temperature nearing 640°C.
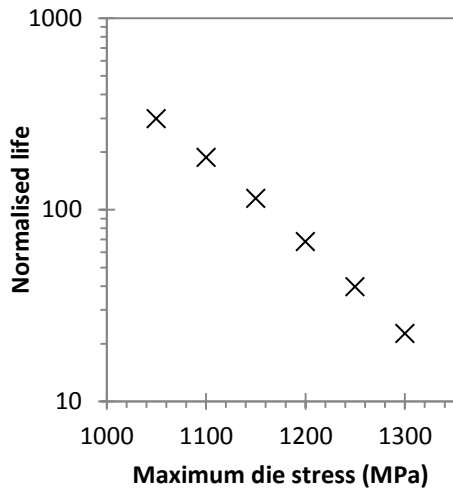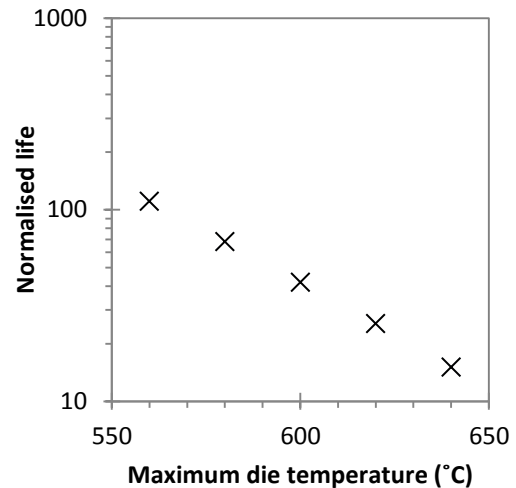
FIGURE 8-7: SENSITIVITY OF DIE LIFE PREDICTION

8.4   MODEL APPLICATION DISCUSSION

A number of factors may explain the discrepancies between the predicted and measured tool lives. These may arise from the material model, the boundary conditions or the failure criteria. These aspects are discussed in the following section.

8.4.1   THE MATERIAL MODEL

One cause for error in life prediction lies in the deficiencies of the plastic flow model. The deficiencies that have been identified within the model are listed below:

Temperature dependencies

The model in the current form does not account for supersolvus behaviour of the subgrain interior particle phase. The phenomenological approach to capturing the temperature dependence of the particle phase has resulted in a low solvus temperature. This problem is not currently an issue for the thermal loading of interest.

Over-aging behaviour

The model does not predict the over-tempering behaviour at high temperature. The role of over-tempering is small in the forging process of interest, mitigating the impact of this deficiency in this application of the model.

Work hardening rate

The model does not capture the initial fast rate of work hardening. The low initial rate of work hardening predicted by the model incurs lower life prediction opposed to higher life prediction. As the model predicts greater life than observed in the forge, a different cause of error has a greater impact upon life prediction.

Work hardening temperature sensitivity

The model does not predict the temperature sensitivity of cold work. The inability to capture the temperature sensitivity of cold work is not an issue in the boundary conditions of interest. Figure 8-8 shows the model predictions for the first cycle. It can be seen that deformation of the tool is only predicted at relatively high die temperatures, above 450°C.
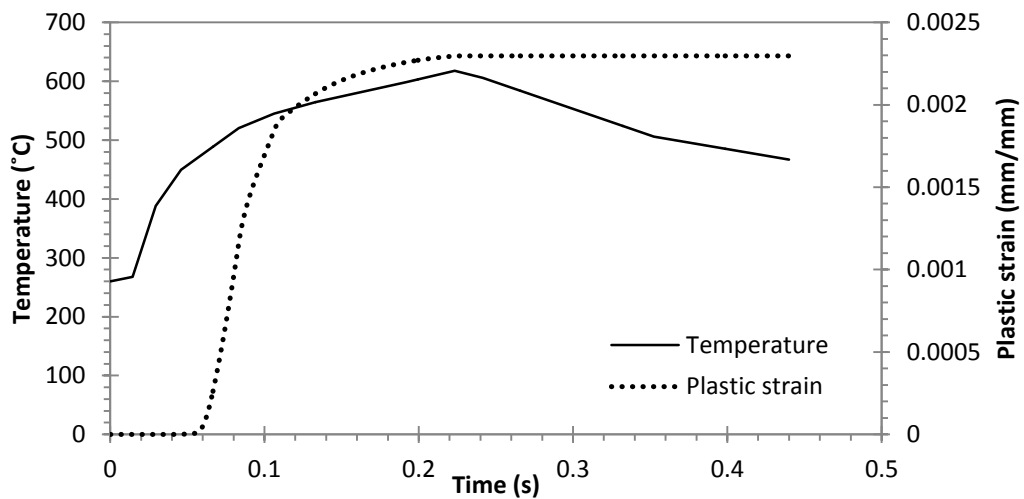
FIGURE 8-8: PLASTIC STRAIN PREDICTIONS DURING THE FIRST FORGING CYCLE

Transient cyclical softening

The model does not include the initial transient cyclical softening observed in the fatigue loading of similar tool steels. This behaviour was not measured in the fatigue tests in the as-heat treated condition, so was not included within the material model.

8.4.2 THE BOUNDARY CONDITIONS

The difference in the life prediction may arise from the assumptions made regarding the boundary conditions. The boundary conditions include the material starting conditions, the mechanical loading, and the thermal loading.

The problem has been simplified by assuming the nitride layer acts as a non-deforming region. The thermo-mechanical loading has been taken at a location representative of the nitride-substrate interface. This approach ignores the stress transferred from the soft substrate to the plastically hard nitride layer. The stress transferral results in less stress applied to the plastically deforming substrate and would lower the stress input into the lifing model. As the model over predicts life, it is assumed that this deficiency is not the dominant cause of model inaccuracy.

Another simplification is that residual stress has not been included. The nitride case hardening results in a compressive stress within the nitride layer and a tensile stress within the substrate (Withers and Bhadeshia 2001). The tooling is machined in the as-heat treated condition, relieving residual stresses that arise from the quenching operation.

Da Silva Rocha et al (1999) measured the residual stress in nitrided M2 high speed tool steel. The residual stresses measured within the diffusion zone of the nitride layer are shown in Figure 8-9 for two different gas compositions and different nitriding temperatures. It can be seen that the residual stress resulting from nitriding is significant.
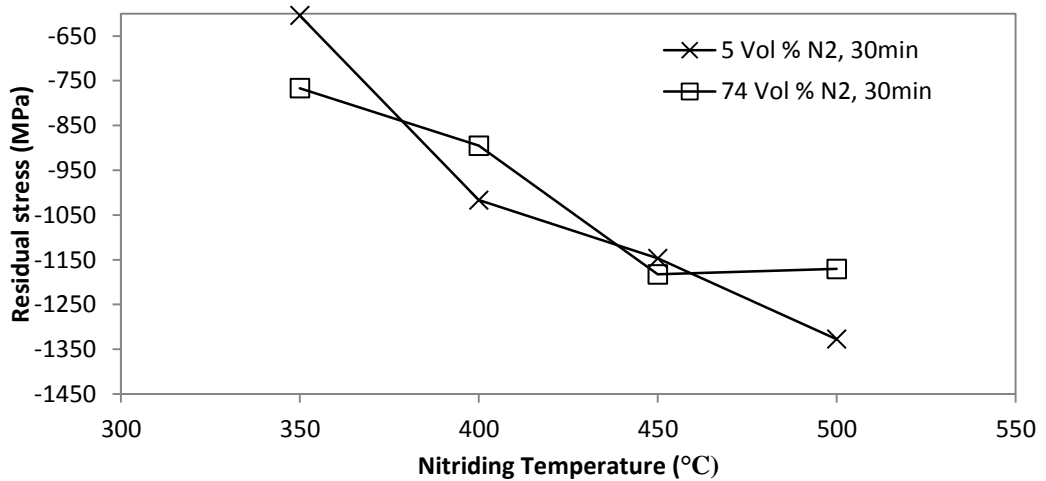
FIGURE 8-9: RESIDUAL STRESS WITHIN THE DIFFUSION ZONE OF M2 HIGH SPEED TOOL STEEL (DA SILVA ROCHA, STROHAECKER ET AL. 1999)

The residual stress resulting from nitriding and the impact of the non-deforming nitride layer is one source of error currently not addressed within this work.

The nitriding operation results in the over-tempering of the substrate. The strength of the substrate is reduced by repeated nitriding operations performed upon re-cut tooling. This is shown in Figure 4-7. The model is capable of predicting this over-tempering behaviour adequately for 100 hours as shown in Figure 6-15. The predicted life of tooling re-cut three times with 24 hour nitriding is shown in Figure 8-10. The predictions have been normalised against the average die life measured from the forge.
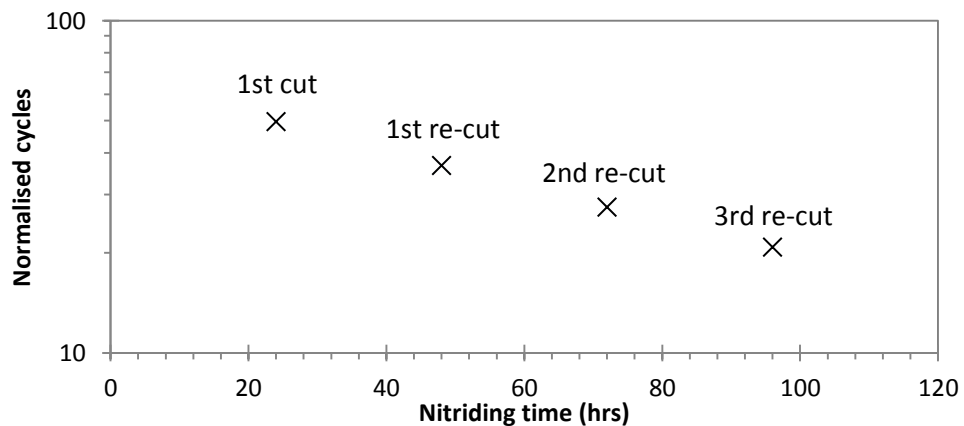
FIGURE 8-10: IMPACT OF REPEATED NITRIDING OPERATIONS UPON LIFE PREDICTION

Figure 8-10 shows the predicted reduction in life as a result of repeated nitriding operations. This relationship was not observed in die life measured from the forge. Significant scatter was measured in die life. The cause of the scatter may be variation in the applied thermo-mechanical loading and variation in die material mechanical properties.

The thermo-mechanical loading differs due to process variation. Examples of process variation include variation in the amount of graphite lubrication applied to the tooling, variation in the glass thickness on the workpiece, differences in workpiece transfer time and variation in the flywheel of the press.

Lin (2009) has measured the impact of variation in lubrication upon the heat transfer and friction within the forging conditions of interest. Ring tests were performed with workpiece glass thicknesses varying between 30μm and 90μm and the amount of graphite varying between 2.82×10^{-5} g/ mm^2 to 12.70×10^{-5} g/ mm^2. The heat transfer coefficient varied between 18kW/ m^2°C to 27kW/ m^2°C. The friction shear factor varied between 0.08 and 0.2 for the different lubricant conditions. The upper and lower boundaries considering the heat transfer and friction shear factor may be used to assess the impact upon the thermo-mechanical loading of the tooling. The variables used are shown in Table 8-2.

TABLE 8-2: UPPER AND LOWER BOUNDS OF HEAT TRANSFER AND FRICTION

	Heat transfer (kW/ m^2°C)	Friction shear factor
Upper bound	27	0.2
Lower bound	18	0.08

The die temperature and stress has been approximated using FEA following the assumptions given in section 3.1.3 using the boundary conditions shown in Table 8-2. Figure 8-11 reports the approximated von Mises stress and temperature predictions from either the upper or lower values for the boundary conditions. Figure 3-32 identifies the locations examined.

VON MISES STRESS   **TEMPERATURE**
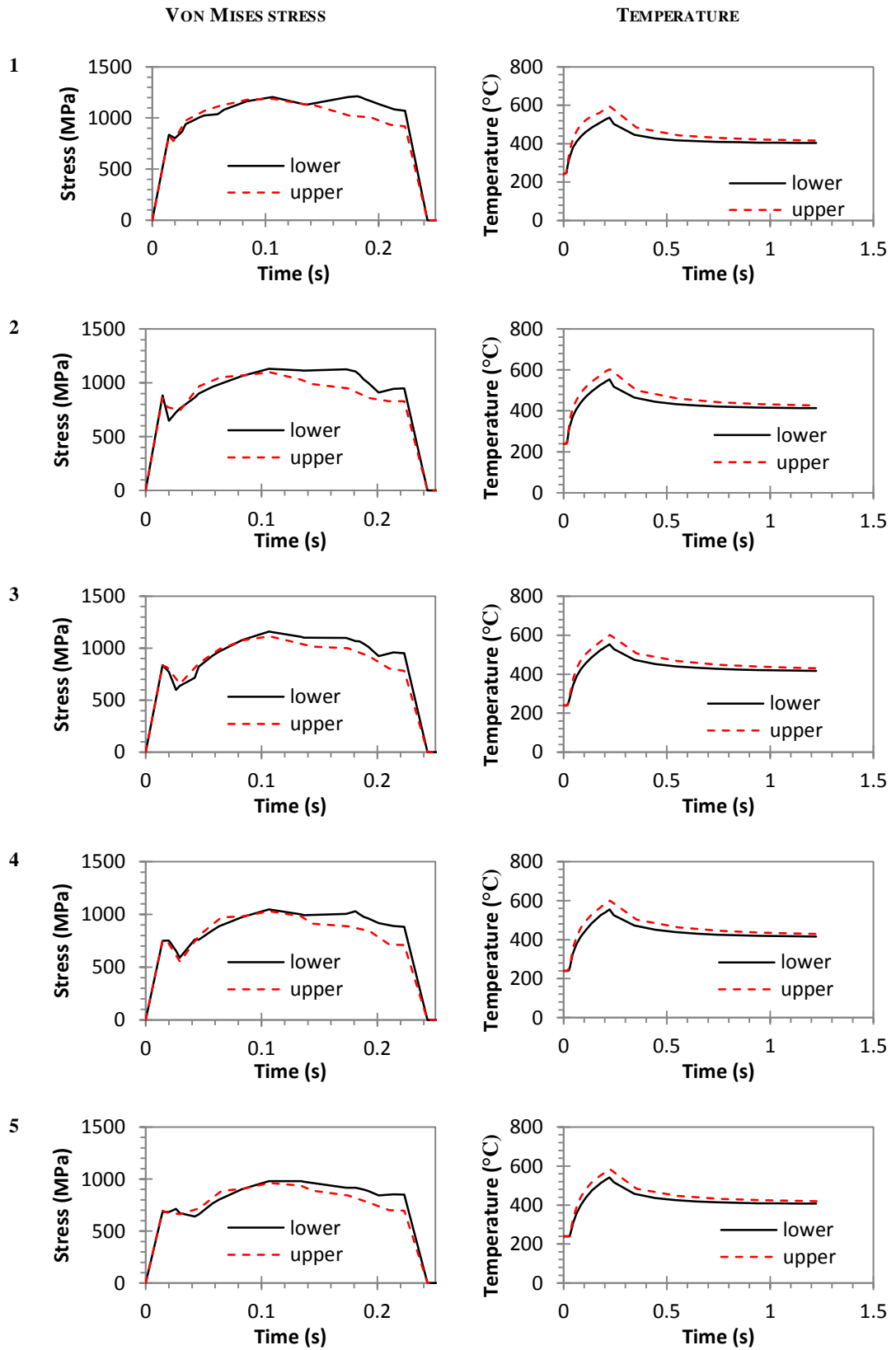
FIGURE 8-11: COMPARISON OF UPPER AND LOWER THERMO-MECHANICAL CYCLE APROXIMATED FROM FEA

254
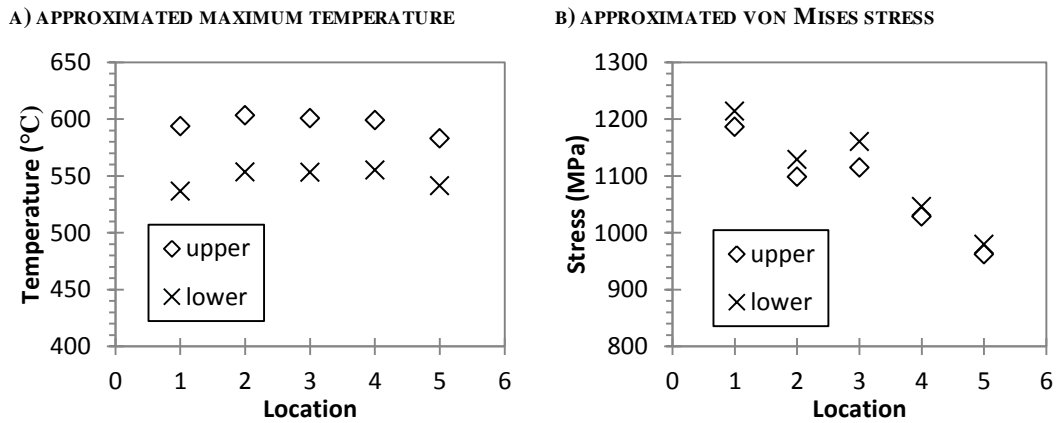
FIGURE 8-12: COMPARISON OF MAXIMUM TEMPERATURE AND STRESS

Figure 8-12 compares the maximum von Mises stresses and temperatures. A maximum difference of 45.6MPa and 57°C in peak values of stress and temperature has been approximated when comparing the upper and lower boundary conditions considering variation in lubrication across the locations of interest. This corresponds to a variation of 4% in maximum stress and a variation of 10% in maximum die temperature.

It is assumed that the variation in peak stress and temperature follow a normal distribution and are in phase. An increase in maximum die stress is associated with an increase in maximum die temperature. The justification for this assumption is that an increase in die temperature is a result of greater heat transfer from the workpiece and\ or friction. Greater friction is associated with higher die stress. A higher rate of heat transfer results in the "die chilling" effect upon the workpiece. The chilled surface of the workpiece requires greater flow stress for deformation and thus greater stresses applied to the dies.

This relationship is not true when forging a workpiece of temperature lower than the process window. The cold workpiece results in higher flow stress with lower die temperature. It is assumed that all workpieces are forged within the process window specified by the forge.

The impact of process variation may be included through using a pseudo-random number generator to determine the maximum peak stress and peak

255

temperature of each cycle. It has been assumed that the variation follows a normal distribution with the standard deviation half of the difference approximated from the FEA analysis. This relates to a standard deviation of 2% for the maximum stress and a standard deviation of 5% for the peak temperature.

Figure 8-13 shows the impact of including different extents of variation in the thermo-mechanical loading for different cuts of the die. The values shown describe the standard deviation applied to the mean peak stress and temperature of 1200MPa and 580°C respectively. The conditions with variation have been repeated three times to illustrate the resultant scatter in life prediction.

The model predictions are most similar to observed die life when including process variation with standard deviations of 6% and 15% applied to the peak stress and peak temperature respectively. Figure 8-14 is a boxplot from performing 100 life predictions assuming such variation in thermo-mechanical loading for different cuts of the tool. The life predictions show less scatter than measured die life form the forge. The model still predicts a clear relationship between the total nitriding time and die life.

Additional scatter in predicted die life results from variation in mechanical properties in the die material. The variation in mechanical properties is due to differences in the key microstructural features. The material model assumes that the key microstructural features are the subgrain interior particles and the volume fraction of subgrain boundaries.

The variation in the key microstructural features within a batch or between batches of die material is unknown; however reasonable approximations have been made to examine the impact upon life prediction.

It has been assumed that the initial subgrain interior particle radius may vary between 1.15nm and 1.25nm following a normal distribution. This has been modelled assuming a standard deviation of 4.1% in the initial particle radius.

A) **24 hours of nitriding (as cut)**
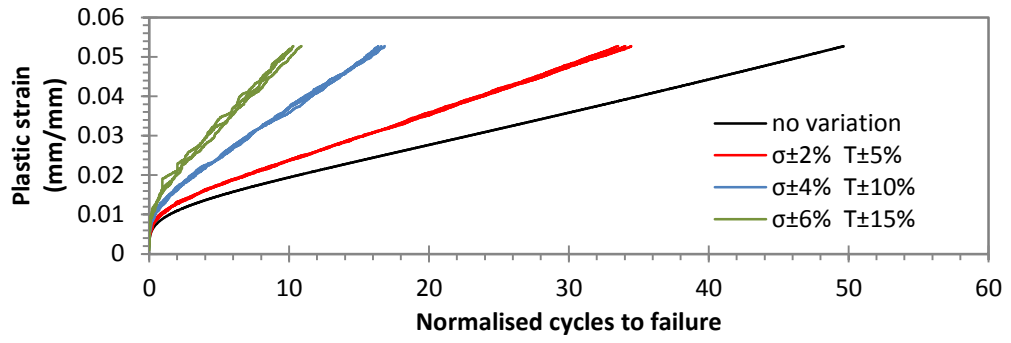
B) **48 hours of nitriding (1ST re-cut)**
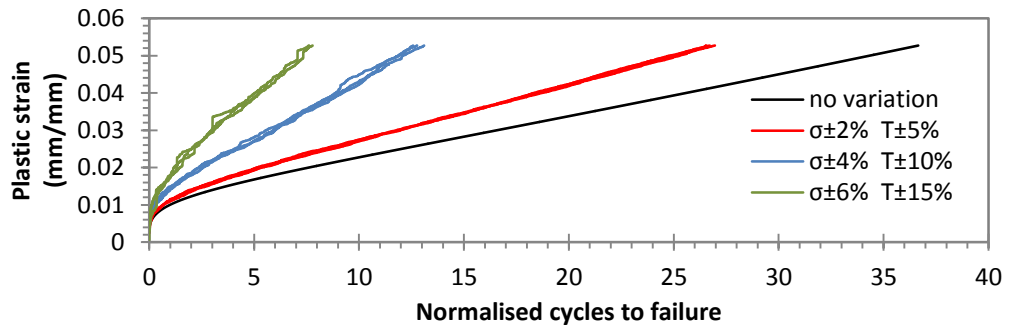
C) **72 hours of nitriding (2ND re-cut)**
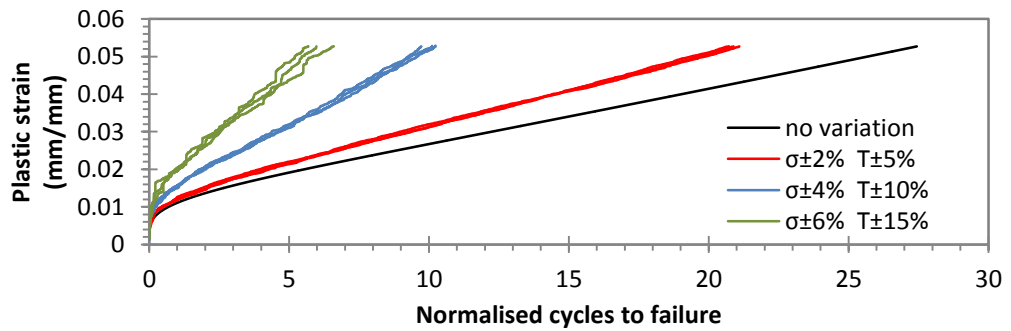
D) **96 hours of nitriding (3RD re-cut)**
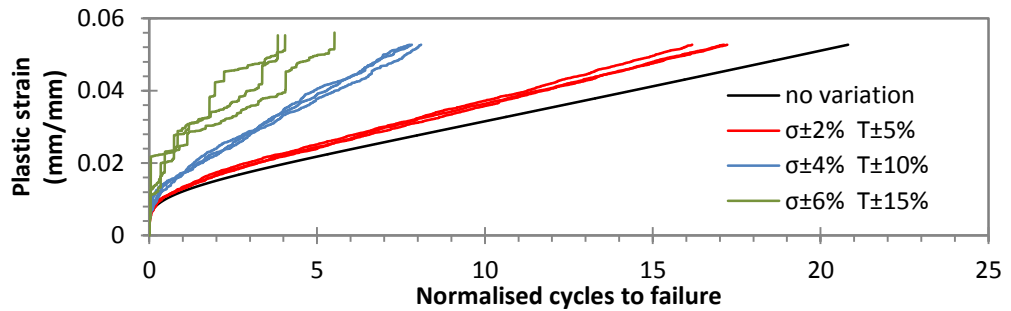
FIGURE 8-13: IMPACT OF PROCESS VARIATION AND NITRIDING UPON LIFE PREDICTION
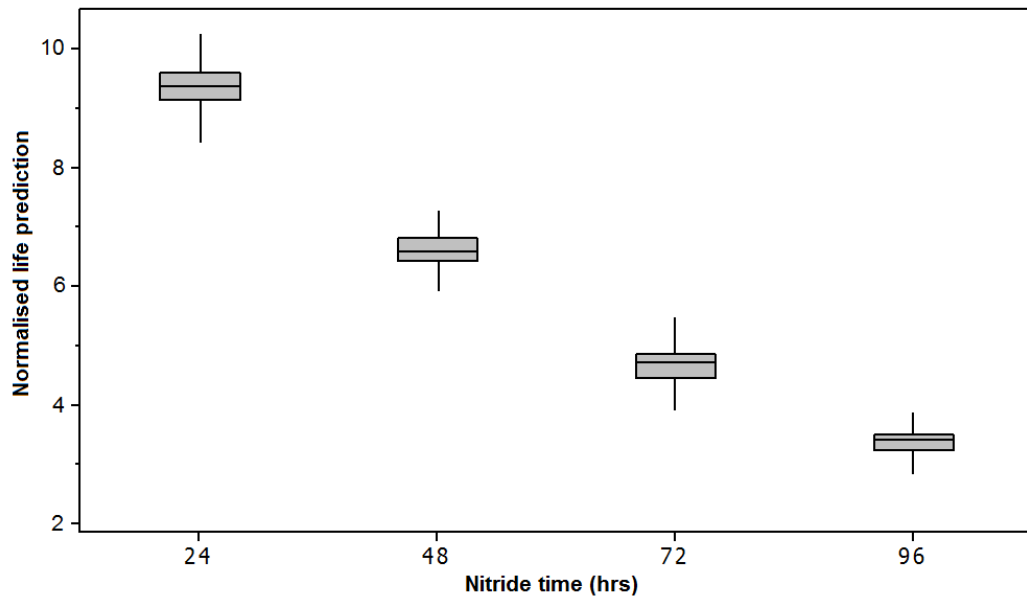
FIGURE 8-14: BOX PLOT OF LIFE PREDICTION INCLUDING VARIATION IN THERMO-MECHANICAL LOADING

The model assumes a relationship between the subgrain diameter and the mobile dislocation density. It is only necessary to vary the initial mobile dislocation density to account for variation in the dislocation structure. The initial mobile dislocation density is assumed to vary following a normal distribution with a standard deviation of 12%. This relates to a subgrain diameter of between 661nm and 745nm.

Figure 8-15 is a boxplot of life predictions when included both process variation and variation within the material. The variation to material and thermo-mechanical loading is shown in Table 8-3. The life predictions have been normalised against the measured average die life.

TABLE 8-3: BOUNDARY CONDITIONS AND MATERIAL VARIATION

σ_{max} (MPa)	T_{max} (°C)	r_p (nm)	ρ_m (m^{-2})
1200 ±6%	580 ±15%	1.1 ±4.1%	2×10^{14} ±12%
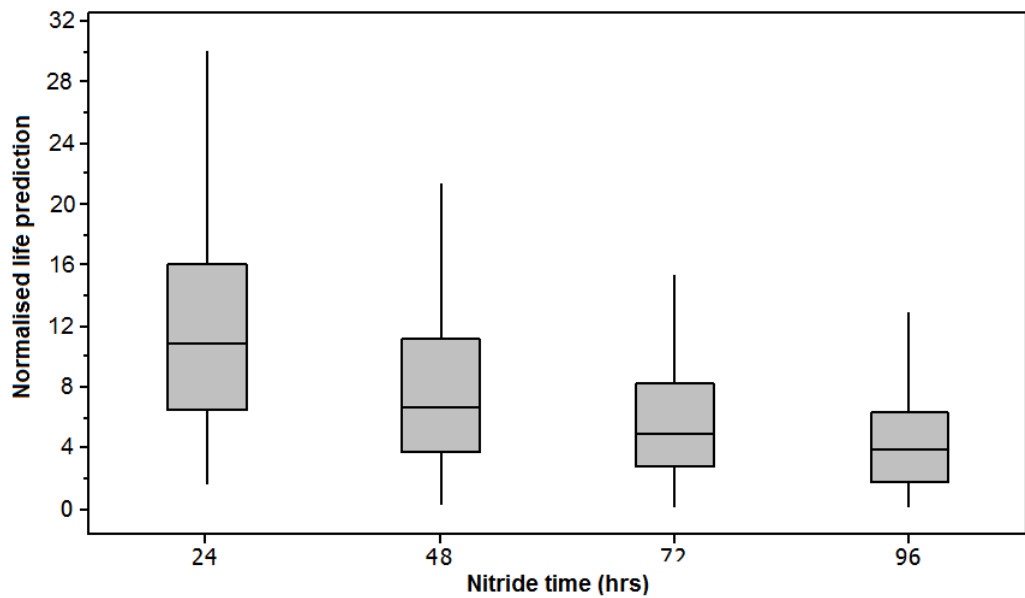
FIGURE 8-15: IMPACT OF DIE MATERIAL AND PROCESS VARIATION UPON DIE LIFE PREDICTION.

The inclusion of variation in microstructural properties has increased the variation in life prediction significantly. The scatter predicted by the model is closer to the scatter observed in die life in the forge with a less clear relationship between total nitriding time and die life.

8.4.3 THE FAILURE CRITERION

The assumptions made in determining the failure criterion may contribute to prediction error. The "smiley face" forging defect may be better described by measuring the plastic shear strain at the location of failure. The plastic shear strain associated with failure has been measured from the angles observed in the deformed phase segregation, as shown in Figure 8-16 A). Figure 8-16 B) shows the plastic shear strain approximated at each location.

A) PHASE SEGREGATION
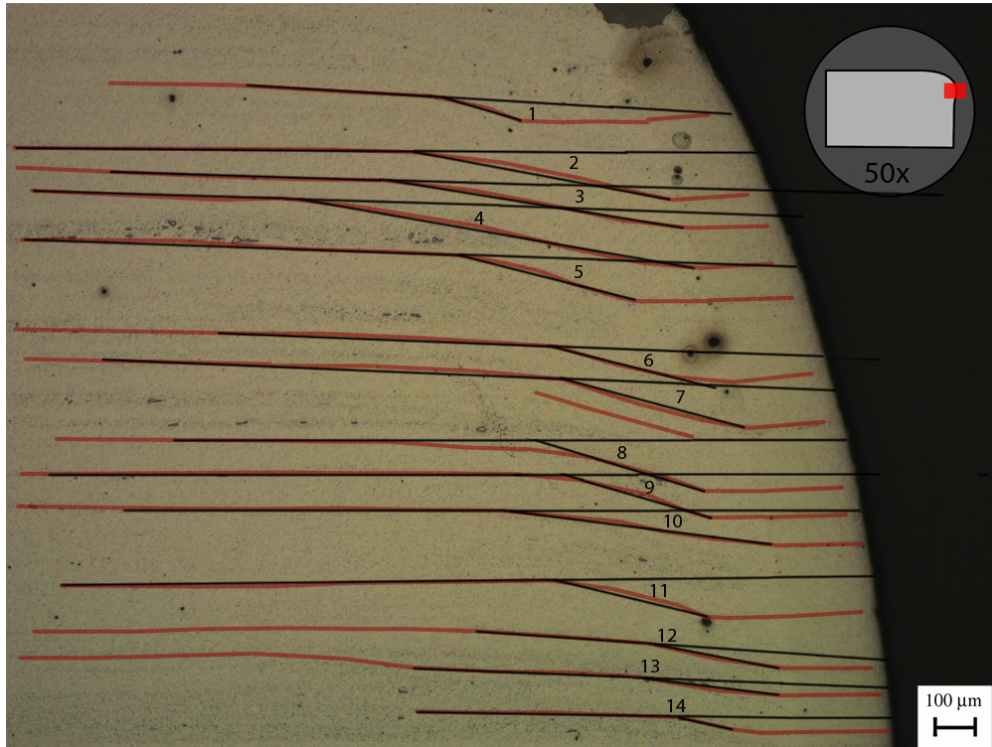
B) PLASTIC SHEAR STRAIN
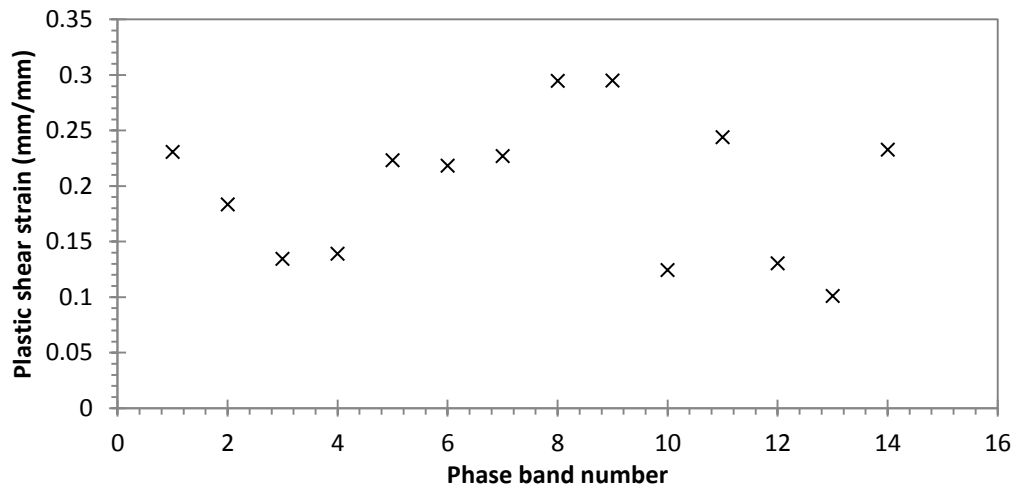
FIGURE 8-16: SHEAR PLASTIC STRAIN APPROXIMATION

The approximated shear strains are larger than the longitudinal strain. For a conservative lifing approximation, the longitudinal strain component has been used as the failure criterion.

$$\varepsilon = \ln\left(\frac{l}{l_o}\right)$$

A better approach would be to use a critical amount of deviation in either the particle spacing or the subgrain spacing as the failure criterion. This approach would allow the use of the model to tooling where the plastic strain relating to failure is unknown. Such an approach assumes that significant microstructural changes occur within hot forging tooling during production, and that these changes result in die failure.

8.5   MODEL APPLICATION SUMMARY

The life of upsetting tooling has been predicted through applying the model shown in section 6.6 to the boundary conditions shown in section 8.2 and with the failure criteria determined in section 8.1.

The model predicts small change in microstructure within the lifetime of the tool. The model does not predict a transition from compressive to tensile plastic strain, reducing the accumulative plastic deformation within a cycle, reducing the amount of subgrain coarsening predicted by the model. The small time scales for over-tempering to occur reduces the significance of particle coarsening upon life prediction. Quantitative measurements of the microstructural features of worn tooling are needed to verify this finding.

The difference in measured and predicted die life is reduced when accounting for the reduction in strength resulting from repeated nitriding operations. The material model is capable of predicting acceptable softening behaviour for 100 hours of nitriding at 525°C.

The inclusion of process variation impacting the thermo-mechanical loading results is one source of the scatter in die life observed from the forge. The impact of variation in die stress and temperature resulting from variation in lubrication has been assessed. Finite element analysis was used to determine appropriate levels of variation.

Variation in thermo-mechanical loading captures the scatter observed in die life measured within the forge. This variation occurs through differences in lubrication, transfer times and variation in the fly wheel of the crank press.

The approach allows for the inclusion of material variation through the microstructural parameters input into the model.

8.6 MODEL APPLICATION CONCLUSION

A die life prediction model has been developed for hot forging tooling. The approach used the physical based model developed in chapter 6, the thermo-mechanical loading predicted from FEM reported in chapter 3 and a failure criterion determined by analysing micrographs of the failed tool.

The application of the model to the upsetting tooling examined in chapter 3 resulted in an over-prediction of life by a factor of 63.

The model suggests that for the given conditions, the tooling does not experience significant microstructural instability and that failure is a result of the applied loading. This finding indicates that life may be improved through increasing the yield strength of the tool material and that stability of the alloy during use as forging tooling is not a concern.

The difference between measured and predicted die life may be caused by errors in the boundary conditions, material model and failure criteria. The most probable causes of error originate from the assumptions made regarding the boundary conditions.

Accounting for the softening resulting from repeated nitriding operations improved the prediction accuracy. The scatter in die life observed from the forge is a result of variation in either the process or material. Process variation has been accounted for through varying the thermo-mechanical loading for each cycle. Scatter in material behaviour has also been included by varying the microstructural parameters of the physical based model.

Further work is required to refine the description of the boundary conditions, the material model and failure criteria.

The mechanical loading of the tool needs to more accurately described, accounting for the impact of the nitride layer.

The material model may be improved through including more detail regarding the dislocation structure. Inspiration may be taken from the approach developed by Ghoniem et al (1990).

A failure criterion that corresponds to a deviation in microstructure would allow for the lifing model to be applied to different tooling without approximating the plastic strain descriptive of die failure.

The model developed in this section progresses die life prediction capability. The capability developed may be applied through calibrating the failure criteria to fit predictions to measured die life. Alternatively, the model may be used to predict a relative measure than can assess different preform designs, process conditions or tool materials.

9   CONCLUSION AND FUTURE WORK

The purpose of this research was to identify and model the dominant failure mode in hot forging tooling. The specific forging operation was the forging of single ended aerofoil compressor blades made out of nickel based superalloy and forged on a mechanical crank press. The findings have been summarised below:

9.1   IDENTIFICATION OF THE DOMINANT FAILURE MODE

- Finite element analysis has been performed to analyse the thermo-mechanical loading of the tooling.
  - The locations prone to plastic deformation have been identified.
  - The temperature of the tooling has been approximated, for use in determining the role of thermal softening in the degradation of the tooling.
- Micrographs have been taken of the damaged surface layers from worn extrusion and upsetting tooling, with the following observations:
  - Plastic deformation of the substrate has been observed in both extrusion and upsetting tooling.
  - The substrate is present at the surface of the tool at the locations of most damage relating to the crimping/ scoring defects.
  - The nitride is mainly intact, reducing the role of abrasive wear in the formation of the scoring/ crimping defects.
  - The nitride layer has been observed to plastically deform.
  - At the regions of interest, the nitride layer is regularly fractured. The possible causes of the fracture include thermo-mechanical fatigue, the elastic deflection of the die and to accommodate the plastic deformation of the substrate.
  - The cracks in the nitride cracks extend into the substrate near the regions of most damage.
  - The compound layer has been observed to fracture delaminate.
- The thermal loading has been examined using a combination of thermal measurement from a thermal camera and from finite element analysis.
  - The temperature of the tooling does not increase over a production run as a result of repeated forging operations.

- o The time scales for over-tempering of the die material is too short for significant thermal softening.
- 3D scans of the tooling have been taken before and after use in production to measure displacement and determine the role of plastic deformation and material loss through abrasive wear.
- The dominant failure mode of nitrided hot forging tooling used to forge nickel based superalloy on a crank press has been found to be plastic deformation of the substrate. Previous understanding was that the dominant failure mode was abrasive wear.

9.2 MATERIAL CHARACTERISATION

- The plastic flow behaviour of AISI H13 has been measured under tension and symmetrical tension-compression fatigue loading.
  - o Tensile tests ranging from 20°C to 600°C and strain rates at either 0.01/ s or 0.1/ s.
  - o Pre-strained tensile tests have been performed to better understand the flow behaviour of the alloy.
  - o Tensile tests have been taken from over-tempered specimens.
  - o Isothermal strain controlled tension-compression tests performed at temperatures varying between 500°C to 600°C and a strain rate of 0.01/ s
- The particle coarsening behaviour has been examined from over-tempered coupons of AISI H13.
- The lath size of AISI H13 has been measured using the line intercept method applied to back scatter images and to EBSD maps.

9.3 CONSTITUTIVE MODELLING

- The physical mechanisms that impact the behaviour of tempered martensitic hot work tool steels under thermo-mechanical loading descriptive of hot forging tooling have been identified.
- An examination of the mechanical threshold stresses relevant to tempered martensitic hot work tool steel suggest that precipitate strengthening best describes the material.

- The Dyson model has been applied to capture the strain rate sensitive behaviour of hot work tool steel.

- The Basoalto model has been applied to capture the athermal flow behaviour of hot work tool steel.

- The work hardening behaviour, thermally induced softening behaviour and strain induced softened behaviour has been captured following the Semba-Dyson-McLean model.

- The microstructural measurements of hot work tool steel have been used to calibrate the physical based model.

    o The lath interior precipitate size and volume fraction measured by Bischof et al (2008) have been used to describe AISI H13.

    o The range in mobile dislocation densities, volume diffusion coefficient, and thermal activation energy values reported to describe tempered martensitic steel have been used to determine a suitable values for AISI H13.

    o The thermally induced softening behaviour has been calibrated to the particle coarsening measurements taken from Bischof et al (2008).

    o The lath coarsening measurements of Sauzay et al (2008) have been used to determine appropriate strain induced softening behaviour.

- The description of work hardening through plastically hard regions does not capture the temperature sensitivity of the back stress.

- The model does not capture the non-linear cyclical softening behaviour observed in the over-tempered fatigue test and reported by Bernhart et al (1999).

- The model successfully captures the impact of varying the strain amplitude upon the linear cyclical softening behaviour.

9.4   DIE LIFE PREDICTION

- The life of upsetting tooling has been predicted, using the physical based material mode, the thermo-mechanical loading approximated from finite

element analysis and the plastic deformation associated with a "smiley face" as the failure criteria.

- The lifing model suggests that the upsetting tooling fails through plastic deformation with minimal impact from microstructural instability.

- Process variation has been accounted for by varying the thermo-mechanical loading for each cycle. It is possible to predict the distribution of die life possible for a given process.

- Material variation has been accounted for by varying the microstructural parameters for simulations of production runs.

- The model over predicts life by a factor of 63. Errors arise from the assumptions made within the constitutive model, the boundary conditions, or the failure criteria.

- An improved description of the impact of the nitride layer within the boundary conditions may improve predictions.

9.5 FUTURE WORK

9.5.1 MATERIAL CHARACTERISATION

A comprehensive TEM examination of AISI H13 would allow for the improvement of the material model. The focus of the examination should be the subgrain interior particle spacing, mobile dislocation density and the dislocation structure. To capture the relevant microstructural instability, the TEM examination needs to measure the impact of over-tempering upon the dislocation density within the subgrain interior and the subgrain interior particle spacing. Subgrain formation and coarsening may be examined from interrupted fatigue specimen.

Measuring the distributions of these key microstructural features would assist in understanding the variation present within the tool material which may then be linked to variation in material properties.

The model suggests minimal microstructural changes occur within failed tooling due to the small accumulation of plastic deformation and short time scales for over-tempering. A TEM examination may verify this finding through the comparing specimen from worn and new tooling. Examining specimen from

tooling that have forged different numbers of components would allow the measurement of the progression microstructural change.

The residual stress within the nitride layer should be measured. This information is required to improve the understanding of the stress state of the tooling.

9.5.2   MATERIAL MODEL

The model may be improved through considering a new approach to modelling work hardening that is based upon dislocation pile ups. The model would have to include thermally induced dislocation annihilation and the impact of the reversal of slip direction during fatigue loading.

If the Taylor back stress from dislocation interaction is higher than the Orowan stress for particle bypass, a new thermal model is required for describing flow behaviour for such a condition. One approach would be to use Basoalto's viscous drag of jogs model (Basoalto and Brooks 2011).

The material model may be extended to predict thermo-mechanical fatigue by including the physical mechanisms of either cavity nucleation or cavity growth, as shown by Dyson (2000).

9.5.3   DIE LIFE PREDICTION: BOUNDARY CONDITIONS

The thermo-mechanical loading may be more accurately defined, accounting for the residual stress within the nitride layer. The mechanical loading to the substrate may have a transition between tensile and compressive loading, allowing for greater accumulated plastic deformation within a forging cycle. The accumulative plastic deformation would drive subgrain coarsening, improving life predictions.

9.5.4   APPLYING THE LIFING MODEL

The model may be applied to optimising die life considering changes to process conditions. The potential uses of the model are listed below:

- Identifying the optimum tool temperature for highest die life (such work would need to consider the impact of temperature upon the adhesion between the graphite lubricant and the tool surface).

- Identifying the optimum ram movement for highest die life. The optimum ram movement for forging nickel based superalloys is a compromise between reducing the strain rate of deformation and reducing the heat lost from the workpiece.

- Optimising preform design for improved die life.

- Evaluating new tool materials for improved die life. The microstructural features descriptive of an alternative die material could be used to compare the impact upon die life. Ideally, the model would account for fatigue life so that the associated change in toughness may also be considered.

- Approximating die life for new products. The material model may be implemented within finite element analysis to evaluate die life. Such information would be useful in production planning.

10 REFERENCES

Abe, F. (2008). "Precipitate design for creep strengthening of 9% Cr tempered martensitic steel for ultra-supercritical power plants." Science and Technology of Advanced Materials **9**(1): 013002.

Agamennone, R., W. Blum, C. Gupta and J. K. Chakravartty (2006). "Evolution of microstructure and deformation resistance in creep of tempered martensitic 9-12%Cr-2%W-5%Co steels." Acta Materialia **54**(11): 3003-3014.

Aliya, D. (2002). ASM Handbook Volume 11 Failure analysis and Prevention, ASM International.

Antony, J., R. Bañuelas and A. Kumar, Eds. (2006). World Class Applications of Six Sigma: Real World Examples of Success. GB, Taylor & Francis Ltd.

Archard, J. F. a. H., W (1956). Wear of metals under unlubricated condiions. Procedeedings of the Royal Society of London, London, Mathematical and Physical Sciences.

Ardell, A. J. (1972). "On the coarsening of grain boundary precipitates." Acta Metallurgica **20**(4): 601-609.

Babu, S., D. Ribeiro and R. Shivpuri (1999). Material and Surface Engineering For Precision Forging Dies. Ohio State University, Precision Forging Consortium Ohio Areospace Institute and National Center for Manufacturing Sciences.

Basoalto, H. C. (2012). Athermal flow behaviour considering steady state dislocation generation and annihilation. M. J. Anderson.

Basoalto, H. C. and J. W. Brooks (2011). Modelling the high temperature deformation of titanium alloys. 12th International Conference on Titanium. Beijing.

Basoalto, H. C., B. F. Dyson and M. McLean (2002). A quantitative physics-based approach to creep and LCF life prediction: Application to nickel-base superalloys. Advanced Materials and Processes for Gas Turbines, September 22, 2002 - September 26, 2002, Copper Mountain, CO, United states, Minerals, Metals and Materials Society.

Bazazi, A., A. (2009). Evolution of microstructure during long-term creep of a tempered martensite ferritic steel. PhD.

Bernhart, G., G. Moulinier, O. Brucelle and D. Delagnes (1999). "High temperature low cycle fatigue behaviour of a martensitic forging tool steel." International Journal of Fatigue **21**(2): 179-186.

Berti, G. A. and M. Monti (2009). "Improvement of life prediction in AISI H11 tool steel by integration of thermo-mechanical fatigue and

creep damage models." <u>Fatigue & Fracture of Engineering Materials & Structures</u> **32**(3): 270-283.

Biglari, F. R. and M. Zamani (2008). <u>Die wear profile investigation in hot forging</u>. World Congress on Engineering 2008, London, ENGLAND, Int Assoc Engineers-Iaeng.

Bischof, M., P. Staron, D. Caliskanoglu, H. Leitner, C. Scheu and H. Clemens (2008). "On the overaging behaviour of tool steel X38 CrMoV 5-3." <u>Materials Science and Engineering: A</u> **472**(1-2): 148-156.

Bohler (2010). Bohler W302. <u>Hot work tool steels</u>. B. Uddeholm.

Cai, W., V. V. Bulatov, S. Yip and A. S. Argon (2001). "Kinetic Monte Carlo modeling of dislocation motion in BCC metals." <u>Materials Science and Engineering: A</u> **309–310**(0): 270-273.

Chattopadhyay, R. (2001). <u>Surface Wear: Analysis, Treatment, and Prevention</u>, ASM International.

Cser, L., M. Geiger, K. Lange, J. A. G. Kals and M. Hansel (1993). "TOOL LIFE AND TOOL QUALITY IN BULK METAL-FORMING." <u>Proceedings of the Institution of Mechanical Engineers Part B-Journal of Engineering Manufacture</u> **207**(4): 223-239.

da Silva Rocha, A., T. Strohaecker, V. Tomala and T. Hirsch (1999). "Microstructure and residual stresses of a plasma-nitrided M2 tool steel." <u>Surface and Coatings Technology</u> **115**(1): 24-31.

Dubey, J. S., H. Chilukuru, J. K. Chakravartty, M. Schwienheer, A. Scholz and W. Blum (2005). "Effects of cyclic deformation on subgrain evolution and creep in 9-12% Cr-steels." <u>Materials Science and Engineering: A</u> **406**(1-2): 152-159.

Dyson, B. (2000). "Use of CDM in materials modelling and component creep life prediction." <u>Journal of Pressure Vessel Technology-Transactions of the Asme</u> **122**(3): 281-296.

Dyson, B. F. (2009). "Microstructure based creep constitutive model for precipitation strengthened alloys: Theory and application." <u>Materials Science and Technology</u> **25**(Compendex): 213-220.

Engberg, G. and L. Larrson (1988). "Elevated-temperature low cycle and thermomechanical fatigue properties of AISI H13 hot work tool steel." <u>ASTM STP</u> **942**: 576-587.

Estrin, Y. and H. Mecking (1984). "A UNIFIED PHENOMENOLOGICAL DESCRIPTION OF WORK-HARDENING AND CREEP BASED ON ONE-PARAMETER MODELS." <u>Acta Metallurgica</u> **32**(1): 57-70.

Fang, J. R., Q. C. Jiang, Q. F. Guan and S. Q. Wang (2002). "The characteristics of fatigue under isothermal and thermo-mechanical

load in Cr-Ni-Mo cast hot work die steel." <u>Fatigue & Fracture of Engineering Materials & Structures</u> **25**(5): 481-488.

Frost, H., J and M. Ashby, F. (2011). "Deformation-Mechanism Maps, The Plasticity and Creep of Metals and Ceramics." from http://engineering.dartmouth.edu/defmech/.

Ghoniem, N., A. Matthews and R. Amodeo (1990). "A dislocation model for creep in engineering materials." <u>Res Mechanica</u> **29**: 197-219.

Groseclose, A., C. Choir, J. L. Gonzalez-Mendez and T. Yelich (2008). Estimation of die stresses and wear in warm forging of steel pinion shafts. Ohio, Columbus, The Ohio State University.

Hodowany, J., G. Ravichandran, A. J. Rosakis and P. Rosakis (2000). "Partition of plastic work into heat and stored energy in metals." <u>Experimental Mechanics</u> **40**(2): 113-123.

Hull, D. and D. Bacon, J (2001). <u>Introduction to dislocations</u>. Oxford, Butterworth-Heinemann.

Jadhav, P. (2011). Process Characterisation with Data Mining & FEM. <u>AFRC00019</u>, AFRC.

John, A., R. Meran, O. Roenpage and C. Staudter (2009). Six Sigma + Lean Toolset. S. Lunau, Springer Berlin Heidelberg**:** 3-26.

Kachanov, L. (1958). "On Rupture Time Under Condition of Creep." <u>Ivz. Akad. Nauk SSSR</u>(8): 26-31.

Kadoya, Y., B. F. Dyson and M. McLean (2002). "Microstructural stability during creep of Mo- or W-bearing 12Cr steels." <u>Metallurgical and Materials Transactions A: Physical Metallurgy and Materials Science</u> **33**(Compendex): 2549-2557.

Kchaou, M., R. Elleuch, Y. Desplanques, X. Boidin and G. Degallaix (2009). "Failure mechanisms of H13 die on relation to the forging process - A case study of brass gas valves." <u>Engineering Failure Analysis</u> **In Press, Corrected Proof**.

Kim, D. H., H. C. Lee, B. M. Kim and K. H. Kim (2005). "Estimation of die service life against plastic deformation and wear during hot forging processes." <u>Journal of Materials Processing Technology</u> **166**(3): 372-380.

Kirchner, H. (1971). "Coarsening of grain-boundary precipitates." <u>Metallurgical and Materials Transactions B</u> **2**(10): 2861-2864.

Kocks, U. F., A. S. Argon and M. F. Ashby (1975). "THERMODYNAMICS AND KINETICS OF SLIP." <u>Progress in Materials Science</u> **19**: 1-281.

Krumphals, F., B. Reggiani, L. Donati, T. Wlanis and C. Sommitsch (2012). "Deformation behaviour of a ferritic hot-work tool steel with

respect to the microstructure." Computational Materials Science **52**(1): 40-45.

Krumphals, F., C. Wlanis, C. Sommitsch, I. Holzer, B. Sonderegger and V. Wieser (2009). "Modelling of microstructure evolution in hot work tool steels during service." Computer methods in material science **9**(2): 228-233.

Kuhlmann-Wilsdorf, D. (1999). "The theory of dislocation-based crystal plasticity." Philosophical Magazine a-Physics of Condensed Matter Structure Defects and Mechanical Properties **79**(4): 955-1008.

Kuhlmann-Wilsdorf, D. (2001). "Q: Dislocations structures -- how far from equilibrium? A: Very close indeed." Materials Science and Engineering A **315**(1-2): 211-216.

Kuhlmann-Wilsdorf, D. (2002). "Why do dislocations assemble into interfaces in epitaxy as well as in crystal plasticity? To minimize free energy." Metallurgical and Materials Transactions a-Physical Metallurgy and Materials Science **33**(8): 2519-2539.

Kuhlmann-Wilsdorf, D. and N. Hansen (1991). "Geometrically necessary, incidental and subgrain boundaries." Scripta Metallurgica et Materialia **25**(7): 1557-1562.

Lee, H. C., B. M. Kim and K. H. Kim (2003). "Estimation of die service life in hot forging, considering lubricants and surface treatments." Proceedings of the Institution of Mechanical Engineers Part B-Journal of Engineering Manufacture **217**(7): 1011-1022.

Lemaitre, J. and J.-L. Chaboche (1990). Mechanics of solid materials. Cambridge, Cambridge University Press.

Li, C. X., Y. Sun and T. Bell (2000). "Factors influencing fretting fatigue properties of plasma-nitrided low alloy steel." Materials Science and Engineering A **292**(1): 18-25.

Lin, J., Y. Liu and T. A. Dean (2005). "A review on damage mechanisms, models and calibration methods under various deformation conditions." International Journal of Damage Mechanics **14**(4): 299-319.

Lin, Y.-P. (2009). Investigation of die wear by modelling the extrusion of Inconel 718. PhD, The University of Birmingham.

Mebarki, N., D. Delagnes, P. Lamesle, F. Delmas and C. Levaillant (2004). "Relationship between microstructure and mechanical properties of a 5% Cr tempered martensitic tool steel." Materials Science and Engineering A **387-389**(Compendex): 171-175.

Medvedeva, A., J. Bergström, S. Gunnarsson and J. Andersson (2009). "High-temperature properties and microstructural stability of hot-

work tool steels." <u>Materials Science and Engineering: A</u> **523**(1-2): 39-46.

Mughrabi, H. (1987). "A two-parameter description of heterogeneous dislocation distributions in deformed metal crystals." <u>Materials Science and Engineering</u> **85**: 15-31.

Nes, E. (1995). "RECOVERY REVISITED." <u>Acta Metallurgica Et Materialia</u> **43**(6): 2189-2207.

Nes, E. (1997). "Modelling of work hardening and stress saturation in FCC metals." <u>Progress in Materials Science</u> **41**(3): 129-193.

Orlova, A. (2000). "Two versions of a refined composite model of internal stress field in subgrain structures." <u>Physica Status Solidi (A) Applied Research</u> **179**(Compendex): 117-123.

Ou, H., B. Lu, J. Markem, G. Cecil, S. Nikov and A. Rennie (2008). <u>Development of a virtual die shape optimisation system for net-shape forging of aeroengine components</u>. Proceedings of the 12th International Conference on Metal Forming "Metal Forming 2008".

Painter, B., R. Shivpuri and T. Altan (1996). "Prediction of die wear during hot-extrusion of engine valves." <u>Journal of Materials Processing Technology</u> **59**(1-2): 132-143.

Pavlina, E. J. and C. J. Van Tyne (2008). "Correlation of Yield Strength and Tensile Strength with Hardness for Steels." <u>Journal of Materials Engineering and Performance</u> **17**(6): 888-893.

Persson, A., S. Hogmark and J. Bergström (2005). "Thermal fatigue cracking of surface engineered hot work tool steels." <u>Surface and Coatings Technology</u> **191**(2-3): 216-227.

Pessin, M. A., M. D. Tier, T. R. Strohaecker, A. Bloyce, Y. Sun and T. Bell (2000). "The effects of plasma nitriding process parameters on the wear characteristics of AISI M2 tool steel." <u>Tribology Letters</u> **8**(4): 223-228.

Polcik, P., T. Sailer, W. Blum, S. Straub, J. Bursik and A. Orlova (1999). "On the microstructural development of the tempered martensitic Cr-steel P 91 during long-term creep - a comparison of data." <u>Materials Science and Engineering A</u> **A260**(Compendex): 252-259.

Prasad, S. (1997). <u>Hot working guide: a compendium of processing maps</u>, ASM International.

Rabotnov, Y. (1969). "Creep problems in structural members." <u>Appl. Mech. Cong.</u>: 342-349.

Ratke, L. and P. Voorhees, W (2002). <u>Growth and Coarsening: Ostwald Ripening in Material Processing</u>. Evanston, Springer-Verlag Berlin Heidelberg New York.

Saiki, H., Y. Marumo, A. Minami and T. Sonoi (2001). "Effect of the surface structure on the resistance to plastic deformation of a hot forging tool." Journal of Materials Processing Technology **113**(1-3): 22-27.

Sauzay, M., B. Fournier, M. Mottot, A. Pineau and I. Monnet (2008). "Cyclic softening of martensitic steels at high temperature - Experiments and physically based modelling." Materials Science and Engineering a-Structural Materials Properties Microstructure and Processing **483-84**: 410-414.

Sawada, K., M. Takeda, K. Maruyama, R. Ishii, M. Yamada, Y. Nagae and R. Komine (1999). "Effect of W on recovery of lath structure during creep of high chromium martensitic steels." Materials Science and Engineering A **267**(1): 19-25.

Sedlácek, R. (1995). "Internal stresses in dislocation wall structures." Scripta Metallurgica et Materialia **33**(2): 283-288.

Sedlacek, R., W. Blum, J. Kratochvil and S. Forest (2002). "Subgrain formation during deformation: Physical origin and consequences." Metallurgical and Materials Transactions a-Physical Metallurgy and Materials Science **33**(2): 319-327.

Semba, H. (2003). Creep modelling of microstructurally unstable martensitic steels. PhD, Imperial College.

Semba, H., B. Dyson and M. McLean (2005). Microstructure-based Creep Modelling of a 9% Cr Martensitic Steel. ECCC Creep Conference. London.

Semba, H., B. Dyson and M. McLean (2008). "Microstructure-based creep modelling of a 9%Cr martensitic steel." Materials at High Temperatures **25**(3): 131-137.

Semiatin, S. L. (2005). ASM handbook 14A: Metalworking: Bulk Forming. Ohio Materials Park.

Smoljan, B. (2009). "An analysis of relationships between behavior and microstructure constitution of hot-work tool steel." Materials and Manufacturing Processes **24**(Compendex): 786-790.

Strafford, K., N., R. Smart, St, C., I. Sare and C. Subramanian (1995). Surface engineering processes and applications. Lancaster, Technomic Publishing Company, Inc.

Subramanian, C., K. N. Strafford, T. P. Wilks and L. P. Ward (1996). On the design of coating systems: Metallurgical and other considerations. International Conference on Advances in Materials and Processing Technologies (AMPT 93), Dublin, Ireland, Elsevier Science Sa Lausanne.

Summerville, E., K. Venkatesan and C. Subramanian (1995). "Wear processes in hot forging press tools." Materials & Design **16**(5): 289-294.

Sun, L., M. J. Thomas, B. P. Wynne, E. J. Palmiere, K. P. Mingard and B. Roebuck (2010). "Mapping microstructure inhomogeneity using electron backscatter diffraction in 316L stainless steel subjected to hot plane strain compression tests." Materials Science and Technology **26**(12): 1477-1486.

Tan, X. (2007). "Friction of plasticity: application of the dynamic friction model." Proceedings of the Institution of Mechanical Engineers Part J-Journal of Engineering Tribology **221**(J2): 115-131.

Taylor, J. (2010). Foundation Level Infrared Training, Land Instruments International Ltd.

van der Voort, G. F. and E. P. Manilova (2004). "Metallographic characterization of the microstructure of tool steels." Cailiao Rechuli Xuebao/ Transactions of Materials and Heat Treatment **25**(Compendex): 169-173.

Velay, V., G. Bernhart, D. Delagnes and L. Penazzi (2005). "A continuum damage model applied to high-temperalture fatigue lifetime prediction of a martensitic tool steel." Fatigue & Fracture of Engineering Materials & Structures **28**(11): 1009-1023.

Wagner, C., Z (1961). "Theorie der Alterung von Niederschlagen durch Umlosen." Zeitschrift Fur Elektrochemie **65**: 581-591.

Wang, S. Q., M. Wei, F. Wang, X. H. Cui and C. Dong (2008). "Transition of Mild Wear to Severe Wear in Oxidative Wear of H21 Steel." Tribology Letters **32**(2): 67-72.

Weertman, J. and J. Weertman, R. (1980). Moving dislocations. Dislocations in Solids. F. R. N. Nabarro. Amsterdam**:** 1-59.

Withers, P. J. and H. Bhadeshia (2001). "Overview - Residual stress part 2 - Nature and origins." Materials Science and Technology **17**(4): 366-375.

Yan, H., J. Hua and R. Shivpuri (2007). "Flow stress of AISI H13 die steel in hard machining." Materials & Design **28**(1): 272-277.

Zander, J. (2009). Development of tools for integrated optimisation and use of alluminium alloys. MSC, Brinnellvagen.

Zhang, Z., D. Delagnes and G. Bernhart (2002). "Anisothermal cyclic plasticity modelling of martensitic steels." International Journal of Fatigue **24**(6): 635-648.

Zhang, Z., D. Delagnes and G. Bernhart (2004). "Microstructure evolution of hot-work tool steels during tempering and definition of a kinetic

law based on hardness measurements." <u>Materials Science and Engineering a-Structural Materials Properties Microstructure and Processing</u> **380**(1-2): 222-230.

Zhang, Z., D. Delagnes and G. Bernhart (2007). "Ageing effect on cyclic plasticity of a tempered martensitic steel." <u>International Journal of Fatigue</u> **29**(2): 336-346.

Zhang, Z. P., G. Bernhart and D. Delagnes (2008). "Cyclic behaviour constitutive modelling of a tempered martensitic steel including ageing effect." <u>International Journal of Fatigue</u> **30**(4): 706-716.

11 APPENDIX

11.1 TEST PROCEDURES

The test specimens have been cut from a H13 die block with the specimen axis aligned with the rolling direction of the die material as shown in Figure 11-1.
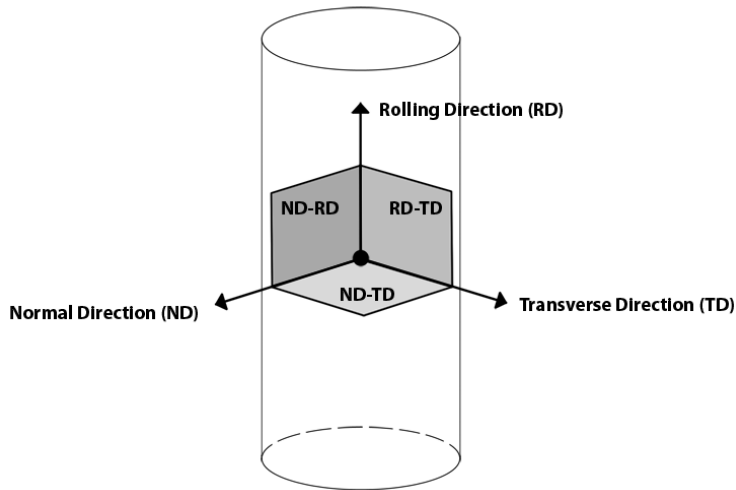

FIGURE 11-1: SPECIMEN ORIENTATION

The following sections detail the mechanical test procedures and the metallurgical preparation methods.

11.1.1 FATIGUE TEST PROCEDURE

The fatigue tests have been performed to ASTM E606 standard using cylindrical fatigue test specimen shown in Figure 11-2. The test specimens were obtained from un-used die blocks with the specimens axis orientated in the rolling direction.
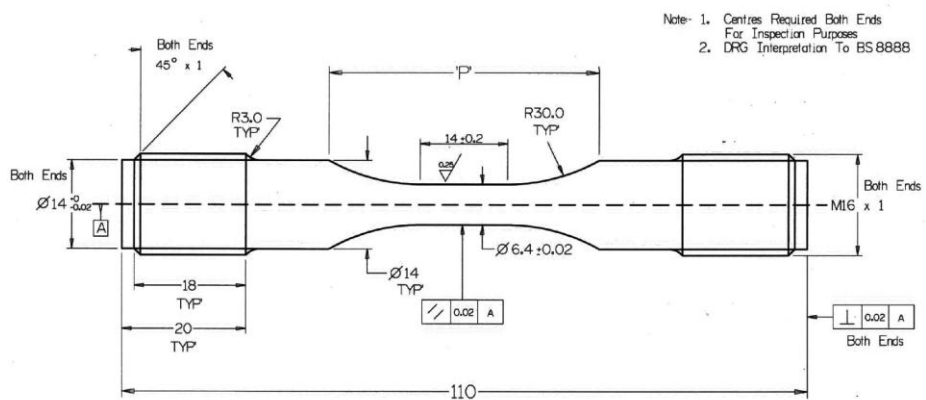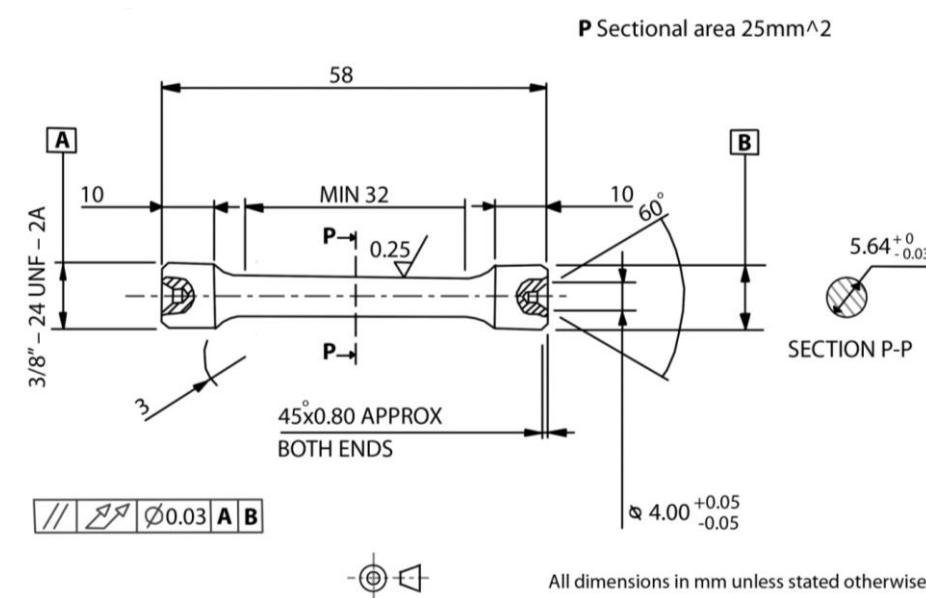
FIGURE 11-2: FATIGUE SPECIMEN DIMENSIONS

The fatigue tests were performed by Westmoreland Mechanical Testing and Research Ltd. A clip on extensometer was used to measure strain. The test procedure included an hour soak time. The temperature dependence of the elastic modulus of the grade of AISI H 13 of interest was measured during the fatigue tests.

11.1.2 TENSILE TEST PROCEDURE

The test standard ASTM E21 has been followed using a Zwick/ Roell Z250 screw press. A pre-load of 250N was applied during heating to compensate for thermal expansion of the press. The test specimen geometry is shown in Figure 11-3.

FIGURE 11-3: TENSILE TEST SPECIMEN DIMENSIONS

The test specimen strain was measured using the cross-head travel of the press. This method of strain measurement includes both deformation of the specimen and that of the press. The elastic behaviour measured from the tensile tests have been corrected to align with the elastic modulus measured from the fatigue tests.

11.1.3 METALLURGICAL PREPARATION PROCEDURE

The metallurgical preparation procedure follows the approach outlined by Voort and Manilova (2004). The metallurgical samples were cut using a Buehler Isomet 5000 abrasive grinding wheel and cleaned using acetone prior to mounting. The samples were hot mounted using a Buehler Simplimet 3000. The mounting material was either Buehler Phenocure or conductive Buehler Probemet depending upon whether the samples were to be examined using light microscopy or electron microscopy. Grinding and polish was performed on a Buehler Automet 300. The steps taken to grind and polish the samples are shown in Table 11-1.

TABLE 11-1: METALLURGICAL SAMPLE PREPARATION PROCEDURE

	Surface	Abrasive	Load (N)	Speed (rpm) Head	Table	Direction	Time (min)
1	SiC grinding paper	P220	27	60	250	COMP	2
2	SiC grinding paper	P320	27	60	250	COMP	3
3	SiC grinding paper	P600	27	60	150	COMP	3
4	SiC Grinding paper	P1200	27	60	150	COMP	2
5	Hard woven no nap	9μm diamond suspension	35	60	150	CONTRA	2
6	Soft woven no nap	3μm diamond suspension	35	60	150	CONTRA	2
7	Soft woven Small nap	0.05μm colloidal silica	35	60	50	CONTRA	1:10

The etchants used and their purpose is listed in Table 11-2. Nital was used to examine worn tooling to reveal the nitride layer, precipitates and tempered martensitic laths. The carbides within the structure may be revealed with 4% Picral however electro-etching with 10% Oxalic acid gave a more consistent and controlled etch.

The microstructural features of interest were examined using a scanning electron microscope. A FEG-SEM was used to collect imaging from back-scatter (BS) and secondary electrons (SE).

To prepare the specimen for EBSD analysis the process shown in Table 11-1 was applied up to final polishing. The samples were cleaned and then vibratory polished using 0.02μm colloidal silica for 6-8hours using a Buehler VibroMet 2 vibratory polisher at 10% power. The specimens were then ultrasonically cleaned in ethanol for 15 minutes.

TABLE 11-2: ETCHING METHODS

Etchant	Composition	Purpose
2% Nital	5mL HNO3 and 95mL alcohol	3 second etch to reveal the nitride layer. 30 second etching time required to reveal the martensitic structure
4% Picral	4g picric acid and 100mL ethanol	20 second etch to reveal the carbides. 1 minute etch to reveal martensite.
10% Oxalic acid	10g Oxalic salt, purified water	10 second electro-etch using 8V to reveal particles. Increased time or voltage to reveal particles and martensitic lath boundaries.

11.2 THE TEST CONDITIONS OF INTEREST

The flow behaviour of tempered martensitic hot work tool steel is of interest under conditions descriptive of hot forging tooling used in a crank press to forge nickel based superalloy. The temperature range, strain rate range and fatigue conditions are determined in this section.

11.2.1 TEMPERATURE RANGE

FEA of the forming process has approximated maximum temperatures of 742°C and 682°C in the extrusion and upsetting operations respectively. These values relate to the tool surface. FEA approximates maximum substrate temperatures of 637°C and 578°C for the extrusion and upsetting operations respectively. The temperature range for mechanical testing is to vary between 250°C to 600°C to capture the behaviour of interest.

### 11.2.2 STRAIN RATE RANGE

Martensitic tool steels have been found to become strain rate sensitive at temperatures above the tempering temperature (Zhang, Delagnes et al. 2007). Strain rates of $10^{-2}s^{-1}$ are typical for mechanical presses (Zhang, Bernhart et al. 2008).

FEA has approximated die stress assuming the elastic bodies to describe the tooling. The assumption allows for the approximated die stress to be greater than the yield strength of the material. As a result, higher strain rates are approximated from this approach.

The stress and temperature at two locations in the extrusion operation have been considered. These locations relate to the extrusion radius where the tool fails through the "scoring" part defect. Figure 11-4 shows the locations of interest and also the approximated temperature, effective stress and strain rate.

Figure 11-4 shows that the maximum strain rates are around 0.3-$0.4s^{-1}$. It is known that strain rate sensitivity is only significant at temperatures higher than $500°C$ (Zhang, Delagnes et al. 2002). The average strain rate of the die at temperatures when the tool material is sensitive to strain rate is $0.04s^{-1}$. A strain rate ranging from 0.1 and 0.01 s^{-1} may characterise the behaviour of interest.
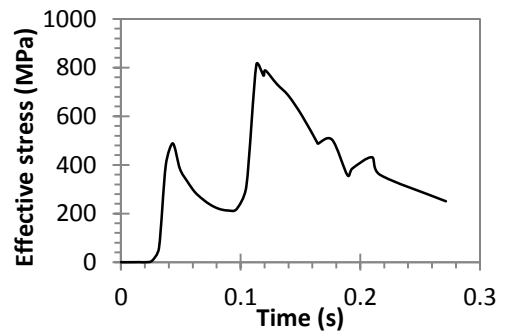
Sectioned isometric   Close up of extrusion radius
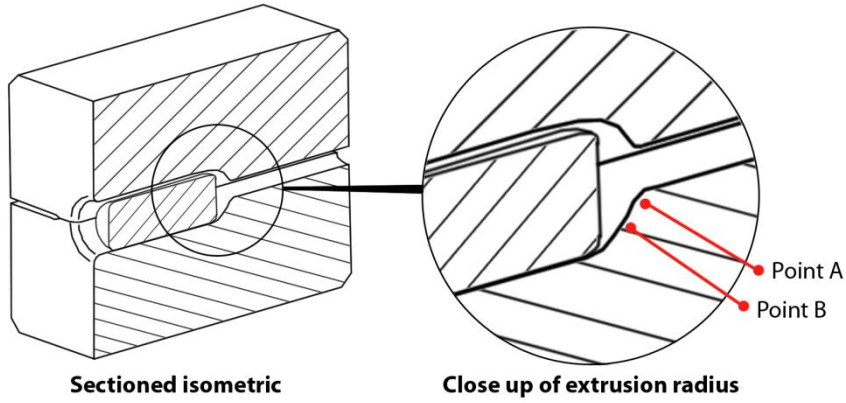
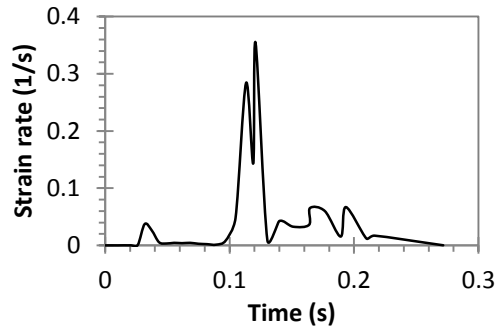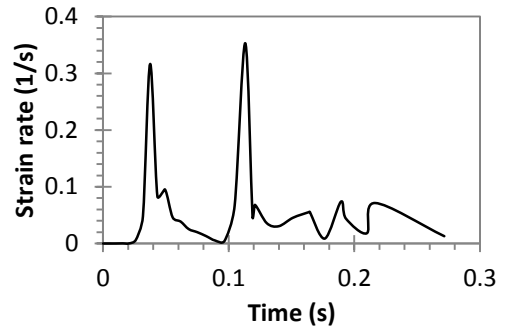B) EFFECTIVE STRESS AT POINT A
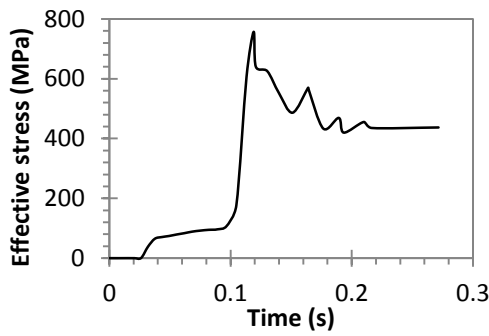
C) EFFECTIVE STRESS AT POINT B
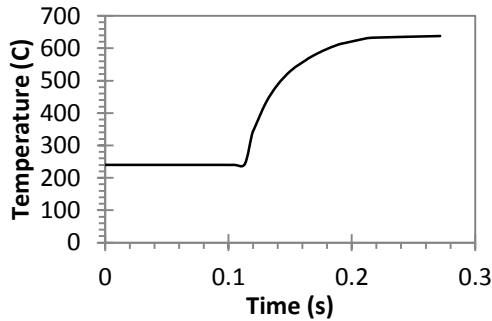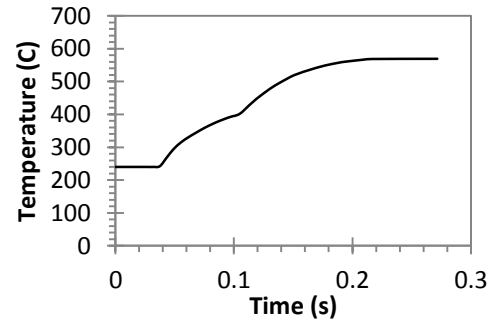

D) STRAIN RATES AT POINT A

E) STRAIN RATES AT POINT B

F) TEMPERATURES AT POINT A

G) TEMPERATURES AT POINT B

FIGURE 11-4: APPROXIMATED STRAIN RATES OF THE EXTRUSION TOOL

11.2.3 ISOTHERMAL FATIGUE TEST CONDITIONS

The impact of cyclical loading upon the mechanical strength of the tool may be examined through strain controlled or stress controlled fatigue testing. As the material displays strain rate sensitivity, strain controlled fatigue testing has been chosen.

Many authors have characterised the fatigue behaviour of AISI H11. Symmetrical tension-compression loading tests have been conducted for strain amplitudes ranging between ±0.4% and ±1.8 (Zhang, Delagnes et al. 2002; Velay, Bernhart et al. 2005). Zhang et al (2002) performed compression only tests with strain amplitudes varying between -1% and -1.25%. Tension only tests have been examined by Velay et al (2005) with tension strain amplitudes ranging from 0.4% to a maximum of 1.8%.

Symmetrical tension-compression loading has been chosen to evaluate the material behaviour. It is possible to choose different waveforms and dwell times in the loading cycle. The material can be adequately characterised using triangular waveforms with no dwell time. The strain amplitude has been chosen to obtain plastic deformation within the hysteresis loops without reducing the number of cycles to failure to below 300 cycles.